Exploring the Collective Behavior of Small Collision Systems

Igor Kozlov

Department of Physics
McGill University
Montréal, Québec
Canada

A Thesis submitted to the
Faculty of Graduate Studies and Research
in partial fulfillment of the requirements for the degree of
Doctor of Philosophy

Contents

List of Figures

List of Tables

Abstract

We performed 3+1D viscous hydrodynamic calculations of proton-lead (p-Pb) and lead-lead (Pb-Pb) collisions at top LHC (Large Hadron Collider) energy. We show that existing data from high-multiplicity p-Pb events can be well described in hydrodynamics. We proposed a more stringent test of the hydrodynamic behavior in small systems by studying the detailed momentum dependence of two-particle correlations. We calculated a relevant observable, r_n, and made predictions for its value and centrality dependence. These predictions were subsequently confirmed. This provides a non-trivial confirmation of the nature of the correlations seen in small collision systems, and a tool for determining where the hydrodynamic description stops being valid. Lastly, we probed what can be learned from r_n, finding that, contrary to most of the commonly considered observables, it is less sensitive to viscosity than to the aspects of the initial state of the system, such as the transverse length scale of the fluctuations.

Résumé

Nous avons effectué des calculs 3+1D d'hydrodynamique visceuse de collisions d'un système proton-plomb (p-Pb) et d'un système plomb-plomb (Pb-Pb) à haute énergie du LHC (Grand collisionneur de hadrons). Nous avons démontré que les données des événements p-Pb à haute multiplicité peuvent être décrites par un modèle hydrodynamique. Nous avons suggéré un test plus rigoureux de l'applicabilité de la théorie hydrodynamique à de petits systèmes, en étudiant la dépendance de corrélation de paires de particules. Nous avons calculé un observable approprié, r_n, et avons fait des prédictions sur sa valeur et sa dépendance de centralité. Ces prédictions ont été confirmées par la suite. Cela suggère que nous avons correctement décrit la nature de la corrélation constatée dans les petits systèmes de collision, et fournit un outil permettant de déterminer à partir d'où la description hydrodynamique n'est plus valide. Enfin, nous avons examiné ce que l'on pouvait apprendre de r_n, en découvrant que, contrairement à la plupart observables communément considérés, r_n est moins sensible à la viscosité qu'aux aspects de l'état initial du système, comme l'échelle de longueur transverse des fluctuations.

Acknowledgments

I am grateful to my supervisor, Prof. Charles Gale, for his help going above and beyond the academic requirements.

Novel interesting scientific results, only part of which are being presented in this thesis, were obtained by me in a stimulating atmosphere of international collaboration with research groups of McGill University, Lawrence Berkeley National Laboratory, Brookhaven National Laboratory, Relativistic Heavy Ion Collider (RHIC), the Large Hadron Collider (LHC), and with considerable support of the Compute Canada supercomputing infrastracture, and specifically McGill High Performance Computing center Guillimin – memeber of Calcul Quebec. Here I mention only people that contributed to the project being descibed in this work and I do it in hronological order. I would like to thank Dr. Matthew Luzum, Dr. Gabriel Denicol, Prof. Sangyong Jeon, Dr. Bjoern Schenke, Dr. Chun Shen, M.Sc. Chanwook Park, M.Sc. Scott MacDonald, and Dr. Sangwook Ryu, who performed UrQMD modeling based on my hydrodynamic calculations, see Fig. 4.10 and 4.11. However, I deeply appreciate all the amazing people that I met and worked with over the time of my PhD studies – I remember you all and thank you for being a bright part of my life.

I acknowledge generous funding through the Canadian Institute of Nuclear Physics scholarship, Richard H. Tomlinson Doctoral Fellowship, FQRNT Bourses de stages internationaux (Scholarships for International Internships) which made this work feasible.

Statement of originality

Contributions of the thesis to original knowledge specified by author:

- Chapter 1: A comprehensive review of the relevant literature on theoretical methods of studying of strong interactions, processes taking place in hadron collisions (that provide an experimental opportunity to test our theoretical understanding), and the possibility of quark-gluon plasma (QGP) formation in these experiments. This chapter is written by me (the manuscript author). References to the used literature are included in the text.

- Chapter 2: A detailed review of the description of heavy-ion (large) collisions within the hydrodynamical paradigm that assumes existence of the QGP phase in the system's evolution. This chapter is written by me. References to the used literature are included in the text.

- Chapter 3: An introduction of the original fluid dynamics framework that I used for the initial exploration of the applicability of hydrodynamics to small systems. It is based on the original works [139, 209] of which I am the primary author. I emphasize our following original findings:

  - Simultaneous description of high multiplicity distributions in collisions of various sizes within our model (Fig. 3.2 and Fig. 3.3)
  - Explorational analysis of the parameter space and the ability of our model to at least qualitatively describe conventional flow observables, $v_n\{2\}(p_{\mathrm{T}})$, $\bar{v}_n\{2\}$, that are considered to be evidences of collective behavior in large systems (Fig. 3.5, right panel of Fig. 3.6, left panel of Fig. 3.7)
  - Our model's ability to describe experimentally observed triangular flow similarity in (small) p-Pb and (large) Pb-Pb systems (left panel of Fig. 3.6)

- Chapter 4: Additional tests of hydrodynamics applicability to small systems. I start with a discussion of signatures of collective behavior in two-particle correlations and methods of its study, including the $r_n(p_{\mathrm{T}}^a, p_{\mathrm{T}}^b)$ observable analysis that has the ability to test hydrodynamics applicability to the description of

hadron collisions independent of the specific details of the model's implementation. References to the used literature are included in the text. The rest of the chapter is dedicated to the study of the $r_n(p_{\mathrm{T}}^a, p_{\mathrm{T}}^b)$ observable that I performed using our model. I emphasize the following original ideas and findings:

  - In [139] of which I am the primary author, we proposed to experimentally measure $r_n(p_{\mathrm{T}}^a, p_{\mathrm{T}}^b)$ in small systems and provided our *prediction* of the observable in p-Pb collision experiments at $\sqrt{s} = 5.02\,\mathrm{TeV}$. Our quantitative *prediction* was confirmed by the CMS collaboration [143], which strongly supports the hypothesis of QGP formation in small systems (Fig. 4.7)
  - Performed by me explorational analysis of the parameter space of the $r_n(p_{\mathrm{T}}^a, p_{\mathrm{T}}^b)$ revealed that contrary to the conclusions of previous studies it is more sensitive to the granularity of the initial conditions than to the shear viscosity of QGP making it a promising observable (compared to the conventional flow ones) of the initial hadron collisions stage that is currently theoretically challenging to describe (Fig. 4.6)
  - Modeling of the effects of the final state particle collisions on the $r_n(p_{\mathrm{T}}^a, p_{\mathrm{T}}^b)$ observable performed by Dr. Sangwook Ryu using UrQMD framework and based on my hydrodynamic calculations revealed that they have moderate effect on the transverse observables and do not affect any of the aforementioned conclusions (Fig. 4.10 and 4.11)

- Chapter 5: Further advancements of our hydrodynamic model. I start with an overview of the recent theoretical extensions of fluid dynamics frameworks that include bulk viscosity and longitudinal fluctuations in the initial conditions. References to the used literature are included in the text. Then I explain how I implement those ideas to extend our hydrodynamic model, compute both longitudinal and transverse observables for p-Pb collisions at $\sqrt{s} = 5.02\,\mathrm{TeV}$, compare them to experimental data. The most distinct original results include:

  - Hydrodynamic calculation of the recently measured $r_n(\eta^a, \eta^b)$ longitudinal fluctuations observable in small systems [143] that our model can reasonably describe (Fig. 5.14)
  - Exploration of the effects of bulk viscosity in small systems confirming that $r_n(p_{\mathrm{T}}^a, p_{\mathrm{T}}^b)$ is a promising probe of the initial conditions granularity (Fig. 5.10)

– Ability of our extended model to at least qualitatively describe an exhaustive list of longitudinal and transverse observables in small systems allows us to provide an estimate of the produced in p-Pb collisions matter characteristics – $\sigma = 0.4\,\mathrm{fm}$, $\eta/s = 0.08$, $\zeta/s \sim 0.03$ – that are in line with the ones obtained in the studies of large systems this way supporting the hypothesis of the plausibility of QGP formation in collisions of all sizes (Fig. 5.15)

1

Introduction

Science (from Latin scientia, meaning "knowledge") is a systematic enterprise that builds and organizes knowledge in the form of testable explanations and predictions about the Universe [1]. The goal of physical science is to understand the world at the level of inanimate subjects: matter and its interactions. To accomplish this, one creates theoretical models that are tested against experimental data.

At the present time, the most successful approach in fundamental physics is the Standard Model (SM), which is a Quantum Field Theory (QFT) that classifies all discovered elementary particles, see Fig. 1.1. It also describes three out of four know interactions (excluding the gravitational force). According to the model, all matter consists of six quarks, six leptons, and five bosons. The latter are transmitters of one of the three forces – photons for electromagnetic; W, Z-bosons for weak; and gluons for strong – and the Higgs boson is the "generator" of effective masses for those model's constituents that can interact. A scheme of the allowed interactions between particles is represented in Fig. 1.2.

The SM is specifically valued for its predictive power. Its formulation led to the discovery of multiple particles [3, 4], including the top quark [5, 6], tau neutrino [7], and the Higgs boson [8].

However, despite all its successes, this theory faces a number of challenges. For example, the experimentally observed neutrino oscillations [9, 10] prove that neutrinos have masses, which contradicts the SM. Similarly, SM does not include the theory of General Relativity, which was directly confirmed when gravitational waves were registered [11]. Moreover, cosmological observations suggest that described with the

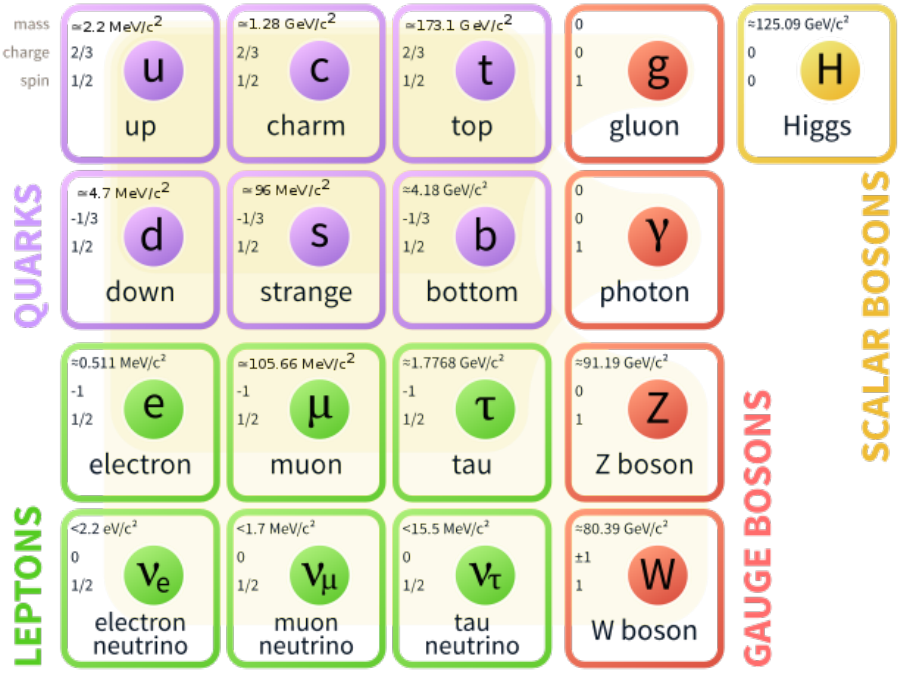

Figure 1.1: Graphical representation of the SM elementary particles and their properties (mass, electric charge, and spin are correspondingly measured in MeV/c^2, units of positron charge, and magnitude of $\hbar$). Figure from [2].

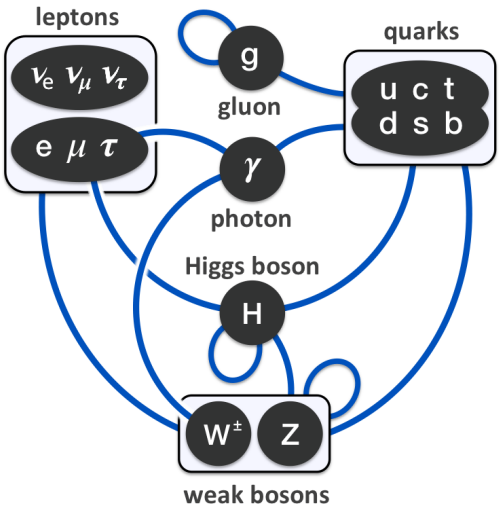

Figure 1.2: Graphical representation of the allowed by the SM elementary particles interactions. Figure from [2].

SM matter composes only about 5% of the Universe content [12].

Thus, SM is an effective theory and further attempts towards creation of fundamental theories are required. One of the candidates for the "Theory of everything" is String theory (ST). It states that everything consists of strings, which are one-dimensional energy objects that propagate through space and interact with other similar entities. Different excitations of strings represent all elementary particles and transmitters of all four interactions. This idea is appealing already because it addresses the problem of the divergences emerging in all QFTs, which is due to the zero dimensionality of particles [13, 14]. However, it is very challenging to observe the internal structure of elementary matter constituents, which is expected to be of the Planck length (10^{-35} meter) [15]. To get a sense of the energies at which particles will reveal their dimensional (string) properties we can turn to the Heisenberg principle, which states that the collision energy is inverse proportional to the resolution magnitude of the experimental setup. We brought up here the notion of a collision for two reasons. First, to discern internal structure of any object we need to use another object as a (detector) tool. Second, the most impactful degree of interaction that can currently be obtained in a controlled fashion takes place at "colliders" – machines built to smash particles against each other. Nowadays the largest one is the Large Hadron Collider (LHC) operating in CERN, Geneva. This facility has a vibrant program and hosts several collaborations, including ALICE, ATLAS, and CMS, which we will talk about later. The maximum collision energy per particle pair[1] achieved in these studies is of the order of $\sim 10^{12}$GeV (about a trillion times higher than the temperature/kinetic energy of particles inside the Sun), which allows one to resolve distances of $\sim 10^{-15}$ meter (or $\sim$ 1 fm – size of a proton). This is, however, ten million times smaller than the Planck (energy) scale ($\sim 10^{19}$GeV) – energy necessary to reveal the intrinsic dimensional nature of string objects (if they exist). Thus, a direct confirmation of ST is currently out of reach. However, one of the indirect

[1]One of the most common collided particles is a proton, and thus proton-proton (p-p) collisions is a common reference.

evidences supporting this paradigm would be discovery of Supersymmetry (SUSY), which is inherent to the ST and its low energy approximation of Quantum Gravity. SUSY among other things helps to resolve the theoretically unsatisfying assumption of fine tuning that is currently required in the SM to explain the large separation of scales between the mass of the Higgs boson and the Planck energy, which is also called the Hierarchy problem. The Minimal Supersymmetric Standard Model [16], which provides one of the least radical extensions of the SM that includes SUSY, predicts existence of new particles – superpartners of the SM constituents. Those, however, have not been found yet, which means that the ST paradigm should still be considered as an abstract concept, however appealing.

Although, the SM is an effective theory, it is plausible that some of its components could be treated as fundamental. If they are free of theoretical inconsistencies, they could be low energy approximations of the fundamental theory that has not been found yet. Quantum Chromodynamics (QCD) that describes the physics of strong interactions is considered to be an element of the SM that can be considered a fundamental theory. This allows, in principle, to describe any strong process at a desired accuracy. However, in practice, this is challenging, because of the complexity of the calculations. The theory is non-linear due to self-interaction of gluons, see Fig. 1.2. This in particular leads to the emergence of such characteristic QCD effects as asymptotic freedom and confinement, which we will discuss in more details later. Thus, in order to study phenomena involving strong interactions, one uses various effective approaches/models, which are valid only within certain applicability domains. In this work, we will study a recently discovered (experimentally) state of matter – quark-gluon plasma (QGP) – which was the dominant form of matter during the first microseconds after the Big Bang. This will require application of various effective frameworks to study QCD (as strong interactions play the key role in the process). Thus, in Section 1.1 we will describe them. Then, in Section 1.2 we will discuss how the process of QGP formation happens in experiments. Finally, in Section 1.3 we will explain the challenges that emerged in the recent experimental studies of QGP and

outline how we aim to address them in this work.

1.1 Theoretical frameworks of studying QCD

QCD [17, 18] is the accepted theory of strong interaction and it is described with the following action:

$$S \equiv S_{\mathrm{QCD}} = \int d^4x \left(\bar{\psi}_i \left(i(\gamma^\mu D_\mu)_{ij} - m\,\delta_{ij} \right) \psi_j - \frac{1}{4} G^a_{\mu\nu} G^{\mu\nu}_a \right), \tag{1.1}$$

$$G^a_{\mu\nu} = \partial_\mu A^a_\nu - \partial_\nu A^a_\mu + g f^{abc} A^b_\mu A^c_\nu, \quad D_\mu = \partial_\mu - ig A^a_\mu t^a, \tag{1.2}$$

where the ψ_i field describes quark, and A^a_μ are gluon fields; $i, j = 1, 2, 3$ are flavor indices; $a, b, c = 1, \ldots 8$ enumerate color degrees of freedom; $\mu, \nu = 0, \ldots 3$ – Minkowski (one) time and (three) space coordinates. t^a and f^{abc} are respectively generators and structure constants of the internal color $SU(3)$ symmetry – their role is to relate transformations in color and Minkowski space. Finally, g is the strong coupling.

Graphical representation of strong interactions is shown in Fig. 1.3. It can be obtained by matching corresponding contributions to the scattering amplitudes defining probabilities of arbitrary quantum processes [21, 22] that are calculated in the S-matrix [23, 24] and the Path Integral [25] formalisms. While the former method is based on evaluating coordinate space integrals over products of (ψ and A) terms constituting the integrand of equation (1.1), the latter one implies summation over all possible "histories" of transition between the initial and the final states of the considered process[1]. Those can involve multiple gluon and quark emissions. Feynman rules determine one-to-one correspondence between each such history and the (ψ and A) terms whose product should be calculated to determine the probability of such scenario.

Note the consistency between the conclusions one can draw from Fig. 1.3 and Fig. 1.2. For example, gluons can interact with quarks and other gluons, see quark-gluon, 3- and 4-gluon vertices in Fig. 1.3. Note that the latter two diagrams could be interpreted as a process of gluon emission from a quark and another gluon respectively.

[1] See also equation (1.10).

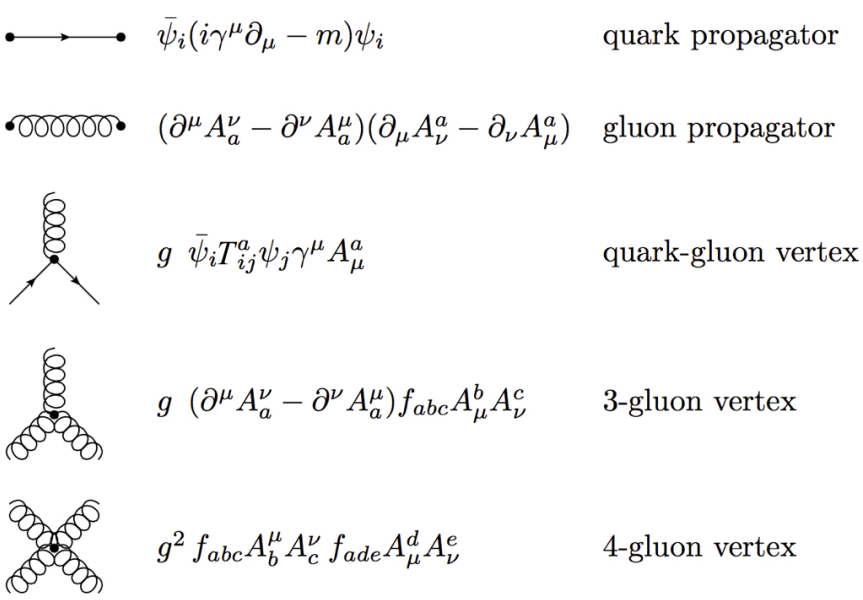

Figure 1.3: Graphical representation of the strongly interacting particles' dynamics, which is known as Feynman diagrams [19]. Solid lines correspond to quarks and curly lines correspond to gluons. Figure from [20].

Corresponding Lagrangian terms have a strong coupling prefactor, g. Thus, its value directly affects the rate of the strong processes. For that reason it is important to study it in more details. An effective approach to do it at small values of g is the perturbative technique.

1.1.1 Perturbative QCD

We will start this section with the discussion of the process of charge screening, as it helps to understand the idea behind the energy dependence (or "running") of the strong coupling [26].

The parameter g that enters (1.1) is known as the "bare" coupling. Feynman rules suggest that it should be equal to the quark's and gluon's charge, see quark-gluon and 3-gluon vertices in Fig. 1.3. However, another quantity – the "dressed" (or "running") charge – is actually what is measured in experiments. To estimate some (source) particle's charge, one scatters off it another (probe) particle and observes

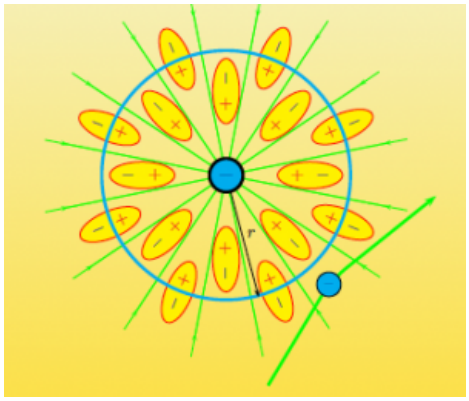

Figure 1.4: Illustration of the scattering process that can be used to probe one particle's electric charge by another one. Figure from [27]. The experimental set-up assumes that the particles (represented with circles) pass each other at a distance r. Dipoles denote electron-positron pairs that get created (and annihilated) from (into) the vacuum.

how the trajectory of the latter changes due to the presence of the former. In general, the magnitude of this effect can depend on the distance between the source and the probe particles, or equivalently on their collision energy-momentum, as it defines how close particles approach each other. Let us illustrate this idea using electro-magnetic interactions, see Fig. 1.4.

It is known that the magnitude of the particle's electric field in dielectric materials decreases due to the orientation polarization effect that takes place when matter constituents' fields, which can be well described in the dipole approximation, get aligned to oppose the external field. Similar phenomenon takes place when a particle is embedded in vacuum. Due to quantum effects, electron-positron pairs, which resemble dipoles, get randomly created. They get polarized in the particle's field, reducing it.

Because the process of vacuum polarization is a dynamical quantum phenomenon, one should utilize QFT framework to describe it. In this approach, the quantum correction to the interaction between two particles is determined by the process in which the photon emitted by the source creates an electro-positron pair that subsequently annihilates into another photon that is absorbed by the probe. Scenarios involving

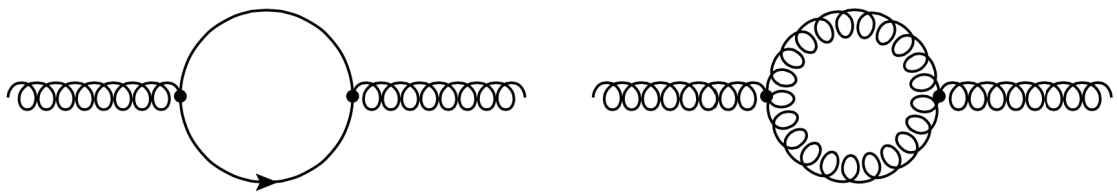

(a) (b)

Figure 1.5: Feynman diagrams of leading-order processes causing the screening of the strong charge in QCD. Process (a) corresponds to the emission of the quark-anti-quark pair from a propagating gluon and involves two "quark-gluon" vertices. Process (b) corresponds to the emission of the pair of gluons from a propagating gluon and involves two "3-gluon" vertices.

multiple annihilation processes are also possible, but their probability is proportional to higher orders in the coupling constant, and thus their contribution is usually accounted for order by order. The dynamics of the photon exchange in vacuum depends on its energy, Q. One absorbs this dependence into the definition of the "running" coupling, $g(Q)$. Thus, effectively the particle's charge depends on the energy of the collision in which it is probed.

Similar effect takes place in QCD vacuum with strong interaction. However, in this case the gluon that was emitted by the source particle can reach the probe particle after creation and annihilation of either a quark-anti-quark pair or a pair of gluons, see Fig. 1.5 (a) and (b) correspondingly. To account for these effects one needs to calculate the so-called β function of the renormalized ("running") coupling α:

$$\alpha \equiv \frac{g(Q)^2}{4\pi}, \tag{1.3}$$

$$\beta(\alpha) = -(b_1 \cdot \alpha^2 + b_2 \cdot \alpha^3 + \dots), \tag{1.4}$$

$$b_1 = \frac{11C_A - 4n_f T_R}{12\pi} = \frac{33 - 2n_f}{12\pi}, \tag{1.5}$$

$$b_2 = \frac{17C_A^2 - 4n_f T_R(10C_A + 6C_F)}{24\pi^2} = \frac{153 - 19n_f}{24\pi^4}, \tag{1.6}$$

where C_A, T_R are so-called Casimir operators, which describe the color group $SU(N_c)$ ($N_c = 3$ for QCD); N_f is the number of flavors in the theory (for QCD N_f depends on the energy scale, its maximum value is 6); b_n coefficients correspond to the n-th order loop contributions (here calculated in the widely used $\overline{MS}$ scheme [28]). We provide results of the 1st and 2nd order loop calculations (1.5-1.6). They indicate that the beta function of QCD is negative – qualitatively this is the most important conclusion[1]. To get a quantitative estimate we can now substitute the derived expression (1.4) into the renormalization group equation (1.7) that governs physical variables' response to the change of the energy scale Q, [30, 31]:

$$Q^2 \frac{\partial \alpha}{\partial Q^2} = \beta(\alpha) = -(b_1 \alpha^2 + b_2 \alpha^3 + \dots) < 0. \tag{1.7}$$

From the negativity of the QCD $\beta(\alpha)$ function (1.4) and the form of equation (1.7) one can conclude that at large energy scale interaction coupling α (and thus gauge coupling g) considerably decrease in size. This phenomenon is called asymptotic freedom [17, 18] and is closely related to confinement. Before getting to its description in the next section, let us observe the following. First, there is a spectacular agreement between the predicted behavior of the running coupling and the results of its indirect extraction using perturbative methods from multiple experimental results that holds across four orders of magnitude in the exchange momentum, Q, see Fig. 1.6. This clearly advocates in favor of QCD validity and supports the applicability of perturbative techniques in the region of high energy/momentum transfer. Second, from the dimensional analysis it follows that, as α is a dimensionless quantity and Q is measured in units of energy, there should emerge another dimensional quantity, Λ_{QCD}. It should enter the solution of equation (1.7), which is defining the "running" of the renormalized coupling, in the following way:

$$\alpha = \alpha \left(\frac{Q}{\Lambda_{QCD}} \right). \tag{1.8}$$

[1]Noteworthy, the sign of the β functions of the electro-magnetic and the weak interactions is positive. Thus, these theories (unlike QCD) encounter the "Landau pole" problem [29] which predicts infinite growth of the coupling constant if measured at some high (but finite) energy. This suggests that the SM model should be extended to describe processes happening at the energies above $\sim 10^{16}$ GeV.

This parameter Λ_{QCD}[1] is estimated to be of the order of ~ 0.2GeV (or ~ 1fm in spacial dimension units) and it sets the scale of the confinement-deconfinement transition.

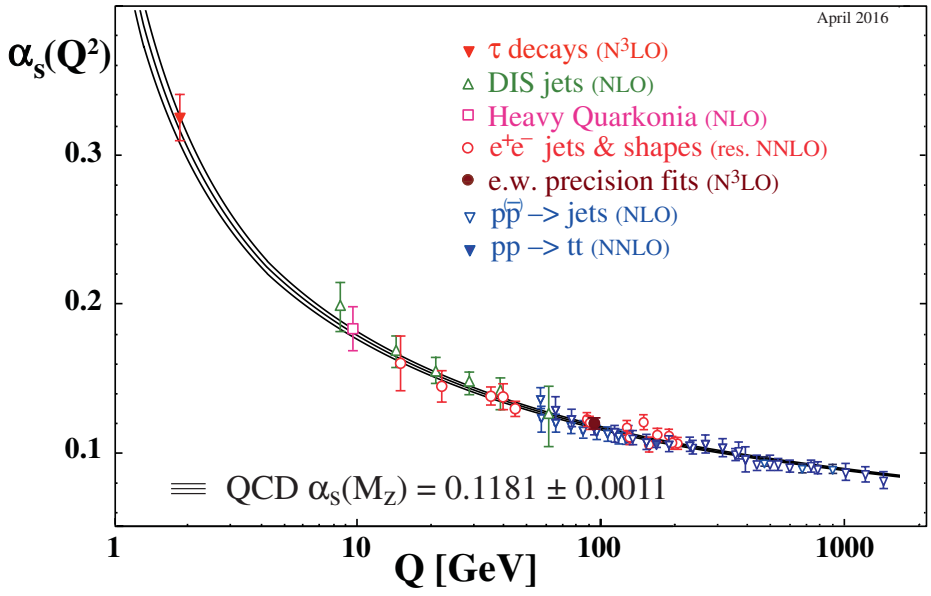

Figure 1.6: Summary of measurements of α_s as a function of the energy scale Q. The respective degree of QCD perturbation theory used in the extraction of α_s is indicated in brackets (NLO: next-to-leading order; NNLO: next-to-next-to leading order; res. NNLO: NNLO matched with resumed next-to-leading logs; N3LO:next-to-NNLO). Figure from [34].

1.1.2 Lattice QCD

Despite the success of the perturbative technique in the regime of asymptotic freedom it is clear that this approach can not be applied ubiquitously. For example, the nature of the hadrons' mass formation is strictly non-perturbative. Specifically,

[1]Existence of Λ_{QCD} anomalously breaks conformal invariance [32]. Its appearance is an example of the dynamical scale generation in renormalization group equations, which is also known as dimensional transmutation [33]. We will observe this phenomenon several times in this work.

dependence of the π-meson mass on the coupling constant α can not be represented as a perturbative power series:

$$m_\pi \sim f\left(-\frac{C}{\alpha}\right) \not\sim \sum_{i=0}^{\infty} a_i \, \alpha^i, \tag{1.9}$$

where f is an analytic function, C and a_i $(i = 0, \ldots \infty)$ are some constants [35].

This behavior has to deal with the already mentioned previously confinement phenomenon: color charged (strongly interacting sub)particles (quarks and gluons) at normal conditions are not observed individually. They merge together into color-neutral compounds (hadrons). If one takes a color-neutral particle (say π_0 meson) and tries to pull its color charged constituents (u and $\bar{u}$ quarks) apart one will result with having two color-neutral particles (π_- and π_+ mesons): it will be more energy efficient to create a color–anti-color pair from vacuum ($d\bar{d}$ quark pair) in between pulled apart constituents (and thus form two color-neutral objects: $d\bar{u}$ and $u\bar{d}$ which are exactly π_- and π_+ mesons) then to further increase the separation distance (between u and $\bar{u}$ quarks)[1]. On the contrary, at high energies/temperatures[2] quarks and gluons, which as we mentioned at normal conditions are "confined" within particles (hadrons) as its constituents, become free and travel over macroscopic distances. This state of matter is called QGP. It was the dominant form of matter during the first microseconds after the Big Bang. That is one of the main reasons its study draws considerable interest. It is worth noting that there are very strong indications that QGP is produced in the recent Heavy Ion Collisions (HIC) experiments [36]. This makes the HIC research program to be the only controlled way of directly studying processes taking place during the formation of the Universe.

In principle, knowing the action (1.1), it is theoretically possible to calculate every aspect of QCD dynamics numerically by taking advantage of the Feynman path integral formulation of QFT [25] and Monte-Carlo methods of evaluating integrals in multiple dimensions [37]. In quantum theory every physical observable corresponds

[1] This mechanism is related to Fig. 1.6: at small momentum, Q, (or at large distance) $\alpha(Q)$ will grow.
[2] We will later discuss the notion of thermalization, and how it relates energy and temperature in HIC.

to some operator – let us call it O. An interesting quantity to calculate is a Green's function, which describes how physical observable O measured at space-time coordinates x and y are related. To obtain it, one can first calculate a partition function $Z[J]$ (or generating functional at zero temperature):

$$Z[J] = \int \mathcal{D}[A\psi\bar{\psi}] e^{i(S+\int d^4x J(x)\cdot O(x))}, \tag{1.10}$$

where J is a current corresponding to the conservation of a certain O-related symmetry/charge (e.g. baryon charge); $\mathcal{D}$ is a path integral measure that indicates that averaging of the "$J \cdot O$" term with a weight of e^{iS} goes over all possible field configurations, $A\psi\bar{\psi}$. Then evaluation of any (say two-point) Green's function is straightforward:

$$< T\, O(x)O(y) >= \left. \frac{\delta^2 \ln Z[J]}{i\delta J(x)\, i\delta J(y)} \right|_{J=0}, \tag{1.11}$$

where T stands for time-ordering of space-time coordinates x and y; and δ-s denote functional derivatives.

However, in practice numerical calculation of (1.10) is extremely challenging due to the highly oscillating integrand , which makes application of random sampling Monte-Carlo methods of integration in multi-dimensional[1] space challenging. Quantity e^{-S} is relatively better behaved as it takes only positive values, and for that reason does not vanish during averaging.

Thus, in lattice QCD it is more common to perform a Wick rotation, [38]:

$$t \to -i\tau, \qquad e^{iS} \to e^{-S_E}, \qquad < T\, O(x)O(y) > \longrightarrow < O(x)O(y) >_T . \tag{1.12}$$

This allows to achieve desired behavior of the integrand (1.10) but at the expense of turning to imaginary time. It can be shown that the new "Wick rotated" theory describes statistical mechanics of a field system in three dimensional Euclidean space at thermal equilibrium, which means that the system is at temperature T, all energy/matter flows are absent, and fundamental thermodynamic relations apply. Noteworthy, the new system, which is described with Euclidean action S_E, is static.

[1] To be precise it is infinite-dimensional as one needs to consider all possible field configurations.

τ no more represents time evolution – it is a compactified variable related to the value of the system's (inverse) temperature T ($\tau \in [0, 1/T]$). Derivatives of partition function (1.10) subjected to the Wick rotation instead of Green's functions (1.11) will evaluate correlators[1].

In this way the desired outcome is achieved: Z is now real, positive, and attainable to be calculated on the "lattice". This allows one to derive from the "first principles", (1.1), such important thermodynamical properties of QCD as energy density ϵ and pressure P:

$$\epsilon = -\frac{1}{V}\frac{\partial \ln Z}{\partial \beta}, \qquad P = T\frac{\partial \ln Z}{\partial V}, \tag{1.13}$$

where $\beta = 1/T$, and V is the system's volume. See Fig. 1.7.

To summarize, lattice theory attempts a head-on approach to the solution of QCD using numerical integration methods. The main advantage of this approach is that the exact theory of strong interactions is probed without any simplifying approximations. This allows to calculate even non-perturbative observables. On Fig. 1.8 (a), one can see results of the running coupling evaluation on the lattice. One of the advantages of this result is that it allows to assess the precision of the perturbative techniques in its applicability region, $\mu > \Lambda_{QCD}$. On Fig. 1.8 (b), one can find hadron spectrum calculated directly from the action, (1.1). Provided comparison of this result to experimental data supports the validity of QCD as a theory of strong interactions.

The main downside of the method is that lattice computations are well suited for evaluation of static quantities only. Even calculations of quasi-stable resonance[2] masses face considerable challenges [43]. Their decay widths should have imaginary contribution [44]. However, one performs Wick rotation on the lattice, in the first place, to shift calculations to the real numbers field. In order to overcome this limitation there were developed techniques of reconstruction of the real time spectral

[1] $< O >_T$ stands for the value of physical quantity O measured when the entire system is embedded into a heat bath at temperature T, while $< O >$ denotes vacuum expectation (or Green function) of the same observable.

[2] Quasi-stable resonances are particles with finite lifetime of the order of $\sim 1\,\text{fm}$ [34]. They subsequently decay strongly into stable particles.

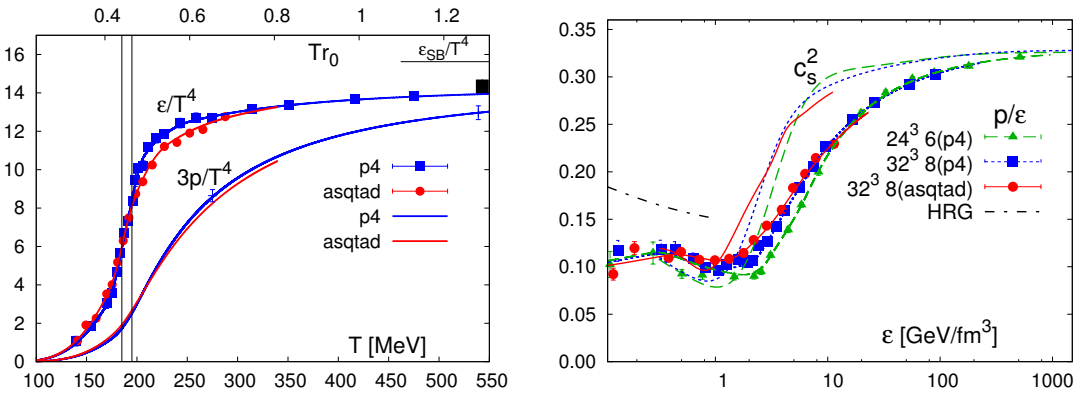

(a) (b)

Figure 1.7: Energy density and three times the pressure calculated in units of temperature to the fourth power on the lattice using two (numerically) different (but physically equivalent) methods denoted as "p4" and "asqtad" (left). The black bars at high temperatures indicate the systematic shift of data that would arise from matching to a hadron resonance gas model (HRG). The vertical band indicates the approximate location of the confinement-deconfinement transition region. The right hand figure shows pressure divided by energy density (p/ϵ) and the square of the velocity of sound (c_s^2). Lines without data points give the square of the velocity of sound calculated analytically from $c_s^2 = \frac{\partial P}{\partial \epsilon}$ using the interpolating curves for ϵ/T^4 and P/T^4. The dashed-dotted line at low temperatures gives the result for p/ϵ from a HRG. Figures from [39].

function, ρ, from Euclidean correlators and trace anomaly[1] [45, 46, 47]. This allowed to calculate, for example, temperature dependence of bulk viscosity ζ near the confinement-deconfinement phase transition, [48, 49]:

$$\zeta = \frac{1}{9} \lim_{\omega \to 0} \lim_{\mathbf{k} \to 0} \frac{1}{\omega} \rho^{ii,jj}(\omega, \mathbf{k}), \tag{1.14}$$

where ρ is represented in momentum space, $(\omega, \mathbf{k})$, with Latin indices, i/j, denoting spatial coordinates and Einstein summation convention is assumed. Still, the

[1] In a conformal theory energy-momentum is traceless. However, Λ_{QCD} breaks conformal invariance and thus the value of $\epsilon - 3P$ is not zero.

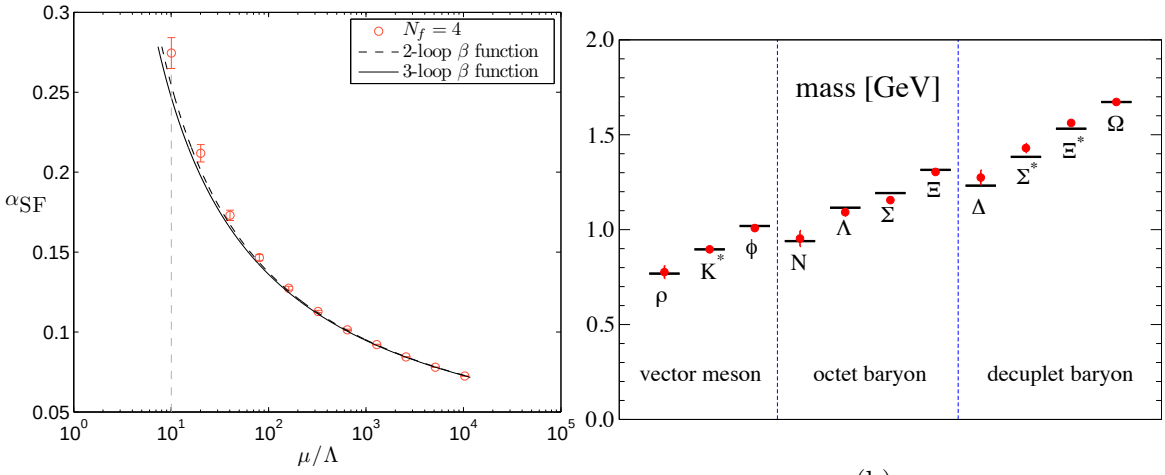

(a) (b)

Figure 1.8: Panel (a): Dependence of the running coupling α on the energy scale. Lattice results [40] are compared to the perturbative calculation in the 2-nd and 3-rd loop order [28]. Figure from [40]. Panel (b): Light hadron spectrum evaluated on the lattice by the PACS-CS collaboration [41] and measured experimentally by the Particle Data Group [42]. Figure from [41].

unavoidable difficulty of extracting a continuous function from a finite discrete set of noisy lattice data makes this calculations challenging and systematic errors large. It appears that in order to obtain the desired transport coefficient with reasonable accuracy, one has to make certain assumptions about the form of the spectral function. But this contradicts the initial intention of using lattice QCD as a method of calculating observables based on first principles.

This is a shortcoming of the method, because one is specifically interested in studying the dynamical properties of QGP. As we know, the Universe was not created in equilibrium. Rather it was quickly expanding, cooling down, and possibly undergoing phase transition to the confinement phase. This QCD regime is characterized by a growing value of the running coupling α, which makes techniques suited for description of strongly coupled field theories particularly interesting. One of such frameworks that allows to calculate dynamical properties of strongly coupled QFTs that are very similar to QCD is called the AdS/CFT correspondence.

1.1.3 AdS/CFT correspondence

It was observed that there is a direct correspondence between the evolution of strongly coupled field theories and a gravitational theory in an extended number of dimensions[1] [50]. The entire class of these approaches is referred to as AdS/CFT correspondence/duality. It was found that a conformal field theory (CFT) of $\mathcal{N} = 4$ Super-Yang-Mills (SYM) in flat $R^{3,1}$ geometry[2] with metric

$$ds^2 = (-dt^2 + d\mathbf{x}^2) \tag{1.15}$$

is dual to the theory of quantum gravity in ten-dimensional $AdS_5 \times S_5$ space[3]

$$ds^2_{10} = \frac{r^2}{L^2}(-dt^2 + d\mathbf{x}^2) + \frac{L^2}{r^2}dr^2 + L^2 d\Omega^2_5, \tag{1.16}$$

where L is a constant related to the string tension, and couplings of the ten-dimensional supergravity and SYM. See Fig. 1.9.

Thus, in order to calculate any physical observable in a QFT theory one could instead obtain a dual quantity in AdS. For example, viscosity of CFT could be evaluated in AdS by calculating Green's function of the gravitational stress-energy tensor. It was done in [51] by additionally taking advantage of the Kubo formula that relates time-correlation function[4] to the value of this transport coefficient:

$$\chi = -\lim_{\omega\to 0}\lim_{\vec{k}\to 0}\frac{1}{\omega}\mathrm{Im}G_R(\omega, \vec{k}). \tag{1.17}$$

The biggest advantage of this approach is that the strong coupling regime of CFT/QFT corresponds to the weak one in AdS and thus perturbation technique is applicable on the gravity side.[5] The dictionary "translating" observables from one language (CFT)

[1] This interesting perspective came from the studies of the ST and its low energy limit described by quantum supergravity. This suggests that an extension of the SM that includes gravitational effects might be a ST.

[2] This is the regular three space, $\mathbf{x}$, and one time, t, dimensional geometry that we live in.

[3] For brevity, one usually omits the S_5 when talking about AdS/CFT.

[4] To be precise, it is the retarded Green's function in momentum space, which is closely related to the spectral function ρ that we discussed in Section 1.1.2, see Equation (1.14).

[5] With the proviso that perturbation theory works on the gravity side – see discussion of (1.9). Fortunately, it does for a wide range of observables, see further discussion.

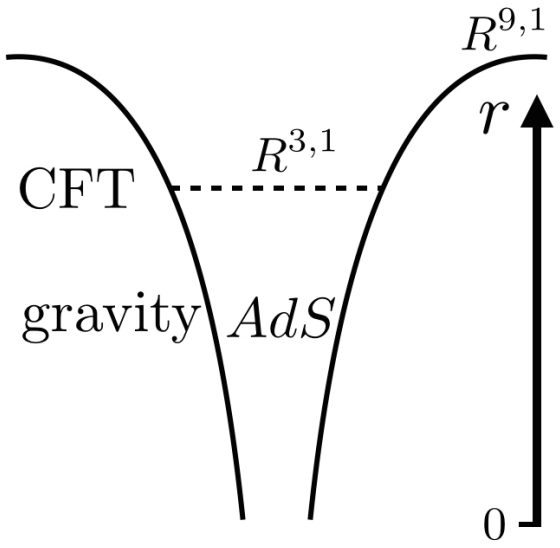

Figure 1.9: Illustration of embedding of $R^{3,1}$ into $AdS_5 \times S_5$. There is a region of ten dimensional $R^{9,1}$ flat space, where the geometry is curved and can be described with $AdS_5 \times S_5$ metric, (1.16). Gravitation acts in the entire $AdS_5 \times S_5$ space, while CFT "lives" only on its $r \to \infty$ border, which has the metric of the $R^{3,1}$ flat space, (1.15).

into another (AdS) is growing and many interesting results have been obtained. For example, see calculation of the Green's functions [52, 53].

However, there are still important challenges to be faced. First, although CFT is a strongly interacting theory and hence it could be relevant for confinement, it is not exactly QCD. For example, in CFT the β function is exactly 0, which means that the gauge coupling is not running. Thus, this theory lacks confinement-deconfinement phase transition. For the same reason, it does not have such important quantity of QGP dynamics as bulk viscosity. In CFT it is exactly zero, while lattice calculations show its non-trivial behavior in QCD and particularly near the confinement-deconfinement phase transition. To overcome these difficulties, the class of "CFT" theories that have a string dual is being constantly extended. Modifications include addition of quarks (fundamental matter [54]); discretization of the excitations' spectrum, which is necessary for confinement and breaking of conformality ("hard wall" and Polchinski-Strassler background [55, 56]); inclusion of temperature in order to

reproduce QGP state of matter (Witten's black hole and Sakai-Sugimoto model [57]). Even though the dual of exact QCD have not been found yet, it was shown that the high temperature behavior of all confining theories demonstrates similarity and thus AdS/CFT correspondence provides an excellent tool for studying QGP. Moreover, the already mentioned lattice calculation of trace anomaly indicates that at high enough temperatures QCD approaches CFT, as $(\epsilon - 3P) \to 0$, see Fig. 1.7. In this way interesting estimates of the values of shear and bulk viscosities have been obtained in[1] theories with a QCD-like equation of state, [58, 59, 60, 61, 62, 63]:

$$\frac{\eta}{s} \gtrsim \frac{1}{4\pi}, \qquad \frac{\zeta}{\eta} \gtrsim 2\left(\frac{1}{3} - c_s^2\right), \tag{1.18}$$

where η and ζ are values of shear and bulk viscosities; s is entropy density; c_s is the speed of sound.

We discussed an number of approaches that are suitable for studying various aspects of QCD (asymptotic freedom and confinement, equation of state, transport coefficients). However, none of them can alone describe dynamics of matter undergoing substantial geometrical and phase transformations that are taking place in HIC experiments. One needs a framework that would be able to sew together all analytically/numerically accessible (weak/strong, static/dynamic) regimes of QCD and provide description of strongly interacting medium in the transition region. This is the only way to compare our current theoretical understanding of the processes taking place at high energies/temperatures to experimental data, test existing models, and advance our knowledge. Importantly, this method should also be able to treat time-dependent scenario of QCD matter evolution. This is when the effective theory of fluid dynamics comes into play.

1.1.4 Hydrodynamics

Hydrodynamics describes collective behavior of medium that can interact so strongly that it is impossible to disentangle individual quasi-particles. The condition of its

[1] Currently, QCD has no dual theory. There are only string theories that are "QCD-like".

applicability can be defined with the Knudsen number:

$$Kn = \frac{\lambda}{L}, \tag{1.19}$$

which is the ratio of microscopic, λ, and macroscopic, L, scales of the system dynamics. As hydrodynamics describes evolution of continuous medium, Kn should not exceed the value of one. In a sense, hydrodynamics considers a coarse-grained image of the underlying constituents' dynamics. Hence, it does not have the means of studying the process at micro level, e.g. at distances smaller than λ.

Equations of motion of (ideal) hydrodynamics are well known and represent conservation laws of energy and momentum coupled to the assumption of local thermal equilibrium, [64]:

$$\partial_\mu T^{\mu\nu}_{\text{ideal}} = 0\,, \tag{1.20}$$

where $T^{\mu\nu}_{\text{ideal}}$ is the ideal, i.e. locally thermally equilibrated, energy-momentum tensor.[1] Thus, (1.20) describes four conservation equations: one for energy and three for spatial components of the momentum. As mentioned above, these equations describe evolution of a system at the macro scale, i.e. at large wavelength or small momentum. Hydro is valid without knowing the micro-dynamics. However, to do any calculations, one needs to specify the equation of state and the transport coefficients of the fluid. This is where perturbative QCD, lattice QCD, and AdS/CFT results come in handy.

In the case of HIC, we are interested in the evolution of strongly interacting systems that do not necessarily start in local thermodynamical equilibrium. Thus, we want to relax the aforementioned assumption and consider systems that are close to local equilibrium:

$$T^{\mu\nu} = T^{\mu\nu}_{\text{ideal}} + \Pi^{\mu\nu}, \tag{1.21}$$

where $\Pi^{\mu\nu}$ is the viscosity tensor that describes the out-of-equilibrium correction to the ideal energy-momentum one. Usually it is divided into two parts:

$$\Pi^{\mu\nu} = \pi^{\mu\nu} + \Pi\ \Delta^{\mu\nu}, \tag{1.22}$$

[1] Einstein notation of summation over repeated Greek indices is assumed in (1.20) and further. Greek indices μ/ν take values $0, \ldots 3$ enumerating time-space coordinates. They can be contracted with the metric tensor $g^{\mu\nu} = \text{diag}(1, -1, -1, -1)$.

which correspond to the shear and bulk contributions respectively. $\Delta^{\mu\nu} = g^{\mu\nu} - u^\mu u^\nu$ is a projection operator on the fluid velocity vector, u^μ. To first order[1], this leads to the well known viscous hydrodynamics Navier-Stokes (NS) equations of motion [64, 66]. Those have to be complimented with the generalized second law of thermodynamics, which constitutes that the entropy of any out of equilibrium system can not decrease:

$$\partial_\mu s^\mu \geq 0\,, \tag{1.23}$$

where s^μ is the Lorentz-covariant generalization of the entropy current. From the physical point of view, this is necessary to break the time symmetry of the "mechanical" conservation equations of motion and show the only "valid" time direction for the evolution of an out-of-equilibrium system. In this way energy-momentum conservation equations get extended with ones for the shear and bulk viscosity tensors:

$$\pi^{\mu\nu} = \eta \nabla^{<\mu} u^{\nu>}\,, \quad \Pi = -\zeta \partial_\mu u^\mu\,, \tag{1.24}$$

where ∇^μ is a projected spatial gradient and $\nabla^{<\mu} u^{\nu>}$ stands for the traceless part of symmetrized velocity gradient tensor $\nabla^\mu u^\nu$. Specifically, we use the following notations:

$$\nabla^\mu = \Delta^{\mu\nu}\partial_\nu, \quad A^{\langle\mu\nu\rangle} \equiv \Delta^{\mu\nu}_{\alpha\beta} A^{\alpha\beta}, \quad \Delta^{\mu\nu}_{\alpha\beta} \equiv \frac{1}{2}\left(\Delta^\mu_\alpha \Delta^\nu_\beta + \Delta^\mu_\beta \Delta^\nu_\alpha - \frac{2}{3}\Delta^{\mu\nu}\Delta_{\alpha\beta}\right). \tag{1.25}$$

However, it was observed that NS equations of motion contain certain problems. Specifically, they allow for an onset of short wavelength excitations propagating with super-luminal velocities [67, 68]. In principle, this is not a shortcoming of the hydrodynamical theory as it claims to correctly describe only long wavelength evolution. However, it would create challenges when solving equations numerically in the case of relativistic applications. For that reason gradient expansion of fluid dynamics is usually extended to include second order corrections. If smaller than the first order ones, they should not change the long wavelength behavior of the system. At the same time they suppress the unphysical modes, successfully fix the problem of

[1] Expansions goes in the orders of Kn or spatial gradients. Time derivatives get substituted with spatial ones by the means of using the lower order equations of motion [65].

super-luminal excitations, and make numerical treatment of fluid dynamics feasible. Corresponding modification of equations (1.24) is referred to as Müller-Israel-Stewart (MIS) equations [69, 70].

It is worth noting that the discussed in Section 1.1.3 correspondence between "fundamental" gravitational theories and quantum field theories suggests that "QGP" of CFT should also have a regime that could be described with hydrodynamics. Indeed, following the mentioned above prescription of expanding energy-momentum tensor in higher order gradients, it is possible to obtain equation of conformal hydrodynamics. They reproduce the form of the regular fluid dynamics equations, but possess an additional symmetry with respect to the Weyl transformations.[1] This essential in string theory conformal invariance allows to construct non-trivial fluid dynamics solutions [71]. Those should be valid in the approximately conformal early stage of the matter evolution in HIC. For that reason they can and were used to test numerical implementation of the hydrodynamical framework that is used in this thesis.

1.1.5 Kinetic theory

During the late stage of the HIC evolution, expanding QGP that is described with fluid dynamics is expected to cool, undergo confinement-deconfinement phase transition, and form particles (hadronize). The interplay between the constituents will become weaker and one would be able to distinguish quasiparticle excitations. The characteristic micro- and macro-scopic scales of the system will be comparable, which is the requirement of the kinetic theory approach applicability, although the former is expected to be still smaller than the latter. The Knudsen number should thus be less then one, which coincides with the requirement of applicability of hydrodynamics. Hence, in this regime both hydrodynamics and kinetic theory should be valid and thus could be directly related to one-another.

The fundamental variable in kinetic theory is the phase space one-particle distri-

[1] They preserves angles, but not sizes.

bution function:

$$f(t, \mathbf{x}, \mathbf{p}) \sim \frac{dN}{d\mathbf{x}d\mathbf{p}}, \tag{1.26}$$

of on-shell, $p_\mu p^\mu = m^2$, constituents that could be treated in the quasi-classical limit under the aforementioned assumptions. Its evolution is controlled by the Boltzmann equation, [72]:

$$p^\mu \partial_\mu f = -\mathcal{C}[f]\,, \tag{1.27}$$

where $\mathcal{C}[f]$ is the so-called collision term that describes the constituents' interactions at the microscopic scale. Straight from definition (1.26) follows the formula for energy-momentum tensor [66].

$$T^{\mu\nu} = \int d\chi\, p^\mu p^\nu f(x,p)\,, \tag{1.28}$$

where we used the following notation:

$$\int d\chi \equiv \frac{d^4p}{(2\pi)^3}\delta(p^\mu p_\mu - m^2)2\theta(p^0). \tag{1.29}$$

Similarly to the case of hydrodynamics, it is common to separate ideal (equilibrium) and viscous (out-of-equilibrium) contributions:

$$f(x,p) = f_0\left(\frac{u_\mu(x)\,p^\mu}{T(x)}\right)\left[1 + \delta f(x,p)\right]\,, \tag{1.30}$$

where δf should be a small correction to f_0.

Viscous correction, δf, is defined by the requirement of matching the energy-momentum tensor in the hydrodynamic and kinetic theory approaches, which is required by conservation laws. Thus, from the comparison of equations (1.28) and (2.58) to (1.21) and (1.22), one obtains:

$$\pi^{\mu\nu} = \Delta^{\mu\nu}_{\alpha\beta}\int d\chi\, p^\alpha p^\beta f_0(x,p)\delta f(x,p), \quad \Pi = -\frac{1}{3}\Delta_{\alpha\beta}\int d\chi\, p^\alpha p^\beta f_0(x,p)\delta f(x,p). \tag{1.31}$$

It is worth mentioning that equations (1.31) are not enough to uniquely constrain the dependence of δf on momentum. It was shown that various microscopic model lead to different prescriptions of the viscous correction [73]. The quadratic (second power in momentum) ansatz is the most commonly used in hydrodynamical calculations, see

Section 2.4, but further studies of the viscous correction dependence on momentum are necessary to reduce the related to it systematic uncertainty.

The correspondence between the kinetic theory and fluid dynamics can also be observed in the following way: it is possible to derive the laws of hydrodynamic evolution from the Boltzmann equation. To do it, one has to evaluate $n = 0, 1, 2$ moments of the latter, see equation (1.27):

$$\int d\chi\, p^{\mu_1}\, p^{\mu_2} \dots p^{\mu_n}\, p^{\mu} \partial_{\mu} f = -\int d\chi p^{\mu_1}\, p^{\mu_2} \dots p^{\mu_n} \mathcal{C}. \tag{1.32}$$

Zeroth order moment[1] will reproduce hydrodynamical equation for charge conservation[2]:

$$\int d\chi p^{\mu} \partial_{\mu} f = \partial_{\mu} \int d\chi p^{\mu} f = \partial_{\mu} j^{\mu} = 0, \tag{1.33}$$

where j^{μ} would be the corresponding, for example baryon, charge current.

First order moment will be equivalent to the energy-momentum conservation equation (1.21):

$$\partial_{\mu} T^{\mu\nu} = \int d\chi\, p^{\nu}\, p^{\mu} \partial_{\mu} f = -\int d\chi p^{\nu}\, \mathcal{C} = 0\,, \tag{1.34}$$

where the last equality holds due to the Lorentz covariance.

Finally, the second order moment will correspond to the MIS equations [74]. To write those explicitly one would need to expand the viscous correction in low momentum region, [75, 76]:

$$\delta f(x^{\mu}, p^{\mu}) = c + p^{\alpha} c_{\alpha} + p^{\alpha} p^{\beta} c_{\alpha\beta}\,, \tag{1.35}$$

provide expression for the collision term, $\mathcal{C}$, which would also define the ideal distribution function $f_0(x, p)$. Derivations of MIS equations are available for various models, i.e. the massless particle limit of Boltzmann statistics. Kinetic theory also allows to calculate the values of transport coefficients as it has direct access to the model at the microscopic level, i.e. through the collision term, $\mathcal{C}$.

Interestingly, MIS equations obtained from Boltzmann equation, (1.32), and from the generalized form of the second law of thermodynamics, (1.23), differ [77]. They

[1] Both sides of equation (1.27) are directly integrated over $d\chi$.

[2] $\int d\chi\, \mathcal{C} = 0$ should be satisfied in this case.

will, however, coincide if one recalls that they were both derived under the assumption of small deviations from equilibrium and gradient "power counting" should be used for proper comparison [78]. Importantly, both approaches will accurately reproduce NS equations in the limit of long wavelengths with no super-luminal modes, which was the main motivation of using the higher order expansion in gradients.

Note that the Boltzmann equation could be obtained in the weakly coupled limit from the Yang-Mills theory at finite temperature [79, 80, 81, 82, 83] in the Hard Thermal Loop approximation [84, 85, 86, 87, 88]. In addition to this fact, there are indications that kinetic theory might be the first order in gradients approximation of a more general quantum gravity field theory [89] and thus it is missing higher order corrections. For example, calculation of transport coefficients in the strongly coupled $\mathcal{N} = 4$ SYM theory using AdS duality signals that kinetic theory approach does not capture the entire dynamics [90, 91, 92, 93].[1] Thus, hydrodynamics obtained using higher order gradient terms is one of the equally reliable approaches to studying strongly interacting systems.

1.2 QCD plasma in HIC

So far, we discussed theoretical frameworks that proved to be successful in exploring various aspects of QCD. We mentioned that experimentally strong interactions are studied in hadron collisions. The QCD phenomenon that recently captured the attention of the scientific community is QGP, as due to the latest technological advancements physical conditions necessary for its creation were reproduced in the laboratory. Yet technical limitations do not allow to observe QGP directly. The strong indirect evidence of QGP formation in HIC is based on the capability of hydrodynamics to describe experimental results in the so-called large collision systems, such as lead-lead (A-A). We will discuss this topic and the related fluid dynamics framework in details in Chapter 2. In Chapters 3, 4, and 5, we will utilize the same hydrodynamic

[1] In some sense this is not surprising, as kinetic theory should be applied to quasi-particle excitations, which one can show are absent in this regime.

approach to the so-called small collision systems, and, specifically, proton-lead (p-A), in order to study whether it is applicable in this case. If this is true, it would attest that QGP is produced in small collision systems as well as it was shown before for the large ones.

It is important to dispel the impression that hydrodynamics could be applied ubiquitously. It is not the case. Moreover, certain aspects of the fluid dynamics framework applicability for the description of HIC still need to be clarified. For example, it is challenging to theoretically explain the duration of the QGP formation process ($\sim 1 - 10\,\mathrm{fm}$), which is consistent with the time scale ($\sim 0.1 - 1\,\mathrm{fm}$) required by hydrodynamic models to successfully describe experimental data. For the sake of completeness, in Section 1.2.1, we review a framework of QGP creation in HIC, which is called "bottom-up" thermalization. Although, it provides a parametrically larger estimate of the formation time, one believes it accurately captures the essence of the phenomenon. Specifically, it offers an easy way to illustrate how a dense gluon layer gets formed in the vicinity of the collision and how the collective behavior gets established, which is valuable in order to qualitatively understand why hydrodynamics could be applicable in hadron collisions.

In Section 1.2.2, we provide a schematic overview of the theory of Color-Glass Condensate (CGC) that studies early stages of the HIC. During this times hydrodynamics cannot be applicable. And, indeed, CGC does not describe thermalization. For that reason, there are two possible courses of action. First, one can utilize CGC to specify the initial conditions of the hydrodynamics stage of HIC evolution, which we do in details in Section 2.2. In this case, one assumes that, although one currently does not understand how in details, the process of QGP formation takes place and the matter density profile in thee early stage of fluid evolution can be well approximated with the prescription coming from the CGC theory. Second, one supposes that experimental data on hadron collisions can be described without hydrodynamics [94, 95, 96]. This approach is based on the expectation that matter density will not be high enough to form QGP in small systems (and peripheral collisions of large systems, see Section

2.1). Indeed, early experimental results [97] indirectly confirm this conjecture – we will discuss this question and how the recent small collision systems data allows to reevaluate the conclusions on the applicability of fluid dynamics in this case in Chapter 4. Thus, it is important to discuss at least qualitatively the theory of CGC before moving to the main part of this work, where we will be describing HIC only in the framework of fluid dynamics.

1.2.1 Bottom-up thermalization

In HIC experiments nuclei collide at very high energies. While at the partonic scale ($\sim 10^{-3}$ fm) nuclei consist of quarks and gluons, at the nucleonic scale (~ 1 fm) one is able to discern only protons and neutrons. Those interact indistinguishably from the perspective of strong interactions[1]. Thus, one usually talks about "nucleons" as the only type of the nuclei's "building blocks".

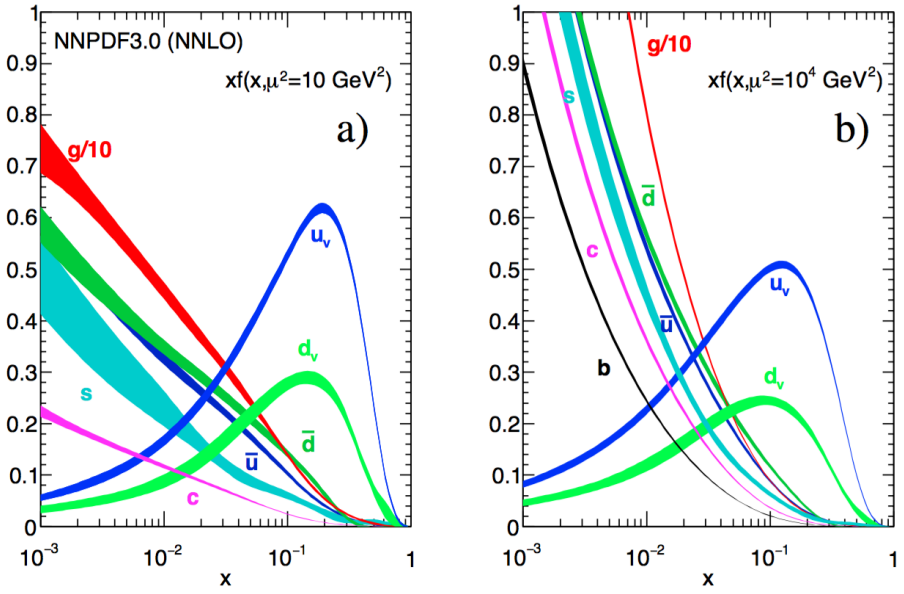

Figure 1.10: The bands are x times the unpolarized parton distributions $f(x)$. They were obtained in the NNLO NNPDF3.0 global analysis [98] at the scales $\mu^2 = 10\text{GeV}^2$ (left) and $\mu^2 = 10^4\text{GeV}^2$ (right), with $\alpha_s(M_Z^2) = 0,118$. Figures from [98].

Experiments on Deep Inelastic Scattering (DIS) show that at high energies a cloud

[1]Influence of other forces on nuclear matter evolution in hadron collisions is considerably smaller.

of virtual quarks and gluons is observed inside protons. In Fig. 1.10, one can see dependence of the Parton Distribution Function (PDF), $f(x, \mu^2)$, describing probability to observe some quark/gluon constituent inside a proton. x is the fraction of the total proton's longitudinal momentum that this constituent carries. μ is the energy scale at which the proton is probed. According to the estimates of the CMS collaboration, the typical value of x for proton's constituents at the LHC energies is 10^{-4} [99]. From Fig. 1.10 (a), one can conclude that even at the energies well below those typical for the LHC, $\mu \sim 10^3$ GeV, the proton's content is dominated by the soft gluons, $x \ll 1$. This trend becomes even more pronounced at higher energies, see Fig. 1.10 (b). Thus, one expects to observe a tremendous amount of soft gluons in HIC. Quantitatively this effect is described with the CGC model, which we will discuss in the next section.

The process of the bottom-up thermalization unfolds as follows, see Fig. 1.11. Soft gluons start expanding into vacuum reducing their density to the extent that they could be treated non-perturbatively as a gas of individual particles. It is instructive to see what happens in the plane that is orthogonal to the beamline and is passing through its origin, which coincides with the collision point.[1] Soon the only gluons to be observed there will be those with very small longitudinal momentum, because the rest will leave the plane. However, they can still have relatively high transverse momentum, of the order that they had inside the nuclei before those collided.

The system will thermalize only once the magnitudes of the longitudinal and transverse momenta of its constituents become equal. This can happen due to multiple interactions. Initially, the processes of elastic collisions and emissions of very soft gluons, which are shown in the lower part of Fig. 1.11 (a), are the main channels of the momentum isotropization.[2] As more of these very soft gluons are produced, the medium becomes denser. This increases the rate of relatively rare bremsstrahlung processes, see the lower part of Fig. 1.11 (b). Those lead to significant energy loss and as result the medium reaches a thermalized state, see Fig. 1.11 (c).[3]

[1] This is the so-called mid-rapidity region. See Section 2.3.1 for the precise definition.

[2] The circular (red) area highlights the already equilibrated part of matter.

[3] We do not discuss here plasma instabilities, which are also believed to contribute to the process and

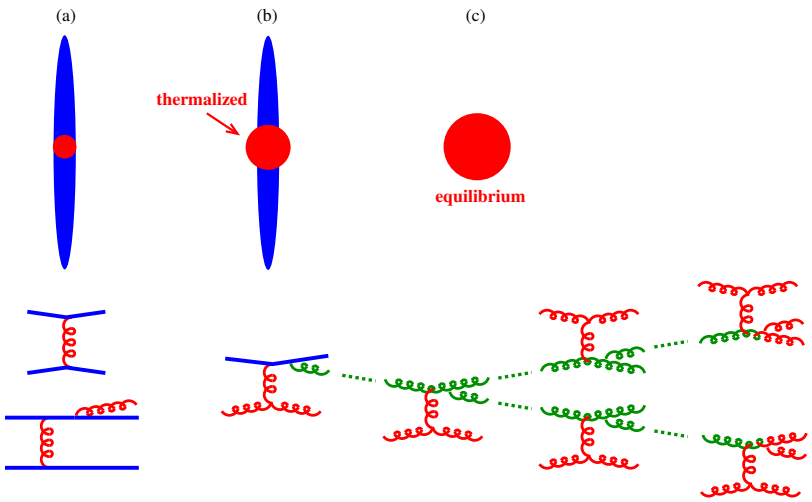

Figure 1.11: Consecutive stages of the bottom-up thermalization. Figure from [100]. The top row of pictures describes gluons' distribution in momentum space. The horizontal axis is aligned with the beamline. The vertical one represents any spatial direction that is orthogonal to it, as the dynamics at the origin is assumed to be rotationally invariant for the purpose of the discussion. The lower row of illustrations depicts the main types of the collision processes that bring the system to equilibrium.

Although this framework is believed to correctly capture the physical mechanisms that take place in the early stage of HIC, it is puzzling why the thermalization time calculated this way is rather big $\sim 2.5\,\mathrm{fm}$ [101]. If collective motion underlies the HIC phenomena, one expects QGP to be formed much faster. The majority of the hydrodynamical models that reasonably describe experimental data assume that the fireball expansions starts no later than $\sim 1\,\mathrm{fm}$ [102, 103, 104, 105, 106]. In this way the estimate of the thermalization time of $\sim 0.3\,\mathrm{fm}$ in AdS/CFT seems to be more appropriate [107]. Ultimately, this raises questions of whether our understanding of the early HIC phase could be improved and whether there are alternative explanations of the observed experimental data.

thus are being actively studied.

1.2.2 Color Glass Condensate and Glasma

The separation of the regions of applicability of perturbative methods into only two, hard and soft energy/momentum exchange processes, is too restrictive. It was found that in a certain kinematic limit there emerges also a semi-hard scale. Historically, this Regge-Gribov QCD regime despite its seeming perturbative form did not provide computational advantage when used for describing strongly interacting medium [108]. It was another, Bjorken QCD limit that gave interpretable insight into the physics inside a proton. We will use Deep Inelastic Scattering (DIS) process of scattering electron off a hadron to illustrate both regimes, see Fig. 1.12.

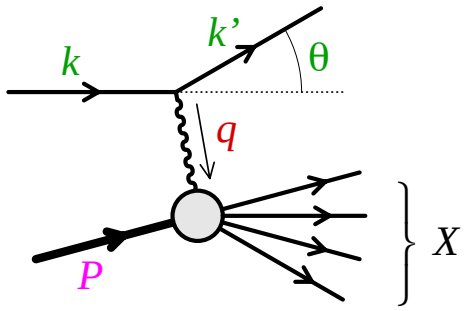

Figure 1.12: DIS of electron off a hadron. Figure from [95]. Initial momenta of particles are respectively k^μ and P^μ. Rest frame energy of the collision is $\sqrt{s} = \|k - P\|$. Virtual photon exchange momentum, q^μ, is space-like. For that reason one uses $Q^2 \equiv -q^2 > 0$. X denotes hadronic final products of the collision.

The following relation of kinematic Lorentz invariants holds in DIS processes:

$$xy = \frac{Q^2}{s}, \tag{1.36}$$

where x is the fraction of the longitudinal momentum of the parton that is interacting with the electron by the means of a virtual photon; Q^2 is their squared momentum exchange; s is the squared energy of the collision in the center of mass frame; y is the ratio of the photon to electron energy in the proton rest frame, which is instructive to fix for further discussion.

The Bjorken limit corresponds to the fixed values of variables x and Q, and

$s \to \infty$. At these conditions the results of the electron's probing of the hadron's content would look like the latter is constructed of several hard scattering centers (valence quarks grouped together in nucleons), while the rest of the volume would seem dilute (populated with small x gluons and sea quark pairs).[1] The perturbative and non-perturbative regimes are separated by scale Q and parton density evolution with respect to it is described with the Dokshitzer-Gribov-Lipatov-Altarelli-Parisi (DGLAP) equations [109, 110, 111] see Fig. 1.13.

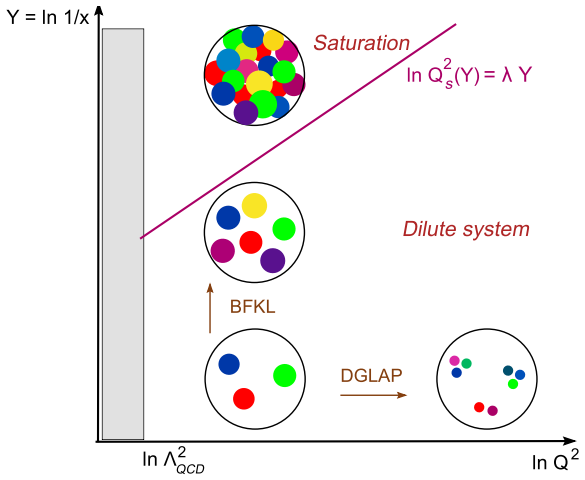

Figure 1.13: Graphical representation of different regimes of QCD on the example of DIS. Figure from [112]. Gray rectangular region corresponds to the deeply non-perturbative regime, which currently can be studied only using lattice QCD. Color circles denote hard scattering centers in Bjorken and Regge-Gribov regimes. In the former case they are valence quarks, and in the latter – gluon color charge lumps.

The Regge-Gribov limit corresponds to the fixed value of variable Q, while $x \to 0$ and $s \to \infty$. Its study became possible with the advancement of experimental techniques, when collision energies became high enough to ensure that $Q \geq 1\,\text{GeV}$. Evolution in the x variable is described by the Balitsky-Fadin-Kuraev-Lipatov (BFKL)

[1] An easy way to understand this is to recall that, due to the Lorentz time dilation, valence quarks interact with the electron on a much shorter time scale than the typical one for the interaction between each other.

renormalization group equation [113, 114, 115]. It is a stochastic equation that includes description of the occupation numbers' dynamics with respect to the change of x due to the gluon splitting, recombination, and non-locality of the emission vertex. The latter mechanism gets activated when the transverse momentum, k_{T}, of an emitting gluon gets shared between the produced constituents. It can be modeled with a diffusion process, which explains the probabilistic nature of the BFKL equation.

BFKL is a particular case of the Fisher-Kolmogorov-Petrovsky-Piscounov reaction-diffusion class of equations [116, 117]. Those have a characteristic solution, which describes propagation of a dynamically created density saturation front without distortions. In the case of BFKL this effect would correspond to the scaling of the so-called saturation momentum, Q_s:

$$Q_s^2(Y) \simeq Q_0^2 e^{\lambda_s Y}, \tag{1.37}$$

where $Y \equiv \ln(1/x)$, $\lambda_s \sim \alpha_s$, and Q_0 is some arbitrary non-perturbative scale, which should be greater than Λ_{QCD}. Equation (1.37) marks the boarder of the saturation region, in which hadronic matter is in the CGC state, see Fig. 1.13.

The physics of this regime could be described in the following way. As the number of gluons grows with $x \to 0$, see Fig. 1.10, at some point their density reaches the critical value where it saturates, because the processes of emission and recombination start to occur at the same rate, see Fig. 1.14 (a). In this state QCD is described with two effective degrees of freedom: classical Yang-Mills fields, A^μ, and their "sources" represented with the color charge density, ρ. Actually, both entities are fundamentally gluon fields separated by the value of the longitudinal momentum, which is usually measured with respect to the hadron's one, (1.36). Thus, they can undergo transition from one "state" into another. This evolution of the color charge density is described with the Jalilian-Marian, Iancu, McLerran, Weigert, Leonidov, Kovner (JIMWLK) renormalization group equation [118, 119, 120].[1]

[1]In the spirit of any other renormalization group equation, JIMWLK liberates the physical color charge density variable from the the dependence on the unphysical separation scale quantity $\Lambda_0 = xP$, see Fig. 1.14 (b).

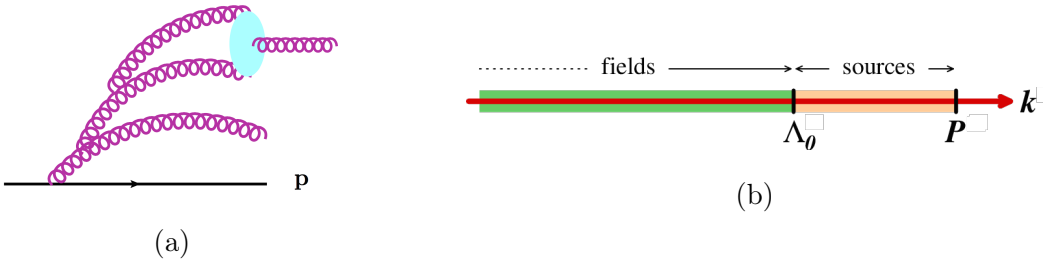

(a) (b)

Figure 1.14: Panel (a): Processes of gluon emission and recombination. Solid line represents time evolution of the (color source) gluon that carries large momentum fraction, x. Curly lines illustrate dynamics of soft gluons, which have small x values. They can undergo emission from the color source, splitting, and recombination. Figure from [121]. Panel (b): Illustration of the nature of the JIMWLK equation. Gluons, depending on the value of their longitudinal momentum, k, are split into two types: fields and sources. If $k < \Lambda_0$ gluon is considered to represent "fields", otherwise – "sources". Longitudinal momentum of gluons can not exceed the hadron's total value, P. Figure from [95].

The name CGC originates from the properties of its constituents. Color sources' interactions are considerably slowed down due to the special relativity effects and their positions are stochastically distributed from event to event. These properties resemble the non-crystalline amorphous solid structure of glass. At the same time soft gluon fields have large occupation number of $O(1/\alpha_s)$. This value corresponds to the maximum above which the theory would be unstable in the $s \to \infty$ limit. Hence the "condensate" part of the CGC name – saturation of gluons (bosons) reminds one of the Bose-Einstein condensate.

In HIC one talks about creation of "Glasma" that is described within the CGC framework. Nuclei consist of randomly distributed (gluon lumps) that are coherent in the transverse plane on distance of $\sim 1/Q_s$. Soft gluon fields, which due to saturation effects occupy low transverse momenta values and thus have characteristic scale of $k_\perp \sim Q_s$, can be described using strong classical fields. The last property provides the opportunity to describe a seemingly non-perturbative system with perturbative

methods. The reason is that saturation effects suppress all quantum effects: occupation numbers are so high that stochastic creation or annihilation of another degree of freedom does not alternate the dynamics of the system. Extended in the longitudinal direction strong color field regions are called QCD strings, see Fig. 1.15 (a).

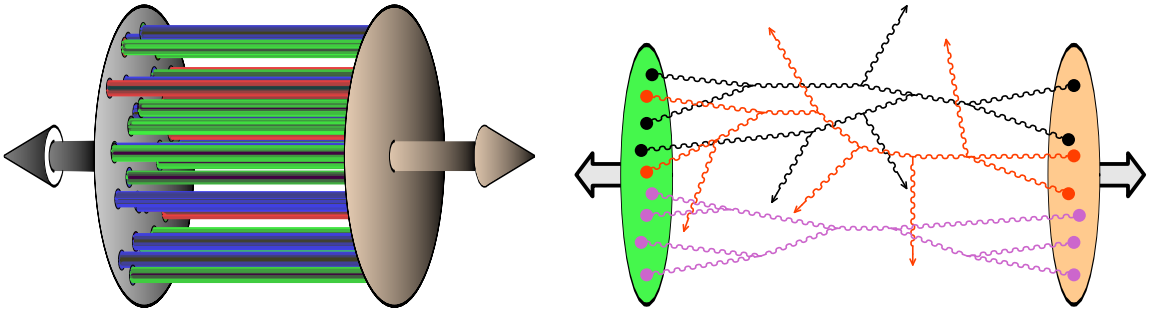

(a) (b)

Figure 1.15: HIC of a large A-A system within the CGC framework. Panel (a): Formation of color flux tubes. Panel (b): Gluon fields' dynamics in the leading order. Figures from [122].

One can calculate the gluon dynamics within the CGC framework, see Fig. 1.15 (b), and subsequently hadronize produced partons into particles. This was recently done for the case of p-A collisions[1] [130]. Authors were able to explain the order of magnitude value of the experimentally measured elliptic flow, which is usually considered as an argument in favor of the QGP creation and applicability of hydrodynamics.[2] However, there are several reasons to believe that hydrodynamical model is still a viable candidate for the proper HIC evolution description. First, it describes quantitatively at a higher level of accuracy a larger number of experimental observables. Second, CGC saturation assumption holds only during the initial stage, $\tau \sim 1/Q_s$, of the HIC evolution. This is the reason that one expects that glasma could provide an accurate description of the initial conditions but later should be

[1] This one of many works suggesting that collective signals in small systems are caused by initial-state correlations, see, for example [123, 124, 125, 126, 127, 128, 129].

[2] See Section 2.2 for details.

evolved using effective theory model, such as hydrodynamics [131, 132].[1] Third, as one can see in Fig. 1.15 (a), glasma initial conditions assume boost invariance in the longitudinal direction. Effectively this makes the system 2-dimensional. While this approximation is believed to be accurate enough for the consideration of large A-A systems and their observables around the beamline origin, one expects that smaller p-A systems will need a proper 3-dimensional description. Although the work in this direction is under way at McGill, there is currently no realistic 3-dimensional model of p-A collisions based on the CGC approach.[2]

1.3 Summary and outline of thesis

In this chapter we provided an overview of the current state of knowledge of the physics of strong interactions. In Section 1.1, we described the developed theoretical methods and their domains of applicability. In Section 1.2.2, we qualitatively discussed the theory describing the dynamics of QCD degrees of freedom in the early stage of nuclei collisions. We mentioned that from the theoretical perspective the exact mechanism of thermalization is currently not entirely clear, although we outlined what microscopical processes contribute to it in Section 1.2.1. However, the ability of the hydrodynamical paradigm to describe the experimental results of HIC collisions strongly suggests that QGP is formed in these systems, see Chapter 2.

Recent measurements from collisions of protons and deuterons with heavy nuclei reveal that high multiplicity events display features that are strikingly similar to those previously seen in large HIC systems [134, 135, 136, 137, 138]. This raises the question of whether these small systems also behave hydrodynamically, whether the physics

[1] Glasma initial conditions are constructed from classical fields, which do not include thermalization mechanisms. Thus, similarly to the bottom-up framework, it is challenging to explain fast thermalization within the CGC framework.

[2] The closest to it is the idea of slicing 2-dimensional glasma initial conditions at several points in longitudinal direction using solutions of JIMWLK equation [133]. However, in this approach there is no physical interaction between the slices at different longitudinal distances, which is expected to be important in small systems.

governing the two systems is different and the similarity in observables is merely a coincidence, or whether the data from heavy-ion collisions have been misinterpreted. Various explanations for the observed correlations in these small systems have been proposed, but a definitive answer is not yet available. In this work we perform 3+1D event-by-event viscous hydrodynamic calculations of p-Pb collisions at 5.02 TeV in order to determine whether existing data is consistent with a fluid medium, and whether new measurements could be devised in order to provide a definitive resolution to the question of the correct description of the system.

Our work is of exploratory nature and aims to make general conclusions on the applicability of fluid dynamics in small collision systems. There is still a number of open questions in the field, including the mechanism of QGP formation, the treatment of sub-nucleonic degrees of freedom, the calculation from first principles of the viscous correction to particle distribution, the accurate evaluation of transport coefficients, that can affect the results of hydrodynamic calculation. For that reason we use a robust model, including all the relevant effects such as quantum fluctuations at nucleonic level, shear and bulk viscosities, longitudinal asymmetry of the collision geometry, and vary its parameters in broad physically reasonable ranges to get a good idea of their relative contributions to various experimental observables. Thus, even though our understanding of the theory (at microscopic level) could be improved, we can still answer the main and very general question (at macroscopic level): can hydrodynamics describe signs of collective behavior in small systems?

Our discussion will follow a historical path. In Chapter 2, we will discuss the hydrodynamical paradigm of HIC and the way it got established. We will describe all stages of the HIC system dynamics starting from the propagation of nuclei towards each other and finishing with the free streaming of the created in the collision particles towards the collider's detectors. We will show how the frameworks of studying QCD that we discussed in Section 1.1 are used to describe all these evolution phases. Our main focus will be directed towards the introduction of the "conventional" flow observables that are considered to be the evidences of collective behavior in large

(A-A) systems.

In Chapter 3, we will discuss our first attempt to apply the hydrodynamic paradigm to small (p-A) systems [139]. We will introduce a robust fluid dynamics model that included all the physical features that were considered relevant at time of the appearance of the first detailed study of the high multiplicity p-Pb collisions at 5.02 TeV [140] that motivated this work. Specifically, it includes quantum fluctuations at nucleonic level, anisotropy of the system in the longitudinal direction, shear viscosity that is known to have a considerable effect on collective behavior. We will show that the model was able to qualitatively describe all conventional flow observables in p-Pb collisions. Moreover, it was able to explain similarity of the triangular flow in small (p-Pb) and large (Pb-Pb) systems that was considered to be challenging for hydrodynamics [140]. We will explore the parameter space of our model to assess its capabilities to describe experimental data, its robustness, and to identify further ways towards its improvement.

In Chapter 4, we will use another approach towards testing hydrodynamics applicability to small systems. It was developed and applied for the same reasons for the case of large systems [141] and its advantage is that it gives the means of testing fluid dynamics falsifiability [142] independent of its particular implementation. This test deals with the study of the $r_n(p_{\mathrm{T}}^a, p_{\mathrm{T}}^b)$ observable. We suggested to study it in small systems and, using the model described in Chapter 3, made a *prediction* of its behavior in p-Pb collisions [139] that was later confirmed [143]. We also discuss our discovery that the $r_n(p_{\mathrm{T}}^a, p_{\mathrm{T}}^b)$ observable can be used as a probe of estimating the size of quantum fluctuations in the early QGP.

In Chapter 5, we introduce to our model two new features: bulk viscosity and fluctuations of matter density in longitudinal direction. These, improvements were dictated by the necessity to describe the recent p-Pb experimental data [143] and to assess the effects of bulk viscosity, which appeared to be important when describing large systems [144]. We show that they help to further improve the agreement of our model's calculations with p-Pb data and support the generality of the conclusions that

we made based on the analysis of the results that were obtained using the model's implementation discussed in Chapter 3.

Finally, in Chapter 6, we summarize all our findings, make a conclusion on the applicability of hydrodynamics to the description of small systems, and propose directions of future research.

2

Heavy ion collisions in the hydrodynamical paradigm

In this chapter we will discuss how theories described previously apply in the case of HIC. We will start with a more technical recount of the collision stages. For that we will need to introduce definitions of physical coordinates and observables that allow to transcribe qualitative intuitions into quantitative analysis.

2.1 HIC in a nutshell

At colliders nuclei are accelerated to ultra-relativistic velocities, v. Those are less than one ten thousandth of a percent smaller than the absolute maximum limit for moving matter, which is the speed of light, c. Lorentz factor corresponding to these velocities is of the order of[1]:

$$\gamma = \frac{1}{\sqrt{1 - \frac{v^2}{c^2}}} \sim 10^2 - 10^3.^2 \tag{2.1}$$

This leads to a considerable contraction of the nuclei sizes along the direction of their movement in the laboratory reference frame. Thus, a typical nucleus, whose shape in its own reference frame could be well approximated with a sphere, is observed as a "pancake" of matter with its dimensions being of the order of 10 fm and 0.1 fm (or smaller) in the transverse and longitudinal directions respectively, see Fig. 2.1.

To observe the collision dynamics, nuclei are headed in opposite directions along the beam axis, z. Impact parameter vector, $\mathbf{b}$, stretched between the nuclei centers defines the orientation of axis x and thus of the reaction plane $x-z$, and the transverse plane $x-y$. The smaller its length, b, the larger will be the region impacted in the (inelastic) collision[3].

Nuclei therefore move towards each other along axis z almost at the speed of light. They interact strongly when passing through each other. This happens at the time

[1] In this chapter, we mostly discuss early HIC experiments in which QGP formation was discovered. Those were carried out at lower energies than those currently available, but high enough to observe the phenomenon. Thus, we will use a low limit (threshold) estimate of the γ factor and other kinematic variables in the discussion below.

[2] The lower estimate corresponds to RHIC energies of $\sqrt{s} \sim 10^2$ GeV per nucleon pair, the higher one is typical for LHC experiments with $\sqrt{s} \sim 10^3$ GeV.

[3] This might provide some intuition on why b is called the "impact parameter".

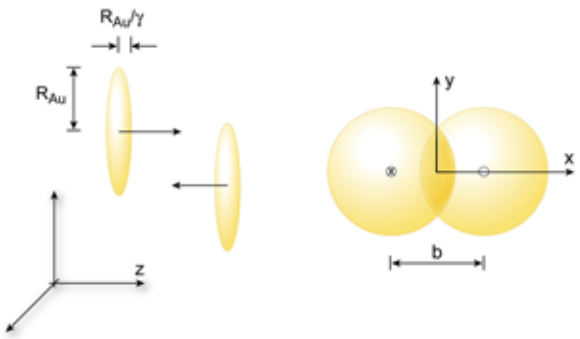

Figure 2.1: Experimental setup of nuclei collisions demonstrated on the example of a Au-Au system. Figure from [145].

scale of $\sim 0.1\,\mathrm{fm}/c$[1]. Then they proceed with their movement along axis z and play no further role in the dynamics of the system that was created in the collision. They leave behind a thin, but dense, almond shape layer of (soft) low energy gluons. Energy of these gluons will be eventually converted into the particle multiplicity, which grows monotonically with the increase of the collision overlap area in the transverse plane[2].

Precisely, as we discussed in Section 1.2.1, soft partons that were created in the collision of the passing through each other nuclei thermalize into QGP, which undergoes subsequent hydrodynamical expansion, see Fig. 2.2. Thermalization of the left behind gluon layer happens so quickly that the formed QGP fireball at the beginning of its evolution has the almond-like collision geometry shape, Fig. 2.2 (b).[3] Once

[1]This estimate is based on the following assumptions: the size of the nuclei is $\sim 10\,\mathrm{fm}$, the Lorentz γ factor is $\sim 10^2$, and the nuclei velocities approximately equal the speed of light.

[2] In this section, we provide an overview of the framework that proved to be successful in describing HIC evolution of large A-A systems [146]. Later in this work we will be applying it to small p-A systems. It might seem that the notion of the non-trivial collision overlap area, which will be important for the further discussion, is not applicable for the p-A case: one expects it to be always circular due to the nearly round shape of the proton and the much larger radius of the lead nucleus. We will address this misconception in Section 2.2.2, where we will show that quantum fluctuations in the initial conditions allow to extend the logic applied for the description of large A-A systems to the small p-A ones. However, we will right away mention that the distance between the nuclei centers is not an appropriate measure of the collision impact, if one wants to apply it to systems of all sizes. One can instead utilize for that purpose collision's multiplicity, which we do further.

[3]Thermalization happens at the time scale of $\sim 1\,\mathrm{fm}/c$, while the lead nucleus size is $\sim 10\,\mathrm{fm}$.

created, QGP medium starts its expansion into vacuum. The tremendous pressure ($\sim 30\,\mathrm{GeV/fm^3}$ [147]) in the center of the fireball drops to the zero vacuum value at its periphery. The border of the QGP system is very roughly elliptical. Thus, pressure drop will be more rapid in the direction of axis x than axis y. Pressure gradients drive the magnitude of the medium's local velocity[1] [148]. It, in turn, defines the preferred direction of the particle thermal emission from the fireball, which is affected by the special relativity effects. Thus, one expects that the particle momentum distribution will peak in the direction of the x axis and will gradually decrease when rotating towards the y axis, Fig. 2.2 (c). Indeed, this is what is observed in the HIC experiments, which register particle distributions in the transverse plane [149].

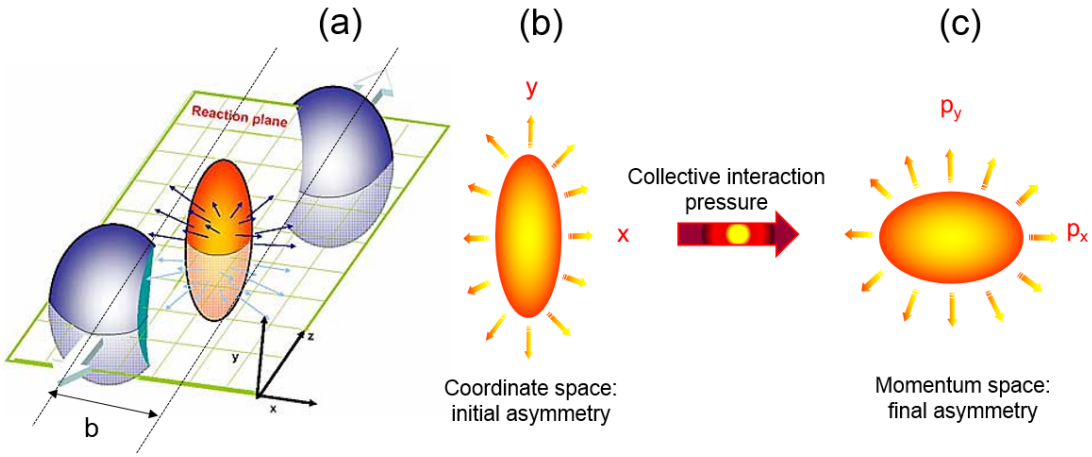

Figure 2.2: Subsequent phases of the almond shape gluon layer dynamics: (a) QGP fireball was formed (thermalized) and is plotted in the early stage of its expansion alongside the nuclei that are quickly receding the place of the collision; (b) transverse plane cross-section of the just thermalized into QGP gluon layer, arrows correspond to the direction of the hydrodynamical pressure gradients; (c) transverse plane cross-section of the momentum distribution of particles created by the cooling down expanding QGP fireball. Figure from [150].

This characteristic property of the transverse particle momentum distribution is

[1]It can also be seen if one explicitly writes out the spatial dimensions' part of equation (1.20): $Du^i = \nabla^i P/(\epsilon + P)$, where $D \equiv u^\mu \partial_\mu$.

not the only evidence supporting the hypothesis of the QGP formation in HIC. However, it will be the central one in this work, because it allows one to indirectly study properties of the QGP medium using Fourier analysis. We will discuss qualitative intuition behind this study later in the section and will introduce strict mathematical definitions in Chapter 3. Currently we will mention that this effect is referred to as anisotropic flow [151].

2.1.1 Evidence of QGP formation

As we explained in Chapter 1, HIC happen so fast that current technological methods do not allow to directly observe the processes taking place in these experiments. Thus, one has to use indirect indications to confirm that QGP is formed in the collisions [152]. We will list them below for an overview and will provide accurate mathematical definitions in the coming sections. In this work, we group these evidences into three categories: flow effects, energy loss, and other experimental observables.

To the first category we refer: the anisotropic flow, which reveals the presence of the collective motion by analyzing one-particle momentum distributions; the mass ordering, which stems from the fact that all particle species emitted by the QGP medium have equal velocities, but different momentum distributions and thus flow coefficients; the ridge effect that describes how QGP defines the structure of the long range two-particle correlations, and which we will discuss in details in Chapter 4.

Energy loss phenomena relate to the fact that if QGP is created in HIC then particles traversing through this medium will transmit part of their energy to it [153]. Consequences of this effect can be observed in the suppression of high energy particle yields and excessive for this collision energy production of lighter, compared to the charm and bottom quarks, strange quarks. This "jet quenching" mechanism is studied by measuring the nuclear modification factor:

$$R_{AA} = \frac{N^{AA}}{N_{\text{coll}}\, N^{pp}}.$$

It equals the ratio of the total particle yield in the A-A, N^{AA}, and p-p, N^{pp}, systems

scaled by the number of (binary[1]) nucleon-nucleon collisions, N_{coll}, taking place in the A-A case. The idea behind this calculation is to evaluate the effect of QGP formation on particle production. If no medium effects were present in A-A collisions, R_{AA} would be identically one (up to isospin effects that can be seen when one compares PDFs of a proton and a large nucleus). The particle yield would be equal to that created in a linear superposition of p-p collisions, while QGP is not expected to be formed in this case [154]. Similarly, one could investigate the effects of the medium creation on the two-particle production subject to the local (momentum, charge) conservation laws in back-to-back jets [155] which we will also discuss in Chapter 4.

To give an example of the other experimental techniques, we will mention Hanbury-Brown-Twis (HBT) interferometry [156]. Developed for astrophysical applications, this method is based on the observation that two-particle emissions from various points of an extended source are correlated. This technique was initially applied to assess the size of extra terrestrial objects. However, it was later successfully utilized to extract the dimensions of QGP fireballs [157, 158]. Again, the fact that this method works proves that the emission of particles in HIC does not take place independently in various spatial points thus suggesting presence of collective dynamics [159, 160] which can be attempted to be described hydrodynamically.

2.1.2 Phases of HIC

In the previous section we listed arguments that support the hypothesis of QGP formation in HIC. In this section we will describe the paradigm of the stages of a HIC with QGP evolution being one of them. We will follow illustrations in Fig. 2.3 from left to right.

Before the collision happens, nuclei are headed towards each other. Blue arrows in the first illustration of Fig. 2.3 indicate the directions of their motion. Nuclei have the shape of "pancakes" due to Lorentz contraction. Similarly, special relativity time dilation effect slows down all physical processes inside nuclei by at least two orders of magnitude, see Section 1.2.2. This explains why the colored spots that represent the

[1] See Section 2.2.1 for details, specifically equation (2.9).

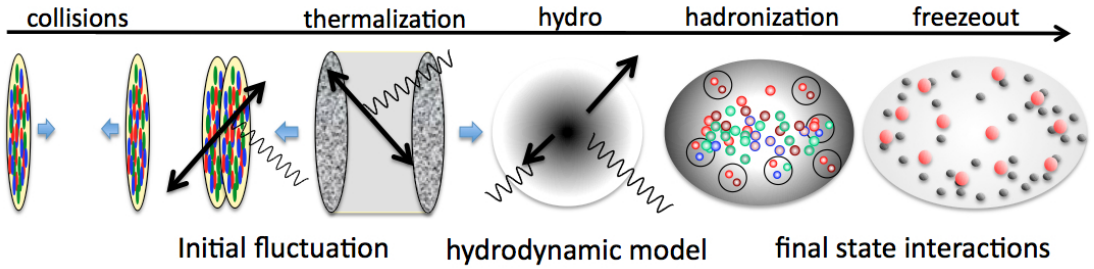

Figure 2.3: Stages of a HIC as observed in the lab/detector frame. Figure from [161]. See text for explanations.

hard scatterers' configuration do not move within the nuclei, while the nuclei cover the distance separating them along axis z.

The next "initial fluctuation" stage's snapshot represents the moment when nuclei start interacting strongly while they are passing through each other. The black arrows denote high energy particles created in hard collisions, while the wave line represents soft and hard electro-magnetic particle emission. Both processes could be described using perturbative techniques. One of the biggest challenges in the theory of HIC is the description of the initial conditions stage. This and the next stage of the matter evolution has to deal with the physics of dynamical phase transitions, which is historically the most difficult to describe. Thus, we will discuss the initial conditions modeling in details in Section 2.2. We point out that it is highly desirable to obtain constraints on these models from experimental data, which we did in Section 4.6.

In the next diagram one can see the dense gluon layer (in gray) that is left behind by the receding nuclei, whose velocities are again designated with blue arrows. Strongly and electro-magnetically interacting particles have to travel through this dense medium, while it goes through the quick ($\sim 0.1 - 1\,\mathrm{fm}$) thermalization phase. Description of the pre-equilibrium stage constitutes another challenge. It has been analyzed with perturbative (both pQCD [162] and AdS/CFT [163])[1], kinetic, and hydrodynamic methods, as in this transition region all of them are valid subject to

[1] AdS/CFT approach allows to describe non-perturbative CFT dynamics using classical gravity, which can be treated perturbatively. See Section 1.1.3 and references therein.

certain constrains, discussed in Chapter 1. Considerable progress has been achieved, but the current state of research suggests that the effect of the out-of-equilibrium dynamics is moderate on the flow observables [164, 165].

Thermalization: in this stage the system has (nearly) equilibrated to form ultra-relativistic fluid. QGP, unlike pure gluon medium, can emit particles in the electro-magnetic channel. These particles traverse QGP fireball alongside the earlier created hard counterparts, which is also indicated in the figure. Both types of the afore-mentioned particles, which are represented with solid and wavy lines, can escape the QGP medium. The hard particles can do it, if they were created next to the edge of the fireball with an energy considerably exceeding that of the surrounding matter constituents, which will allow them to penetrate the layer of strongly-interacting environment on their way out and still stand out in the energy-momentum distribution spectrum with respect to the rest of the yield in order to be detected. The electro-magnetic ones – because the QGP fireball is optically thin due to the considerable smallness of the electric coupling constant, $\alpha_e \sim 10^{-2}$. In this way both types of produced particles can help in the studies of the processes taking place in the QGP medium. The former particles are used in the "jet quenching" analysis that we discussed before. The latter are the main subject of the research field, which is called "electro-magnetic probes". Specifically, electro-magnetic observables can be used as a "thermometer" of the QGP fireball core, as they do not exchange energy with the medium after their emission. The analysis of electro-magnetic probes in HIC with hydrodynamics in large repeats the approach that we use in this work for studying hadron flow in Chapter 3. The main difference is in the framework utilized for the description of particle creation. For example, in case of photons one needs to use models of thermal emission from QGP plasma such as AMY[1] [166]. We will not be discussing this area of research in more details in this work, because the main focus of this thesis is whether QGP is formed in small collision systems. However, we refer the interested reader to a publication on this topic, which the author of this work

[1]Instead of the Cooper-Frye method that is utilized for hadron emission, see Section 2.4.

also co-authored [167].

Hydrodynamic expansion will last for about 10 fm/c. This is the longest phase of the created in HIC matter evolution, during which the medium undergoes substantial transformations. Its study constitutes the main focus of this thesis. Expanding hydrodynamically, the QGP fireball will be increasing its volume, and thus will necessarily be cooling down due to energy conservation. For the same, reason the peripheral regions of the QGP fireball will have lower temperature, and thus will be the first to go through the phase transition and to emit particles. One can see this process of hadronization in Fig. 2.3. Quarks are in free state in the hotter center of the QGP medium. While at the border, they combine into duplets or triplets forming mesons or hadrons. Graphically confinement is represented with solid lines that encircle groups of colored dots that denote quarks. This hadronization process will be modeled within the Cooper-Frye framework [168, 169].

The strongly-interacting phase of QGP evolution is over at this point in time as all degrees of hadronic freedom "froze out"[1] (formed particles). However, there is one more stage of HIC dynamics – "final state interactions" – that needs to be considered as it affects the experimentally observed particle distribution. Specifically, after freeze-out particles collide and change their direction. In this work we used UrQMD model to model this stage of HIC [170, 171]. Predating the detailed description, we found out that the final state effects do not considerably modify the flow coefficients in the case of small systems. The total number of produced particles appeared to be too dilute in p-A collisions. Our calculations show that less than one percent of the yield undergoes a final state collision.

In the next sections we will describe all these stages quantitatively. However, at the qualitative level, we can already conclude that for the goal of this work the most important stages of the matter evolution are the initial conditions and the hydrodynamic expansion. They contribute the most to the values of the physical

[1] To be precise, there are two types of freeze-out: chemical (where the particle numbers do not change) and kinetic (where the distribution function of particle yield does not change). We will discuss this difference in more details in Section 4.4.

observables that serve to be the evidences of the QGP creation. For that reason, we need to primarily focus on them when modeling HIC in small systems.

2.2 Initial conditions for hydrodynamics

In Section 1.2.2, we discussed first principles approach to the studies of the initial stage of hadron collisions. There we mentioned that the mechanics of early matter thermalization is not precisely known, although it is schematically clear as we shown in Section 1.2.1. In this section, we will discuss the topic of the initial conditions modeling assuming that QGP is formed at a time scale of $\sim 0.1 - 1\,\text{fm}$. We will do it by following its historical development path. The first collision systems to be considered were those consisting of identical spherically shaped nuclei, such as Au-Au, which are shown in Fig. 2.4.

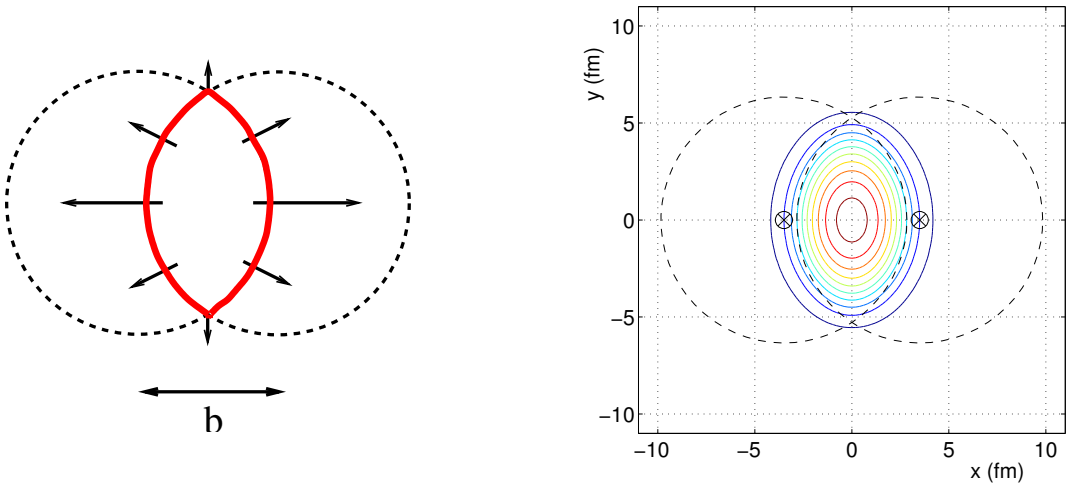

Figure 2.4: Au-Au HIC. Figures from [172]. Impact parameter value $b = 7\,\text{fm}$, see also Fig. 2.1. Dashed contours correspond to the perpendicular projection of the passing nuclei to the event plane, $x - y$. Red line on the left panel indicates the boarder between the QGP fireball and the vacuum. Length of the arrows corresponds to the magnitude of the local pressure gradients. Colors of the ellipses on the right panel indicate the magnitude of the nuclear density from the lowest value (in purple) at the boarder to the highest one (in red) next to the origin.

As we discussed in Section 2.1.2, collision geometry of the initial conditions leads to the almond-shape energy density profile, see left panel of Fig. 2.4. It creates pressure gradients that accelerate matter and eventually lead to its anisotropic momentum distribution at the time when it reaches the detector.

To quantify the degree of the initial conditions' asymmetry, it was suggested to introduce a variable that was later called (standard) eccentricity, [173]:

$$\varepsilon_{\text{std}} \equiv \frac{\int d\mathbf{r}\, \rho(\mathbf{r})\, (y^2 - x^2)}{\int d\mathbf{r}\, \rho(\mathbf{r})\, (x^2 + y^2)}, \tag{2.2}$$

where $\rho(\mathbf{r})$ can be either the energy or the entropy density distribution of the QGP fireball in coordinate space at the time of the collision.

Similarly, an observable describing the anisotropy of the final state particle distribution was defined, [174]:

$$v_2 \equiv \frac{\int d\mathbf{p}\, \frac{dN}{d\mathbf{p}}\, (p_y^2 - p_x^2)}{\int d\mathbf{p}\, \frac{dN}{d\mathbf{p}}\, (p_x^2 + p_y^2)}, \tag{2.3}$$

where N is the number of particles carrying momentum $\mathbf{p}$. It is usually referred to as "flow"[1]. The ratio of flow to eccentricity is called hydrodynamic response – it measures to which extent QGP evolution modifies the matter anisotropy in HIC.

We note that, unlike "flow", eccentricity cannot be measured experimentally. Indeed, according to (2.2), one needs a model of the initial energy density distribution to assess its value. One of the first being used was the Optical Glauber Model, described in the next section.

2.2.1 Optical Glauber Model

It is challenging to experimentally probe energy density distribution inside a nucleus. To assess it, one assumes that it follows the charge density one. The latter was measured experimentally by scattering electron off hadrons. Woods-Saxon parametrization describes it well:

$$\rho(r) = \frac{\rho_0}{1 + \exp\left(\frac{r-R}{a}\right)}, \tag{2.4}$$

[1] We note here that v_2 is the "standard" definition of flow that was later replaced with more generalized and sophisticated ones. See Section 3.2 and specifically equations (3.6), (3.7) for definitions of $v_n(p_{\text{T}})$, $\bar{v}_n$. See also Section 4.2.1 and equations (4.4), (4.5) for definitions of $v_n\{2\}(p_{\text{T}})$, $\bar{v}_n\{2\}$.

where R is the effective nucleus radius, and a is the width of the transition region between hadronic matter and vacuum. Examples of Wood-Saxon distribution for Au and Cu nuclei are plotted in Fig. 2.5.

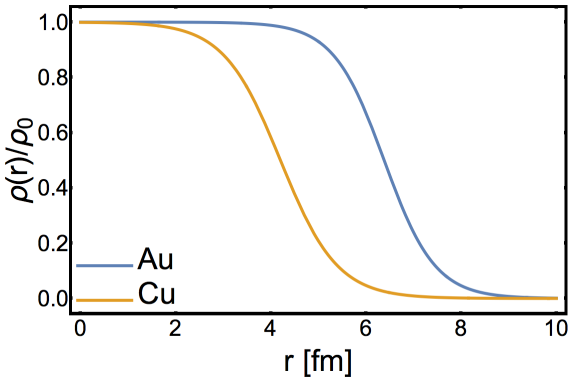

Figure 2.5: Wood-Saxon potential, which describes forces applied on a nucleon inside a nucleus.

The Optical Glauber Model describes the distribution of nuclear density in the transverse plane. The longitudinal dynamics of a symmetric A-A collision next to the lab frame origin can be described with the boost invariant Bjorken solution [175]. Thus, one can use a constant energy density longitudinal profile in this case. For an asymmetric p-A system this prescription will not be appropriate and we will discuss this question in Section 3.1.

In a nutshell, the Optical Glauber Model is based on the idea that the initial conditions profile at a certain point of the overlap region that is formed by the nuclei perpendicular projections onto the transverse plane should correspond to the amount of hadronic matter passing through it, see Fig. 2.6.

The model operates with the notion of "thickness functions", $T_{A/B}$:

$$T_A(\vec{s}) = \int \hat{\rho}_A(\vec{s}, z_A) dz_A, \qquad T_B(\vec{s} - \vec{b}) = \int \hat{\rho}_B(\vec{s} - \vec{b}, z_B) dz_B, \tag{2.5}$$

where $\hat{\rho}_{A/B}$ stands for the nucleon probability density per unit volume inside the respective nucleus that is normalized to unity. The number of nucleons of nucleus A/B that are being observed at coordinate $\vec{s}$ equals to the flux tube value T at this

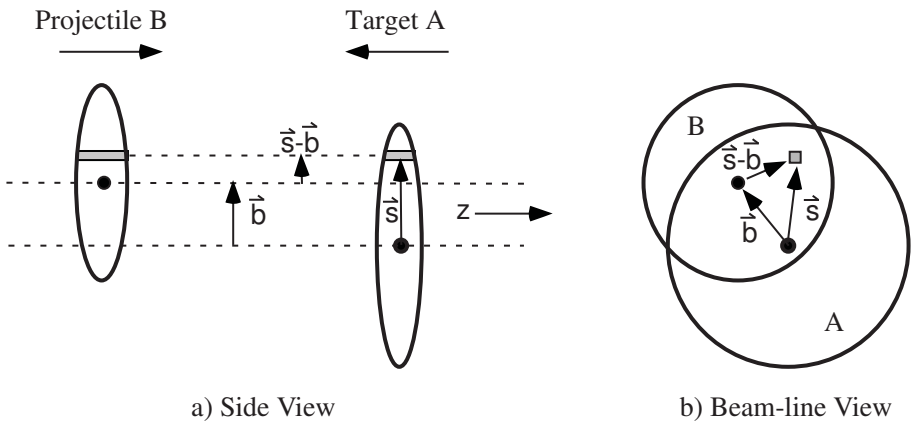

Figure 2.6: Longitudinal (a) and transverse (b) cross-sections of a HIC. Figures from [176]. For convenience, nuclei are referred to as a target (A) and a projectile (B). **b** is the impact parameter vector. Arbitrary point in the overlap region is denoted with vector **s**.

spatial point. Thus, the probability density of a nucleon-nucleon collision at $\vec{s}$, as well as the amount of deposited energy, is proportional to the product:

$$T_A(\vec{s})T_B(\vec{s}-\vec{b})d^2\vec{s}, \tag{2.6}$$

where $d^2\vec{s}$ is the differential area in the transverse plane. The total probability per unit area of a given nucleon in A to interact with any counterpart in B will then be equal to the value of the "thickness function":

$$T_{AB}(\vec{b}) = \int T_A(\vec{s})T_B(\vec{s}-\vec{b})d^2\vec{s}. \tag{2.7}$$

It can be interpreted as the effective overlap area of the described above nucleon-nucleon event. Multiplied by the cross-section of a certain process, $\sigma^{NN}_{\text{process}}$, it will yield the probability of a collision in the corresponding channel. Nucleons can interact elastically and inelastically. In the Glauber model, the former collisions are not considered, because their contribution to the total energy deposition is negligible compared to that of the latter. Thus, the probability of n nucleon-nucleon collisions

at given impact parameter b is equal to:

$$P(n,\vec{b}) = \binom{AB}{n} \left[T_{AB}(\vec{b})\sigma_{\rm inel}^{\rm NN}\right]^n \left[1 - T_{AB}(\vec{b})\sigma_{\rm inel}^{\rm NN}\right]^{AB-n}, \tag{2.8}$$

where A/B denotes the number of nucleons in the respective nucleus, and $\sigma_{\rm inel}^{NN}$ is the experimentally measured inelastic cross-section. The total number of the relevant nucleon-nucleon collisions is:

$$N_{\rm bn}(\vec{b}) = \sum_{n=1}^{AB} nP(n,\vec{b}) = A\,B\,T_{AB}(\vec{b})\,\sigma_{\rm inel}^{\rm NN}. \tag{2.9}$$

Another useful quantity is the number of wounded nucleons:

$$\begin{aligned} N_{\rm wn}(\vec{b}) = A \int T_A(\vec{s}) \left(1 - [1 - T_B(\vec{s}-\vec{b})\sigma_{\rm inel}^{\rm NN}]^B\right) d^2\vec{s} \\ + B \int T_B(\vec{s}-\vec{b}) \left(1 - [1 - T_A(\vec{s})\sigma_{\rm inel}^{\rm NN}]^A\right) d^2\vec{s}, \end{aligned} \tag{2.10}$$

which corresponds to the total number of nucleons that underwent at least one collision [177, 178].

The energy deposition scheme that follows the distribution of wounded nucleons provides a good description of the HIC initial conditions. This profile describes lower-energy gluon background that leads to the formation of the QGP fireball. Hard binary collisions have a different mechanism of energy loss. Their profile merely superimposes higher-energy spots in the initial energy distribution. Thus, although a linear combination of both prescriptions can be used:

$$\epsilon(x,y,\vec{b}) = (1-\alpha)N_{\rm wn}(x,y,\vec{b}) + \alpha N_{\rm bn}(x,y,\vec{b}), \tag{2.11}$$

the value of the parameter α does not exceed 10% [179]. By setting α to zero, we effectively exclude it from the list of the model's free parameters. This prescription is called "wounded" Glauber model.

Our choice is motivated by the following consideration. The goal of this work is to answer the principal question of whether QGP is formed in small collision systems. If we succeed in constructing a hydrodynamical model that includes all fundamental

physical mechanisms of QGP formation in HIC and captures general experimental trends, we will achieve our goal. Future work could then be directed towards improving the agreement between the model's calculation results and experimental data. At that stage inclusion of phenomena that contribute to the fine structure of experimental trends would be important.

However, keeping in mind the overfitting problem in statistics [180] the increase of the model's complexity should be done cautiously. For example, introduction of sub-nucleonic interactions proved to be beneficial for describing flow data [181]. Because their description is based on the experimentally confirmed advancements of CGC[1] research, fitting of the corresponding model's parameters can lead to the physically meaningful results. However, in this thesis, we work at the nucleon level[2], as the physical effects characteristic to this energy scale contribute the most to the effect of QGP formation. Thus, we exclude all phenomenological parameters that play sub-leading role in the process. They, indeed, can improve the agreement with experimental data but at the expense of affecting the generality of the obtained results due to the excess of fitting parameters.

2.2.2 Monte-Carlo Glauber Model

Working at the nucleon level, one can improve the Optical Glauber Model by statistically sampling individual constituents from both nuclei. The Monte-Carlo (MC) Glauber Model deals with individual nucleons that on average reproduce the Woods-Saxon distribution. Those travel along the z-axis at the same speed when observed in the center of mass frame. And one assumes that the nucleons' velocities are not affected by the collisions. Constituents coming from different nuclei interact in case the distance between the orthogonal projections of their centers onto the transverse

[1] See Section 1.2.2 for the discussion of the CGC model.

[2] It is worth mentioning that there is currently no unified approach that describes both large A-A and small p-A systems using fluctuations at the nucleonic level [182, 183]. For that reason we mostly focus on small systems.

plane is less than:

$$d = \sqrt{\frac{\sigma_{\text{inel}}^{\text{NN}}}{\pi}}. \tag{2.12}$$

The difference between the Optical and MC-Glauber models is due to the non-commuting property of the averaging operation. To illustrate it, we cite here formulae of the A-B nuclear system cross-section for MC-Glauber, [177]:

$$\begin{aligned}\sigma_{AB} = \int d^2\vec{b} \int d^2\vec{s}_{A_1} \cdots d^2\vec{s}_{A_A} T_A(\vec{s}_{A_1}) \cdots T_A(\vec{s}_{A_A}) \times \\ \int d^2\vec{s}_{B_1} \cdots d^2\vec{s}_{B_B} T_B(\vec{s}_{B_1}) \cdots T_B(\vec{s}_{B_B}) \times \\ \left\{ 1 - \prod_{i=1}^{A} \prod_{j=1}^{B} [1 - \hat{\sigma}(\vec{b} - \vec{s}_{A_i} + \vec{s}_{B_j})] \right\},\end{aligned} \tag{2.13}$$

where $\int d^2\vec{s}\hat{\sigma}(\vec{s}) = \sigma_{\text{inel}}^{\text{NN}}$. In the optical limit it reduces to:

$$\sigma_{AB} = \int d^2\vec{b} \left\{ 1 - \left[1 - T_{AB}(\vec{b}) \sigma_{\text{inel}}^{\text{NN}} \right]^{AB} \right\}. \tag{2.14}$$

In this approximation, individual nucleons "see" the approaching nucleus as a smooth density. Formulae (2.13) and (2.14) are equivalent when $\sigma_{\text{inel}}^{\text{NN}}$ is small. Optical approximation misses all the fluctuation terms, which proved to be important when describing HIC. Specifically, large value of the flow observable that was measured in Au-Au experiments was considered to be an indication of QGP formation [184]. Similar in magnitude final particle anisotropy was observed in Cu-Cu systems, see Fig. 2.7 (a). However, it was puzzling that if both results are of hydrodynamic origin then what explains the difference between the values of hydro response, see Fig. 2.7 (b). It was shown that this discrepancy was due to the disregard of quantum fluctuations in the initial state. To take them into account, one needs to generalize the definition of eccentricity, see (2.15) and (3.11). With that, the results of hydro response evaluation in both HIC systems agree, see Fig. 2.7 (c).

An illustration of the difference between the Optical- and MC- Glauber Models and the importance of fluctuations in HIC is shown in Fig. 2.8. In the former approach, the system has axial symmetry, as one can deduce from observing the contours of the nuclei transverse projections onto the reaction plane (RP). In MC-Glauber Model, the

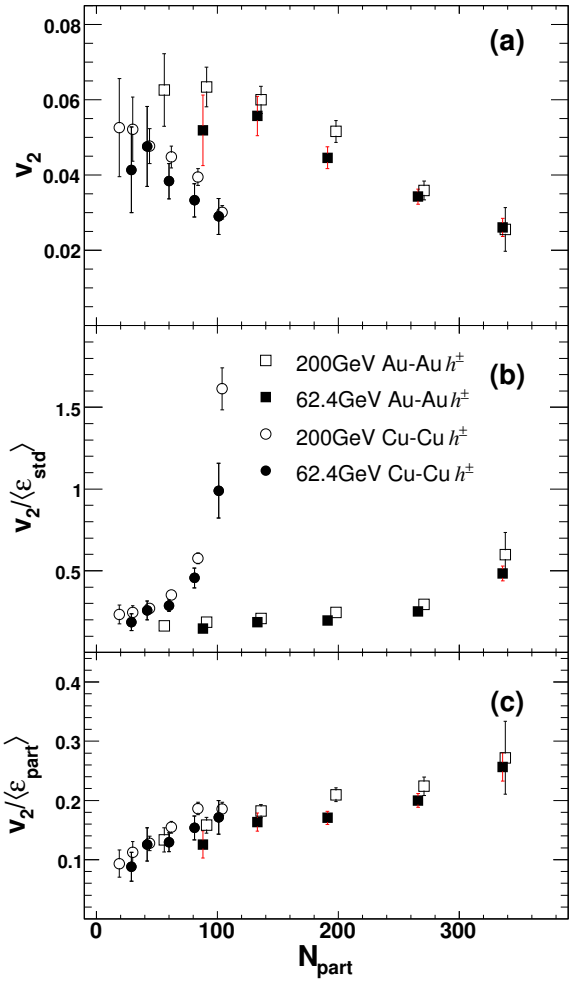

Figure 2.7: (a) Flow coefficients of Au-Au and Cu-Cu systems at collision energies of $\sqrt{s} = 62.4$ and 200 GeV [185, 186]. (b) Ratio of final particle to initial energy density anisotropies. This is the standard definition of hydro response, which relies on the Optical Glauber Model. (c) Hydro response defined based on the systems' participants. This definition is in the spirit of the MC-Glauber Model. It reveals scaling for all systems/energies and this way supports the conjecture of the hydrodynamical origin of the response. Figures from [185].

system does not necessarily have axial symmetry. Initial energy density anisotropy is set to be "symmetric" (diagonal) with respect to the new coordinate system, which

is called participant plane (PP). Specifically, the following conditions should hold:

$$\int d\mathbf{r}\,\epsilon(\mathbf{r})\,x = \int d\mathbf{r}\,\epsilon(\mathbf{r})\,y = 0. \tag{2.15}$$

The mentioned discrepancy in the results steamed from the difference in the definitions of eccentricity. This highlights the importance of the proper choice of observable in order to arrive at a meaningful physical conclusion. It also indicates the key role that fluctuations play in HIC. We will return to the discussion of the generalized definition of eccentricity later in Section 3.3. However, one can already conclude from Fig. 2.8 that quantum fluctuations of initial conditions create higher order harmonics response in azimuthal angle.[1]

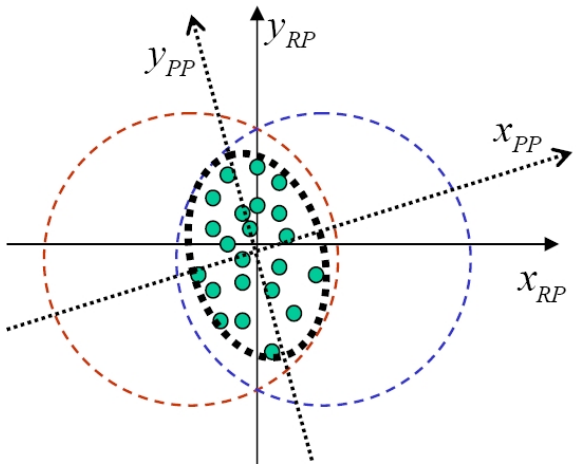

Figure 2.8: Illustration of the axial symmetry breaking in an A-A system that can be captured by the MC-Glauber, but not the Optical-Glauber Model. Figure from [188].

2.2.3 MC-KLN Model

We will describe here another well known model of initial conditions – MC-KLN [179]. Its main advantage is that, by using intuitions of saturation and color freeze-out

[1]Similar observations of the final particle momentum anisotropy in seemingly symmetric Au-Au collisions lead to the discovery of the triangular flow. It served to be another convincing evidence of the QGP creation in large collision systems [187].

coming from the CGC model, it provides a description of sub-nucleonic fluctuations. At the same time, it faces challenges with explaining experimental results of the triangular flow [189]. Its extension to small systems has also not yet been developed. However, we discuss this prescription for two reasons. First, to keep our discussion of the HIC models complete, as we want to compare the widely used approaches in Section 2.2.5. Second, to illustrate that modeling of initial conditions is an evolving field and a unified prescription for HIC systems is currently not available.

As we discussed in Section 1.2.2, in the Regge-Gribov regime semi-hard processes cross-sections become comparable with spatial dimensions of hadrons. This allows to assess the number of gluons in the initial state using k_T-factorization formula, [190]:

$$\frac{dN}{d^2\vec{x}_T dy} = \frac{4\pi^2 N_c}{N_c^2-1}\int \frac{d^2\mathbf{p}_\mathrm{T}}{p_T^2}\int d^2\mathbf{k}_\mathrm{T}\alpha_s(Q^2)\phi_A(x_+,\mathbf{k}_\mathrm{T}^2,\mathbf{x}_\mathrm{T})\phi_B(x_-,(\mathbf{p}_\mathrm{T}-\mathbf{k}_\mathrm{T})^2,\mathbf{x}_\mathrm{T}), \tag{2.16}$$

where

$$x_\pm = p_T e^{\pm\frac{y}{\sqrt{s}}}, \quad Q^2 = \max(\mathbf{k}_\mathrm{T}^2,(\mathbf{p}_\mathrm{T}-\mathbf{k}_\mathrm{T})^2). \tag{2.17}$$

y and p_T are correspondingly rapidity and transverse momentum of the produced gluon. The following prescription for the unintegrated gluon distribution, ϕ, is used:

$$\phi(x,\mathbf{k}_\mathrm{T}^2,\mathbf{x}_\mathrm{T}) = \begin{cases} \frac{\kappa(N_c^2-1)}{4\pi^3 N_c\alpha_s(Q_s^2)}\frac{Q_s^2}{Q_s^2+\Lambda_{QCD}^2}, & k_T \le Q_s, \\ \frac{\kappa(N_c^2-1)}{4\pi^3 N_c\alpha_s(Q_s^2)}\frac{Q_s^2}{k_T^2+\Lambda_{QCD}^2}, & k_T > Q_s, \end{cases} \tag{2.18}$$

It was motivated by the simplified assumption that it should resemble perturbative distribution behavior, $\sim 1/k_T^2$. This form differs from the one obtained using McLerran-Venugopalan model, which predicts logarithmic suppression, $\sim \ln(Q_s^2/k_T^2)$, and was used in the IP-Glasma model. Similarly, a perturbative form was chosen for the gluon density distribution[1]:

$$xf(x,Q^2) = K\ln\left(\frac{Q^2+\Lambda_{QCD}^2}{\Lambda_{QCD}^2}\right)x^{-\lambda}(1-x)^n, \tag{2.19}$$

where parameters K,λ,n are used to control the saturation scale behavior for various collision systems.

[1] It is related to the unintegrated counterpart in the following way: $xf_A(x,Q^2) = \int^{Q^2} d^2k_T \int d^2\vec{x}_\perp \phi_A(x,\vec{k}_T^2,\vec{x}_\perp)$.

Finally, the spatial dependence of saturation scale, Q_s, in the transverse plane is determined by solving equation:

$$Q_s^2(x, \mathbf{x}_\mathrm{T}) = \frac{4\pi^2 N_c}{(N_c^2 - 1)} \alpha_s(Q_s^2) x f(x, Q_s^2) T_\mathrm{wn}(\mathbf{x}_\mathrm{T}), \tag{2.20}$$

where $T_\mathrm{wn}(\mathbf{x}_\mathrm{T})$ describes local participants density, which is obtained using the MC-Glauber procedure [191].

2.2.4 IP-Glasma Model

In this section we will describe at the quantitative level[1] one of the most advanced implementations of the CGC inspired initial conditions – IP-Glasma [131, 192]. In addition to the description of CGC within the classical McLerran-Venugopalan framework [193] it includes the impact parameter[2] dependence of the saturation scale, which is based on the application of the IP-Sat model[3] [194, 195]. This allows to describe experimental data on multiplicity distributions in p-p collisions [196] which confirms that IP-Glasma properly reproduces general microscopic properties of the initial HIC phase.

The idea behind the IP-Sat model is that processes involving scattering of a particle in an excited state[4] can be treated within a dipole formation framework. A real photon would pass the proton's saturated gluon cloud without interaction, as it does not have any color charge. However, a virtual one, γ^*, can split into a quark-antiquark pair (dipole), and then its constituents can undergo elastic scattering off the proton (they have color charge), see Fig. 2.9 (a).

The dipole differential cross-section:

$$\frac{d\sigma_{q\bar{q}}}{d^2\vec{b}} = 2\left[1 - \exp\left(-\frac{\pi^2}{2N_c} r^2 \alpha_s(Q^2) x f(x, Q^2) T(b)\right)\right] \tag{2.21}$$

depends on the dipole size, r; the energy scale of the collision, Q; the gluon density inside the proton, $xf(x, Q^2)$; the strong coupling constant, $\alpha_s(Q)$; and the proton

[1] See Section 1.2.2 for a qualitative overview.

[2] With respect to the color source (not the nuclei) centers.

[3] Hence the name IP-Glasma.

[4] They are called diffractive collisions.

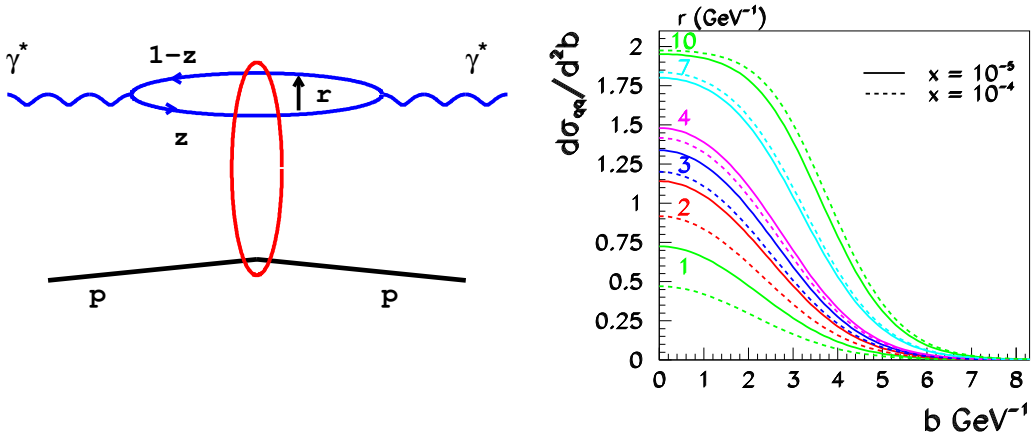

(a) (b)

Figure 2.9: Panel (a): Schematic representation of the virtual gluon scattering on hadron by the means of forming a quark–anti-quark dipole. p, γ^* denote proton, virtual photon paths respectively. r is the dipole's size. Panel (b): Dependence of the differential dipole cross-section, $\sigma_{q\bar{q}}$ on the impact parameter, b, for fixed values of the dipole size, r, and carried momentum fraction, x, see kinematic equation (1.36). Figures from [195].

thickness function, $T(b)$. The ansatzes for the gluon density and thickness functions can be tuned to fit the experimental data on inclusive and diffractive electron-proton DIS by HERA [197]. Specifically, one uses:

$$T(b) = \frac{1}{2\pi B_p} \exp\left(-\frac{b^2}{2B_p}\right), \quad xf(x, Q_0^2) = A_p x^{-\lambda_p}(1-x)^{5.6}, \tag{2.22}$$

where A_p, B_p, λ_p are constants, and gluon density is evolved to arbitrary scale, $Q \equiv \sqrt{1/r^2 + Q_0^2}$, using DGLAP equations.

One can see in Fig. 2.9 (b), that the obtained differential cross-section at first rapidly increases with the decreasing value of the impact parameter, b, but then saturates. Thus, the IP-Sat model correctly captures the physics of the process: the effect of the proton's field on the dipole grows inversely proportional to the distance between them, but hits a plateau as the gluon density can not exceed the saturation

scale. The size of the plateau can be assessed from the equation:

$$\frac{d\sigma_{q\bar{q}}}{d^2\vec{b}} = 1, \tag{2.23}$$

which at given values of Q, x, b is satisfied at a certain value of the dipole size, r_d. The value of the saturation scale is then:

$$Q_s(Q, x, b) = \frac{\sqrt{2}}{r_d(Q, x, b)}, \tag{2.24}$$

which is used in the IP-Glasma model.

The prescription of the initial conditions is then rather straightforward. As in all other models, it starts with the described in Section 2.2.2 MC-Glauber sampling of nucleons in the transverse plane using Woods-Saxon distribution. Then for every spatial position in the transverse plane, $\mathbf{r}_\perp$, the saturation scale, Q_s, is determined as a sum over all nucleons:

$$Q_s^2(Q, x, \mathbf{r}_\perp) = \sum_i \left[Q_s^i(Q, x, \mathbf{r}_\mathrm{T}^i - \mathbf{b}_\mathrm{T}^i)\right]^2, \tag{2.25}$$

where $\mathbf{r}_\mathrm{T}^i$ is the position of the nucleon center, i. The reason behind it is that saturation scale is proportional to the color density per unit area:

$$Q_s^2(Q, x, \mathbf{r}_\mathrm{T}) = C_g g^2 \mu^2(Q, x, \mathbf{r}_\mathrm{T}), \tag{2.26}$$

where the constant C_g is chosen to match the final particle multiplicity after the hydro evolution; typical value of x can be estimated for the fit of $\langle p_T \rangle(s)/\sqrt{s}$ to experimental data, [99].[1]

Once the color charge density distributions in participating nuclei is determined, one samples $\rho(\mathbf{x}_\mathrm{T})$ in every event from the Gaussian distribution in transverse plane subject to the following correlation condition:

$$\langle \rho^a(\mathbf{x}_\mathrm{T}) \rho^b(\mathbf{y}_\mathrm{T}) \rangle = \delta^{ab} \delta^2(\mathbf{x}_\mathrm{T} - \mathbf{y}_\mathrm{T}) g^2 \mu^2(\mathbf{x}_\mathrm{T}), \tag{2.27}$$

where $a/b = 1, \ldots 8$ are color indices.

[1] For a $\mathbf{r}_\perp$ dependent estimate of x, see [131, 192].

It is possible to show that the color field energy momentum tensor at early times can be described at leading order with the classical Yang-Mills (YM) equations, [198]:

$$[D_\mu, F^{\mu\nu}] = J^\nu. \tag{2.28}$$

Thus, one uses the color charge samples as initial conditions for the external currents:

$$J^\mu = \delta^{\mu\pm}\rho_{\substack{\mathrm{A}\\\mathrm{B}}}(x^\mp, \mathbf{x}_\mathrm{T}), \tag{2.29}$$

where $x^\pm \equiv (x^0 \pm x^3)/\sqrt{2}$ are the light-cone observables.

The solver of these equations is currently implemented only in a 2+1D case [131, 192]. Thus, one neglects any longitudinal dynamics. This is done to takes advantage of the simplifications that originate from the boost invariance assumption, such as light speed and "zero width" of the colliding nuclei, and absence of gradients in the longitudinal direction. By solving YM equations in time, one can calculate the color fields and thus their energy-momentum tensor. The latter can be matched to the hydrodynamic. This is how the IP-Glasma model of initial conditions works.

It is worth reminding that currently there is no initial conditions model that can describe subnucleonic fluctuations in asymmetric systems, see Section 1.2.2. For that reason one cannot use MC-KLN or IP-Glasma approaches described in Sections 2.2.3 and 2.2.4 in case of the p-A system that we study in this work. This is the reason we use an extension of the MC-Glauber model that although describes fluctuations at nucleonic level but allows to capture the longitudinal dynamics of the collisions. We discuss it in details in Section 3.1. In the next section we compare the discussed above initial conditions models, which are applicable when one considers dynamics of symmetric A-A systems next to the lab frame origin, see Section 2.1.

2.2.5 Model comparison

In Fig. 2.10 we provide graphical representation of the initial conditions for the MC-Glauber, MC-KLN, and IP-Glasma models. It is not possible to perform one to one comparison, because they have different characteristic values of the initial proper time, τ. Thus, no units are provided for their energy densities.

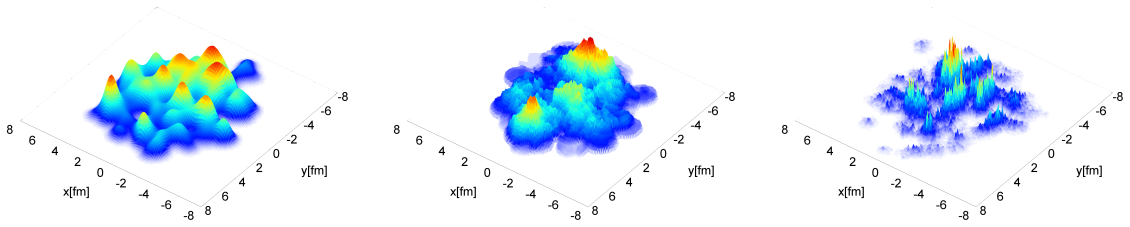

(a) (b) (c)

Figure 2.10: Graphical comparison of HIC initial conditions. Figures from [131]. On panel (a): MC Glauber. On panel (b): MC KLN. On panel (c): IP-Glasma.

However, recalling that all of them start with sampling of the nucleon positions using Woods-Saxon distribution, one can notice that the intuitive treatment of the CGC framework within the MC-KLN model creates additional sub-nucleonic structure in the initial energy profile, and IP-Glasma refines it even further. At the same time, the latter two approaches do not consider longitudinal evolution, which can play an important role in small systems. For that reason, in this work we choose to proceed with an improved MC-Glauber model, which we will introduce in Section 3.1. One does not expect that this approach will be as accurate in describing the structure of quantum fluctuations in the initial conditions, as the CGC ones. However, it will correctly capture their averaged size at the nucleon scale, which is important to further constrain the initial conditions models using experimental data, as they are still under development.

To highlight that the description at the nucleon level plays the leading role in the models of initial conditions, we mention here the recently introduced TRENTO framework [199]. It "effectively" unifies all of the discussed above models in one parametrization [200]. In this approach HIC initial conditions' density is defined as a superposition of the nuclei ones:

$$S(p; S_{\mathrm{A}}, S_{\mathrm{B}}) = \left(\frac{S_{\mathrm{A}}^{p} + S_{\mathrm{B}}^{p}}{2} \right)^{\frac{1}{p}} . \tag{2.30}$$

Here $S_{\mathrm{A/B}}$ are the regular MC-Glauber densities:

$$S_{\mathrm{A/B}} = \frac{w_{\mathrm{A/B}}}{2\pi\sigma^2} \exp\left[\frac{(\mathbf{x}_\perp - \mathbf{x}_{\perp\mathrm{A/B}})^2 + (\mathbf{y}_\perp - \mathbf{y}_{\perp\mathrm{A/B}})^2}{2\sigma^2}\right], \tag{2.31}$$

where $w_{\mathrm{A/B}}$ are the normalization pre-factors fitted to match final particle multiplicity; σ is the initial conditions effective transverse scale; $\mathbf{x}_{\perp\mathrm{A/B}}$ are transverse plane projections of nucleons in respective nuclei, A/B.

Dimensionless parameter p approximates between types of the initial conditions: $p = 1$ corresponds to the wounded nucleon model; $p = -0.67$ – MC KLN, [201]; $p = 0$ – glasma-like EKRT [202]. IP-Glasma model provides a more accurate microscopical description of the subnucleonic fluctuations in the initial conditions and is not reproduced by the formulated at the nucleon level TRENTO model [203]. However, in terms of the approximate accuracy of its phenomenological applications and the glasma physical foundations that it is based on it remotely resembles the EKRT model [204], which can be approximately described with the TRENTO parametrization.

With this qualitative comparison of the popular initial conditions models we conclude this section and turn to the detailed description of the next phase of the collisions – hydrodynamical evolution.

2.3 Implementation of hydrodynamics

In the previous section, we discussed several approaches to the modeling of the initial conditions' fluctuations in the transverse plane. Similarly, anisotropies are created in the longitudinal direction [205]. We will discuss them in more details in Chapter 5, keeping in mind that for small asymmetric systems longitudinal evolution is expected to be important. Here we will introduce kinematic variables that facilitate HIC description along the longitudinal axis, z. They are often used when describing the hydrodynamical evolution and the hadronization stages.

2.3.1 Kinematics

In the previous sections we saw that the discussed models of initial conditions assume intricate energy distribution in the transverse plane and trivial Bjorken boost

invariant profile in the longitudinal direction. This explains why a special choice of coordinates is utilized when describing dynamics along the beam-line direction.

For a particle with momentum, p^μ:

$$p^\mu = (E, p_x, p_y, p_z) = (m_\mathrm{T} \cosh y, p_x, p_y, m_\mathrm{T} \sinh y) \equiv (m_\mathrm{T} \cosh y, \mathbf{p}_\mathrm{T}, m_\mathrm{T} \sinh y). \tag{2.32}$$

Here E, m_T, y are correspondingly energy, transverse mass, rapidity of the particle:

$$E = \sqrt{m^2 + p^2}, \quad m_\mathrm{T} = \sqrt{m^2 + p_x^2 + p_y^2} \equiv \sqrt{m^2 + p_\mathrm{T}^2}, \quad y = \frac{1}{2} \ln \frac{E + p_z}{E - p_z}. \tag{2.33}$$

It is beneficial to use rapidity variable for two reasons. First, it transforms linearly under Lorentz boosts, which simplifies vector transformations to the lab frame and back, ubiquitously used in HIC. Second, it provides a geometrical interpretation of the particle's momenta. For that the particle's mass should be smaller compared to its spatial momenta, which is true for the majority of the produces in HIC yield. Specifically, if $p \gg m$:

$$y = -\ln \tan \frac{\theta}{2} \equiv \eta, \tag{2.34}$$

where η is known as the particle's pseudorapidity. Relation (2.34) is useful, because in order to determine the particle's rapidity, one needs to identify its species. This procedure leads to the introduction of an irreducible systematic error. However, it is easy to measure the particle's pseudorapidity, as it depends only on the value of the polar angle θ[1], see Fig. 2.11.

For future reference we note here, that the used by experimentalists $|\eta| < 2.4$ and $|\eta| < 5$ pseudorapidity cuts capture correspondingly about 90% and 99% of the entire azimuthal region. This allows to consider in the analysis the majority of particles that carry the memory of the underlying medium's collective behavior.

In the similar fashion, one deals with spatial vectors, x^μ. One switches to the $\tau - \eta_s$ coordinates that are called the proper time and the spatial rapidity:

$$\tau \equiv \sqrt{t^2 - z^2}, \quad \eta_s \equiv \frac{1}{2} \log \left(\frac{t + z}{t - z} \right). \tag{2.35}$$

[1]The angle between the particle's spatial momentum, $\mathbf{p}$, and the direction of the beam-line, $\hat{z}$.

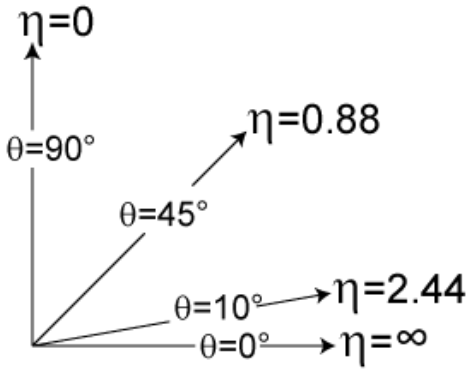

Figure 2.11: Illustration of the correspondence between the particle's rapidity η and its polar angle θ. Figure from [206].

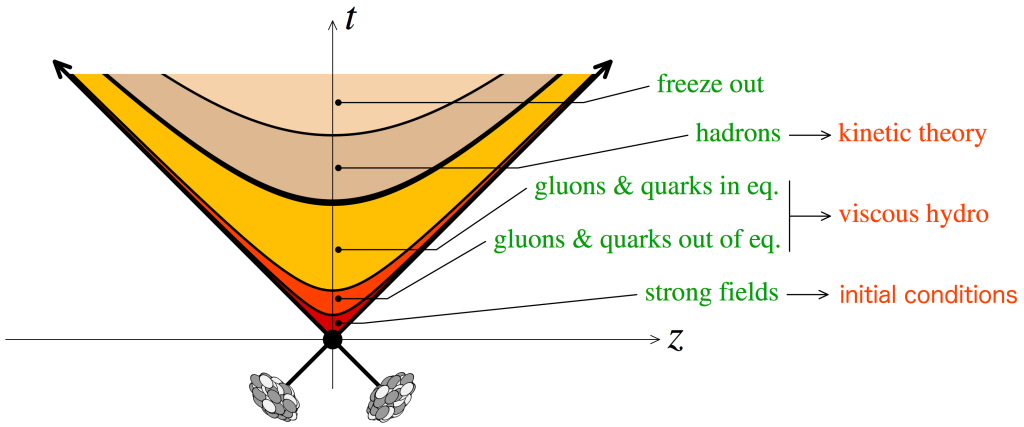

Figure 2.12: $t-z$ plane view of the HIC evolution stages. Figure from [207].

Then the coordinate four-vector, x^μ, can be represented in the following form:

$$x^\mu = (t, x, y, z) = (\tau \cosh \eta_s, x, y, \tau \sinh \eta_s) \equiv (\tau \cosh \eta_s, \mathbf{x}_\mathrm{T}, \tau \sinh \eta_s). \tag{2.36}$$

This explains why initial conditions are usually set at a constant τ rather than t. Spacial surfaces with fixed values of τ represent hyperbolas in the $t-z$ plane, see Fig. 2.12.

2.3.2 Hydrodynamics equations

As we discussed in Section 1.1.4, in this work we will use hydrodynamical model in the second order in gradients approximation. It is described with the following system

of differential tensor equations, [208, 209]:

$$\begin{cases} \partial_\mu T^{\mu\nu} = 0 & (2.37) \\ \tau_\pi \dot{\pi}^{\langle\mu\nu\rangle} + \pi^{\mu\nu} = 2\eta\,\sigma^{\mu\nu} - \delta_{\pi\pi}\pi^{\mu\nu}\theta + \varphi_7\pi_\alpha^{\langle\mu}\pi^{\nu\rangle\alpha} - \tau_{\pi\pi}\pi_\alpha^{\langle\mu}\sigma^{\nu\rangle\alpha} + \lambda_{\pi\Pi}\Pi\,\sigma^{\mu\nu} & (2.38) \\ \tau_\Pi\dot{\Pi} + \Pi = -\zeta\,\theta - \delta_{\Pi\Pi}\Pi\,\theta + \lambda_{\Pi\pi}\pi^{\mu\nu}\sigma_{\mu\nu}, & (2.39) \end{cases}$$

where:

$$T^{\mu\nu} = \epsilon\,u^\mu u^\nu - (P+\Pi)\,\Delta^{\mu\nu} + \pi^{\mu\nu} \tag{2.40}$$

is the energy-momentum tensor of the fluid with ϵ and P being respectively its energy density and pressure. It is worth mentioning that we chose to follow Landau framework[1] [64] in which the "ideal" part of the energy-momentum tensor has the following form in the rest frame of a fluid cell:

$$T^{\mu\nu}_{\text{ideal}} = \begin{pmatrix} \epsilon & 0 & 0 & 0 \\ 0 & P & 0 & 0 \\ 0 & 0 & P & 0 \\ 0 & 0 & 0 & P \end{pmatrix}. \tag{2.41}$$

Π and $\pi^{\mu\nu}$ are bulk and shear viscosity tensors. They need to be found by solving differential equations (2.38) and (2.39). They reduce to the NS form, (1.24):

$$\sigma^{\mu\nu} \equiv \nabla^{<\mu}u^{\nu>} = \frac{1}{2}\left[\nabla^\mu u^\nu + \nabla^\nu u^\mu - \frac{2}{3}\Delta^{\mu\nu}(\nabla_\alpha u^\alpha)\right], \quad \theta = \nabla_\mu u^\mu, \tag{2.42}$$

in the absence of the higher order terms $\tau_\pi, \tau_\Pi, \delta_{\pi\pi}, \varphi_7, \tau_{\pi\pi}, \lambda_{\pi\Pi}, \delta_{\Pi\Pi}, \lambda_{\Pi\pi}$, which originate from the second order gradient expansion. As discussed in Section 1.1.4, the values of these parameters could with certainty be determined only experimentally. However, one could calculate them in certain limits. Specifically, they were derived from the Boltzman equation in the limit of small, but finite, masses [208].

$$\frac{\delta_{\pi\pi}}{\tau_\pi} = \frac{4}{3}, \quad \varphi_7 = \frac{18}{35}\frac{1}{\epsilon+P}, \quad \frac{\tau_{\pi\pi}}{\tau_\pi} = \frac{10}{7}, \quad \frac{\lambda_{\pi\Pi}}{\tau_\pi} = \frac{6}{5}, \tag{2.43}$$

$$\frac{\delta_{\Pi\Pi}}{\tau_\Pi} = 1 - c_s^2, \quad \frac{\lambda_{\Pi\pi}}{\tau_\Pi} = \frac{8}{5}\left(\frac{1}{3} - c_s^2\right). \tag{2.44}$$

[1] Alternatively one can state that fluid velocity u^μ constitutes an eigenvector of the energy-momentum tensor.

Transport coefficients

$$\tau_\pi = \frac{5\,\eta}{\epsilon + P} \quad \text{and} \quad \tau_\Pi = \frac{\zeta}{15\left(\frac{1}{3} - c_s^2\right)^2 (\epsilon + P)} \tag{2.45}$$

control how fast the viscosity tensors approach their NS limit. For that reason they are respectively referred to as shear and bulk relaxation time.

Equations (2.37), (2.38), (2.39) together describe the laws of energy and momentum conservation. In general case, they should be complemented by the baryon charge conservation equation:

$$\partial_\mu j_B^\mu = 0. \tag{2.46}$$

However, as in this work we will be analyzing results obtained at the LHC, we can omit consideration of equation (2.46). It would provide an insignificant correction that would be beyond the systematic accuracy of the used model. For completeness, we mention here that equation (2.46) plays an important role in the studies of the QGP phase diagram. It is being investigated in the Beam Energy Scan experimental program that is taking place at RHIC. One could find more information on how hydrodynamical model could be used in this case in [210]. Here we will limit our discussion to the qualitative level. In Fig. one can find a (simplified) version of the hadron matter phase diagram, where energy regions corresponding to the experimental programs carried out at RHIC and the LHC are graphically specified.

In the conclusion of this section, we note that finding a general analytic solution to hydrodynamical equations is a very challenging problem even in the first-order (NS) approximation. Actually, it is one of the seven Millennium Problems established by The Clay Mathematics Institute of Cambridge [212]. Although several particular analytical solutions were found recently [71] those do not have direct applications in the studies of HIC systems. For that reason the only way to develop quantitative understanding of the underlying QGP dynamics is to apply numerical methods.

2.3.3 Numerical methods

In this section we will review several standard numerical approaches to solving Partial Differential Equations (PDEs). We will explain why these schemes fall short in de-

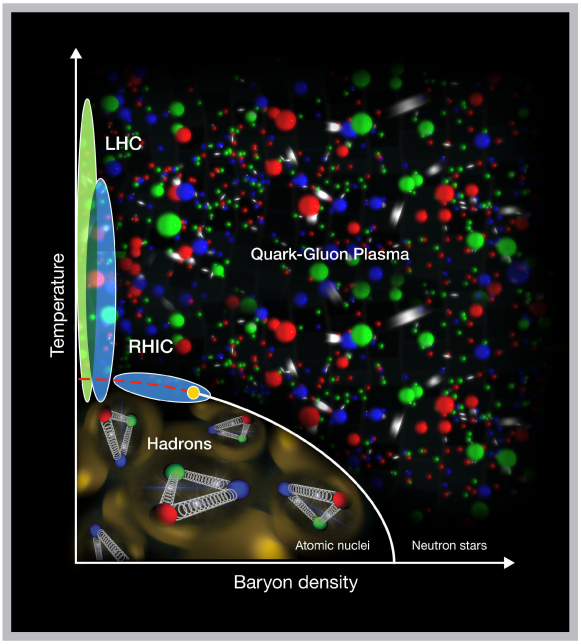

Figure 2.13: Hadronic matter phase diagram. Figure from [211]. Solid line corresponds to the first order phase transition between atomic nuclei and QGP. It ends with the "critical point" (in yellow). The steaming from there dashed line corresponds to the cross-over phase transition that was discovered using methods of lattice QCD. Blue and green ellipses denote the the states in which matter is observed at RHIC and the LHC correspondingly. One can see that in the LHC experiments matter is created at higher temperatures compared to RHIC and with nearly zero baryon density, which explains the reason one omits charge conservation treatment in the analysis.

scribing QGP evolution in HIC, which is governed by equations (2.37), (2.38), (2.39). To arrive at a proper approach one needs to take into account the specifics of the problem. We will illustrate that this is achieved by utilizing the Kurganov-Tadmor algorithm [213]. It was first implemented for that purpose in the numerical package MUSIC [214] which we use in this work.

System (2.37), (2.38), (2.39) that one needs to solve is a generalization of a conservation law equation for current j^{μ}, which could correspond to energy, momentum, baryon or any other density. In order to facilitate graphical visualizations, we will

consider dynamics of the current in one spatial dimension:

$$\partial_t \rho + \partial_x j = 0, \tag{2.47}$$

where ρ and $j \equiv v\rho$ are the appropriate quantity's density and current.[1] Given that the initial density profile at time t_0 is described by $\rho(t_0, x)$, the distribution at a later time t will be given by:

$$\rho(t, x) = \rho(t_0, x - vt). \tag{2.48}$$

Basically, the solution describes propagation of the wave along the x axis at speed v without modification of its shape. To compare different schemes visually we chose a profile with sharp edges, see Fig. 2.14, as it closely resembles the HIC setup when energy, densely concentrated in a small volume, quickly expands into vacuum at a light-like velocity. We will assess suitability of the scheme depending on how well it retains the structure.

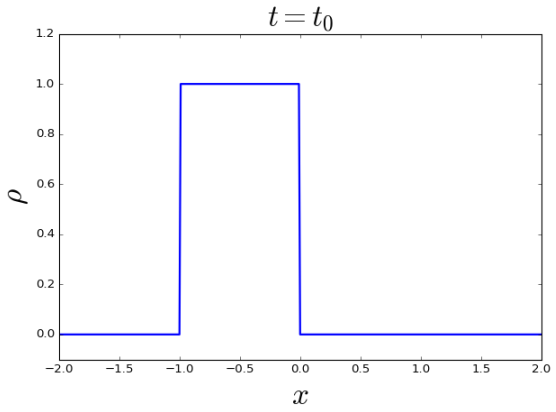

Figure 2.14: Initial density profile with sharp edges. Figure from [215].

The standard approach to solving (2.47) would entail application of the Finite Difference Methods (FDM), such as a forward-time centered-space (FTCS) scheme:

$$\rho_i^{n+1} = \rho_i^n - \frac{v\Delta t}{2\Delta x}(\rho_{i+1}^n - \rho_{i-1}^n). \tag{2.49}$$

Here n and i are indices of the FDM lattice in time and space directions. The lattice knots are separated by distances Δx and Δt in the corresponding directions. One

[1] We assume that the propagation speed v is constant.

can see the result of using the FTCS scheme in Fig. 2.15 (a). Its comparison to the analytic solution reveals that although it works well in the smooth density regions, FTCS experiences difficulties with describing the sharp edges.[1] Specifically, we see that numerically defined density values can be negative, which is non-physical.

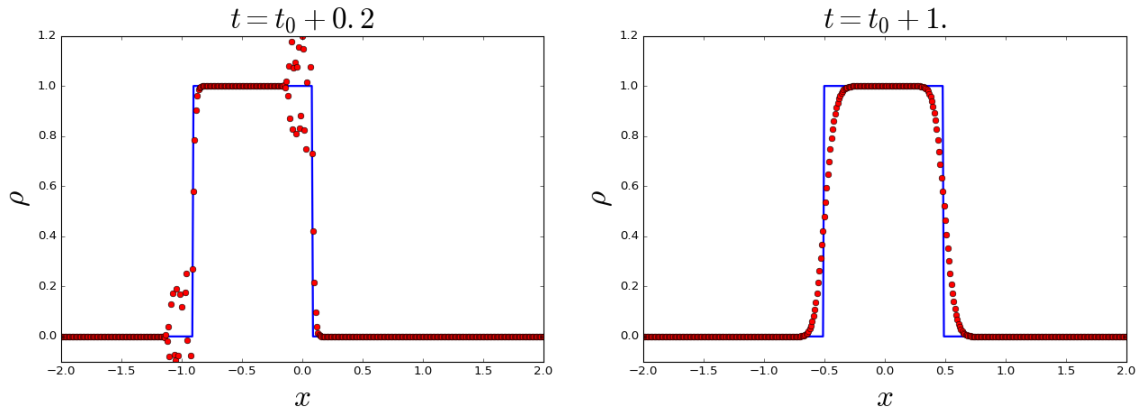

(a) (b)

Figure 2.15: Comparison of the analytic (solid line) to the FDM methods' (dots) solutions. Figures from [215]. Here and later $\Delta x = 0.01$, $\Delta t = 0.001$, $v = 0.5$. On panel (a), FTCS scheme was iteratively applied 200 times. On panel (b), Up-Wind scheme was iteratively applied 1000 times.

First order schemes, on the contrary, are less accurate in the smooth regions, but deal well with the sharp edges. Specifically, they maintain non-negativity of the density profile. This effect is due to the implicit numeric viscosity, which is introduced by this method. For example, in the (positive velocity branch of the) Up-Wind scheme:

$$\rho_i^{n+1} = \rho_i^n - \frac{v\Delta t}{\Delta x}(\rho_i^n - \rho_{i-1}^n) \approx \rho_i^n - v\Delta t\partial_x\rho + \frac{v\Delta t\Delta x}{2}\partial_x^2\rho. \tag{2.50}$$

The last term represents numerical viscosity, which is in this case proportional to the

[1] We here leave behind the questions of the FTCS scheme's stability. It can be shown with Von Neumann analysis that it allows exponential growth of unphysical modes. However, the problem can be fixed with applying backward-time scheme, although at the expense of the necessity to invert lattice size matrix at every iteration.

second spatial derivative. However, it appears to be too big to properly describe the profile evolution, see Fig. 2.15 (b). Sharp edges diffuse at a time inverse proportional to the product of $v\Delta x k^2$, where k describes the gradient of the transition.[1].

There are two conclusions that one can draw from the discussion so far. First, numerical viscosity is essential to ensure the scheme's stability, but needs to be small not to alternate the solution. Second, the regions of smooth and drastic variable change should be treated differently. One of the consequences of the latter observation is the special minmod prescription for defining spatial derivatives:

$$(\partial_x u)_i^n = \begin{cases} 0 & , \rho_i^n < \rho_{i-1}^n, \rho_{i+1}^n \\ 0 & , \rho_i^n > \rho_{i-1}^n, \rho_{i+1}^n \\ \text{sign}(\rho_{i+1}^n - \rho_i^n) \min\left(\theta\frac{|\rho_{i+1}^n - \rho_i^n|}{\Delta x}, \frac{|\rho_{i+1}^n - \rho_{i-1}^n|}{2\Delta x}, \theta\frac{|\rho_i^n - \rho_{i-1}^n|}{\Delta x}\right) & , \text{otherwise,} \end{cases} \tag{2.51}$$

where θ is a hyper-parameter that should be chosen specifically for every problem. Fig. 2.16 illustrates that (2.51) is a better density approximator in the sharp edge discontinuity regions and is equivalent to the (more accurate) central FDM in the smooth regions. Minmod is an example of the "Flux Limiter" methods that are part of the Total Variation Diminishing (TVD) schemes. They are used to suppress propagation of unphysical modes. Mathematically the condition that they impose can be expressed in the following form:

$$\sum_i |\rho_i^{n+1} - \rho_{i-1}^{n+1}| \leq \sum_i |\rho_i^n - \rho_{i-1}^n|. \tag{2.52}$$

In the continuous limit it is equivalent to the condition on $\int |\partial_x \rho| dx$, which controls that numerical implementation of the density derivative satisfies the physical conservation laws.

Another way to implicitly impose conservation laws in numerical calculations is to use Finite Volume Methods. By integrating (2.47), one arrives at:

$$\bar{\rho}_i^{n+1} = \bar{\rho}_i^n - \frac{v}{\Delta x} \int_{t_n}^{t_{n+1}} dt \left(\rho_{i+1/2}^n - \rho_{i-1/2}^n\right), \tag{2.53}$$

[1]The sharper the edge – the larger is the value of k

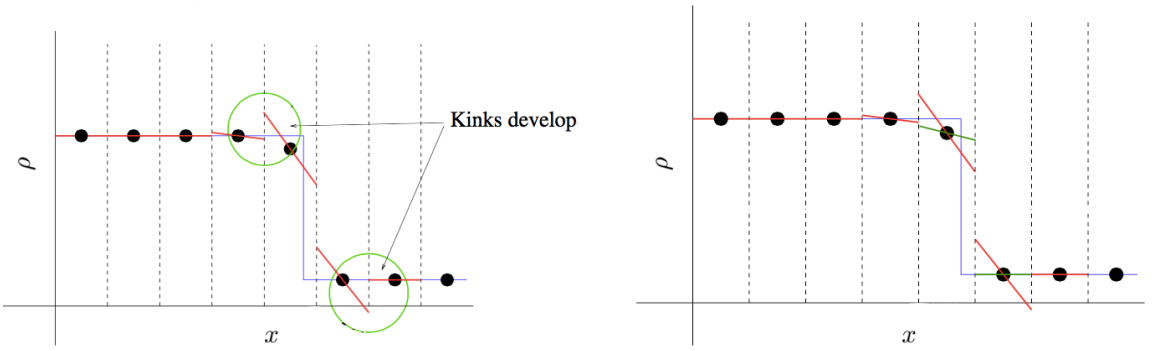

Figure 2.16: Graphical representation of the spatial derivative defined in (2.51). Figures from [215]. Blue solid line corresponds to the analytical solution. (left panel): Red line segments correspond to the central scheme prescription calculated in the vicinity region of every spatial lattice knot. Problematic regions that lead to the development of unphysical kinks are encircled. (right panel): Green line segments are plotted in the regions where the central difference and the minmod methods evaluate to different results. One can see that latter method provides a more accurate description of the analytic solution.

where $\bar{\rho}_i$ stands for the integral of the density within the spatial limits $[x_i - \frac{\Delta x}{2}, x_i + \frac{\Delta x}{2}]$, and $\rho_{i+1/2}$ is the density value evaluated in the mid point between x_i and x_{i+1}. One could use mid-point approximation in the time integral, as it should not have discontinuities typical for the spatial direction, and apply the Leap-Frog method. This would allow to arrive at a solution without the necessity of approximating density values at half-mid points. However, this approach suffers from the "staggered grid" drifting (effective decoupling of integer and half-integer lattices), which prevents it from handling density discontinuities effectively.

Thus, one has to use interpolation ansatz in the spatial direction. The following linear form proved to be effective:

$$\rho^n(x) = \sum_j \left[\bar{\rho}_j^n + (\partial_x \rho)_j^n (x - x_j)\right] \theta(x_{j-1/2} < x \leq x_{j+1/2}), \tag{2.54}$$

where $(\partial_x \rho)_j$ is the minmod spatial derivative at x_j, and θ is a support function that equals one when the argument condition is true and zero otherwise. Importantly, this

ansatz satisfies the conservation laws when being integrated over any symmetrical vicinity of the point it is defined at. Now one could efficiently switch between the "staggered" integer and half-integer grids. If one imposes that the time step must be small enough that the discontinuities can not propagate half of the lattice spacing Δx during one iteration in time, one would arrive at the Nessyahu-Tadmor scheme [216]. It allows to describe sharp edges well, see Fig. 2.17 (a). However, the drawback of the method is that it does not allow to arbitrarily reduce the size of the time step Δt as the value of the numerical viscosity is inverse proportional to it.

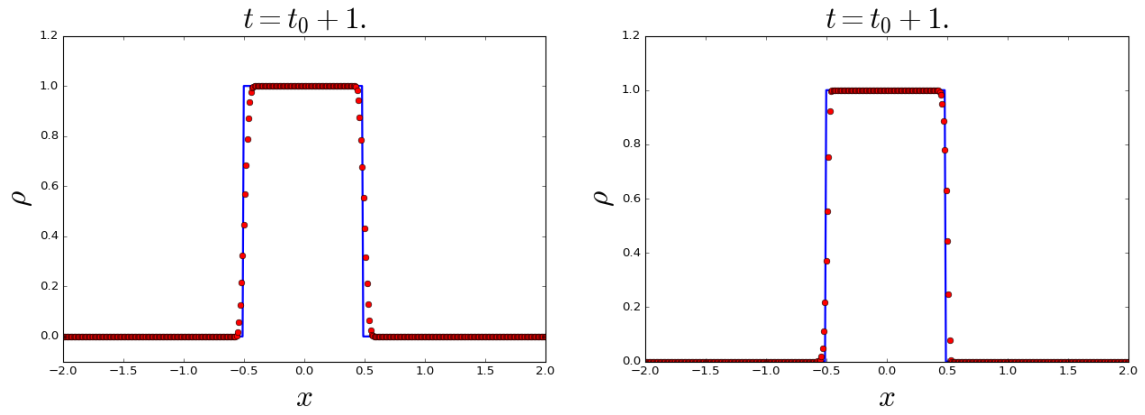

(a) (b)

Figure 2.17: Comparison of the analytic (solid line) to the numeric methods' (dots) solutions for Nessyahu-Tadmor (a) and Kurganov-Tadmor (b) schemes. Figures from [215].

Kurganov-Tadmore algorithm successfully solves this problem by taking into account that in physical problems discontinuities can not propagate faster than at the speed of sound, v. This approach also uses linear interpolation (2.54) when solving equation (2.53) on "staggered grids". But in this method vicinities of the half-integer knots are limited to the $[x_{i+1/2} - v\Delta t, x_{i+1/2} + v\Delta t]$ regions. Time step n density values contribute to the next iteration one, ρ_i^{n+1}, proportionally to the length of the interval they are defined on. Now the time step size can be taken to be arbitrary small[1]. This

[1] Condition $v\Delta t < \Delta x/8$ must still be satisfied.

allows one to arrive at the following set of Ordinary Differential Equations (ODE) that constitute the method[1]:

$$\frac{d\bar{\rho}_i(t)}{dt} = -\frac{H_{i+1/2}(t) - H_{i-1/2}(t)}{\Delta x}, \tag{2.55}$$

where

$$H_{j\pm1/2} = \frac{j(x_{j\pm1/2,+},t) + j(x_{j\pm1/2,-},t)}{2} - \frac{v_{j\pm1/2}(t)}{2}\left(\bar{\rho}_{j\pm1/2,+}(t) - \bar{\rho}_{j\pm1/2,-}(t)\right), \tag{2.56}$$

$$\bar{\rho}_{j+1/2,+} = \bar{\rho}_{j+1} - \frac{\Delta x}{2}(\rho_x)_{j+1}, \quad \bar{\rho}_{j+1/2,-} = \bar{\rho}_j + \frac{\Delta x}{2}(\rho_x)_j. \tag{2.57}$$

The method has small, $\sim (\Delta x)^3$, implicit numerical viscosity and deals with propagation of density discontinuities well, see Fig. 2.17 (b). It was used in this work for calculating QGP hydrodynamics.[2]

2.4 Hadronization of hydrodynamics

As QGP plasma will expand, its volume will grow in size and cool down. At some point one needs to switch to kinetic theory to describe the subsequent matter evolution. To calculate the one-particle distribution, one needs to specify the form of its correction, see (2.58). We use the prescription specified in [73, 217], which follows the theoretical framework of polynomial momentum expansion, (1.35):

$$f(x^\mu, p^\mu) = f_0(x^\mu, p^\mu)(1 + \delta f_{\text{shear}}(x^\mu, p^\mu) + \delta f_{\text{bulk}}(x^\mu, p^\mu)), \tag{2.58}$$

$$f_0 \equiv f_0(x^\mu, p^\mu) = f_0\left(\frac{u_\mu\, p^\mu}{T}\right) = \frac{1}{\exp\left(\frac{u_\mu\, p^\mu}{T}\right) \mp 1}, \tag{2.59}$$

$$\delta f_{\text{shear}}(x^\mu, p^\mu) = (1 \pm f_0)\frac{\pi_{\mu\nu} p^\mu p^\nu}{2\, sT^3}, \tag{2.60}$$

$$\delta f_{\text{bulk}}(x^\mu, p^\mu) = -(1 \pm f_0)\frac{C_{\text{bulk}}}{T}\left[\frac{m^2}{3\,(u_\mu\, p^\mu)} - \left(\frac{1}{3} - c_s^2\right)(u_\mu\, p^\mu)\right]\Pi. \tag{2.61}$$

Here u^μ, s, T are correspondingly the flow velocity, entropy density, temperature of the fluid at x^μ. m is the mass of the particle species under consideration. It

[1] Here we provide the generalized formulae of the method: velocity v can vary in space and time, $j = v\rho$.

[2] Kurganov-Tadmore ODE equations, (2.57), were solved with the second order Runge-Kutta method.

also enters the formula of the particle's energy, $p^0 = \sqrt{m^2 + \mathbf{p}^2}$. Prefactor $C_{\rm bulk}$ includes summation over all particle species. Corresponding particle masses, m_n, and degeneracies, d_n are also taken into account.

$$\frac{1}{C_{\rm bulk}} = \frac{1}{3T}\sum_n d_n m_n^2 \int \frac{d\mathbf{p}}{(2\pi)^3} f_0\,(1 \pm f_0)\left[\frac{m_n^2}{3(\mathbf{p}^2 + m_n^2)} - \left(\frac{1}{3} - c_s^2\right)\right], \tag{2.62}$$

where f_0 also implicitly depends m_n through the value of the particle's energy, p^0. In this work, we include into consideration all know particles and resonances with masses below 2 GeV [218]. This ensures that we do not introduce any systematic error during hadronization, as the maximum temperature of the QGP fireball in small systems is $\sim 0.5\,\text{GeV}$, see (2.59).

We utilize Cooper-Frye framework for hadronization. It assumes that particles are formed in the regions where QGP temperature is below some freeze-out value, $T_{\rm FO}$. According to [168], the momentum distribution of the particle species n is:

$$p^0 \frac{dN_n}{d\mathbf{p}} = \frac{g_n}{(2\pi)^3} \int\limits_{\Sigma_{T_{\rm FO}}} f(x^\mu, p^\mu)\, p^\mu\, d^3\Sigma_\mu. \tag{2.63}$$

Here $\Sigma_{T_{\rm FO}}$ is the manifold of world lines of all QGP medium cells that have temperature $T_{\rm FO}$. It is usually referred to as a freeze-out surface and it is embedded into the four dimensional time-space. $d^3\Sigma_\mu$ defines the local differential normal element with respect to this surface.

$$\Sigma = (\tau_{\rm FO}(x, y, \eta_s)\cosh\eta_s, x, y, \tau_{\rm FO}(x, y, \eta_s)\sinh\eta_s), \tag{2.64}$$

$$d^3\Sigma_\mu = -\varepsilon_{\mu\nu\lambda\rho} d\Sigma^\nu d\Sigma^\lambda d\Sigma^\rho, \tag{2.65}$$

where $\varepsilon_{\mu\nu\lambda\rho}$ is the antisymmetric Levi-Civita symbol, and $\tau_{\rm FO}$ is the proper time when matter temperature at spatial point (x, y, η_s) equals to the freeze-out value, $T_{\rm FO}$. Cooper-Frye prescription, (2.63), resembles the framework of thermal emission of particles from a black body. The difference is that in the former case one particle distribution, $f(x^\mu, p^\mu)$, has shear, (2.60), and bulk, (2.61), corrections.

Formula (2.63) looks specifically instructive in the proper time - spatial rapidity,

$\tau - \eta_s$, basis:

$$\begin{aligned} u_\mu p^\mu &= u^\tau p^\tau - u^x p^x - u^y p^y - \tau^2 u^{\eta_s} p^{\eta_s} \\ &= u^\tau m_T \cosh(y-\eta_s) - u^x p^x - u^y p^y - \tau u^{\eta_s} m_T \sinh(y-\eta_s), \end{aligned} \tag{2.66}$$

$$p^\mu d^3\Sigma_\mu = \left[m_T \frac{\partial\left(\tau_{\rm FO}\sinh(y-\eta_s)\right)}{\partial\eta_s} - \tau_{\rm FO} p^x \partial_x \tau_{\rm FO} - \tau_{\rm FO} p^y \partial_y \tau_{\rm FO} \right] dxdyd\eta_s\,, \tag{2.67}$$

where m_T is the "transverse mass" and y is the rapidity of the produced particle when (2.66) is used in (2.63). One can see that the rapidity of the emitted particle enters the formulae in a linear combination (difference) with the spatial rapidity of the surface element it was created from. This fact illustrates why particle spectra at mid-rapidity will be less affected by the dynamics at higher (in absolute value) rapidities.[1]

However, the obtained particle distribution, (2.63), can change by the time particles reach the detector. There are two reasons for that: resonance decays and rescatterings. We will discussion the latter effect in Section 4.4. The former source of the distribution correction is due to the fact that some of the QGP created particles are unstable. They will undergo subsequent decays into lighter hadrons, which in their turn might also have finite lifetime. In this work we calculate the entire tower of particle distribution corrections due to decays. We use a generalization to three spatial dimensions of the AZHYDRO code [219, 220]. We will illustrate the calculation procedure below.

One starts with considering particle distributions, (2.63), that corresponds to the resonance species, R. Note, that we are interested only in those types of particles, which decay due to strong processes. Excited states undergoing decays through the weak channel have longer lifetimes than those needed to reach the detector. For that reason in our analysis we can consider them as "stable".

Without loss of generality, we may assume that the resonance species R produces particle species j. Our task is to calculate the correction that the particle species' j

[1] Note that formula (2.67) reproduces the 2-dimensional Bjorken result, $(m_T\cosh(y-\eta_s) - p^x\partial_x\tau_{\rm FO} - p^y\partial_y\tau_{\rm FO})\,\tau_f dxdyd\eta_s$, when $\tau_{\rm FO}$ does not depend on spatial rapidity, i.e. when longitudinal profile is trivial.

momentum distribution receives as a result of the decay process. Kinematic analysis of an excitation's splitting is easy to perform when there are only two particles in the final state. If the resonance decays into N particles, one groups all particles into two "effective" ones:

$$M = \sqrt{\left(\sum_{i=1}^{N} p_i^\mu - p_j^\mu\right)^2} \text{ and } m_j, \tag{2.68}$$

where m_R is the mass of the resonance and m_i are masses of its decay products.[1]

In the rest frame of the resonance, R, the absolute momentum and energy of the particle j are:

$$p_* = \frac{\sqrt{\left((m_R + m_j)^2 - M^2\right)\left((m_R - m_j)^2 - M^2\right)}}{4m_R}, \qquad p_*^0 = \sqrt{m_j^2 + p_*^2}. \tag{2.69}$$

One then performs the transformation from the rest frame of the resonance to the lab frame. If one assumes that the decay is isotropic and integrates out the irrelevant for the particle j kinematic variables, which include resonance and "effective" particle's momenta, one arrives at the following formula:

$$\frac{dN_n}{dp_T^2 dy} = \frac{m_R b}{4\pi p_*} \int_{y_R^{(-)}}^{y_R^{(+)}} \frac{dy_R}{\sqrt{m_{jT}^2 \cosh^2(y_j - y_R) - p_{jT}^2}} \int_{m_{RT}^{2(-)}}^{m_{RT}^{2(+)}} \frac{dm_{RT}^2}{\sqrt{\left(m_{RT}^{(+)} - m_{RT}\right)\left(m_{RT} - m_{RT}^{(-)}\right)}} \frac{dN_n}{dp_{RT}^2 dy_R}, \tag{2.70}$$

where y_R and m_{RT} are the resonance's rapidity and transverse mass. Constrained by conservation laws, integration limits of kinematic observables are:

$$y_R^{(\pm)} = y_j \pm \ln\left(\frac{\sqrt{E_*^2 + p_{jT}^2} + p_*}{m_{jT}}\right) \tag{2.71}$$

and

$$m_{RT}^{(\pm)} = m_R \frac{E_* m_{jT} \cosh(y_j - y_R) \pm p_{jT}\sqrt{E_*^2 + p_{jT}^2 - m_{jT}^2 \cosh(y_j - y_R)}}{m_{jT}^2 \cosh^2(y_j - y_R) - p_{jT}^2}. \tag{2.72}$$

[1] Then one repeats the analysis iteratively until all produced particles species are considered.

One can see that the contribution is being calculated at the level of distributions rather than individual particles sampling. Thus, one could expect corrections arising from particle rescatterings. We checked that this effect is insignificant for all observables that we analyzed in this work due to the low final multiplicity in small HIC systems, see Section 4.4. Thus, we proceed to the discussion of the results of our calculation that were obtained using the AZHYDRO framework without loss of generality.

3

Hydrodynamics in small systems

In this chapter we specify the initial conditions model that we used and the results that we obtained for the flow observables, which are used as conventional evidences of the QGP formation in HIC. We compare them with experimental data to find reasonable agreement. We also provide a prediction for the triangular flow, $\bar{v}_3\{4\}$, as a function of multiplicity in small systems. Within our model, we are able to explain the unexpected similarity of the $\bar{v}_3\{2\}$ observable magnitude in large and small systems[1]. We study the origin of this result by comparing both systems' characteristic properties, such as hydrodynamical response, typical size, and asymmetry of the initial profile.

3.1 Model

We model the evolution of the collision system with the 3+1D relativistic viscous hydrodynamics solver MUSIC, [214]. In all calculations, we use the following parameters, which have given reasonable fits to heavy-ion data in the past: thermalization time $\tau_0 = 0.6$ fm/c, freeze out temperature $T_{\text{freeze}} = 150$ MeV, and equation of state s95p-v1 [147].

For initial conditions, we use a modified Monte Carlo Glauber model, where a contribution of entropy density is associated with each participating nucleon. The simplest prescription is to distribute entropy in the transverse plane according to a

[1]This suggests that our model adequately captures the structure of the quantum fluctuations in the initial state, as they define the system's triangular anisotropy in the linear response approximation, see Section 3.3.

2D Gaussian centered at the location of each participant:

$$\rho_{\perp}(\mathbf{x}_{\mathrm{T}}) \equiv \frac{1}{2\pi\sigma^2} \exp\left(-\frac{|\mathbf{x}_{\mathrm{T}}|^2}{2\sigma^2}\right). \tag{3.1}$$

The width of the transverse Gaussian σ is commonly chosen to be between 0.4 fm and 0.8 fm. We will vary the value within this range in order to study the effect of the granularity of the initial state and the transverse length scale associated with density fluctuations in the transverse plane.

For the distribution in spatial rapidity, one should take into account the fact that a proton-nucleus collision is not symmetric. In particular, there are more particles produced in the direction of the nucleus, and the asymmetry is greater in events with a larger multiplicity, see Fig. 3.1). This can be achieved by associating an asymmetric rapidity profile with each participant, peaked in the direction of its motion. Following [223], we take the profile:

$$\rho_{L\pm}(\eta_s) \equiv \left(1 \pm \frac{\eta_s}{y_{\mathrm{beam}}}\right) \exp\left[-\frac{\left(|\eta_s| - \eta_0\right)^2}{2\sigma_\eta^2}\theta\left(|\eta_s| - \eta_0\right)\right], \tag{3.2}$$

with parameters $\eta_0 = 2.5$, $\sigma_\eta = 1.4$, which proved to work well for describing experimental data on large collision systems [224, 225, 226, 227]. We set the value of the y_{beam} to the beam rapidity of 8.58, which corresponds to the case of the $\sqrt{s} = 5.02\,\mathrm{TeV}$ collision energy in p-Pb experiments [222]. So right moving participants have a contribution proportional to ρ_{L+} while left moving participants have a contribution proportional to ρ_{L-}. Events with more participants in one direction will then naturally have an asymmetry.

The total initial entropy density distribution is then given as a sum over participants:

$$s(\mathbf{x}_{\mathrm{T}}, \eta_s, \tau = \tau_0) = \sum_{i=1}^{N_{\mathrm{part}}} s_i \; \rho_{\perp}(\mathbf{x}_{\mathrm{T}} - \mathbf{x}_{\mathrm{T}}^i) \; \rho_{L\pm}(\eta_s). \tag{3.3}$$

Here $\mathbf{x}_{\mathrm{T}}^i$ is the transverse position of each participant nucleon and s_i is the entropy per participant (per unit rapidity at $\eta_s = 0$). Often this is taken to be a constant. However, this is not realistic. It implies, for example, that in the limit of a p-p system,

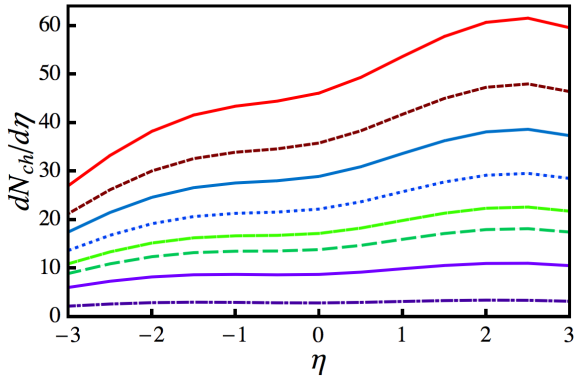

Figure 3.1: Charged hadron multiplicity $dN_{ch}/d\eta$ versus pseudorapidity in our calculation for various centrality bins, to be compared to the data from the ATLAS collaboration shown in Fig. 2 of [221]. From top to bottom curves correspond to centrality bins 0-1%, 1-5%, 5-10%, 10-20%, 20-30%, 30-40%, 40-60%, 60-90%. We do not plot experimental data in this plot, because signatures of collective behavior were found only in the high multiplicity collisions. If one bins events according to this – multiplicity – metrics, like it was done by the CMS collaboration for p-Pb at $\sqrt{s} = 5.02\,\text{TeV}$ [222], one will find that collective effects are clearly seen when the final yield of a collision is $150 < N_{ch} < 280$ charged hadrons. This range corresponds to approximately half of the entire observed experimentally total final multiplicity segment $0 < N_{ch} < 280$, but constitutes only a very small centrality region of $0-2\%$, see Table 3.1. Similarly, we note that the initial analysis of small systems (d-Au at $\sqrt{s} = 200\,\text{GeV}$) at RHIC [97] did not find signatures of collective behavior until after one focused on only the $0-5\%$ top centrality data [137] – we will discuss this fact in more details in Chapter 4. Thus, we conclude that one should not expect fluid dynamics to work in peripheral collisions and that the comparison of our hydrodynamic model results to experimental data should be performed on a multiplicity axis, as the conventionally used in large systems centrality binning does not allow to accurately observe where fluid dynamics stops to provide a reasonable description of experimental results. This is what we do later in all further figures of this work.

every collision will produce the same multiplicity. On the contrary, it is known that p-

p collisions exhibit a wide distribution of multiplicities, with a long tail, which is well described by a negative binomial distribution (NBD). Similarly, this basic Glauber model implies a multiplicity distribution in a p-Pb system that is much narrower than seen experimentally, see Fig. 3.2.

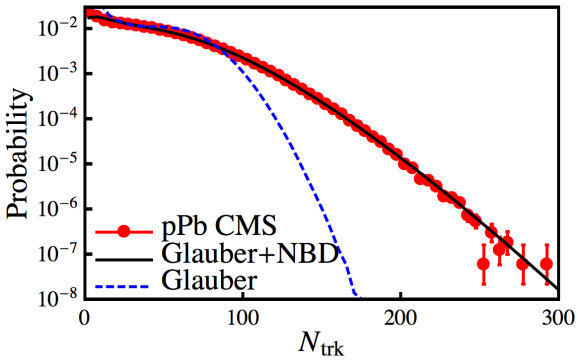

Figure 3.2: Distribution of (uncorrected) multiplicity N_{trk} at $|\eta| < 2.4$ and $p_T > 0.4$ GeV in p-Pb events from the CMS Collaboration [222] compared to the entropy distribution implied by a basic MC-Glauber model with a fixed entropy per participant (Glauber), and the model used in this work that has been supplemented with additional negative binomial fluctuations (Glauber + NBD).

However, instead of a constant, we can sample the factor s_i for each participant according to a NBD:

$$P(s_i) = \frac{\Gamma(s_i + s_0\kappa)(s_0\lambda)^{s_i}(s_0\kappa)^{s_0\kappa}}{\Gamma(s_0\kappa)s_i!(s_0\lambda + s_0\kappa)^{s_i+s_0\kappa}}. \tag{3.4}$$

In this case, the mean entropy per participant is $\langle s_i \rangle = s_0\lambda$. If we choose parameters $\lambda = 5.1$ and $\kappa = 0.6$, the scaled entropy distribution (i.e., with entropy per particle $s_0 \to 1$) approximately fits both p-p and p-Pb data, see Fig. 3.3 and Fig. 3.2. Since the initial entropy is approximately proportional to the final multiplicity in each event, this will result in an approximately correct distribution of multiplicity, when scaled by the proper factor s_0. Note that it is particularly important for this work to have a realistic description of the tail of the multiplicity distribution, since the events with the highest multiplicity are the best candidates for a hydrodynamic description.

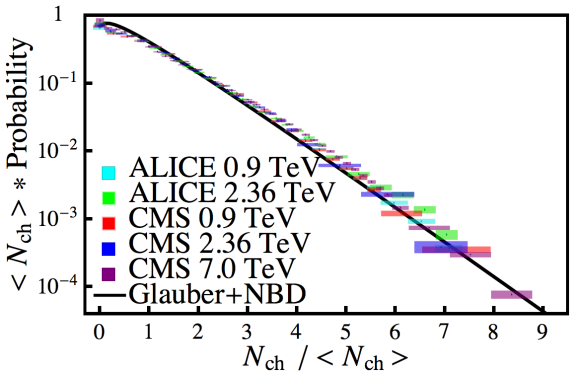

Figure 3.3: Scaled charged hadron multiplicity distributions $\langle N_{ch} \rangle * P(N_{ch}/\langle N_{ch} \rangle)$ at $|\eta| < 0.5$ in p-p collisions at various collision energies from the ALICE Collaboration [228], and the CMS Collaboration [229], compared to the probability distribution of entropy given by our model. Data are not available for the same collision energy as the p-Pb collisions that our model is tuned to, but normalizing by $\langle N_{ch} \rangle$ gives a universal curve that is reproduced for a range of collision energies (KNO scaling).

Finally, in order to facilitate comparisons to experiment, in the p-Pb case we shift from the frame representing the center of mass of an individual nucleon-nucleon collision to the experimental lab frame, which is shifted by a rapidity of 0.465 in the direction of the Pb beam.

With this prescription, we can generate a very large number of initial conditions and place them into "centrality" bins according to their total entropy. By calculating the multiplicity per unit entropy in a set of high-multiplicity events, we can then choose s_0 in (3.3) so that the measured multiplicity in the most central bin (representing a fraction 6×10^{-5} of events) matches the experimental value, $\langle N_{\rm ch} \rangle = 280$ for $|\eta| < 2.4$ and $p_T > 0.4$ GeV [222][1], see Table 3.1. After this has been done, we prepare events in the same multiplicity (entropy) bins in a Pb-Pb system, using exactly the same model parameters, for comparison. Once a sufficient set of initial conditions is prepared, we evolve them with hydrodynamics and calculate the distribution of charged hadrons in each event, parameterized as:

[1]This is done separately for each set of parameters, since the amount of entropy produced in the collision can vary.

$$\frac{dN}{dp_T d\eta d\phi} \equiv \frac{1}{2\pi}\frac{dN}{dp_T d\eta}\left[1 + \sum_{n=1}^{\infty} v_n(p_T,\eta)\cos n(\phi - \Psi_n(p_T,\eta))\right], \tag{3.5}$$

where in general v_n and Ψ_n depend on pseudorapidity η and transverse momentum p_T. In a purely hydrodynamic picture, this single-particle distribution contains all possible information, and observables can be calculated from appropriate event averages, as described in the following section.

Centrality(%)	Fraction	$\langle N_{\rm ch}\rangle$	$\langle N_{\rm ch}\rangle_{\rm CMS}$	$\langle N_{\rm trk}\rangle_{\rm CMS}$
0.00031–0.00631	0.00006	280	280	232
0.00631–0.05631	0.0005	230	236	196
0.05631–0.45631	0.004	190	195	162
0.45631–2	0.015	150	159	132
2–5	0.03	120	132	109
5–12	0.07	95	108	89
12–24	0.12	70	84	69
24–33	0.09	55	66	54
33–43	0.10	45	54	45
43–55	0.12	35	42	35
55–69	0.14	20	30	25
69–100	0.31	8	12	10

Table 3.1: Centrality bins used for the hydrodynamic calculations. The p-Pb hydro events were selected according to the total initial entropy, in bins corresponding to the fraction of the cross-section listed in the first column. The results can then be compared directly to data selected according to multiplicity in bins with the same fraction of the cross-section [222], or rebinned for comparison to other centralities (as in Fig. 3.1). The last column lists the (uncorrected) number of tracks from the respective CMS measurements in [222], to which we map our results when comparing to their data. Calculations with the same cuts in entropy were then performed for Pb-Pb events, to be compared to experimental measurements in the same multiplicity bins.

3.2 Comparison to experiment

The first task is to determine whether a hydrodynamic calculation, with realistic properties, can describe measured data. If so, it is confirmed as a plausible explanation. A number of hydrodynamic calculations suggesting that certain aspects of p-A collisions can be described with hydrodynamics are available [230, 231, 232, 233, 234, 235]. The distinctive feature of this work is that we combine all the relevant existing data and extend far into the high-multiplicity tail. The increasing amount of independent observables that can be described with the hydrodynamics paradigm and the absence of an equally successful competing explanation makes the conjecture of QGP formation in small systems even more plausible. In addition, we explore parameter space of the hydrodynamic model, including granularity of the initial conditions and viscosity of plasma, that has not been studied.

The simplest observables (theoretically) are single-particle measurements. For example, one can measure the average number of charged hadrons in each bin in pseudorapidity. We do this within our hydrodynamic framework for a number of centralities. Results are displayed in Fig. 3.1, showing that our prescription for the longitudinal profile is reasonable.

Next we calculate and compare to experimental data the mean transverse momentum for identified particles and investigate how parameters of our model affect the results, shown in Fig. 3.4. A smaller value of σ from (3.1) corresponds to a more granular initial condition. For future reference we also notice here that in a small p-A collision system, unlike in a larger A-A one, σ also significantly affects overall transverse size of the initial fireball, see Fig. 3.15. The larger gradients in the initial condition then result in a larger average transverse momentum, while shear viscosity has apparently little effect[1] From the above comparison it is clear that mean p_T data can be well described by a hydrodynamic calculation for high multiplicity events[2] – fluid dynamics approach is not expected to work in peripheral collisions, where energy

[1]This observation was also confirmed in [236].

[2]In Chapter 5, we will see that in order to simultaneously describe average transverse momentum and flow observables, one needs to take into account effects of bulk viscosity.

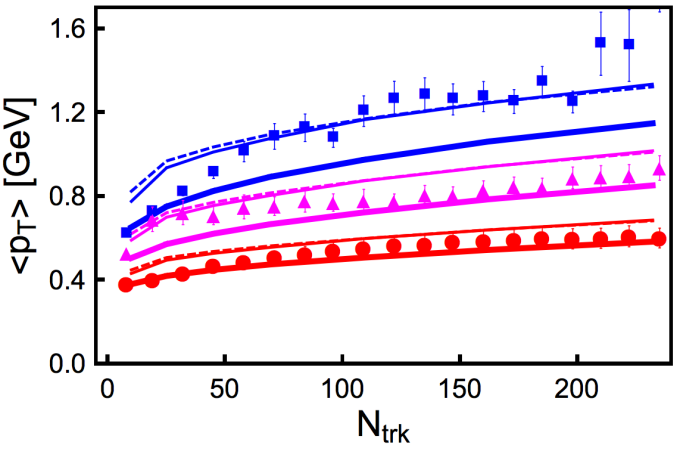

Figure 3.4: Average transverse momentum of identified particles in 5.02 TeV p-Pb collisions compared to CMS data [140]. Top to bottom: protons, kaons, pions. Each particle's mean p_T data was probed to be described with 3 sets of parameters. Thin solid lines correspond to $\eta/s = 0.08$, $\sigma = 0.4$ fm — our base line calculation. Thick lines were obtained by changing the value of σ to 0.8 fm, dashed of η/s to 0.

density of the system is not high enough to melt hadronic matter into QGP.

The most striking aspect of the p-Pb data, however, is the strong azimuthal dependence, which can be captured by Fourier component expansion. Here we provide an explicit definition, which stems from (3.5):

$$v_n(p_{\mathrm{T}})e^{in\Psi_n(p_{\mathrm{T}})} \equiv \frac{\int_0^{2\pi}\int_{|\eta|<2.4} e^{in\phi}\frac{dN(p_{\mathrm{T}},\eta,\phi)}{d\phi dp_{\mathrm{T}}d\eta}d\phi d\eta}{\int_0^{2\pi}\int_{|\eta|<2.4}\frac{dN(p_{\mathrm{T}},\eta,\phi)}{d\phi dp_{\mathrm{T}}d\eta}d\phi d\eta}. \tag{3.6}$$

v_n and Ψ_n are correspondingly called flow coefficients and angles. As we mentioned above, in general case they depend on the values of both transverse momentum, p_{T}, and pseudorapidity, η. We explicitly chose to fix the latter in order to mimic the CMS detector acceptance. If one integrates out p_{T} dependence as well, one will obtain the so-called integrated flow:

$$\bar{v}_n e^{in\bar{\Psi}_n} \equiv \frac{\int_0^{2\pi}\int_{|\eta|<2.4}\int_{.3\mathrm{GeV}}^{3\mathrm{GeV}} e^{in\phi}\frac{dN(p_{\mathrm{T}},\eta,\phi)}{d\phi dp_{\mathrm{T}}d\eta}d\phi d\eta dp_{\mathrm{T}}}{\int_0^{2\pi}\int_{|\eta|<2.4}\int_{.3\mathrm{GeV}}^{3\mathrm{GeV}}\frac{dN(p_{\mathrm{T}},\eta,\phi)}{d\phi dp_{\mathrm{T}}d\eta}d\phi d\eta dp_{\mathrm{T}}}, \tag{3.7}$$

which represents the averaged particle anisotropy of the system weighted with its yield.

In order to compare our model's results to experimental measurements, it is beneficial to calculate the following quantity:

$$\bar{v}_n\{2\}^2 \equiv \frac{1}{N_{\text{events}}} \sum_{\text{events}} \bar{v}_n^2. \tag{3.8}$$

We will explain the reason in detail in Chapter 4.2.2. In a nutshell, there is an unavoidable uncertainty related to the extraction of flow coefficients from one-particle distribution that is relatively large, $\sim 50\%$. It is, however, considerably smaller, $\sim 5\%$, in multi-particle calculations, which are thus broadly utilized. Hence the index $\{2\}$ in (3.8), which indicates that the value of the final particle anisotropy was assessed from the two-particle distribution.

The results of our hydrodynamic calculation for $\bar{v}_2\{2\}$ and $\bar{v}_3\{2\}$ are compared to experimental data in Fig. 3.5. Viscosity has the expected effect of suppressing $\bar{v}_n$. Increasing σ causes a decrease in the spatial eccentricity (due to the increase in the system size), and therefore also has a suppressing effect.

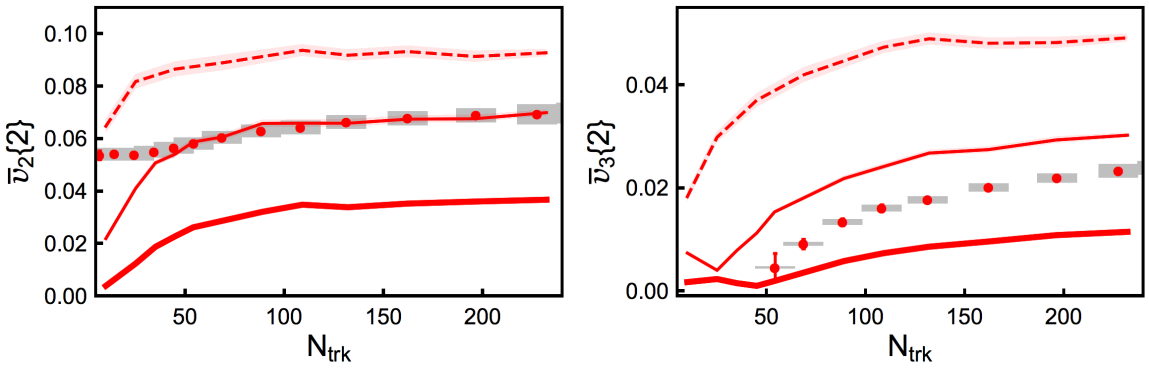

Figure 3.5: Integrated charged hadron $\bar{v}_2\{2\}$ (left panel) and $\bar{v}_3\{2\}$ (right panel) in 5.02 TeV p-Pb collisions for $|\eta| < 2.4$ and $p_T > 0.3$ GeV compared to measurements from the CMS Collaboration [222]. Curve types correspond to the ones used in Fig.3.4. Namely, the thin solid line corresponds to the observable's (in this case $\bar{v}_2\{2\}$) calculation within our model with a set of parameters $\eta/s = 0.08$ and $\sigma = 0.4$ fm, thick line — $\eta/s = 0.08$ and $\sigma = 0.8$ fm, dashed line — $\eta/s = 0$ and $\sigma = 0.4$ fm.

It is worth noting that averaging over events in (3.8) and all the following formulae is essential, because flow coefficients vary event-to-event. This effect is mostly due to the quantum fluctuations pertinent to the initial conditions of HIC. For that reason the study of flow coefficients is expected to shed light upon the physics of the initial state. However, one can see that the viscosity of the hydrodynamic model, η/s, affects the results of the calculation as much as a substantial smoothening of the initial profile, described by σ, see Fig.3.5. Thus, it is hard to disentangle corresponding individual contributions and this way to estimate the characteristic scale of quantum fluctuations from flow coefficients alone.

An interesting feature that was noticed is that if one plots $\bar{v}_3\{2\}$ from p-Pb and Pb-Pb collisions as a function of multiplicity (i.e., comparing high-multiplicity events in p-Pb to peripheral events in Pb-Pb with the same multiplicity), the results are very similar [222]. It has been questioned whether this is natural (or even possible) in a hydrodynamic picture. To answer this, we calculated $\bar{v}_3\{2\}$ in both systems using the set of parameters that reasonably fits the above observables ($\sigma = 0.4$ fm and $\eta/s = 0.08$), and the result is shown in the left panel of Fig. 3.6. While $\bar{v}_3\{2\}$ is still slightly above the data for these parameters, we find that even in our simple model, we see very similar values in the two systems. We will investigate this interesting result further in the following section.

In order to study anisotropy dependence on transverse momentum and following the same motivation that lead to (3.8), one defines differential flow observable:

$$v_n\{2\}(p_{\mathrm{T}}) \equiv \frac{\frac{1}{N_{\mathrm{events}}} \sum\limits_{\mathrm{events}} v_n(p_{\mathrm{T}}) \bar{v}_n \cos n(\Psi_n(p_{\mathrm{T}}) - \bar{\Psi}_n)}{\sqrt{\frac{1}{N_{\mathrm{events}}} \sum\limits_{\mathrm{events}} \bar{v}_n^2}}. \tag{3.9}$$

See the comparison of our model's calculation of $v_2\{2\}(p_T)$ to experimental data for the highest multiplicity bin in the right panel of Fig. 3.6.

An extension of (3.8) that allows to compare calculated in our model flow coefficients to the estimates obtained from experimental four-particle correlations is also

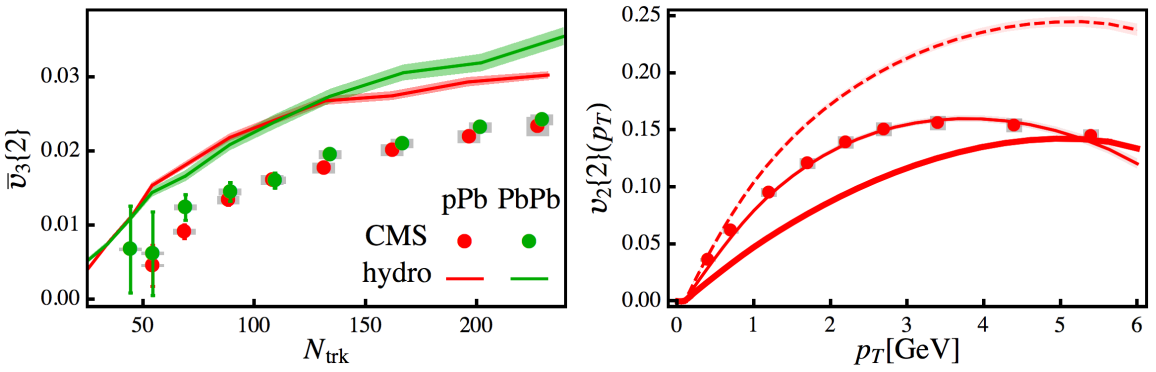

Figure 3.6: Left panel: integrated charged hadron $\bar{v}_3\{2\}$ for the parameter set $\eta/s = 0.08$ and $\sigma = 0.4$ fm in p-Pb compared to Pb-Pb collisions [222]. Right panel: differential charged hadron $v_2\{2\}(p_T)$. For curve types and data reference see caption of Fig. 3.5.

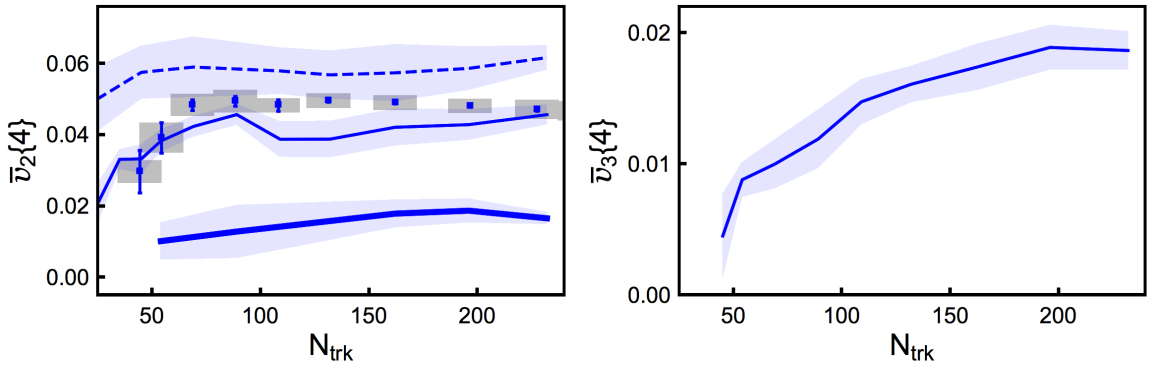

Figure 3.7: Left panel: integrated charged hadron $\bar{v}_2\{4\}$. For curve types see caption of Fig. 3.5. Right panel: predicted integrated charged hadron $\bar{v}_3\{4\}$ in 5.02 TeV p-Pb collisions for $\sigma = 0.4$ fm, $\eta/s = 0.08$, $|\eta| < 2.4$ and $p_T > 0.3$ GeV.

possible:

$$\bar{v}_n\{4\}^4 = 2\left(\frac{1}{N_{\rm events}}\sum_{\rm events}\bar{v}_n^2\right)^2 - \left(\frac{1}{N_{\rm events}}\sum_{\rm events}\bar{v}_n^4\right). \tag{3.10}$$

Because of how the two-particle correlation is subtracted from a four-particle correlation, non-flow effects that complicate the comparison between hydrodynamical models and experimental data get typically suppressed – we will discuss it in more

details details in Chapter 4.3.1. As a result, $\bar{v}_n\{4\}$ calculations performed within models that do not assume strong collective behavior typically give a value very close to zero, while hydrodynamic calculations typically predict a sizable value. Remarkably, high-multiplicity p-Pb experimental data show a large value that is clearly compatible with a hydrodynamic picture, as shown in the left panel of Fig. 3.7. To date, only hydrodynamic model calculations have been able to reproduce this large (real) value of $\bar{v}_2\{4\}$.

We also include a prediction for $\bar{v}_3\{4\}$ in the right panel of Fig. 3.7. We do not expect it to provide an accurate quantitative description of the data, as our calculation of $\bar{v}_3\{2\}$ is systematically above the measurements. However, an experimentally observed non-trivial value of $\bar{v}_3\{4\}$ that our model qualitatively reproduces will provide an additional constraint on the alternative explanations of small systems dynamics, such as jet physics, as they are not expected to even qualitatively explain such non-trivial multiplicity behavior of triangular flow.

In this section, we presented the results of one of the first parameter space explorations of a hydrodynamic framework applied to the description of the high multiplicity p-Pb collisions. We observed that our robust hydrodynamic model that includes all the relevant effects of small hadron collision systems such as longitudinal asymmetry of the collision geometry, the initial conditions fluctuations of the nuclear density, and the shear viscosity of the QGP medium at least qualitatively reproduces flow experimental data. We found out that the parameter values of $\sigma = 0.4\,\text{fm}$ for the transverse fluctuations granularity and $\sigma/s = 0.08$ for the fluid shear viscosity provide a somewhat accurate description of elliptic flow and qualitatively reproduce the shape of the triangular flow dependence on multiplicity. We note that there is a number of effects that lead to irreducible at the moment systematic uncertainties in hydrodynamic modeling of hadron collision systems. Specifically, the temperature dependence of shear viscosity, the viscous correction to particle distribution, and the mechanism of sub-nucleonic fluctuations in the initial conditions are not known with any degree of precision. Our analysis indicates that these effects greatly influence

the results of hydrodynamic calculations and especially the value of the triangular flow, which is expected to be more sensitive to the initial state nuclear density fluctuations. This consideration and the fact that our hydrodynamic model provides a simultaneous qualitative description of flow measurements, which is considered to be a compelling argument towards the creation of QGP in large collision systems, suggests that fluid dynamics is a plausible explanation of experimental data trends observed in high multiplicity p-Pb collisions.

3.3 Investigating the hydrodynamic response

It is interesting to investigate more thoroughly how flow develops, especially in order to better understand the results in the left panel of Fig. 3.6, which displays a striking similarity in triangular flow between p-Pb and Pb-Pb events with the same multiplicity.

In hydrodynamic calculations of nucleus-nucleus collisions, the final flow is understood to be a hydrodynamic response to large-scale properties of the initial density [237]. That is, one can make a direct connection between the final triangular flow and the "triangularity" of the initial state. This triangularity is a vector that has a size ε_3 and orientation Φ_3, which can be conveniently written as the magnitude and phase of a complex number

$$\varepsilon_3 e^{i3\Phi_3} \equiv -\frac{\int r^3 e^{i3\phi} s(\mathbf{x}) d\mathbf{x}}{\int r^3 s(\mathbf{x}) d\mathbf{x}}, \tag{3.11}$$

where $r = \sqrt{x^2 + y^2 + z^2}$, ϕ is the polar angle in the transverse plane, and s is the entropy density distribution.

It has been shown [238, 239] that the flow vector is approximately proportional to the triangularity. That is, in a given centrality class, the magnitude and direction of triangular flow in a given event follows the approximate relation

$$\bar{v}_3 e^{i3\bar{\Psi}_3} \simeq k\varepsilon_3 e^{i3\Phi_3}, \tag{3.12}$$

where the coefficient k encodes all relevant information about the hydrodynamic response (e.g., medium properties), but is independent of the initial conditions. The relevant properties of the initial conditions, on the other hand, are encoded in the triangularity vector.

The accuracy of this relation can be tested quantitatively by calculating the Pearson correlation coefficient Q_3 between the left and right sides of (3.12) over a large set of events

$$Q_3 = \frac{\left\langle \bar{v}_3 \varepsilon_3 \cos 3(\bar{\Psi}_3 - \Phi_3) \right\rangle}{\sqrt{\langle \bar{v}_3^2 \rangle \langle \varepsilon_3^2 \rangle}}. \tag{3.13}$$

If triangular flow is perfectly predicted by the initial triangularity in every event, then $Q_3 = 1$. Otherwise $|Q_3| < 1$, with larger values indicating a stronger linear correlation.

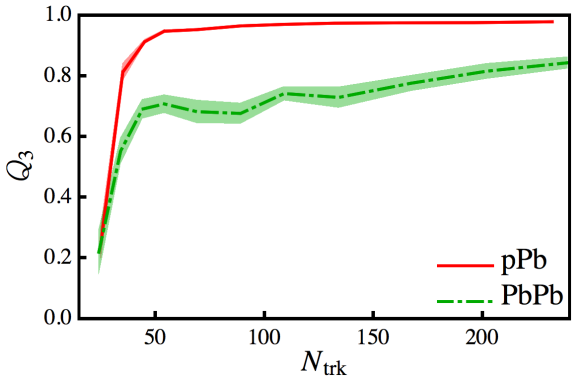

Figure 3.8: Linear correlation Q_3 between the initial triangularity vector and the final flow vector, (3.13), as a function of multiplicity.

In Fig. 3.8 we show Q_3 in various multiplicity bins for both p-Pb and Pb-Pb collisions. The triangularity was calculated at zero spatial rapidity, and integrated triangular flow was calculated in the same kinematic region as in the previous section: $|\eta| < 2.4$, $p_T > 0.3$ GeV. For the multiplicity region of interest, Q_3 is large. Therefore it is plausible to analyze p-Pb events in terms of ε_3, just as in Pb-Pb collisions.

A simple expectation is that the multiplicity scales roughly with the number of participant nucleons N_{part}, so that comparing p-Pb and Pb-Pb events at the same multiplicity is also comparing systems with the same number of participants. Further, since geometric fluctuations are typically expected to be driven by the fluctuating positions of participants within the colliding nuclei, such fluctuations should be similar in these two systems. Since symmetry dictates that ε_3 is generated entirely from fluctuations, the natural expectation would then be that its value is similar in both systems. If the hydro response, k, is similar in both systems, this is a natural explanation for the similar values of $\bar{v}_3$. On the other hand, if the hydro response is different (e.g., because of different system sizes), similar values of $\bar{v}_3$ would be unnatural in a hydrodynamic system. Arguments like this have been made in, e.g. [240, 241], and they explain why the similarity of triangular flow in p-Pb and Pb-Pb collisions was

not trivially expected in a hydrodynamic calculation [222].

Our model suggests that the experimentally observed triangular flow similarity phenomenon is due to the intricate interplay of the following three effects: fluctuations in the initial conditions, peculiarities of the utilized events binning metrics, and the difference of the hydrodynamic properties in systems of different sizes. The modeling of the first effect in our framework is greatly impacted by the NBD of entropy per participant. It allows the individual contributions of wounded nucleons to the initial matter density profile to vary not only in space, like in the discussed in Section 2.2.2 MC Glauber Model, but also in magnitude. Second, particle multiplicity that is used for events binning is an appropriate quantity to compare energies of QGP fireballs formed in p-Pb and Pb-Pb collisions, but it creates a sense of false similarity between the happening inside of these systems dynamics, which should be described using two distinct regimes. Indeed, the region of $150 < N_{\mathrm{trk}} < 250$ multiplicity corresponds to central (0-2%) collisions in p-Pb and to peripheral ones (55-60%) in Pb-Pb [222]. We will show that this leads, for example, to the difference in the characteristic sizes of p-Pb and Pb-Pb fireballs and their hydrodynamic properties. We will now discuss all these effects in order to show that triangular flow similarity in p-Pb and Pb-Pb collisions is not a trivial consequence of the same initial conditions profiles and identical system evolution properties, but a profound and intricate physical phenomenon that our framework is able to capture this way providing additional credibility to the applicability of hydrodynamics towards describing processes in hadron collisions.

We will start by comparing p-Pb and Pb-Pb qualitatively. As we noted above, ultra-central p-Pb and peripheral Pb-Pb collisions have similar multiplicities. In our model, nuclei consist of multiple nucleons distributed inside of them according to the Woods-Saxon distribution, see Fig. 2.5 and equation (2.4). For a large nucleus, such as lead, the nucleon density is constant inside a sphere of an order of magnitude larger size, $R \sim 5\,\mathrm{fm}$, than that of the transition scale, $a \sim 0.5\,\mathrm{fm}$, which describes the distance at which the probability to find a nucleon in the "halo" (outside of the nucleus "core", $r \leq R$) is exponentially smaller. Thus, the lowest multiplicity event

will likely correspond to the Pb-Pb collision in which a nucleon from the periphery of one nucleus will interact with a nucleon from the periphery of another nucleus, see the right panel of Fig. 3.9.

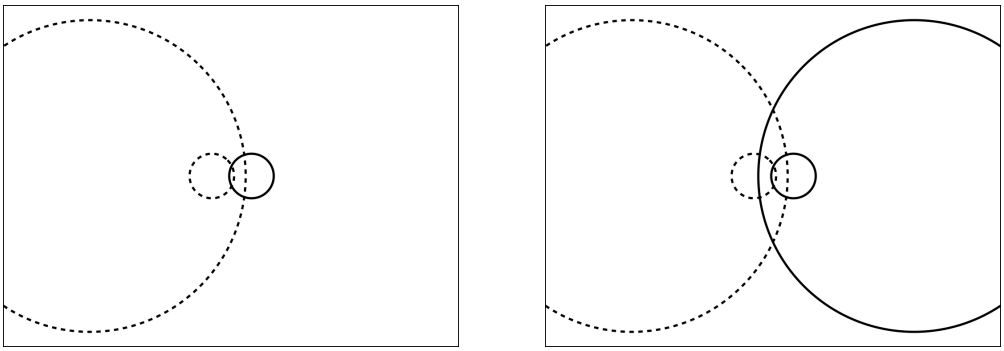

Figure 3.9: Examples of the lowest multiplicity collisions in the standard MC Glauber Model for p-Pb (left panel) and Pb-Pb (right panel) systems. Circles of large radii correspond to the transverse plane orthogonal projections of R-radius spheres plotted around the colliding lead nuclei centers. Small circles correspond to the wounded nucleons in each of the colliding nuclei.

An event with (slightly) higher (than the lowest) multiplicity will probably have three participants. Most likely, one of them will be a nucleon from the periphery of one nucleus, and the other two from either the "halo" or the edge of the "core" of the second one, see the right panel of Fig. 3.10.

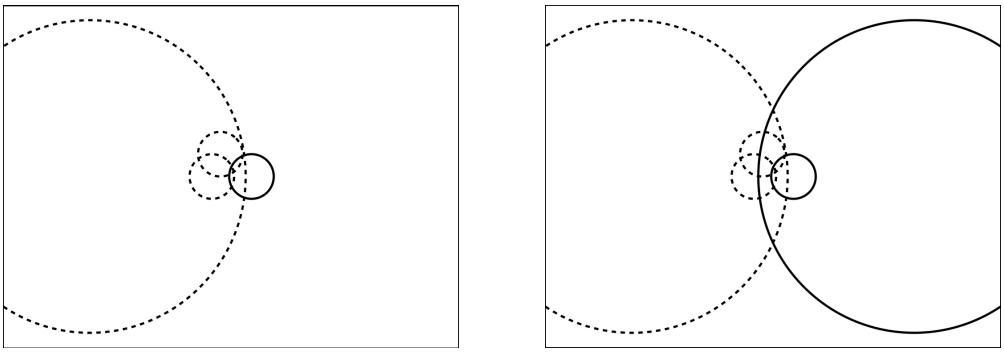

Figure 3.10: Examples of ultra-peripheral collisions in the standard MC Glauber Model for p-Pb (left panel) and Pb-Pb (right panel) systems with multiplicities slightly higher than that of the events shown in Fig. 3.9.

This picture is exactly similar to what happens in low multiplicity p-Pb collisions, except that the proton is probing the periphery of the lead nucleus, see left panels of Fig. 3.9 and Fig. 3.10. This explains why all calculated quantities that we display in this section have same values at nearly zero multiplicity for both p-Pb and Pb-Pb systems, see Fig. 3.13, Fig. 3.14, and Fig. 3.15.

The trend will change once four and more participants interact in an event. In a p-Pb collision it will correspond to the proton colliding with three lead nucleons, see Fig. 3.11. But in the Pb-Pb case, there is another possible scenario: two nucleons

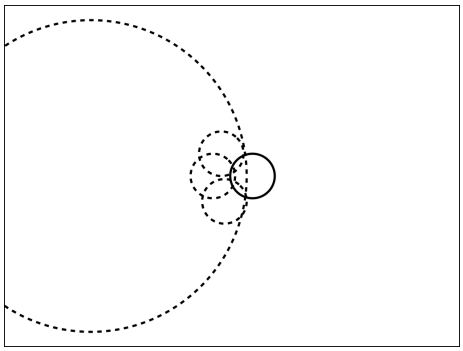

Figure 3.11: An example of ultra-peripheral collision in the standard MC Glauber Model for p-Pb system with multiplicity slightly higher than that of the events shown in Fig. 3.10.

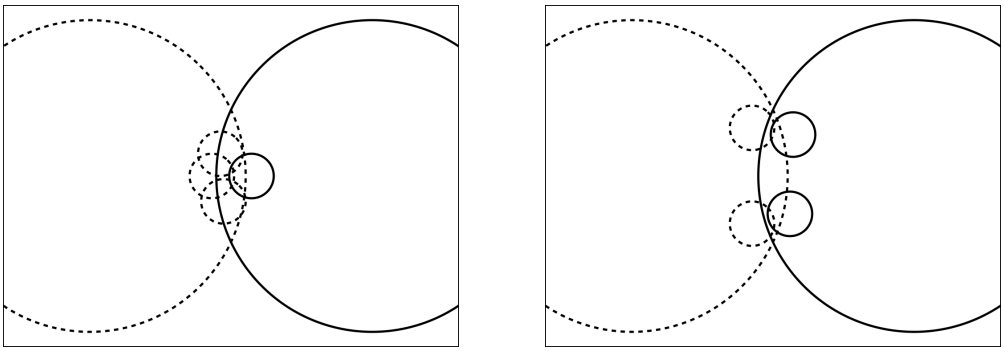

Figure 3.12: Examples of ultra-peripheral collisions in the standard MC Glauber Model for Pb-Pb system with exactly the same multiplicities as that of the event shown in Fig. 3.11.

from one lead nucleus can interact with one (or two) nucleons from the other lead

nucleus, see both panels of Fig. 3.12. It is quite possible that these pairs of wounded nucleons will be set apart by some distance in the transverse collision plane, as it is shown in the right panel of Fig. 3.12. This explains why the system size (and the initial eccentricity) of Pb-Pb system experiences faster grows as a function of multiplicity then the p-Pb one, see Fig. 3.15 (and Fig. 3.14): in the latter case all nucleons are grouped around the proton center. This also explains why the p-Pb system size saturates at $\sim 1\,\mathrm{fm}$, which is the proton radius.

However, the approach described so far does not take into account NBD fluctuations. They become important once the number of participants in a p-Pb collision reaches the threshold of $N_{\mathrm{part}} \sim 10$. This value approximately corresponds to the maximum number of nucleons that a proton can interact with if they are all equally distributed inside a sphere of lead radius (in this case the proton will be crossing the sphere through its center). If every participant is contributing the same amount of entropy to the initial conditions, the final multiplicity is directly proportional to the number of participants. Probability of p-Pb events with a higher multiplicity than the one with the threshold number of participants should roughly follow Poisson distribution (PD), as these events describe (considerable) deviations of the nucleon spatial density from its average values. However, NBD fluctuations allow event's multiplicity with a fixed number of participants to vary event-by-event. Thus, it is also possible that the high multiplicity p-Pb bins contain events in which the average entropy contribution per participant grows faster than the average number of participants. In order to understand which of the these effects (PD or NBD) is stronger, we show the results of our model's calculations in Fig. 3.13.

One can see that in line with our qualitative explanations, p-Pb and Pb-Pb curves coincide at low multiplicities. In the region of $N_{\mathrm{trk}} < 70$, they demonstrate linear correlation between the average number of participants in the event, $< N_{\mathrm{part}} >$, and its multiplicity, N_{trk}. This means that the contribution of every participant is the same and corresponds to the average of the NBD distribution. However, the situa-

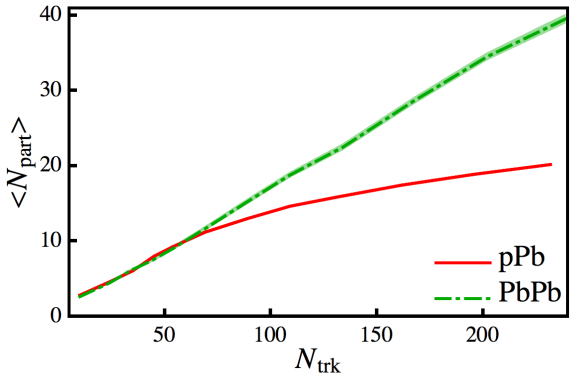

Figure 3.13: Average number of participants versus multiplicity.

tion changes at high multiplicity, where curves separate[1]. The Pb-Pb linear scaling continues, which agrees with our qualitative explanation that at low multiplicities a Pb-Pb collision can be represented as a superposition of several peripheral p-Pb ones. The p-Pb curve, however, bends towards the multiplicity axis. This suggests that the high multiplicity behavior of the curve is less likely to be determined by the growth of the number of participants and NBD fluctuations play an important role in the description of central p-Pb collisions. This should not be a surprise – in Fig. 3.2, we saw that the MC Glauber Model cannot explain p-Pb probability distribution in the high multiplicity region unless accompanied by NBD fluctuations.

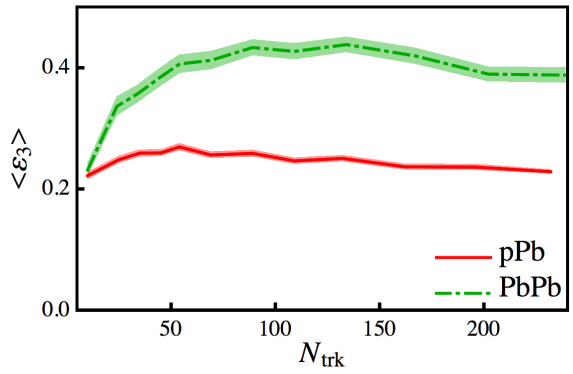

Figure 3.14: Average triangularity $\langle\varepsilon_3\rangle$ versus multiplicity.

Thus, we conclude that when performing the binning of central p-Pb collisions us-

[1]Note that the separation of p-Pb and Pb-Pb curves takes place around $< N_{\text{part}} > \approx 10$, which supports the validity of our qualitative explanation.

ing their multiplicity, one selects events with larger than average entropy contribution per participant. In fact, these rare high multiplicity p-Pb events are often dominated by one or two participants with an uncharacteristically large entropy. Since the contribution from each participant is a symmetric Gaussian, despite a smaller average number of participants, the average triangularity is *smaller* in p-Pb than in Pb-Pb events at the same multiplicity, as shown in Fig. 3.14.

Therefore, in our calculation, the strikingly similar values of $\bar{v}_3$ in the two systems are not in fact a trivial consequence of a similar geometry.

It should be noted that, in principle, the various scales in the system can enter in a complicated way. Therefore, even in the case of nucleus-nucleus collisions, equation (3.12) works best when events are segregated into centrality bins (classes). The expense of this is that the response coefficient k is allowed to depend on centrality. Similarly for p-Pb, grouping all events together and assuming a constant value of k results in a less obvious correlation between $\bar{v}_3$ and ε_3 [233]. More importantly though, p-Pb events and Pb-Pb events can have a significantly different hydrodynamic response to the initial triangularity. So despite having a different initial spatial anisotropy, p-Pb and Pb-Pb events can end up with very similar values of $\bar{v}_3$. This is due in large part to the very different sizes of the two systems, which we show in Fig. 3.15.

Note that the size of the p-Pb system is uncertain, and depends significantly on the treatment of the initial state physics, with some models giving an even smaller size than the model used here [233, 235], and some slightly larger [230]. This smaller size results in a more forceful hydrodynamic response, and a larger ratio of $\bar{v}_3/\varepsilon_3$[1].

[1]The general dependence on system size is not a trivial matter. One does not have a general rule that, at a fixed total multiplicity or entropy, a system that is smaller initially will always have a larger (or smaller) hydrodynamic response $\bar{v}_3/\varepsilon_3$ in a viscous hydrodynamic calculation. Obviously, reducing system size alone should increase pressure gradients and thus enlarge the response. However, one has to consider it along dissipative and freeze out effects that can play a significant role. Which effect wins out depends on the particular scales of the system in question, including transverse size as well as viscosity and freeze out temperature.

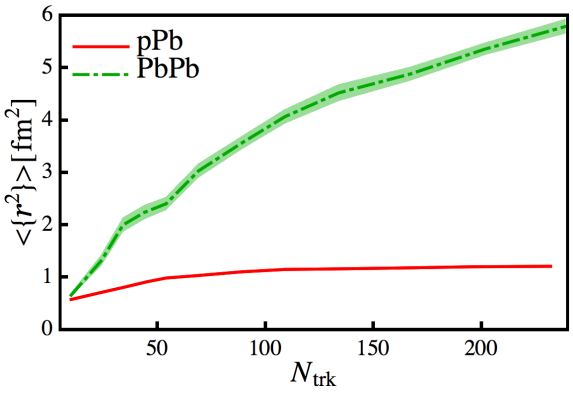

Figure 3.15: Mean square radius of the initial entropy density versus multiplicity.

To summarize, in this section, we discussed in details that our improved MC Glauber model prescribes drastically different initial conditions for p-Pb and Pb-Pb collision systems with similar multiplicity: specifically, their eccentricities and characteristic transverse sizes. It is based on very robust and general foundations: existence of nucleonic degrees of freedom inside nuclei and fluctuations of energy deposition in proton-proton collisions. We emphasize that MC Glauber model is being applied in models, such as HIJING, LEXUS, PYTHIA, UrQMD, that do not assume formation of QGP. Thus, it is valid to state that the MC Glauber model and our extended version of it has nothing to do with hydrodynamics. Moreover, results of fluid dynamics calculation has challenging to predict dependence on the parameters of the initial conditions and properties of plasma. Some of the latter, such as equation of state and an estimate of shear viscosity, we obtained from first principle lattice calculations and AdS/CFT theory that only partially overlap with the subject of studies of hadron collisions. Yet it appeared that within our hydrodynamic framework we observed intrinsic interplay of these independent models and competing effects that led to a natural explanation of the triangular flow similarity in p-Pb and Pb-Pb systems presented in the left panel of Fig. 3.6. This fact strongly supports the fluid dynamics paradigm applicability to the description of high multiplicity hadron collisions independent of their size. Further, given its nontrivial nature, this result may well give valuable insight into medium properties and/or the initial stages of the

collision.

3.4 Conventional flow observables in small systems

It is clear from the results of this chapter that a hydrodynamic model can in principle fit data existing at the time of this work. Specifically, the measured differential $v_n\{2\}(p_{\mathrm{T}})$ and integrated $\bar{v}_n\{2\}(N_{\mathrm{trk}})$ flow coefficients, which we will refer to from here on as the conventional observables as they played instrumental role in the establishment of the hydrodynamic paradigm in HIC, see Section 2.1.1. Even the simple model presented here, gives a reasonable description of the available measurements, and it is clear that a more sophisticated model could likely describe them with even more precision. Thus, the hydrodynamic picture is confirmed as plausible.

One might wonder if there exists an even more stringent test that one could perform to test this picture. For example, could a measurement be made that returns a value that a hydrodynamic calculation could never reproduce, no matter what parameters, transport coefficients, and equation of state are chosen or what model of initial condition is used?

In fact, this is indeed possible. In the following chapter, we explain how this can be done by considering details of the full two-particle correlation matrix that are ignored in conventional flow analyses.

4

Tests of hydrodynamics in small systems

In this chapter we use another observable to test hydrodynamics applicability to small systems. It was introduced in [141], but was so far utilized only for the analysis of A-A collisions. There it confirmed that the region of hydrodynamics applicability coincides with the one determined based on the conventional analysis. The latter consists in the comparison of the flow coefficients measured experimentally and calculated in a hydrodynamic model (we performed this conventional analysis for p-A system in Chapter 3). The power of the new method is that it provides a falsifiability test for hydrodynamics as a model [142]: if the value of the experimentally measured r_n observable exceeds certain range, hydro model will be eliminated as a potential description of this result. Thus, we suggested to measure r_n in small systems, calculated its value in our model [139] and released our *prediction* before the experimental data got available [143]. These results will be discussed in Section 4.3.4. We will start this chapter with the discussion of the context that motivated the introduction of r_n.

4.1 The "ridge"

In Section 2.1.1, we mentioned that one of the evidences of collective behavior in HIC is the so-called (near-side) ridge. Below we introduce its definition and briefly discuss relevant features of two-particle correlations.

From the results of statistical physics of dense systems, we know that by studying correlations of a higher number of particles one can reveal principally new information about the underlying phenomenon of interest [242]. Thus, one could potentially benefit from studies of multi-particle distributions in HIC. We will start with two particles and then extend the analysis to the case of multiple particles.

In HIC experiments, one can reconstruct spatial momenta of particles which reach the detector. Those can be parametrized with three independent variables. As we discussed in Section 2.3.1, those are conventionally transverse momentum p_{T}, azimuthal angle ϕ, and pseudorapidity η. When particles are analyzed in pairs, they are usually indexed as a and b or "trigger" and "associate" – we will discuss the reason for

this naming convention later. Thus, an arbitrary two-particle correlation function can potentially depend on six kinematic variables. However, one cannot measure the absolute value of azimuthal angles ϕ^a and ϕ^b. For that reason, one has access only to the relative orientation of particles in the transverse plane, which is described by $\Delta\phi \equiv \phi^a - \phi^b$. Thus, an experimentally measured two-particle correlation function depends only on the five following variables:

$$\text{2-part-corr} = \text{function}(\Delta\phi, p_{\mathrm{T}}^a, \eta^a, p_{\mathrm{T}}^b, \eta^b). \tag{4.1}$$

One of the first candidates considered for the role of the "function" was particle yield. It was directly measured in the experiment [97] and was expected to be relevant in the studies of "jet" energy loss. High energy particles ($p_{\mathrm{T}} \sim 100$ GeV) created in HIC are called jets and are treated differently from the low energy ones ($p_{\mathrm{T}} \sim 1$GeV).[1] By studying how jets interact with the medium, one gains insights into the interplay between different regimes of QCD. Particularly, as jets are part of the HIC system, then according to the momentum conservation in the transverse plane, they are related to a cascade of associated particles moving in the opposite azimuthal direction. This explains the names ("trigger" and "associate") and commonly used renormalization of the (pair) yield with the number of "jet/trigger" particles, N_{trig}, see Fig. 4.2 and Fig. 4.3.

As it is challenging to analyze and graphically represent data in more than three dimensions, one has to choose at most two out of five variables in (4.1). For that reason, the two-particle yield correlation is plotted as a function of:

$$\Delta\eta = \eta^a - \eta^b \qquad \text{and} \qquad \Delta\phi = \phi^a - \phi^b, \tag{4.2}$$

while the values of transverse momenta of "trigger" and "associate" particles are fixed

[1] This owes to the distinction in the mechanisms of their creation, see Section 2.1.2. While the former originate from the hard parton collisions, which can be well described with perturbative methods, the latter are produced by the strongly interacting expanding medium, which is non-perturbative by nature.

to be in (relatively broad) regions[1].

Typical examples of such correlation functions, in this case for Au-Au and d-Au collision experiments at $\sqrt{s_{\rm NN}} = 200\,\text{GeV}$, are shown in Fig. 4.1. Transverse momenta of particles are bounded within these ranges: $2\text{GeV} < p_{\rm T}^b < p_{\rm T}^a$ and $3\text{GeV} < p_{\rm T}^a < 4\text{GeV}$. Note that only the events from certain multiplicity bins (central for Au-Au and min bias for d-Au) were used in the analysis – this fact will be important later.

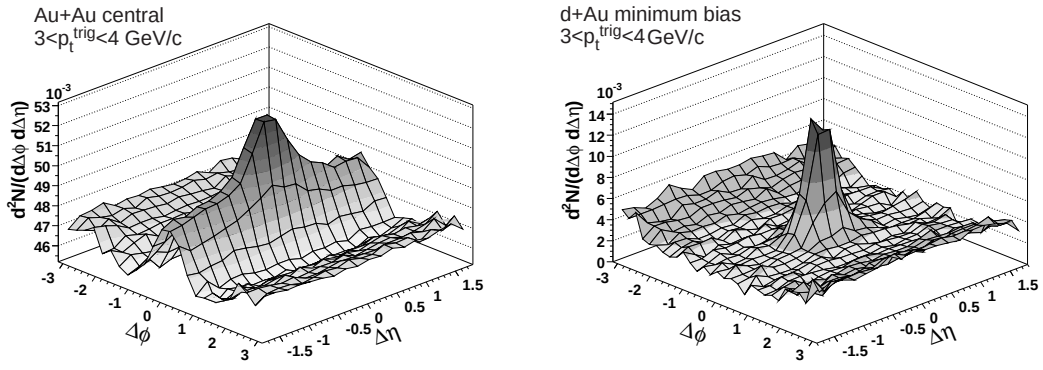

Figure 4.1: Typical shape of a two-particle correlation for a large and a small system is shown in the left and in the right panels correspondingly. One can see that the latter lacks the "ridge". See text for details. Figures from [97].

One can observe the three following characteristic features of the produced in HIC pair distributions, which are also seen more distinctly in Fig. 4.3 (a):

- **The near-side peak at $\Delta\phi \to 0$, $\Delta\eta \to 0$.** As we mentioned, jets have higher energy and momentum compared to plasma constituents. Thus, in case of a head-on collision the latter effectively get carried away by the former towards the original direction of the jet. This results in a pronounced narrow structure at the distribution's origin, which actually gets broadened. It happens because those redirected plasma components undergo subsequent collisions with other QGP constituents, which randomly alternate their momentum and thus spatial orientation away form the original jet's one.

[1]One can alternatively say that the original five-dimensional distribution (4.1) was integrated/averaged over $p_{\rm T}^a$ and $p_{\rm T}^b$ within the aforementioned momentum ranges.

- **The away-side long-range correlation at $\Delta\phi \to \pi$.** This structure again owes its origin to (back-to-back) jets. Those can be arbitrarily directed in space and can pass considerable amounts of momentum to the plasma constituents. Due to momentum conservation in the transverse plane one expects to see a structure in the direction straight opposite to jets, i.e. at $\Delta\phi \to \pi$. It extends to many units of (pseudo-)rapidity in both directions as jet spatial distribution, which defines emitted particles' longitudinal rapidities, is nearly uniform. Similarly to the case of the near-side peak, one can notice characteristic broadening due to the subsequent collisions that associate particles undergo after the moment of the interaction with the jet and before the moment of reaching the detector.

- **The near-side long-range correlation at $\Delta\phi \to 0$ or the "ridge".** This structure looks similar to the away-side correlation, but manifests a different physical phenomena – it has nothing to do with jets. It looks like a ridge extended in many units of (pseudo-)rapidity and shows that particles moving differently in longitudinal direction move alike in the transverse one. This strong azimuthal correlation of particles produced in HIC is a clear evidence of the underlying collective behavior.

The ridge is widely accepted to be of hydrodynamical origin in case of A-A collisions [187, 243]. It was not initially observed in smaller systems (p-p, p-A, d-A), which could be considered as a confirmation that QGP was not created there. Indeed, one needs to exceed certain energy threshold, estimated to be of the order of $1\,\mathrm{GeV}/\,\mathrm{fm}^3$, for the matter to undergo a phase transition. Higher density is easier to achieve in systems with more participating nucleons. For reference, Au/Pb has two orders of magnitude higher number of nucleons than proton/deuteron.

However, recent experiments with p-Pb systems at new higher energies of $\sqrt{s_{\mathrm{NN}}} = 5.02\,\mathrm{TeV}$ per nucleon pair by the CMS collaboration brought a novel perspective[1]

[1] As we mentioned in the comment to Fig. 4.1, centrality selection plays an important role in observing signatures of collective behavior. Only high multiplicity (very central) p-Pb events [134] revealed

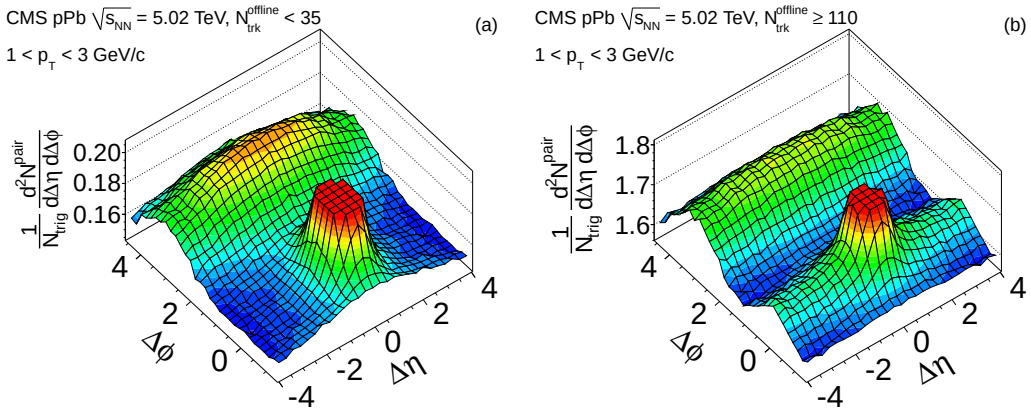

Figure 4.2: Two-particle correlation functions for 5.02 TeV p-Pb collisions system at different multiplicities. Figures from [134]. Both particles in the pair are charged hadrons with transverse momentum from 1GeV to 3GeV. Plot (a) represents analysis based on low-multiplicity events ($N_{\mathrm{trk}}^{\mathrm{offline}} < 35$) and (b) – on high-multiplicity ones ($N_{\mathrm{trk}}^{\mathrm{offline}} \geq 110$). See Table 3.1 in Section 3.1 for more details. The near-side peaks are truncated to have a better view of the functions' structure outside that region.

[134]. Although they confirmed previously observed behavior of the two-particle charged hadrons yield correlation function when multiplicity was low, see Fig. 4.2(a) – one can find the characteristic near-side peak and away-side long correlation, but no near-side ridge. But they also observed an appearance of a very similar to the A-A "ridge" structure at high multiplicity, see Fig. 4.2(b).

For a one-to-one comparison of A-A and p-A systems, see Fig. 4.3. Plots represent two-particle correlations for Pb-Pb and p-Pb in the same multiplicity window. For Pb-Pb system this multiplicity range corresponds to peripheral collisions, while for p-Pb system – most central. One can see that both systems exhibit similar characteristic structures – particularly, presence of the near-side ridge. This observation suggests that QGP plasma could be created in small (p-A) systems at high multiplicity

those signatures – see Section 3.3 for the discussion of the relation between centrality and multiplicity in small systems. In Fig. 4.1, d-Au data was presented without any centrality selection (min-bias). See [137] and [138] for multiplicity-selected analysis of d-Au collisions.

and thus hydrodynamics could be potentially used for the description of experimental results in this case.

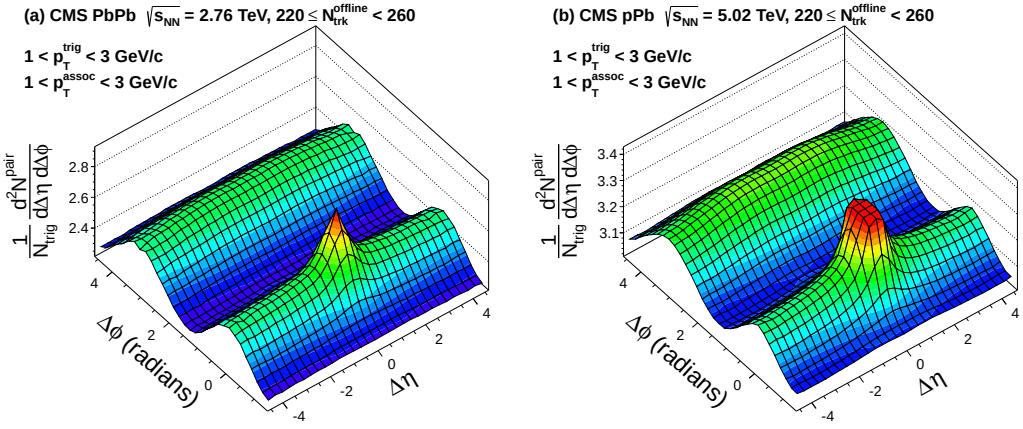

Figure 4.3: The two-particle correlation functions for (a) 2.76 TeV Pb-Pb and (b) 5.02 TeV p-Pb systems. Figures from [222]. Both particles in the pair are charged hadrons with transverse momentum from 1GeV to 3GeV. Only events with (high) multiplicity between 220 and 260 were used, see Table 3.1 in Section 3.1 for more details. The near-side peaks are truncated to have a better view of the functions' structure outside that region.

4.2 Azimuthal angle correlations

4.2.1 Two-particle azimuthal angle correlation function

Pair yield is not the only type of the two-particle correlation, (4.1). Depending on the goals of the study one can use any arbitrarily function of the particles' momenta. One usually takes an arithmetic mean of this observable over particle pairs of certain type that are produced in the event, for example, charged hadrons: pions, kaons, and protons. As we saw in Section 3.2, averaging over events is also typical in this type of analysis. Thus, Figs. 4.1, 4.2, 4.3 represent correlations of charged hadrons and weighting is substituted with implicit averaging over charged hadron pairs in all events. However, usage of different particle types in a pair is also common. For

example, when one studies the effects of flow on electromagnetic observables, one measures correlations of hadrons with photons [245],[246].

As one of the main points of interest in QGP studies is the transverse system dynamics that describes flow, we will further mostly focus on the azimuthal angle correlations:

$$V_{n\Delta}(p_{\mathrm{T}}^a, p_{\mathrm{T}}^b) \equiv \left\langle \langle e^{in(\phi^a - \phi^b)} \rangle \right\rangle, \tag{4.3}$$

where the internal angular bracket indicates averaging of the "integrand" over all pair combinations of charged hadrons in an event and the external angular bracket stands for averaging over events. In this work, we use the CMS collaboration notations and kinematic variables' ranges, see [222] for details.

One can observe that η^a and η^b were fixed in (4.3) – in further analysis they take their values from the range of $|\Delta\eta| > 2$. There is another reason, beyond the dimensionality reduction, to do so. As we saw in Fig. 4.3, jets dominate the two-particle correlation function at $\Delta\eta \to 0$. They have different physical origin than the flow and thus one should subtract their contribution when doing analysis of collective behavior. One of the ways to accomplish this is to introduce wide pseudorapidity cuts, another one is to consider multi-particle correlations – we will discuss this method later.

We should also mention the following general features of the azimuthal angle two-particle correlation.

First, that due to anti-symmetric nature of the integrand, expression (4.3) is real and one could substitute all exponents in its definition with cosines.

Second, final state particle anisotropy can be defined through the two-particle correlation, (4.3), in the following way:

$$\bar{v}_n\{2\} \equiv \sqrt{V_{n\Delta}(\bar{p}_{\mathrm{T}}, \bar{p}_{\mathrm{T}})}, \tag{4.4}$$

and

$$v_n\{2\}(p_{\mathrm{T}}) \equiv \frac{V_{n\Delta}(p_{\mathrm{T}}, \bar{p}_{\mathrm{T}})}{\sqrt{V_{n\Delta}(\bar{p}_{\mathrm{T}}, \bar{p}_{\mathrm{T}})}}, \tag{4.5}$$

where we chose the particles' momenta $\bar{p}_{\mathrm{T}}$ to be in the range $0.3 < \bar{p}_{\mathrm{T}} < 3.0\mathrm{GeV}$ as in the mentioned above p-Pb experiments by CMS at $\sqrt{s_{\mathrm{NN}}} = 5.02\,\mathrm{TeV}$. The

reason one does not use flow coefficients $\bar{v}_n$, $v_n(p_\mathrm{T})$ defined in equations (3.6), (3.7) is because their extraction from a single p-Pb event leads to at least 60% statistical error. Indeed, the magnitude of the biggest (elliptical) flow component is of the order of 10%. At the same time, the maximum event multiplicity is about $N_\mathrm{trk}^\mathrm{offline} \approx 300$ particles, which is equivalent to the yield's statistical error of $1/\sqrt{N_\mathrm{trk}^\mathrm{offline}} \approx 6\%$, which justifies the estimate provided above. To keep the discussion complete, we notice here that there were methods developed to extract flow coefficients in every event using unfolding analysis [247, 248, 249]. However, in order to use them, one has to introduce additional assumptions regarding the form of the response function or rapidity dependence of flow harmonics, which complicates the analysis and introduces systematic errors.

Third, in equations (3.9), (3.8) we showed how $v_n\{2\}(p_\mathrm{T})$, $\bar{v}_n\{2\}$ could be expressed in terms of $v_n(p_\mathrm{T})$, $\bar{v}_n$. This is possible only under certain assumptions, because the latter observables are defined through one-particle correlation, while the former relies on two-particle correlation function, which contains more information about the underlying dynamics.

Before moving to the discussion of the aforementioned assumptions, we here mention for completeness that there is another approach to defining particle anisotropies: the event-plane method [250]. However, it becomes less commonly used because of its complicated dependence on the event multiplicity and thus limited usability compared to the multi-particle correlation method [251]. It also reduces to the latter at low resolution, which is the case for small (p-A) systems.

4.2.2 Theoretical aspects of flow definition

In this section we will dwell on the principal challenges of comparing theoretically calculated and experimentally measured flow observables, and lay foundations of determining irreducible limitations of the hydrodynamical paradigm.

As we mentioned, the principal difference between equations (4.4), (4.5) and (3.8), (3.9) is that they are defined using two- and one- particle correlations respectively. Unlike experimental set-up, which always deals with a finite yield, particle distribu-

tions in theoretical models can be calculated with infinite resolution. However, the fundamental limitation of hydrodynamics stems from the fact that two-particle distribution does not reduce to a product of one-particle distributions on event-to-event basis:

$$\frac{dN_{pairs}}{d\mathbf{p^a}d\mathbf{p^b}} = \underbrace{\frac{dN}{d\mathbf{p^a}}\frac{dN}{d\mathbf{p^b}}}_{\text{flow contribution}} + \underbrace{\delta_2(\mathbf{p^a},\mathbf{p^b})}_{\text{non-flow contribution}} . \tag{4.6}$$

"Flow" is a phenomenon pertinent to the collective motion taking place in QGP plasma that is being created in HIC collisions. It can be observed if one obtains one-particle yield distribution, which describes the effect of collective dynamics on single particle emission. For that reason one should refer to (3.6), (3.7) as the definition of flow. Flow's contribution to the two-particle yield correlation function enters in the form of a product of two single-particle distributions. This term in (4.6) describes what would be the pair yield distribution if particles were emitted from the QGP fireball independently from each other. However, besides flow there exist other physical phenomena that affect pair yield, such as the discussed above jet induced radiation. It is common to explicitly indicate contribution of such effects to (4.6) and refer to them as non-flow. The latter phenomena manifest the principal difference between definitions (4.4), (4.5) and (3.8), (3.9) and highlights that one should be particularly accurate when comparing experimental results to theoretical calculations.

Non-flow contribution is absent by definition in any hydrodynamic calculation. Pair distribution factorizes into a product of single-particle ones in every event:

$$\frac{dN_{pairs}}{d\mathbf{p^a}d\mathbf{p^b}} \overset{\text{hydro}}{=} \frac{dN}{d\mathbf{p^a}}\frac{dN}{d\mathbf{p^b}}. \tag{4.7}$$

This happens because hydrodynamic models assume that QGP radiates particles similar to a thermally equilibrated black-body, i.e. single particle yield correlates with the expanding fireball and not with other emissions. On one hand, this makes hydrodynamics an appropriate tool to describe the flow effect in QGP. On the other hand, it introduces fundamental restrictions on the results of hydrodynamic calculations and thus on the method's applicability overall. Notably, we will see that, contrary to the expectation that a model with a large enough number of parameters can describe

any experimental data, values of certain hydrodynamic results are bounded within certain limits regardless of their particular choice. This creates an opportunity to perform a principle test of hydrodynamics applicability to HIC, which we will discuss in Section 4.3.1.

Absence of non-flow in hydrodynamical approach leads to the following simplifications that were used when calculating (3.8) and (3.9):

$$V_{n\Delta}(p_{\mathrm{T}}^a, p_{\mathrm{T}}^b) \overset{\text{hydro}}{\equiv} \frac{1}{N_{\text{events}}} \sum_{\text{events}} v_n^a(p_{\mathrm{T}}^a) v_n^b(p_{\mathrm{T}}^b) \cos n(\Psi_n^a(p_{\mathrm{T}}^a) - \Psi_n^b(p_{\mathrm{T}}^b)). \tag{4.8}$$

In this section we discussed the difference between definitions of flow that are constructed using one- and two-particle correlation functions. Although one would be able to get access to the "pure" flow phenomenon by studying one-particle correlation, in practice one will never be able to do it, because in every event a finite number of particles is being created and thus direct extraction of the one-particle yield is not possible. For that reason one has to work with two-particle correlations that can be experimentally measured with high precision. Those contain non-flow contributions, which one would like to subtract when studying collective motion of QGP. We mentioned the procedure that is performed to subtract non-flow contributions that emerge due to jets – one introduces (large) rapidity cuts when measuring two-particle azimuthal correlation, (4.3). In the next section we will go over another general method that leads to non-flow suppression.

4.2.3 Multi-particle azimuthal angle correlation function

Flow describes collective behavior of plasma constituents and thus it is a multi-particle effect. For that reason one expects that its relative contribution to the azimuthal angle correlation function will grow with increasing the number of particles considered in the analysis of every event. We will illustrate this idea by considering non-flow contribution coming from jets. If one arbitrary chooses several charged hadrons in a HIC collision event, all of them will carry effect of flow, because it affects all particles. At the same time, the probability that all of the selected particles are coming from the same jet is decreasing when one takes into account more and more particles,

because jet affects QGP constituents only in a very narrow spherical angle around the direction of its propagation. Based on this logic, one needs to consider multi-particle emission rates from a HIC event in order to suppress non-flow contributions. Below we will focus on the relevant case of particle quartets.

Similarly to the pairs case, (4.6), four-particle yield has contribution of flow and non-flow terms, [237]:

$$\begin{aligned}\frac{dN_{quartet}}{d\mathbf{p}^a d\mathbf{p}^b d\mathbf{p}^c d\mathbf{p}^d} &= \\ &= \underbrace{\frac{dN}{d\mathbf{p}^a}\frac{dN}{d\mathbf{p}^b}\frac{dN}{d\mathbf{p}^c}\frac{dN}{d\mathbf{p}^d}}_{\text{flow contribution}} \\ &+ \underbrace{\frac{dN}{d\mathbf{p}^a}\frac{dN}{d\mathbf{p}^b}}_{\text{flow contribution}} \underbrace{\delta_2(\mathbf{p}^c,\mathbf{p}^d)}_{\text{non-flow contribution}} + \text{permutations}(a,\ b,\ c,\ d) \\ &+ \underbrace{\frac{dN}{d\mathbf{p}^a}}_{\text{flow contribution}} \underbrace{\delta_3(\mathbf{p}^b,\mathbf{p}^c,\mathbf{p}^d)}_{\text{non-flow contribution}} + \text{permutations}(a,\ b,\ c,\ d) \\ &+ \underbrace{\delta_4(\mathbf{p}^a,\mathbf{p}^b,\mathbf{p}^c,\mathbf{p}^d)}_{\text{non-flow contribution}},\end{aligned} \tag{4.9}$$

where $\delta_2(\mathbf{p}^a,\mathbf{p}^b)$, $\delta_3(\mathbf{p}^a,\mathbf{p}^b,\mathbf{p}^c)$, $\delta_4(\mathbf{p}^a,\mathbf{p}^b,\mathbf{p}^c,\mathbf{p}^d)$ describe possible non-flow contribution coming from two-, three-, and four-particle processes.

One can notice that unlike in the case of pairs, (4.6), there are terms mixing contributions from flow and non-flow. It is desirable to subtract those for two reasons. First, we want to extract and analyze the flow signal – this was our initial motivation to study multi-particle correlations. Second, these terms are more endurant to the suppression caused by the discussed above increase in the number of particles used in every event's analysis, because they are multiplied by flow terms that are not affected by that change. Thus, these terms contribute to the "noise" background created by non-flow when extracting flow from a multi-particle correlation function. This becomes important also for statistical reasons. Inclusion of one additional particle to the event's analysis (i.e. considering $n+1$- instead of n- particle correlations) considerably decreases the total number of available combinations. For example, given a typical high-multiplicity p-Pb event with several hundred emitted charged

hadrons, averaging of (4.10) over quartets will be performed over a dataset of at least three orders of magnitude smaller than averaging of (4.3) over pairs. Here we introduced four-particle azimuthal angle correlation similarly to the two-particle one, (4.3):

$$\left\langle \left\langle e^{in(\phi^a+\phi^b-\phi^c-\phi^d)} \right\rangle \right\rangle, \tag{4.10}$$

where the internal angular bracket indicates averaging of the "integrand" over all quartet combinations of charged hadrons in an event and the external angular bracket stands for averaging over events. As in the two-particle case, this definition includes relative measurement of particles' azimuthal angles and thus is invariant under rotations in the transverse plane. Finally, the harmonic order of the correlation is defined by the integer number n.

Using cumulant analysis it can be shown [252] that two-particle non-flow effects can be subtracted from the four-particle cumulant. This provides motivation for the mentioned earlier $v_n\{4\}$ observable:

$$-v_n\{4\}^4 \equiv \left\langle \left\langle e^{in(\phi^a+\phi^b-\phi^c-\phi^d)} \right\rangle \right\rangle - 2\left\langle \left\langle e^{in(\phi^a-\phi^b)} \right\rangle \right\rangle, \tag{4.11}$$

which reduces to (3.10) under the assumption that all non-flow effects are subtracted from experimental analysis. Although the aforementioned procedure is not able to entirely subtract all non-flow effects (contributions coming from δ_3 and δ_4 terms of (4.9) still contaminate the flow signal), it leads in practice to their significant suppression [253].

4.3 A Stringent Test of Hydrodynamics

As we saw in the previous sections, the essential aspect of a purely hydrodynamic description is that particles emerge from the fluid independently – that is, the one-particle distribution contains all relevant information, and multi-particle distributions are simply obtained as products of the single-particle one. We also announced that this places non-trivial restrictions on observed multi-particle measurements, even if one is free to choose an arbitrary single-particle distribution.

As a simple example, by comparing (3.8) and (3.10), it is possible to convince oneself that in any hydrodynamic calculation:

$$\bar{v}_n\{4\}^4 \leq \bar{v}_n\{2\}^4. \tag{4.12}$$

However, this does not serve as a non-trivial restriction, because this inequality generically holds in most reasonable physical models and collision systems.

A truly non-trivial restriction on hydrodynamics comes from the data that is not utilized in the conventional flow analysis, which we presented in Chapter 3. Two-particle correlation, (4.3), is experimentally measured for all possible combinations of p_{T}^a and p_{T}^b. For statistical reasons one splits all registered particles into bins of final width. For example, when measuring p-Pb two-particle azimuthal correlation, CMS collaboration uses the following splits for the "trigger" hadrons:

$$\begin{aligned} p_{\mathrm{T}}^a = \{&[1.\mathrm{GeV}, 1.5\mathrm{GeV}], [1.5\mathrm{GeV}, 2.\mathrm{GeV}], \\ &[2.\mathrm{GeV}, 2.5\mathrm{GeV}], [2.5\mathrm{GeV}, 3.\mathrm{GeV}]\}. \end{aligned} \tag{4.13}$$

Similar procedure is being performed with the "associate" particles, although the binning is denser. In this way experimentally measured pair azimuthal angle correlation is a matrix with its elements being evaluated at the aforementioned "trigger" and "associate" particle transverse momenta kinematic bins. Part of it was presented in the averaged way. Indeed, "differential" flow measurement $v_n\{2\}(p_T)$, (4.5), corresponds to the averaging of the matrix over rows, while the "integrated" flow $\bar{v}_n$, (4.4), – over both rows and columns. Thus, the full matrix contains more information than

the "differential" and "integrated" flow observables that one conventionally uses to compare to hydrodynamic calculations in order to test the latter.

The non-trivial restriction arises when we take into account both: peculiarities of the particle emission in the hydrodynamic picture and all the available information contained in the two-particle correlation matrix. We will compare *prediction* of our model to the entire matrix of values measured in p-Pb collisions, which contains four times more data points than used in the conventional analysis of differential and integrated flow. But we will do it using special parametrization, r_n, that will provide additional fundamental constraint on the applicability of the hydrodynamic paradigm.

4.3.1 $r_n(p_{\mathrm{T}}^a, p_{\mathrm{T}}^b)$ observable as a stringent test of hydrodynamics

To begin with, we recall that in any hydrodynamic calculation the azimuthal pair correlation matrix will have the form, (4.8):

$$V_{n\Delta}(p_T^a, p_T^b) \overset{\text{hydro}}{=} \frac{1}{N_{\text{events}}} \sum_{\text{events}} v_n(p_T^a) v_n(p_T^b) \cos\left(n\big(\Psi_n(p_T^a) - \Psi_n(p_T^b)\big)\right). \tag{4.14}$$

Namely, it's the events average of a scalar product between the flow vectors measured at each of the "trigger" and "associate" values of transverse momentum. This form dictates that the elements of the matrix must satisfy a set of inequalities [254].

First, the diagonal elements (that is, when both particles are restricted to the same transverse momentum bin, p_{T}^a) must be positive semidefinite:

$$V_{n\Delta}(p_T^a, p_T^a) \geq 0. \tag{4.15}$$

Second, the off-diagonal elements must be related to the diagonal by a triangle Cauchy-Schwarz inequality:

$$V_{n\Delta}(p_T^a, p_T^b)^2 \leq V_{n\Delta}(p_T^a, p_T^a) V_{n\Delta}(p_T^b, p_T^b). \tag{4.16}$$

We reiterate that these inequalities are inescapable. They will be satisfied in any purely hydrodynamic calculation, and can not be circumvented by engineering

a particular initial condition, tuning parameters, changing the equation of state or transport coefficients.

Whenever the first inequality, (4.15), is satisfied, a convenient way to quantitatively compare azimuthal pair correlation theoretical and experimental results is to use the following ratio, [254]:

$$r_n \equiv \frac{V_{n\Delta}(p_T^a, p_T^b)}{\sqrt{V_{n\Delta}(p_T^a, p_T^a) V_{n\Delta}(p_T^b, p_T^b)}}. \tag{4.17}$$

In hydrodynamics, the second inequality, (4.16), ensures that this ratio must lie in the range $-1 \leq r_n \leq 1$.

However, if hydrodynamics is not the correct description, the quantity is completely unbounded. While the matrix elements, $V_{n\Delta}(p_{\rm T}^a, p_{\rm T}^b)$, can take values only in the range $[-1, 1]$, see (4.3), any real number is allowed for $r_n(p_{\rm T}^a, p_{\rm T}^b)$. Even existing data for differential flow, $v_n\{2\}(p_T)$, does not restrict the latter.

We proposed the entire "double differential" correlation matrix, $V_{n\Delta}(p_{\rm T}^a, p_{\rm T}^b)$, to be measured in the case of p-A collisions and compared against these inequalities, (4.15) and (4.16), as a stringent test of the hydrodynamic picture. Any violation would unambiguously have indicated a breakdown of hydrodynamics as the dominant contribution to correlations, and the presence of at least some significant contribution from non-flow correlations. This measurement provided a significant additional constraint to theoretical models, beyond what had already been measured. It had a chance to either debunk or confirm whether hydrodynamical paradigm is valid in case of small collision systems.

In Section 4.3.4, we will return to the quantitative comparison of our prediction of $r_n(p_{\rm T}^a, p_{\rm T}^b)$ observable,(4.17), against the experimental p-A measurements that were performed after we publicly released our results. Now we will turn to the qualitative analysis of relations (4.15) and (4.16) in order to clarify the mechanism actuating the inequalities and to illustrate that they lead to the non-trivial conclusions regarding the domain of applicability of hydrodynamics.

4.3.2 Factorization breaking

The support for flow was not unanimous at start even in case of large systems. One of the crucial steps that assisted its recognition was the observation of the two-particle correlation function factorization:

$$V_{n\Delta}(p_{\mathrm{T}}^a, p_{\mathrm{T}}^b) \approx v_n(p_{\mathrm{T}}^a) \cdot v_n(p_{\mathrm{T}}^b). \tag{4.18}$$

Specifically, since it was possible (at least within a certain range) to represent a multi-particle observable as a product of single-particle measurements, one could consider QGP to be a plausible explanation.

Experimental results [256, 257, 205] have also shown that factorization, (4.18), was broken for the considerable number of two-particle correlation matrix elements, $V_{n\Delta}(p_{\mathrm{T}}^a, p_{\mathrm{T}}^b)$. It gave rise to some skepticism regarding the possibility of hydrodynamics to describe this effect, as in this approach yield factorization holds identically, (4.7). However, accurate theoretical consideration shows that it is actually possible. Indeed, yield and thus flow factorization holds in hydrodynamics in every event. But after averaging over all events factorization remains valid only under specific conditions: either trivial dependence of the flow angles, $\Psi_n(p_{\mathrm{T}})$, on transverse momentum, or global (i.e., one for all events) dependence of flow coefficients, $v_n(p_{\mathrm{T}})$, on it. Both of these conditions are quite restrictive and thus hold only in a limited domain.

To understand the physics of factorization breaking, it is instructive to observe (using hydrodynamics as a proxy) that it happens after averaging over events. This means that events have different (and non-trivially dependent on transverse momentum) flow coefficients, (3.6). As we discussed in Section 3.3, hydrodynamic response for the second and third flow harmonics is nearly linear. Thus, flow coefficients' non-trivial distribution over events stems from the fluctuations in the initial conditions. Those originate from the quantum effects taking place in the colliding nuclei, such as randomized event-to-event spatial distribution of nucleons in the transverse plane right before the collision. Thus, one expects that factorization breaking will be larger at lower multiplicities, as relative magnitude of fluctuations will become more pronounced. For the same reason, one expects that effect of the initial state fluctuations

will be more noticeable in case of the third flow harmonic, as second one has larger contribution from the initial collision geometry. In terms of variable $r_n(p_{\mathrm{T}}^a, p_{\mathrm{T}}^b)$ these qualitative observations translate into larger deviation of the r_n observable from unity at at lower multiplicities and when switching from the second, $(n = 2)$, to the third, $(n = 3)$, order harmonic; see quantitative comparison for p-Pb system in Fig. 4.5.

Non-trivial nature of the relations (4.15), (4.16) in the analysis of the two-particle correlation factorization breaking was qualitatively demonstrated in case of A-A (Pb-Pb) collisions [141]. First, second, and third orders of pairs correlations, $V_{n\Delta}(p_{\mathrm{T}}^a, p_{\mathrm{T}}^b)$, were used, see Fig. 4.4. ALICE collaboration used the following transverse momentum boundaries: {0.25, 0.5, 0.75, 1, 1.5, 2, 2.5, 3, 4, 5, 6, 8, 15} (in GeV) [256] which allowed the authors to test (though qualitatively) the validity of the hydrodynamic hypothesis against an order of magnitude more experimental results than in the conventional differential and integrated flow analyses.

It was shown that inequalities (4.15) and (4.16) are satisfied in all kinematic regions where hydrodynamics is expected to be valid. Specifically, if one ignores one element (indicated in red in Fig. 4.4) in the second and the third harmonic matrices, which as authors stipulate probably originate from the low statistics in that particular bins, the results do not exclude hydrodynamics as a model that can describe experimental data at low momentum, i.e. at p_{T}^a and p_{T}^b less than 4 GeV. This is exactly the soft momentum regime, which describes the domain of applicability of the (macroscopic) hydrodynamic theory. One can also observe that once the particles' transverse momentum increases above this soft limit threshold, the third harmonic demonstrates clear presence of non-flow effects and thus inapplicability of hydrodynamics. It might seem confusing that the first harmonic indicates dominant non-flow contribution at all, including low, transverse momenta. However, it has long been known that $V_{1\Delta}(p_{\mathrm{T}}^a, p_{\mathrm{T}}^b)$ should have this contribution due to momentum conservation, which is accounted for in hydrodynamics only on average due to the independent nature of the particle emission. It was shown [258] that once this effect is taken into account, the first order correlation is indeed consistent with the hydrodynamic model.

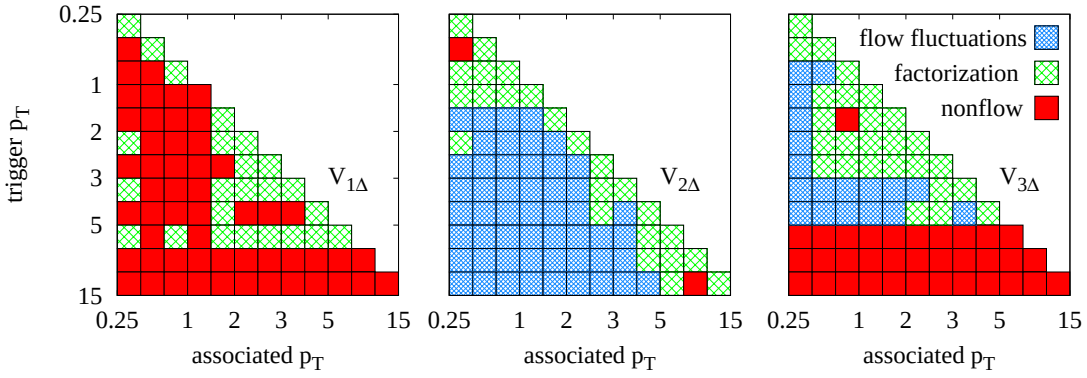

Figure 4.4: Test of inequalities (4.15), (4.16) for the correlation matrix $V_{n\Delta}(p_{\mathrm{T}}^a, p_{\mathrm{T}}^b)$ in case of 0-10% centrality Pb-Pb collisions at $\sqrt{s_{\mathrm{NN}}} = 2.76\,\mathrm{TeV}$. Experimental data was measured by ALICE [256]. Only statistical errors were taken into account in the analysis. Green: inequality (4.16) reduces to an equality within errors, $|r_n| = 1$. Blue: (4.16) holds as a strict inequality and thus it is possible to explain result in this cell with flow fluctuations within the hydrodynamical paradigm, $|r_n| < 1$. Red: either (4.15) or (4.16) inequality is violated, which means that hydrodynamics cannot explain this result, $|r_n| > 1$.

4.3.3 Quantitative analysis of the $r_n(p_{\mathrm{T}}^a, p_{\mathrm{T}}^b)$ observable

While any value between -1 and 1 is mathematically allowed for the r_n observable in hydrodynamics, our calculations indicate that in the highest-multiplicity collisions, it should be expected to be very close to 1. As multiplicity becomes smaller, the transverse size of the fireball and the typical number of participating nucleons are expected to decrease causing relatively larger fluctuations and thus driving r_n further away from unity. In Fig. 4.5, we show the centrality dependence of r_2 and r_3, respectively, for the set of parameters that best fit the above data ($\sigma = 0.4$ fm, $\eta/s = 0.08$), though the trend is general. The 2D matrix is flattened along the first index, such that each set of curves represents a fixed transverse momentum bin for one of the particles (p_T^a, labeled on the bottom), while each point on a curve represents a different p_T^b. We predict that the highest multiplicity collisions should give a value close to 1, and decrease monotonically when reducing multiplicity. Thus, any deviation from this trend would likely indicate a breakdown of a dominantly fluid description.

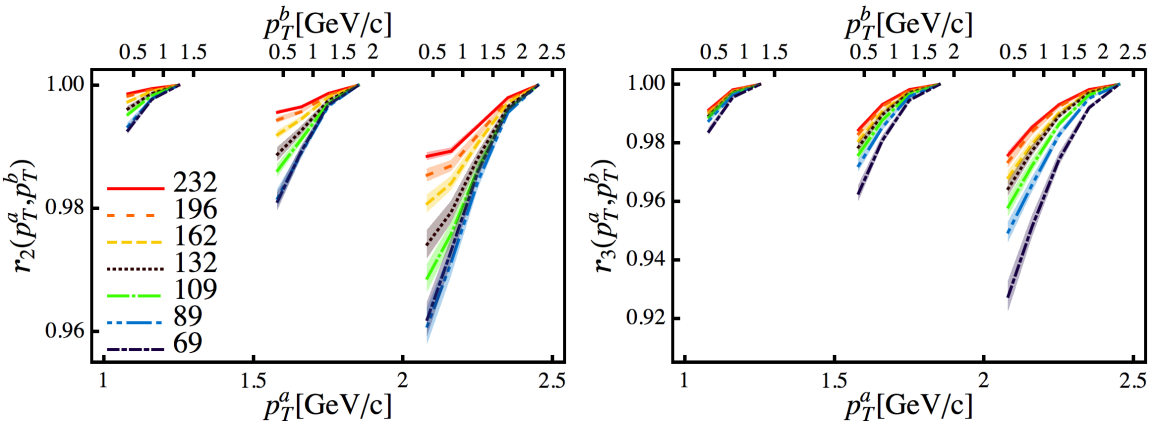

Figure 4.5: r_2 and r_3 dependence on centrality for the seven highest multiplicity bins in Table 3.1.

In Figs. 4.6, we show the effect of varying the viscosity η/s and the granularity parameter σ on r_n. We find that the viscosity actually has a quite small effect.

This observation was confirmed in [259]. In contrast, a variation of σ has a stronger effect on r_n, which indicates that aspects of the initial condition are *more* important. We confirmed that this is still the case in mid-peripheral Pb-Pb collisions. Thus, r_n

could potentially be of special value, since numerous other observables are sensitive to η/s, but no other observable is known to be this sensitive to the granularity of the initial conditions of a heavy-ion collision.

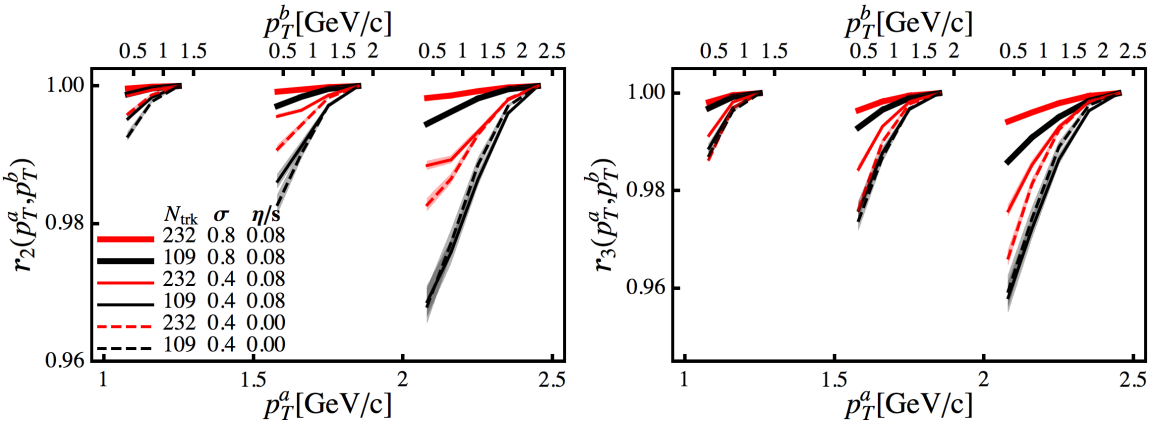

Figure 4.6: r_2 and r_3 dependence on the model's parameters of viscosity, η/s, and granularity, σ, (in fm). Calculations are shown for two centrality bins to illustrate generality of the conclusions.

4.3.4 Confirmation of our prediction with experimental p-Pb data

After our results were made available and predictions sent to the experiments (but before publication), results from all three LHC experiments were released [260, 261, 262, 143]. The results confirm our predictions – for a large range of centrality and p_{T}, the inequalities (4.15) and (4.16) are satisfied, the ratios r_n are close to unity in high multiplicity events, and the value decreases with smaller multiplicity as well as with larger transverse momentum difference $p_{\mathrm{T}}^a - p_{\mathrm{T}}^b$. In fact, the data show strikingly precise quantitative agreement with our predictions.

These results give a strong indication of the collective nature of high multiplicity p-Pb collisions and the likely applicability of hydrodynamic modeling in these systems. They also present a significant test that must be passed for any alternative explanation for the previous measurements.

Interestingly, r_3 rises above a value of 1 for high p_{T} particles in lower multiplicity events, i.e. when both $p_{\mathrm{T}} > 2.5$ GeV and $N_{\mathrm{trk}} < 150$ in the CMS data). This indicates

a violation of inequality (4.16), and therefore a clear signal of physics beyond fluid dynamics. Thus, as we have proposed, the r_n observable can indeed be a useful tool for making a more precise determination of where hydrodynamics is valid.

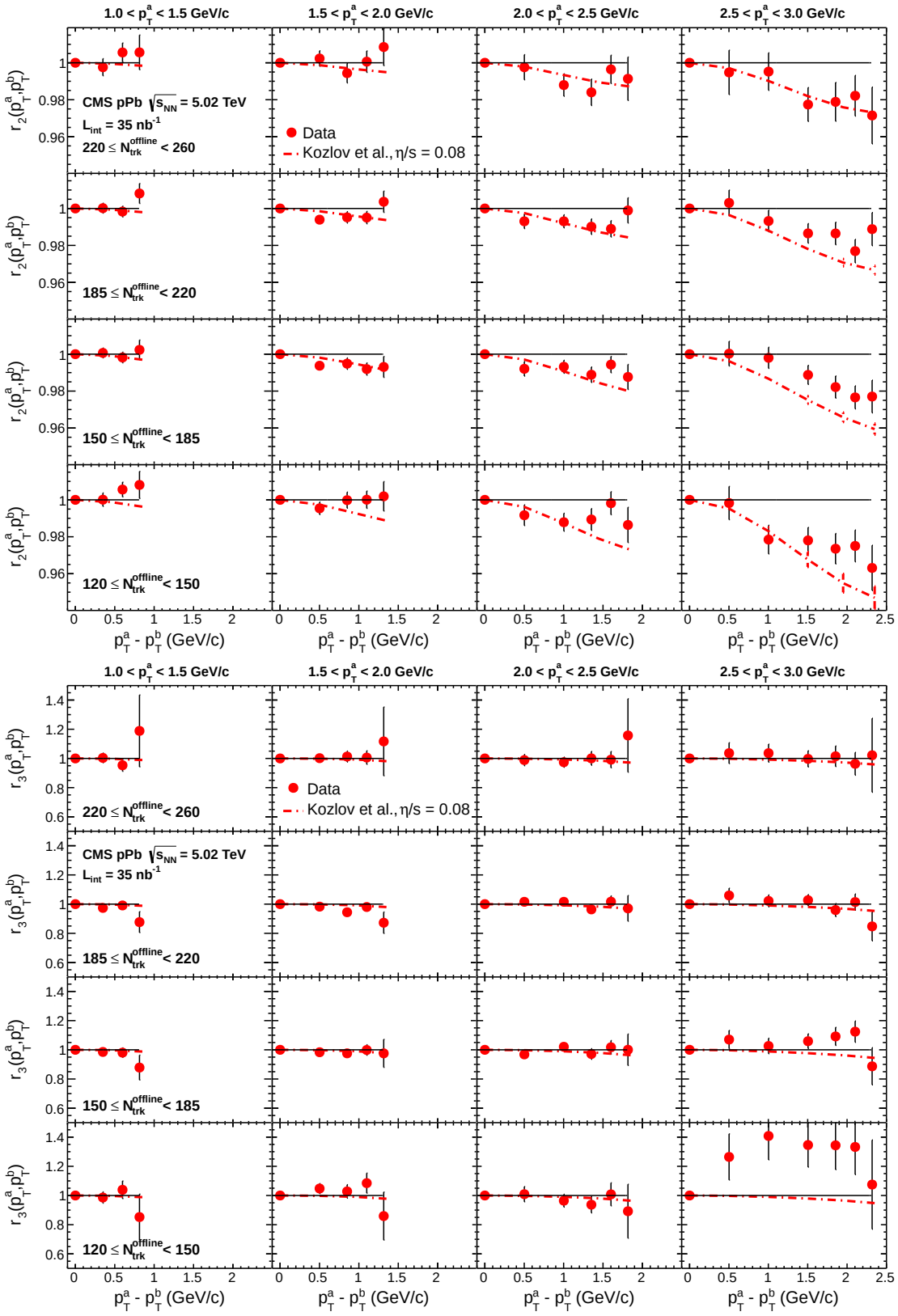

Figure 4.7: Comparison of our *prediction* that was released publicly [139] and sent to the CMS collaboration before they published their experimental results. Figures are from the CMS collaboration [143].

4.4 Final state effects in $r_n(p_{\mathrm{T}}^a, p_{\mathrm{T}}^b)$

In Section 4.3.2, we mentioned that non-flow effects do not play the key role in A-A collisions at least in the low transverse momentum region, $p_{\mathrm{T}} \sim 1\mathrm{GeV}$. We also observed good agreement between the prediction of our hydrodynamic model and the recently obtained experimental data, see Fig. 4.7. This alone confirms that pure fluid dynamics passes the most stringent test one could currently construct. However, to make our analysis exhaustive, in this section we discuss the final state effects on $r_n(p_{\mathrm{T}}^a, p_{\mathrm{T}}^b)$.

To account for non-flow effects, we utilize an afterburner, specifically UrQMD [170, 171]. We follow the approach described in [144], where it was applied to the case of large A-A systems.

4.4.1 Discrete particles hadronization

One uses the freeze-out hypersurface, $\Sigma_{T_{\mathrm{FO}}}$, that was obtained during the hydrodynamic phase of matter evolution. It is parsed element-wise to calculate the number of particles of species n that would be created from every piece, $\Delta\Sigma_\mu$, if one was to use the Cooper-Frye formula, (2.63).[1] The obtained value:

$$\Delta N_n = d_n \left(\int \frac{d^3\mathbf{p}}{(2\pi)^3} f(x, \mathbf{p}) \right) u^\mu \Delta\Sigma_\mu \tag{4.19}$$

is used as an estimate of the average multiplicity coming from this segment.[2] One could think of it as of an average of an ensemble of events in which the freeze-out surface element, Σ_μ, and matter flow velocity vector, u^μ, are the same, but the number of created particles changes around the average, ΔN_n. Then, one uses Poisson distribution to sample representations from this events' ensemble:

$$P(N_n) = \frac{1}{N_n!} \left(\Delta N_n\right)^{N_n} e^{-(\Delta N_n)}. \tag{4.20}$$

[1] So far, this process resembles the calculation of the Cooper-Frye formula, (2.63), using the Riemann sum approximation.

[2] One can say that multiplicity is calculated in every cell. However, we want to avoid the confusion of mixing the discretization used when numerically solving hydrodynamical equations and the mentioned above calculation over the freeze-out hypersurface. The happen in different spaces.

Once the total multiplicity, N_n, coming from this specific hypersurface segment is determined from (4.20), one can sample momenta of these particles individually using distribution:

$$p^0 \frac{dN_n}{d\mathbf{p}} = \frac{d_n}{(2\pi)^3} \left(f_0 + \delta f_{\text{shear}} + \delta f_{\text{bulk}}\right) p^\mu \Delta\Sigma_\mu. \tag{4.21}$$

After iterating this procedure over all particle species, n, and all elements of the freeze-out hypersurface, $\Delta\Sigma_\mu$, one obtains a set of particles with known momenta [263]. Time-space evolution of these individual particles can now be modeled with the UrQMD solver [170, 171]. Before describing it, we need to discuss two caveats of the above sampling approach.

First, numerical modeling of the QGP evolution shows that there are surface elements where flow[1] is directed inwards:

$$u^\mu d\Sigma_\mu < 0. \tag{4.22}$$

To avoid negative multiplicity values, one sets to zero contributions from these surface elements, (4.19). These regions describe the physical situation in which the QGP velocity and the normal to the freeze out hypersurface are oppositely directed. According to the Cooper-Frye framework, in this case QGP should be absorbing particles rather than emitting them. However, it is not possible as QGP expands into vacuum. Along the physical motivation for ignoring these negative contributions, there is a computational one. It was shown [263] that the problematic inward-directed segments appear randomly amidst of the larger outward-directed regions, where the velocity vector was almost orthogonal to the surface normal, and thus their product was nearly zero. Thus, its is possible that those negative contributions are of the numeric origin, as the used computational method guarantees the precision of the calculated value, but not its sign. In any case, we utilize this approach taking into account that it introduces a systematic error of about 10%. This estimate is based on the calculation of the contributions to the total energy of the QGP system and the hadrons' momentum distribution coming respectively from the inward-directed regions of the matter flow and the particles' momenta [263].

[1] In this paragraph we refer to the flow of matter, not the effect of collectivity in HIC.

Second, in Poissonian processes the values of mean and variance are equal. Thus, the following relation holds for the event's multiplicity averaged over the thermally equilibrated ensemble of states, (1.12):

$$\langle N_n^2 \rangle_T - \langle N_n \rangle_T^2 = \langle N_n \rangle_T. \tag{4.23}$$

This property remains valid when particles obey the classical Maxwell-Boltzman statistics [242]. However, for Bose-Einstein and Fermi-Dirac distribution equality (4.23) is violated:

$$\langle N_n^2 \rangle_T - \langle N_n \rangle_T^2 \sim \int d\chi\, p^0 f_0(x^\mu, p^\mu)(1 \pm f_0(x^\mu, p^\mu)) \neq \langle N_n \rangle_T \sim \int d\chi\, p^0 f_0(x^\mu, p^\mu), \tag{4.24}$$

where $f_0(x^\mu, p^\mu)$ was defined in (2.59). Thus, it is not guaranteed that (4.23) would hold for a generalized distribution, $f(x^\mu, p^\mu)$. For that reason it was tested that in a typical HIC collision described within the framework of this work, (2.58), condition (4.23) is satisfied with a 10% accuracy for the switching temperatures in the range from 0.135 to 0.165 GeV. Thus, the systematic error resulting from the usage of the Poisson distribution is consistent with the discussed above uncertainty of the implementation of the Cooper-Frye method.

Our final remark in this section will be regarding the difference in the vocabularies used in the hydrodynamical and kinetic theory descriptions of the HIC. As we discussed in Section 1.1.5, at certain conditions matter evolution could be described using both of the aforementioned approaches.

For hydrodynamic evolution it would be the requirement for the Knudsen number, (1.19), to be less than one. Knudsen number value can be estimated using the formula:

$$Kn = \tau_\pi \partial_\mu u^\mu, \tag{4.25}$$

where τ_π is given by (2.44) and expansion rate, $\partial_\mu u^\mu$, is to be determined from the hydrodynamical calculation [264]. It was shown that for small collision systems Knudsen number is in the range of $0.5 - 0.7$ during the entire evolution [265, 266], see also Fig. 5.8. Thus, application of the hydrodynamical approach is justified all the way to the freeze-out temperature of 0.150 GeV.

For the kinetic theory case, one could use the definition of the Knudsen number, (1.19), as of the ratio between the mean free path, λ, and the characteristic extension of the medium, L. For the former quantity we use the following estimate:

$$\lambda \sim \frac{1}{\sum\limits_n \bar{\sigma}_n \bar{N}_n}, \tag{4.26}$$

where $\bar{\sigma}_n$ and $\bar{N}_n$ are correspondingly the average cross-section and the average density[1] of particles of species n. Pions are the most abundant final state particles in HIC. Their cross-section, used also in the UrQMD package, is $\sigma_{\pi_-\pi_+} = 4$ fm^2. Its average density can be estimated based on the assumption of emission from thermally equilibrated medium, (4.24). The typical temperature and size of the system could be obtained from our hydrodynamical calculation. This is how we arrive at the estimate: $\lambda \sim L \sim 5\,\text{fm}$.

Thus, application of both hydrodynamic and kinematic approaches is justified once the QGP fireball cools down to about $0.130 - 0.170\,\text{GeV}$. In the hydrodynamic framework, hadronization happens at the freeze-out temperature, T_{FO}. In kinetic theory, particles are considered to be created at the switching temperature, T_{sw}. Usually the latter is higher than the former. This is the case, because in the hydrodynamic approach, one assumes that after freeze-out particles undergo free streaming, i.e. propagate freely, without collisions. One turns to kinetic theory when willing to estimate effects of inter-particle interactions during the late stage of the HIC evolution. Thus, one wants to start describing this dynamics as early as possible, i.e. at higher temperatures.

Finally, it is worth mentioning the principal difference between the hydrodynamic and kinetic descriptions. In the former case, one deals with a smooth (averaged over the ensemble) particle distribution, (2.58), while in the latter – with a variety of linear combinations of delta functions (individual configurations from this ensemble). Thus, in the latter case, one needs to repeat the described in this section particle sampling procedure multiple times and average calculated observables over this ensemble. In

[1] Multiplicity, N_n, per unit volume.

this work we iterated the sampling procedure 500 times for every hydrodynamic hypersurface. Before averaging we evolved every sampled configuration using UrQMD package.

4.4.2 UrQMD fundamentals

UrQMD is a numerical package used for modeling particle dynamics at microscopic level. It describes the particle kinetics on the event-by-event basis rather than at the level of the "average" distribution function, $f(x^\mu, p^\mu)$, which satisfies Boltzman equation, (1.27). It incorporates various reaction mechanisms, which are appropriate for different energy levels (among them: compound nucleus, resonance production, string[1] excitation and fragmentation), in order to provide a consistent understanding of the HIC dynamics. One also has to introduce a number of phenomenologically motivated approximations and parameters, as accessible experimental data on microscopic dynamics is rather limited. In this section we will discuss relevant for our discussion physical principals and phenomena that are being utilized in UrQMD.

The model is a successor of RQMD (Relativistic Quantum Molecular Dynamics) [268], which combines the classical propagation of particles with quantum effects, such as stochastic scattering and particle decays. It approaches the challenge of introducing Lorentz-invariant particle dynamics interaction at a distance without field degrees of freedom by utilizing a Hamiltonian framework with $8N$ variables. Those correspond to four spatial, x^μ, and four momentum, p^μ, coordinates of each of the N particles. The system is also subject to $2N-1$ constraints: N are the mass shell restrictions for every particle, and the other $N-1$ correspond to the relative time fixations, as in relativistic systems every physical object has its own proper time. Thus, there are $6N+1$ independent variables that describe the system dynamics with one of them being τ – the system clock.

Although this framework allows to introduce covariant relative distance between

[1]Here we talk about QCD strings, which are phenomenological objects that are being formed by the fluxes of the gluon field, and are not the fundamental building blocks of the ST, see [267]

any two particles, i and j:

$$d_{\text{trans}} = \left\| (x_i - x_j)^\mu - \frac{(x_i - x_j)^\nu (p_j + p_i)_\nu}{(p_i + p_j)^2} (p_i + p_j)^\mu \right\|, \tag{4.27}$$

which is necessary to define the probability of their interaction, it still does not solve the problem of the dependence of the time ordering of particles' collisions on the reference frame.

For that reason, UrQMD approaches the frame-dependence problem in a phenomenological way. Specifically, the distance between every pair of particles, i and j, is defined with respect to their ("primed") rest-frame:

$$d'_{\text{trans}} = \sqrt{(\mathbf{x}'_i - \mathbf{x}'_j)^2 - \frac{\left((\mathbf{x}'_i - \mathbf{x}'_j) \cdot (\mathbf{p}'_i - \mathbf{p}'_j)\right)^2}{\left(\mathbf{p}'_i - \mathbf{p}'_j\right)^2}}. \tag{4.28}$$

Analogous to the the Glauber prescription discussed in Section 2.2.2, particles' collision is considered to happen if they pass each other at a distance:

$$d'_{\text{trans}} \leq \sqrt{\frac{\sigma_{i,j}}{\pi}}, \tag{4.29}$$

where $\sigma_{i,j}$ is the cross-section of particles i and j, which also depends on the collision energy, $\sqrt{s}$. The "system time" of every collision, τ_{coll}, is defined with respect to the nucleus-nucleus reference frame:

$$\tau_{\text{coll}} = -\frac{(\mathbf{x}_i - \mathbf{x}_j) \cdot (\frac{\mathbf{p}_i}{p_i^0} - \frac{\mathbf{p}_j}{p_j^0})}{(\frac{\mathbf{p}_i}{p_i^0} - \frac{\mathbf{p}_j}{p_j^0})^2}. \tag{4.30}$$

The dependence of this prescription on the reference frame was studied numerically for an A-A system and it was found that the particle multiplicities and the number of collisions vary by less than 3% when switching between the detector and nucleus-nucleus reference frames [170]. Thus, one considers that the algorithm provides a reasonable description of the N-body relativistic microscopic dynamics in HIC.

As we mentioned, π-mesons are the most abundant particle species in the final state multiplicity (about 80% of the total yield). For that reason we will briefly discuss here the mechanism that is used to describe their collisions in UrQMD. As we saw in Section 3.2, pions are produced in small systems with average transverse

momentum of about 0.6 GeV. At these ("low") energies pion-nucleon cross-section is large, and this is another reason why collisions with pions are important to discuss. Below 2.2 GeV, they occur through the formation of an intermediate resonance, R:

$$\sigma_{i,j}(\sqrt{s}) = \sum_R \langle j_i, m_i, j_j, m_j | J_R, M_R \rangle \frac{2S_R+1}{(2S_i+1)(2S_j+1)} \frac{\pi}{{p_{i,j}}^2} \frac{\Gamma_{R\to i,j}\Gamma_{\rm tot}}{(M_R-\sqrt{s})^2 + \frac{\Gamma_{\rm tot}^2}{4}}, \tag{4.31}$$

where m, s, j, and M, S, J are respectively the mass, spin, angular momentum of the i, j,R particles. Summation goes over all resonances, R, that could be formed in the collision of particles i and j. Angular bracket stands for the Clebsch-Gordan coefficient between the initial and final states. $\Gamma_{\rm tot}(M_R)$ and $\Gamma_{R\to i,j}(M_R)$ denote correspondingly the resonance's full decay width and the one corresponding to the channel i, j.

In Fig. 4.8, one can see the comparison between the UrQMD parametrization and experimental data for $\pi^+\pi^-$ and $\pi^- p$ processes. The reasonable agreement was achieved by tuning the numerous model's parameters to reproduce data in the exclusive channels, such as $\pi^- p \longrightarrow \eta n$[1]. It is worth mentioning that because the available experimental data [269] has relatively large errorbars, there are several different sets of UrQMD parameters that allow to reproduce it. In our calculation we used the default parametrization of UrQMD.

Sharp peaks in panels (a) and (b) of Fig. 4.8 correspond to the intermediate resonances that are contributing to the total cross-section. Specifically, for the $\pi^+\pi^-$ process it is the ρ resonance, and for the $\pi^- p$ one – N^* and Δ resonances. The relative contribution of different cross-section mechanisms is illustrated in panel (b) of Fig. 4.8. One can see that in the relevant for this work "low" energy/momentum region, resonances dominate, while particle elastic and string inelastic collision contributions have no effect.

In the purely UrQMD approach[2], resonances are mostly created in the initial proton-proton collisions. Masses of the excitations are sampled stochastically from

[1] In this case equation (4.31) should be modified by replacing $\Gamma_{\rm tot}$ with $\Gamma_{R\to\eta,n}$.

[2] In case one chooses to entirely ignore the QGP dynamics in HIC.

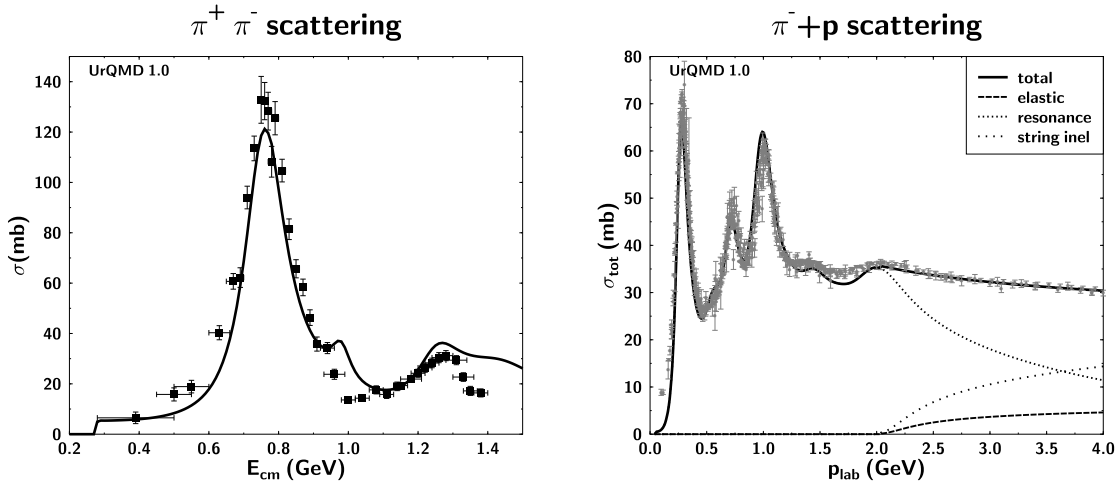

(a) (b)

Figure 4.8: Comparison of UrQMD fits to experimental data for total cross-sections of: (a) $\pi^+\pi^-$ [269] and (b) $\pi^- p$ [270] processes. Figures from [170].

the Breit-Wigner distribution:

$$\mathrm{BW}(M, M_R) = \frac{1}{N} \frac{\Gamma(M)}{(M_R - M)^2 + \frac{\Gamma(M)^2}{4}}, \quad N \equiv \int \frac{\Gamma(M)}{(M_R - M)^2 + \frac{\Gamma(M)^2}{4}} dm, \quad (4.32)$$

subject to kinematic constraints that stem from the energy-momentum conservation laws. The most general form of the relative momenta of the created particles in their rest frame is:

$$p'_{i,j}(\sqrt{s}) = \quad (4.33)$$
$$\int\int \frac{\sqrt{(s - (m_i + m_j)^2)\,(s - (m_i - m_j)^2)}}{2\sqrt{s}} \mathrm{BW}(m_i, m_{R_i}) \mathrm{BW}(m_j, m_{R_j}) dm_i dm_j.$$

If one of the produced particles is stable, the corresponding Breit-Wigner distribution will reduce to the delta function, $\delta(m_R - m)$.[1]

In our work we do not utilize UrQMD code to describe p-Pb collisions from the very beginning (starting at $\tau = 0\,\mathrm{fm}$). We use our own prescription for the initial conditions and then evolve the system hydrodynamically, because we want to test

[1] UrQMD can not straightforwardly deal with N body processes, if $N > 2$. Thus, in the case of many body decays, particles are united into two "effective" ones. See discussion in Section 2.4.

the implications of the strongly interacting medium (QGP) creation. At switching temperature, we perform the discussed above hadronization by sampling particles' species and momenta. Only then we use UrQMD to model the particle kinetics. In this way we aim to understand the effect of particlization (discretization) and whether the used before (average) distribution based approach was accurately capturing the late HIC dynamics.

Thus, we utilize UrQMD procedures for the description of resonances, as similar to all other particles they and their decay products can be created after the initial thermal emission from QGP and can change direction due to collisions before reaching the detector. Resonance lifetime is determined (in a standard way) using Monto-Carlo sampling and assuming exponential decay law with parameter:

$$\tau_R = \frac{1}{\Gamma_R}, \tag{4.34}$$

where Γ_R is the resonance's decay width. For any unstable particle in UrQMD, the total decay width is equal to the sum of the contributions coming from all available channels, i, j:

$$\Gamma_{\mathrm{tot}}(M) = \sum_{i,j} \Gamma_{i,j}(M). \tag{4.35}$$

Widths in various channels, as well as the total one, can depend on the excitation mass, M. This relation is defined with respect to the mass value at the pole, M_R:

$$\Gamma_{i,j}(M) = \Gamma_R^{i,j} \frac{M_R}{M} \frac{1.2 \left(\frac{p'_{i,j}(M)}{p'_{i,j}(M_R)} \right)^{2l+1}}{1 + 0.2 \left(\frac{p'_{i,j}(M)}{p'_{i,j}(M_R)} \right)^{2l}}, \tag{4.36}$$

where l is the angular momentum of the exit channel. An example of a resonance lifetime mass dependence is shown in Fig. 4.9.

Now that we discussed the relevant mechanisms of the UrQMD package, we can assess the non-flow effects on p-Pb observables.

4.4.3 Results comparison of the discretized and "average" descriptions

In Sections 2.4 and 4.4.2, we discussed the implementations of the discretized and "average" approaches to describing final state particle evolution. In a nutshell, in

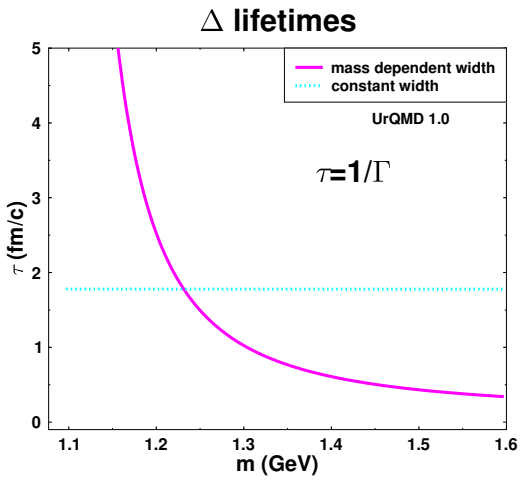

Figure 4.9: Used in UrQMD implementation of the $\Delta(1232)$ excitation lifetime mass dependence (solid line). One can also see how the value of the lifetime would have changed if one used constant width definition instead (dashed line). Figure from [170].

the latter case momentum conservation laws hold on average, while in the former case they are fulfilled in every particle decay and collision. Here we will compare the results of these calculations.

We will start with the conventional flow observables, see Fig. 4.10. One can notice that the results of the UrQMD calculations with switching temperatures, $T_{\rm sw}$, of 0.150 and 0.170 GeV practically coincide with each other and with the result of the "average" framework calculation at "low" transverse momentum, $p_T \leq 3\,\text{GeV}$. From this we can deduce two conclusions. First, as we anticipated in Section 4.4.1, both hydrodynamic and kinetic theory approaches can accurately describe the final state particle evolution. The change of the switching temperature in a rather wide range of values does not alternate the results. For that reason we will fix its value to 0.150 GeV in further analysis. Second, discretization of the final state dynamics provides a negligible correction to the transverse flow observables. This is due to the low final multiplicity in small systems that results in almost no final state particle collisions – approximately one per hydro event. This explains why there is almost no difference

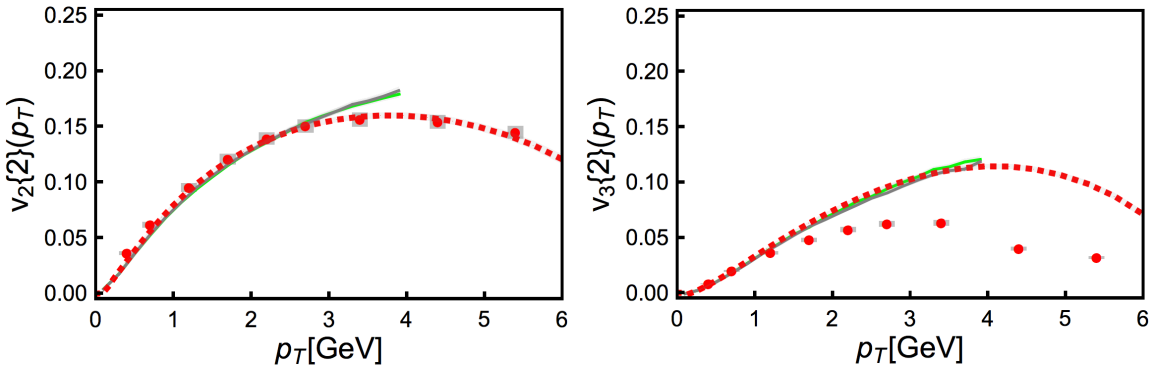

Figure 4.10: Comparison of the differential charged hadron $v_2\{2\}(p_{\mathrm{T}})$ and $v_3\{2\}(p_{\mathrm{T}})$ in the highest multiplicity bin of 5.02 TeV p-Pb collisions. Results are obtained from: circles – experiment (by CMS); dashed line – hydrodynamic model + "average" particle distribution framework (also presented in the right panel of Fig. 3.6), $T_{\mathrm{FO}} = 0.150\,\mathrm{GeV}$; (two entirely overlapping) solid lines – hydrodynamic model + discrete particlization approach with UrQMD. The two latter curves represent calculations performed at switching temperatures $T_{\mathrm{sw}} = 0.150$ and $0.170\,\mathrm{GeV}$.

compared to the result obtained from the superposition of the "average" distributions. There is some discrepancy above $p_{\mathrm{T}} \geq 3\,\mathrm{GeV}$ for $v_2\{2\}(p_{\mathrm{T}})$, but hydrodynamics is not expected to be applicable in this region anyway. All in all, we arrive at a conclusion that MUSIC solver that utilizes "average" particle distributions approach captures experimental trends at "low" momentum in small systems reasonably well.

Now we will turn to the comparison of our prediction for r_n, see Fig. 4.7, but this time using UrQMD approach for the description of the final state dynamics. Although, from the comparison of the flow harmonics, $v_n\{2\}(p_{\mathrm{T}})$, evaluated using both methods, we expect that there will be no considerable difference between the results, one still needs to check it. First, because, as we discussed in Section 4.2.3, the transition between the discretized and "average" distributions formalisms is rather involved and it is challenging to predict the outcome of the comparison. Second, because UrQMD approach describes non-flow effects that might affect the results and this way the generality of our earlier conclusions in Section 4.3.4.

Fig. 4.11 shows the results of the comparison of our prediction for the r_n observ-

able using the "average" distribution approach with freeze-out temperature, $T_{\rm FO} = 0.150\,\text{GeV}$, and discretized UrQMD framework with switching temperature, $T_{\rm sw} = 0.150\,\text{GeV}$. First, one can notice an agreement between the results of both approaches and experimental data for r_2. Second, similar observation holds for the case of r_3, but with one exception. At "low" p_T^b momentum, UrQMD evaluates a non-flow contribution that even further improves agreement with the data. This is a non trivial result, because the effect of UrQMD on v_3 was unnoticeable, see Fig. 4.10 (b), but is clearly visible in r_3.

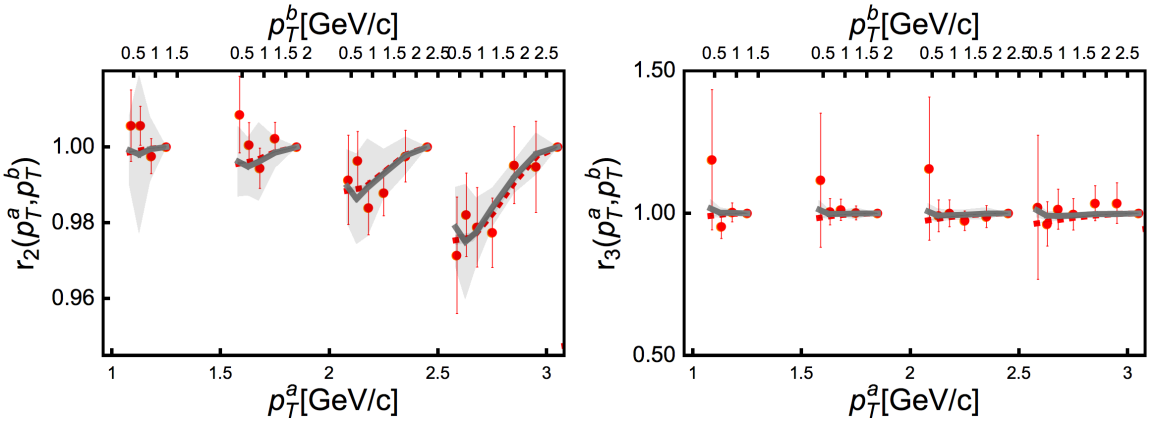

Figure 4.11: Comparison of r_2 and r_3 in 5.02 TeV p-Pb collisions obtained from: dots – experiment, [143]; dashed line – hydrodynamic model + "average" particle distribution framework (our prediction [139] also presented in Fig. 4.7); solid line – hydrodynamic model + discrete particlization approach with UrQMD.

As we expected, (the third harmonic of) $r_n(p_{\rm T}^a, p_{\rm T}^b)$ exceeds unity when UrQMD is used to describe the final state effects. However, this happens at large separation of transverse momenta, $p_T^a - p_T^b$, which also coincides with the limit of the hydrodynamics applicability, and indicates that non-flow effects originating from conservation laws start to play an important role in this kinematic domain.

Usage of UrQMD helps to better explain r_n behavior beyond the region of applicability of hydrodynamics, but does not affect the results obtained with the pure fluid dynamics model within the domain of its validity, where it describes experimental data well, see Fig. 4.7. Thus, we conclude that in the kinematic region of

high multiplicity, $N_{\rm trk} > 150$, and low transverse momentum, $p_{\rm T}^a$ and $p_{\rm T}^b < 2.5$GeV, hydrodynamics is a reasonable model of HIC collisions in small systems.

Studies of the multi-particle flow coefficients' ratios [271], which are less sensitive to the hydro response, show that there is currently no model that can properly describe fluctuations in large and small systems simultaneously. While in the former case QCD-inspired models such as IP-Glasma [131] work better, they fail to reproduce, for example, experimentally observed positive elliptic flow from the four particle correlation, $v_2\{4\}$, in small systems.[1] On the contrary, the discussed in this work Glauber initial conditions model allows to capture experimental trends in p-A system, see Fig. 4.7, but has challenges explaining r_n results in large systems when using the same set of parameters. We discuss this in details in the next section.

4.5 Revisiting $r_n(p_{\rm T}^a, p_{\rm T}^b)$ for A-A

Three previous hydrodynamic calculations of the ratio r_n were made for nucleus-nucleus collisions. The first was a calculation for Au-Au collisions with NEXUS initial conditions and zero viscosity [254]. The next was a Glauber model calculation with $\eta/s = 0.08$ and an MC-KLN calculation with $\eta/s = 0.2$ [273], both for a Pb-Pb system.

The values of r_n in these three calculations were ordered according to the viscosity in the calculation – the lowest viscosity result was farthest from one, while the calculation with the largest viscosity was closest to one. Both of the latter two had reasonable agreement with measured Pb-Pb data. The most natural interpretation was that viscosity reduced the magnitude of fluctuations and causes the ratio to become closer to 1. However, one should note that each of these three calculations also had different initial conditions. As we have shown for p-Pb (small system), viscosity actually has a small affect, while the initial conditions can have a significant effect.

[1] Recently progress has been achieved within the IP-Glasma framework, when each nucleon was effectively treated as a combination of three particles – "gluonic hot spots" [272]. Thus, we believe that further theoretical effort should focus on the modeling of subnucleonic fluctuations to achieve single framework approach to the systems of all sizes.

The latter two calculations neglect the local fluctuations in entropy production that we model with NBD. While these extra fluctuations are typically not believed to be important for observables in heavy-ion collisions, we might guess that they cause r_n to deviate further from one.

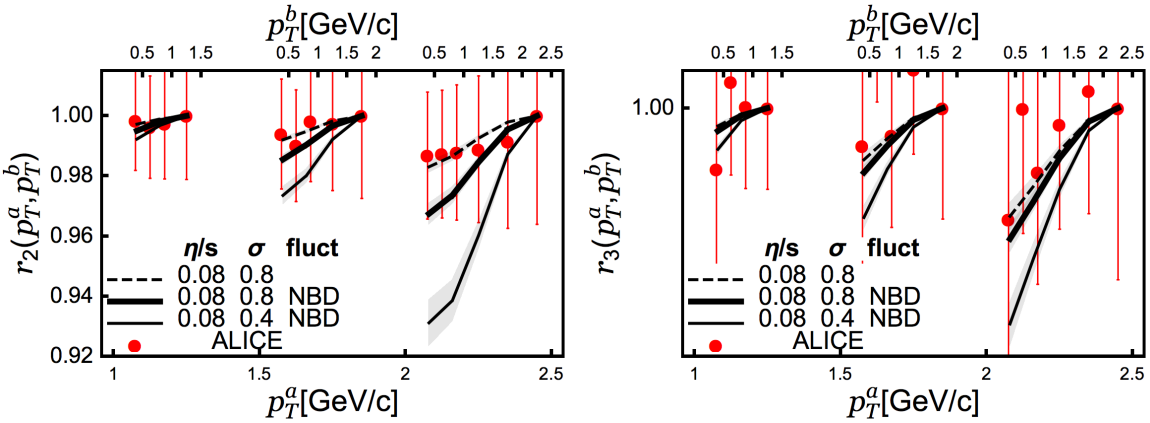

Figure 4.12: r_2 and r_3 in 40–50% centrality Pb-Pb collisions from our model with and without NBD fluctuations in the initial entropy per participant and with different values of the granularity parameter σ (in fm), compared to data derived from ALICE measurements of $V_{2\Delta}$ and $V_{3\Delta}$ [256, 254].

To test this in the case of large systems, we calculated r_n at 40-50% centrality Pb-Pb in the same model as above, but in addition we did a calculation for the same events with the extra NBD fluctuations turned off (i.e., so that every participant had the same contribution to the total entropy). The results are shown in Fig. 4.12.

Our calculations with a more standard Glauber model (i.e. without extra fluctuations) and $\sigma = 0.8$ fm should be close to the previous results, which fit data well. As can be seen in Figs. 4.12, this is the case. However, when we add more realistic NBD fluctuations, the value decreases, away from data. Further, if we change to the model that best fits existing p-Pb data ($\sigma = 0.4$ fm), r_2 falls even further from the measured value. This indicates that a simultaneous fit to *all* data is difficult. Calculations [235, 274, 271] also have trouble simultaneously reproducing p-A and A-A experimental results. This tension may ultimately provide useful constraints on hydrodynamic models.

In particular, it will be interesting to study why NBD fluctuations seem to be incompatible with r_n in peripheral Pb-Pb collisions, despite being necessary to describe the multiplicity distribution and being consistent with r_n in ultra-central heavy-ion collisions [259]. In addition, a simultaneous study of r_n in different collision systems can give valuable information about fluctuations in the initial state at different length scales.

4.6 New properties of the r_n observable and stringent test of hydrodynamics

In order to make a more stringent test of the applicability of hydrodynamics to small systems, we made a proposal to measure the $r_n(p_{\mathrm{T}}^a, p_{\mathrm{T}}^b)$ observable. It uses the full transverse momentum information from two-particle correlations, which is considerably more extensive than the conventional set of experimental observables that is being utilized in testing of HIC models. Thus, just that alone introduces additional constraints on the hydrodynamic model. Moreover, we discussed that $r_n(p_{\mathrm{T}}^a, p_{\mathrm{T}}^b)$ has the potential to rule out hydrodynamics as the correct description of HIC in small systems regardless of the particular implementation of the initial conditions and parameters of the fluid dynamics. However, rather than ruling out a hydrodynamic description, recent measurements of $r_n(p_{\mathrm{T}}^a, p_{\mathrm{T}}^b)$ in p-Pb collisions confirm both generic hydrodynamic expectations and quantitative predictions. This gives major credence to the validity of a fluid dynamic description of high multiplicity proton-nucleus collisions, and provides a significant constraint on other possible descriptions.

Further, we found out that $r_n(p_{\mathrm{T}}^a, p_{\mathrm{T}}^b)$ is less sensitive to viscosity than was previously expected. Thus, it is a promising observable to probe the transverse length scale of fluctuations in the early stages of a heavy-ion collision. We also confirmed with a direct calculation that non-flow effects do not alternate any of the above conclusions.

Finally, using our model, we calculated the $r_n(p_{\mathrm{T}}^a, p_{\mathrm{T}}^b)$ observable in large systems. Our results are consistent with experimental data and previous studies. We provided a new perspective on the challenge of describing experimental data within one model

and using one set of parameters. Specifically, we showed that the essential in the p-Pb case NBD fluctuations seems to be excessive in the case of Pb-Pb systems. This observation is important, because it was based on the analysis of the r_n observable, which as we showed is sensitive to the initial conditions. Thus, we suggest that future work should be focused on modeling of subnucleonic degrees of freedom if one is to find a universal approach to *all* systems.

5

Further advancements of hydrodynamical model

In this chapter we discuss further extensions of our hydrodynamical model. They were implemented after our prediction of the $r_n(p_T^a, p_T^b)$ observable was publicly released [139] and verified [143]. The new model modifications, despite their postdictive nature, provide important insight into the main topic considered in this work. Specifically, they show that our extended hydrodynamical model even better describes experimental data (transverse plane observables) that we discussed in Chapter 3 [140]. It also allows to reasonably reproduce the recently measured structure of the longitudinal observable $r_n(\eta^a, \eta^b)$ [143]. Noteworthy, one would expect a retuning of the model to be needed. However, our extension does not require that. We use the same values of the initial conditions, $\sigma = 0.4\,\mathrm{fm}$, and hydrodynamical evolution, $\eta/s = 0.08$, parameters as in Chapters 3 and 4. The extension of our model also does not modify (within statistical errors) the value of our prediction of the $r_n(p_T^a, p_T^b)$ observable. All this provides another evidence that hydrodynamics can at least qualitatively describe the global dynamics of small collision systems.

5.1 Bulk viscosity

In this chapter we discuss the effects of bulk viscosity on hydrodynamical observables. We outlined how to account for them qualitatively in Section 1.1.4 and quantitatively in Sections 2.3, 2.4. However, as we pointed out in Section 1.1.2, it is challenging to precisely calculate hydrodynamic models' transport coefficients such as bulk viscosity ζ from first principles. For that reason one needs to turn to phenomenological frameworks to get at least a qualitative understanding of the effect.

5.1.1 Estimates of bulk viscosity

In Section 1.1.3, we discussed that AdS/CFT provides a lower limit to the value of shear viscosity[1], η, in strongly coupled nearly conformal theories that closely resemble QCD. We also mentioned that a similar constraint exists for bulk viscosity, ζ, see equation (1.18):

$$\zeta \sim \left(\frac{1}{3} - c_s^2\right)\eta, \tag{5.1}$$

where c_s is the speed of sound in the medium. Computation [275] of the bulk viscosity in weakly coupled QCD to leading order in powers of the running coupling α_s, see Section 1.1.1, leads to the following estimate:

$$\zeta \sim \left(\frac{1}{3} - c_s^2\right)^2 \eta. \tag{5.2}$$

Note that both estimates, (5.1) and (5.2), contain a prefactor $\left(\frac{1}{3} - c_s^2\right)$ [276]. In conformal theories it is exactly zero. In general, its value depends on the equation of state, which defines the speed of sound in the medium:

$$c_s^2 = \frac{\partial P}{\partial \epsilon}. \tag{5.3}$$

In our model, we use equation of state s95p-v1 from [147], see Section 3. It was obtained using lattice calculations from the first principles of QCD and for that reason is expected to provide a reliable description of the matter dynamics. According to it, c_s^2 drastically deviates from $\frac{1}{3}$ only in the phase transition region, $T_c \sim \Lambda_{\mathrm{QCD}}$, where plasma constituents merge to form hadron degrees of freedom, see Figs. 1.7 and 5.2[2].

Thus, it is reasonable to expect that bulk viscosity provides a negligible contribution that does not affect the results of hydrodynamical calculations, unless the freeze-out temperature corresponds to the region where ζ/s peaks [144]. An observation that bulk effects could be detected in experimental data was made in [277]: it was pointed out that despite bulk viscosity, ζ, being suppressed in weakly coupled

[1] To be precise, it is a constraint on the shear viscosity to entropy density ratio, η/s, see equation (1.18).

[2] In Fig. 5.2, the $\zeta(T) = \frac{1}{2\pi}\left(\frac{1}{3} - c_s^2(T)\right)^2$ function was plotted. One can see that $\zeta(T)$ quickly decreases when moving away from T_c, which equivalently means that $c_s^2(T)$ quickly approaches $\frac{1}{3}$.

theories by the second power of $\left(\frac{1}{3} - c_s^2\right)$, the corresponding bulk viscous correction to the particle distribution function, δf_{bulk}, is affected only proportionally to the first power, see equation (2.61).

Phenomenological evaluations of bulk viscosity were made based on microscopic models of hadronic resonance gas (HRG) [278, 279]. They obtained an estimate of:

$$\frac{\zeta}{s} \sim 0.03, \tag{5.4}$$

which was used in hydrodynamical calculations [217, 280], see Fig. 5.1. Relation

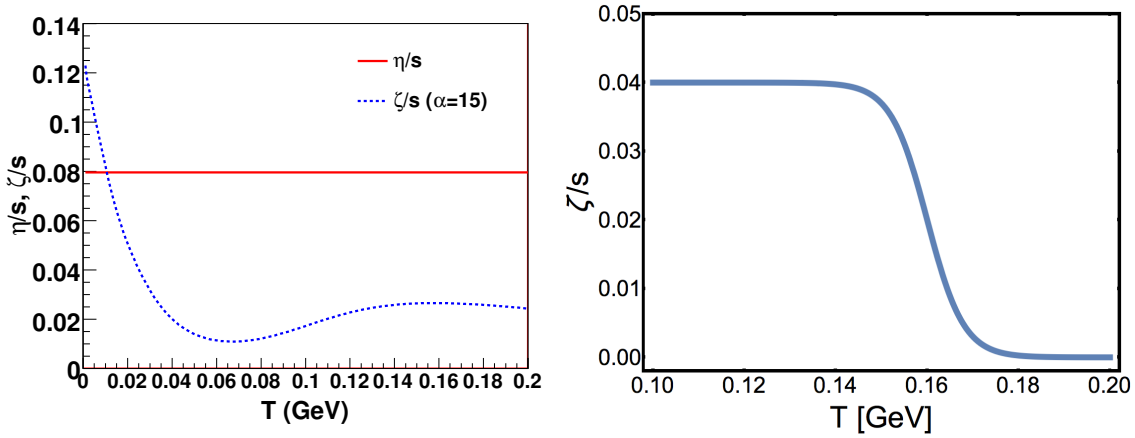

(a) (b)

Figure 5.1: Dependence of bulk viscosity to entropy ration, ζ/s, on temperature, T, from: (a) [280] (Figure from [280]), and (b) [281, 217]. Prescription (a) uses relation (5.2) with the coefficient of proportionality $\alpha = 15$.

(5.4) is expected to be valid in the low temperature region, which is below the critical value, T_c, that corresponds to the confinement-deconfinement transition. Above T_c one expects bulk viscosity to be suppressed and quickly approach zero following the trend specified by equation (5.1), see Fig. 5.2.

Studies [286, 287, 288] of bulk viscosity behavior around T_c suggest that it peaks in this region. Lattice calculations [48, 289] suggest an order of magnitude higher value there than the one obtained with perturbative methods, see equation (5.4):

$$\frac{\zeta}{s} \sim 0.3. \tag{5.5}$$

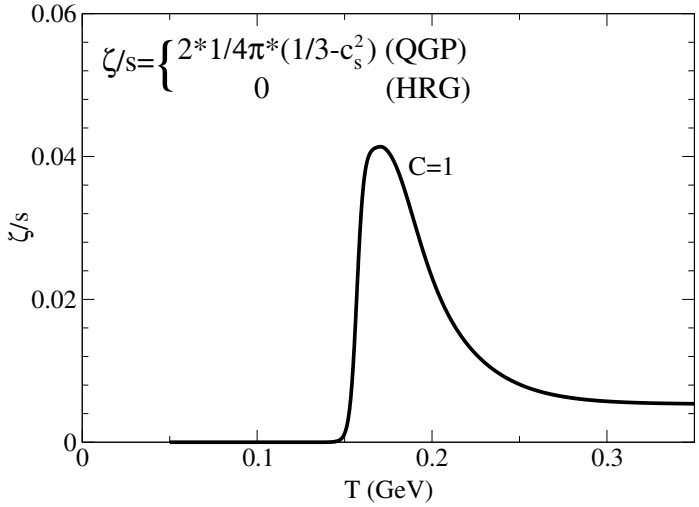

Figure 5.2: Dependence of bulk viscosity to entropy ration, ζ/s, on temperature, T, that was used in [282]. Figure from [282]. It is based on the AdS/CFT estimate, see equations (1.18), (5.1), and [61]. As an exact gravity dual theory of QCD has not been found and thus the precise dependence of bulk on temperature is yet to be determined, authors of [282] use a multiplicative factor C when modeling the ζ/s profile. They also point out that there is no agreement in the literature on the temperature dependence of bulk viscosity below T_c other than that its absolute value should be small [283, 284, 285]. Thus, they use $\zeta/s = 0$ in the hadron gas phase.

Due to the significant difficulties that are pertinent to the extraction of transport coefficients in lattice calculations, see Section 1.1.2, it is challenging to determine the temperature profile of bulk precisely from a direct calculation of the correlation function of the trace of the energy-momentum tensor. An alternative way to study bulk behavior in the critical temperature region using sum rules derived from low-energy theorems of broken conformal invariance and lattice data [49] confirmed the peak value estimate of the variable. However, similarly to the aforementioned direct lattice calculation framework, the authors of the latter method had to use an ansatz for the spectral density of the correlation function of the energy-momentum tensor, which greatly contributed to the uncertainty of the calculation. Nevertheless, an expectation of the rapid growth of bulk in the transition region and the results of the hadron

gas (HG), (5.4), and lattice (QGP), (5.5), calculations led to the parametrization proposed in [290] and illustrated in Fig. 5.3. One can describe it as an exponential

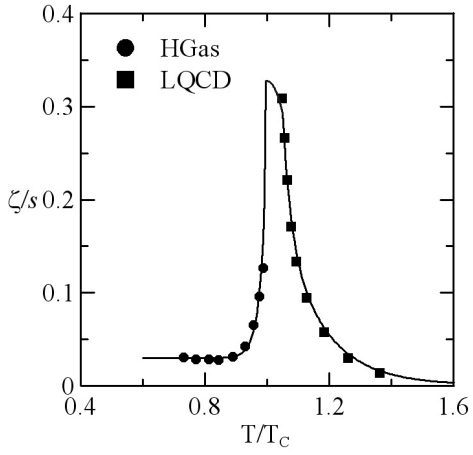

Figure 5.3: Interpolating fit of the bulk viscosity to entropy ratio, ζ/s, dependence on temperature, T, measured in units of its critical value, T_c [290]. Figure from [290]. HGas corresponds to the values obtained in hadron gas model [279]. LQCD indicates results of bulk extraction from lattice calculations [49].

decrease of the bulk magnitude away from its peak value, which is reached at the critical temperature.

Qualitatively similar parametrization of the bulk viscosity coefficient

$$(\zeta/s)(T) = \frac{(\zeta/s)_{\max}}{1 + [(T - T_c)/(\zeta/s)_{\text{width}}]^2} \tag{5.6}$$

was used in a massive attempt to constrain parameters of hydrodynamical models from the comparison to experimental data using Bayesian analysis and TRENTO prescription of initial conditions [200, 291]. The results of the calculation surprisingly agree better with the estimate (5.4) than (5.5). Specifically, it was shown that one cannot with certainty determine either the magnitude of the peak or its position. Noteworthy, similar difficulty of resolving the fine structure of the bulk viscosity profile was observed in the calculation using IP-Glasma initial conditions, see Fig. 5.4. From this we conclude that the models of initial conditions play a role in the uncertainty of the obtained results and the precision is yet to be achieved in the

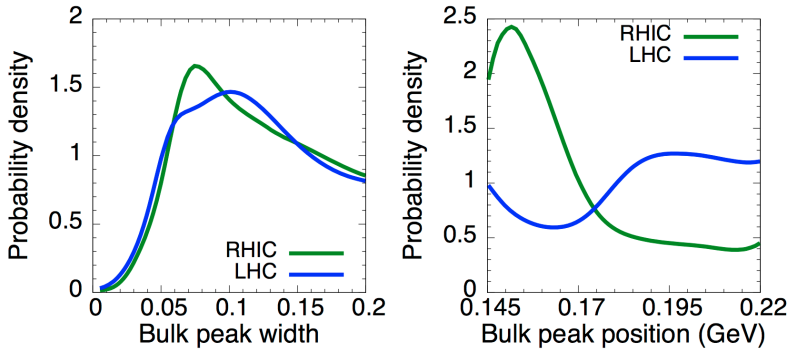

Figure 5.4: Extraction of the bulk viscosity ansatz (5.6) parameters using hydrodynamical modeling of A-A collisions at RHIC and LHC energies with IP-Glasma initial conditions [292]. Figures from [292].

quantitative studies of the bulk viscosity temperature dependence, which agrees with [293].

Nevertheless, we are interested in estimating the effect of bulk viscosity on hydrodynamic observables at least qualitatively. First, we want to learn whether it helps to improve agreement with the experimental data on the average transverse momentum of identified hadrons the way it does in large A-A systems [144]. Second, we aim to verify the generality of the conclusion on the property of the $r_n(p_{\mathrm{T}}^a, p_{\mathrm{T}}^b)$ observable to probe transverse granularity of the initial conditions, see Section 4.6. We also want to verify whether it has a drastic effect on the result of our prediction for $r_n(p_{\mathrm{T}}^a, p_{\mathrm{T}}^b)$.

5.1.2 Bulk effects in small systems

In Section 5.1.1 we discussed various approaches to calculating bulk viscosity, ζ. We concluded that the existing estimates agree on its schematic dependence on temperature – it should peak around T_c and decay on both sides of it – but not on the values of the profile parameters, such as the height, the width, and the position of the peak.

Notice that the ansatz used in [282], which is plotted in Fig. 5.2, matches the aforementioned description. There, it was shown that large, up to an order of magnitude, multiplicative variations of this parametrization affect flow observables less than moderate modifications of shear viscosity, which were varied in the vicinity of

its minimum value (at least in the conformal theories) of $\eta/s = 1/4\pi$. Thus, one can conclude that as soon as hydrodynamical approach remains valid, bulk viscosity with a temperature profile that peaks only around T_c should have a moderate effect on the collective flow.

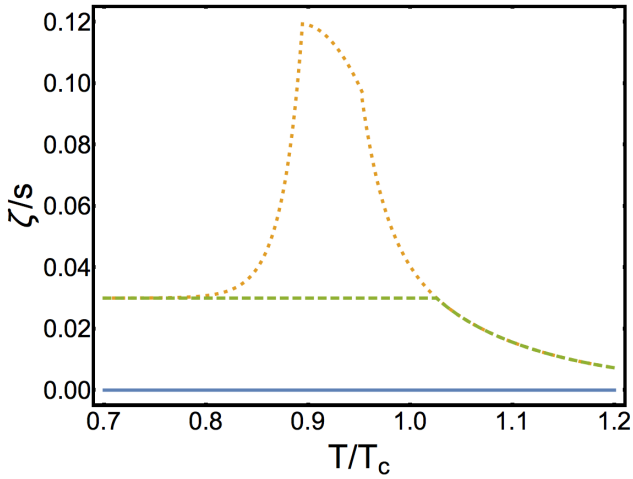

Figure 5.5: Our model's three scenarios of the bulk viscosity to entropy ratio, ζ/s, dependence on temperature, T, measured in units of its critical value, $T_c = 180\,\mathrm{MeV}$. Dotted line corresponds to the ansatz with the "peak" at the value of $\zeta/s = 0.12$ – this prescription resembles the one from [290], which was used together with IP-Glasma initial conditions, see also Fig. 5.4. Dashed line profile has a wide "plateau" at $\zeta/s = 0.03$ – it closely resembles the results obtained [200], which though used a different (TRENTO) model of initial conditions. Finally, the solid line describes "flat" parametrization with zero bulk, $\zeta/s \equiv 0$, – this profile was used in our calculations that were discussed in Chapters 3 and 4.

In this work, we took as a basis the ansatz proposed in [290], which is illustrated in Fig. 5.3. We did not alternate the hadron gas part of the parametrization, but proportionally reduced the rest of it (the magnitude at the peak and the region above T_c) with a multiplicative prefactor, which we varied similarly to what was done in [282]. As we discussed above, the fine structure of the profile seems to play a limited role when estimating bulk viscosity effects on flow observables. Thus, we provide only graphical representations of the three prescriptions that we used, see Fig. 5.5.

We refer to them as a "peak", a "plateau", and a "flat" bulk profile. Note that the maximum value of the "peak" ansatz is (considerably) three times smaller compared to the one from [290]. Yet, it is (considerably) by a factor of four larger than the estimate obtained for bulk viscosity in [200], see also (5.4). We attempted larger values of bulk viscosity at T_c up to the one obtained in lattice calculations [48], see (5.5). However, it appeared to have a too drastic effect on the average p_{T} observables, see Fig. 5.6.

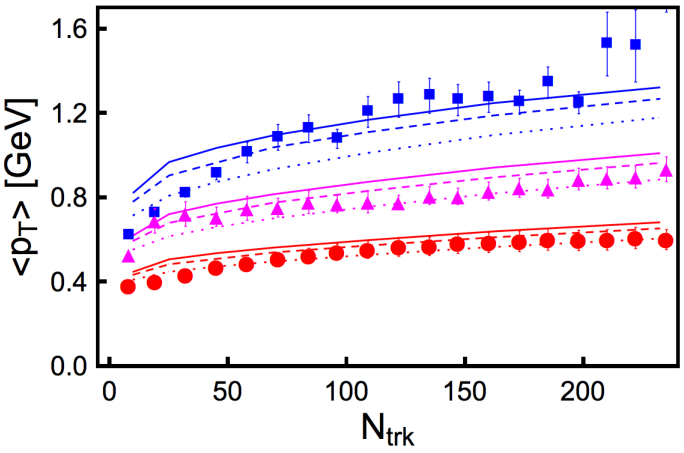

Figure 5.6: Effect of bulk viscosity on average transverse momentum of identified particles. Top to bottom: protons, kaons, pions. See Fig. 3.4 for more details. We try three different scenarios of bulk profile, which are illustrated in Fig. 5.5. Dotted line corresponds to the ansatz with the "peak" at the value of $\zeta/s = 0.12$, dashed line indicates the one that has a wide "plateau" at $\zeta/s = 0.03$, and the solid line specifies the trivial "flat" case of $\zeta/s \equiv 0$.

From the results shown in Fig. 5.6, we conclude that in our model the "plateau" profile with $\zeta/s = 0.03$ of up to $T \sim T_c$ provides the best fit to the experimental data on the average transverse momentum of identified particles. We point out that shear viscosity does not have any visible effect on the same observable, see Fig. 3.4. This has to do with the fact that bulk viscosity contributes to the effective total isotropic pressure, $P + \Pi$, which determines the acceleration of the QGP fireball expansion and

thus of the particle transverse momenta, while shear viscosity does not[1]. One can quantify this effect by noting that the magnitude of the bulk correction to the effective pressure, Π, grows with the increase of the bulk transport coefficient, ζ: $\Pi \sim -\zeta\theta$, where $\theta \equiv \partial_\mu u^\mu$ is the so-called expansion rate that is positive for any expanding medium, see equation (1.21). This relation explains why the average transverse momentum of charged hadrons is suppressed more in the scenario of the (larger) "peak" than the (smaller) "plateau" ansatz of ζ/s and why the overall inclusion of the bulk viscosity into the hydrodynamic calculation leads to the decrease of the $< p_{\rm T} >$ observable. We also note that particle transverse momentum was also affected by the transverse granularity of the initial conditions, see Fig. 3.4. Thus, bulk effects prevent one from directly assessing the magnitude of the initial conditions fluctuations from experimental data on particles transverse momenta. In other words, we confirm our earlier finding that the nature of the initial conditions also affects the extraction of ζ/s.

In Fig. 5.10, we show how bulk viscosity affects flow observables: $\bar{v}_n\{2\}$, $v_n\{2\}(p_{\rm T})$, $r_n(p_{\rm T}^a, p_{\rm T}^b)$. We use the three aforementioned prescriptions for the bulk profile, see Fig. 5.5.

Before proceeding to the description of these results, we note that the concern on the larger than in HIC matter gradients pertinent to small systems that could potentially lead to the uncontrolled growth of the bulk effects was addressed in [281, 230, 231, 232, 265, 181]. In these calculations even larger values of bulk viscosity compared to the present work were used, but no evidences of the aforementioned problem were found. For completeness, we perform here our own consistency check.

We start with showing the relative bulk viscosity contribution to effective pressure in one of our hydrodynamic 5.02 TeV p-Pb system calculations in Fig. 5.7. We, on purpose, choose an event from the highest multiplicity bin, see Table 3.1, and use the (extreme) "peak" scenario for the bulk viscosity, see dotted profile in Fig. 5.5. All the

[1]The Landau-Lifshitz frame condition that we chose for our implementation of the fluid dynamics equations requires shear tensor to be traceless, $u_\mu \pi^{\mu\nu} \equiv 0$ [64].

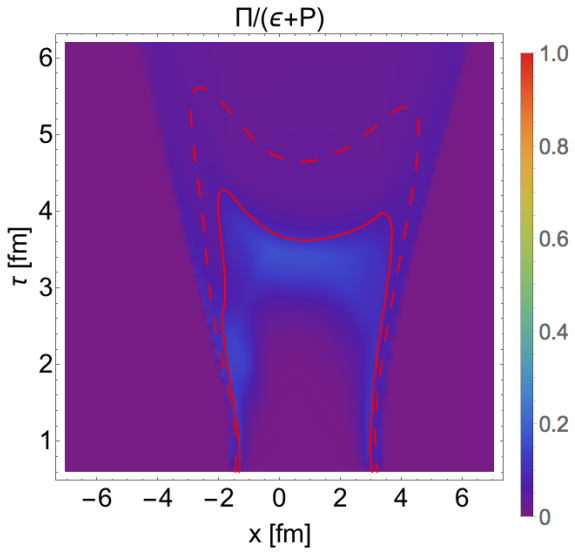

Figure 5.7: Distribution of the relative bulk contribution to effective pressure in one hydrodynamic event of our calculation of p-Pb collisions at 5.02 TeV in the top centrality bin, see Table 3.1. We use the (extreme) "peak" scenario for the bulk viscosity, see dotted profile in Fig. 5.5. Contour lines correspond to the surfaces of constant temperature at $T = 0.15\,\mathrm{GeV}$ (dashed line) and $T = 0.17\,\mathrm{GeV}$ (solid line).

rest of our calculations should have smoother gradients and smaller viscosity values. In Fig. 5.7, we see that even in the extreme case, bulk correction does not exceed 20% in the entire region where fluid dynamics framework is applied and that it is of the order of 5-10% on the freeze-out surface of constant temperature $T = 0.15\,\mathrm{GeV}$ that we use in our calculations. This means that introduction of bulk viscosity does not violate the applicability of hydrodynamics to the description of small collision systems and its effect on flow observables should be moderate, see Fig. 5.9. Now let us proceed with assessing the effects of shear viscosity and testing the general requirement of fluid approach consistency numerically.

In Fig. 5.8, we evaluate the inverse Reynolds and the Knudsen numbers. Both observables should be less than one for viscous effects to remain perturbative and fluid paradigm to be applicable, see Sections 1.1.4 and 1.1.5. One can see that this is, indeed, the case within the regions of the system where the temperature of the

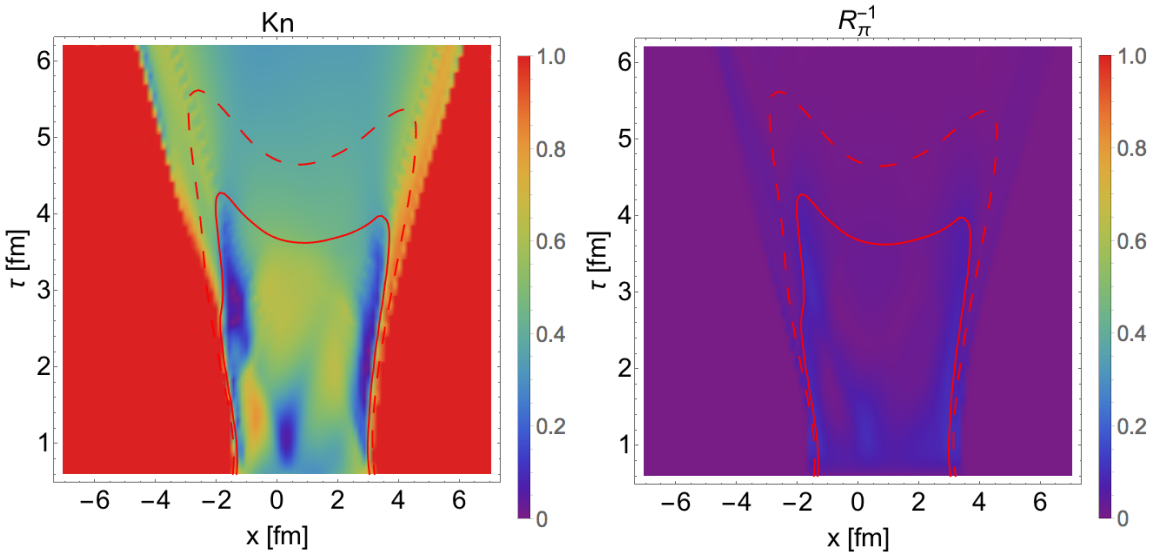

Figure 5.8: Distributions of the inverse Reynolds (left panel) and the Knudsen (right panel) numbers. Definitions of $\mathrm{Kn} = \frac{5\eta}{\epsilon+P}\partial_\mu u^\mu$ and $\mathrm{R}_\pi^{-1} = \frac{\sqrt{\pi_{\mu\nu}\pi^{\mu\nu}}}{\epsilon+P}$ are taken from [264]. See description of the calculation and of the contour lines in Fig. 5.7.

medium is above $T = 0.15\,\mathrm{GeV}$. Moreover, one can see in the left panel of Fig. 5.8 that the values of the Knudsen number along the constant temperature ($T = 0.15\,\mathrm{GeV}$ and $T = 0.17\,\mathrm{GeV}$) contours are relatively high and almost reach the magnitude of unity. This means that our calculation is self-consistent in both kinetic theory, see Section 1.1.5, and hydrodynamics, see Section 4.3.4, cases. Furthermore, we correctly identify the temperature range of hydrodynamics applicability in small systems – the edge of the QGP medium corresponds to the freeze-out surfaces of $T = 0.15\,\mathrm{GeV}$ that we use. One might wonder whether it will be an issue if the freeze-out surface appears to be slightly in the region where the Knudsen number is of the critical order of unity, as hadronization in the Cooper-Frye framework takes place along it, see Section 2.4. Left panel of Fig. 5.8 shows that it is likely to happen only in the early stage of the evolution for those hyper-surface elements whose normal vector $d^3\Sigma^\mu$ is orthogonal to the τ-axis. But such elements contribution to the total yield is negligible, see Equation (2.63) [263]. Thus, hydrodynamics provides an appropriate description of the system dynamics throughout its entire evolution and viscous corrections should

not be expected to greatly affect the results of our flow calculation.

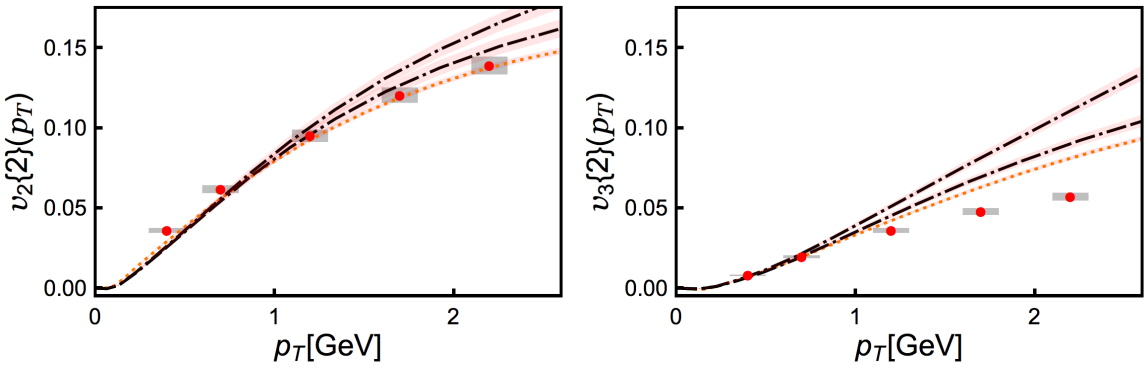

Figure 5.9: Effects of shear and bulk viscous corrections on flow observables. Dotted curve corresponds to the calculation of $v_n\{2\}(p_{\mathrm{T}})$ using the "peak" scenario for the bulk viscosity, see dotted profile in Fig. 5.5, and our model's standard prescription for the particle distribution function $f(x^\mu, p^\mu)$, see (2.58), which includes shear, $\delta f_{\mathrm{shear}}(x^\mu, p^\mu)$, and bulk, $\delta f_{\mathrm{bulk}}(x^\mu, p^\mu)$, viscous corrections. Dot-dashed and dot-double dashed lines correspond to the calculations of the same observable, but using a modified definition of the particle distribution function, $f(x^\mu, p^\mu)$. In the former case, both $\delta f_{\mathrm{shear}}(x^\mu, p^\mu)$ and $\delta f_{\mathrm{bulk}}(x^\mu, p^\mu)$ contributions were set to zero. In the latter case, the standard prescription (2.60) was used for $\delta f_{\mathrm{shear}}(x^\mu, p^\mu)$, but $\delta f_{\mathrm{bulk}}(x^\mu, p^\mu)$ was set zero.

In Fig. 5.9, we show that the bulk (and shear) viscosity correction, indeed, represents a small contribution to the calculated values of flow observables, which should be the case according to the theoretical assumptions that the viscous fluid dynamics framework is based on. This quantitatively confirms that the effect of bulk (and shear) viscosity is under control even in the most extreme of the bulk profile scenarios that we use in this work.

From the first pair of plots in Fig. 5.10, we conclude that bulk viscosity suppresses the magnitude of the integrated flow observables, $\bar{v}_n\{2\}$. The physics of the process is identical to one resulting in the decrease of the particles transverse momenta. Specifically, bulk creates negative contribution to the total pressure during the expansion phase of the QGP fireball, see equation (1.24). This slows down the velocity of mat-

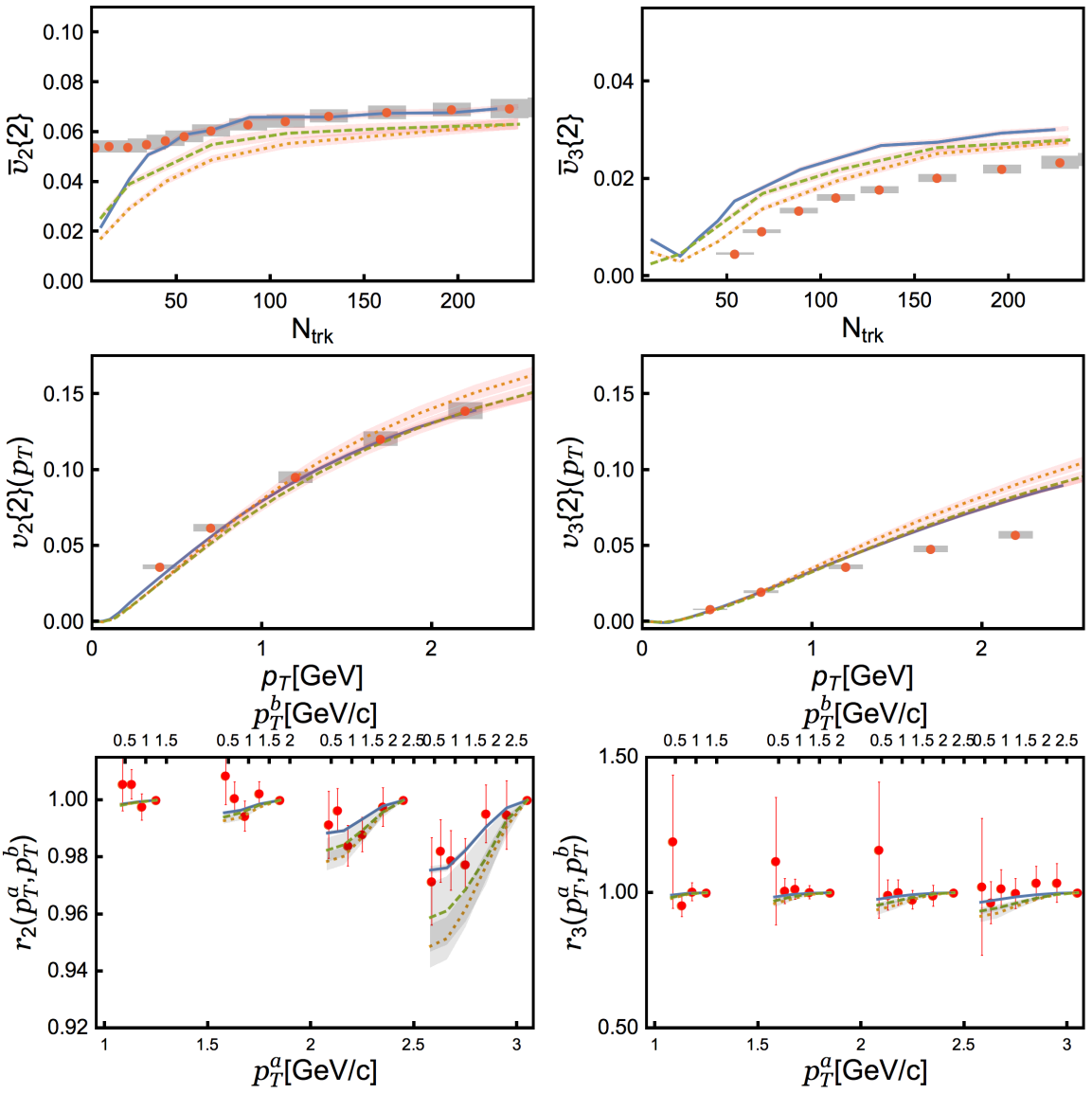

Figure 5.10: Effect of bulk viscosity on flow observables. We try three different scenarios of bulk profile, which are illustrated in Fig. 5.5, see legend of Fig. 5.6.

ter propagation and thus reduces the development of the final particle anisotropy, see Section 2.1.

From the second pair of plots in Fig. 5.10, one can study the transverse momentum dependence of the bulk flow suppression effect. At low transverse momentum the value of flow coefficients, $v_n(p_\mathrm{T})\{2\}$, is decreased compared to the calculation with zero bulk viscosity. At higher transverse momentum one observes an inverse trend: the larger

the bulk viscosity the higher is the value of $v_n(p_T)\{2\}$. However, as the majority of particles have low transverse momentum of $p_T \approx 0.5\,\mathrm{GeV}$, see 5.6, the magnitude of the integrated flow coefficients, $\bar{v}_n\{2\}$, is reduced compared to the calculation without bulk.

These two aforementioned conclusions agree with the ones observed previously in the hydrodynamic modeling of large A-A systems [294]. We also confirm the finding made in [144] that bulk viscosity helps to improve agreement of the hydro calculations results with experimental data. It remains valid is small systems, as well. However, we note that due the small magnitude of the used bulk profile ($\zeta/s \sim 0.03$, "plateau" scenario, dashed line in Fig. 5.5), unlike the authors of [144], we do not need to considerably alter the value of the shear viscosity in order to improve agreement of our results with experimental data on flow observables. Integrated elliptic flow, $\bar{v}_2$, practically touches the data points within errors even once we use the ("plateau") non-zero bulk prescription. The agreement with integrated triangular flow, $\bar{v}_3$, data requires systematic improvement of the initial conditions model using sub-nucleonic fluctuations, as we suggested in Section 3.2. Similar observations can be made from the graphs representing differential flow, $v_n(p_T)\{2\}$, results. We believe that the difference between the bulk profiles used in [144], [200], and this work has to do with the initial conditions (IP-Glasma, TRENTO, improved MC-Glauber). We suggest to study this topic in the future in more details – at this point it is premature to make any conclusions on the dependence of the bulk viscosity, ζ/s, on temperature as it should be model independent. Once this question is addressed, it would be reasonable to re-tune the model using a global statistical approach of the MADAI type [295] and assess the values of shear and bulk viscosity from the comparison to experimental data, see also Section 5.2.

Finally, we turn to the third pair of plots in Fig. 5.10. One can see that bulk effect (even in the severe "peak" scenario, see dotted profile in Fig. 5.5) does not modify the validity of our r_n prediction – the calculation goes through the experimental data within errorbars. It is specifically important because it confirms the conclusion

that we made in 4.6 that r_n observable can serve as a probe of the initial conditions granularity, as it is less sensitive to the effects of either shear or bulk viscosities.

All in all, we conclude that our model with (the "plateau" scenario of) bulk viscosity and without any other additional change of parameters is able to at least qualitatively describe experimental data. We reiterate that initial conditions' models should be the main focus of future research in order to further improve agreement of hydrodynamical models with experimental data. Studies of small systems will especially benefit from the development of three dimensional models that rigorously consider sub-nucleonic fluctuations, such as IP-Glasma.

5.2 Longitudinal fluctuations

We mentioned in Sections 1.2.2 and 2.2.4 that the currently available models of initial conditions with sub-nucleonic fluctuations, such as IP-Glasma, are defined only for symmetric systems and only in the transverse (collision) plane. However, p-Pb collisions are strongly asymmetric and require a prescription for defining the initial matter density profile along the beam axis. One expects to get valuable insights on the physics of the QGP formation from studying longitudinal dynamics of p-Pb systems. Specifically, one is interested in analyzing the flow factorization observable, $r_n(\eta^a, \eta^b)$, that was recently measured as a function of pseudorapidity [143]. As models with sub-nucleonic fluctuations are not suitable in the p-Pb case, it was suggested to modify the MC-Glauber model in order to capture the longitudinal dynamics of the system [296]. The idea was tested using a framework that was based on a modified MC-Glauber prescription for the initial matter density profile, but that did not include modeling of the subsequent system's evolution using hydrodynamics or kinetic theory [297]. In this chapter, we provide for the first time a full hydrodynamic calculation of $r_n(\eta^a, \eta^b)$ in a small p-Pb system and compare our results to experimental data.

5.2.1 Longitudinal flow factorization

In order to study two-particle correlations in longitudinal direction, equation (4.1) should be modified to:

$$V_{n\Delta}(\eta^a, \eta^b) \equiv \left\langle \langle e^{in(\phi^a - \phi^b)} \rangle \right\rangle, \tag{5.7}$$

where the internal angular bracket indicates averaging of the "integrand" over all pair combinations of charged hadrons in an event and the external angular bracket stands for averaging over events. Note that bins a and b are defined in (5.7) differently then in (4.3). We here follow the introduced by the CMS collaboration conventions, see [143]. Specifically, particles from bin a are restricted to be in the pseudorapidity limit $|\eta^a| < 2.4$, and those from bin b must have values from the segment $3.0 < |\eta^b| < 5.0$.

The reasoning behind splitting particles into sets a and b is conditioned by the need of subtracting considerable short-range jet induced correlations when studying collective effects, see Section 4.2.2. We mentioned in the discussion of equation (4.3) that in the analysis of the transverse plane two-particle correlations, CMS uses cuts of two units of pseudorapidity [222]. Thus, it would be preferable to impose even stricter constraints on the definition of the particle bins a and b: $|\eta^a| < 2.4$ and $4.4 < |\eta^b| < 5.0$. We will discuss this topic in more details later.

One expects that factorization equation (4.18) in case of longitudinal variables can be rewritten as:

$$V_{n\Delta}(\eta^a, \eta^b) \approx v_n(\eta^a) \cdot v_n(\eta^b), \tag{5.8}$$

where, similarly to (3.6), flow coefficients

$$v_n(\eta) e^{in\Psi_n(\eta)} \equiv \frac{\int e^{in\phi} \frac{dN(p_{\mathrm{T}},\eta,\phi)}{d\phi dp_{\mathrm{T}} d\eta} d\phi dp_{\mathrm{T}}}{\int \frac{dN(p_{\mathrm{T}},\eta,\phi)}{d\phi dp_{\mathrm{T}} d\eta} d\phi dp_{\mathrm{T}}} \tag{5.9}$$

are defined based on the one-particle distribution in every event, see equation (3.5). Thus, the simplest non-trivial quantity to be considered as a probe of factorization breaking in a symmetric (A-A) HIC would be, [143]:

$$r_n(\eta^a, \eta^b) \equiv \frac{V_{n\Delta}(-\eta^a, \eta^b)}{V_{n\Delta}(\eta^a, \eta^b)}, \tag{5.10}$$

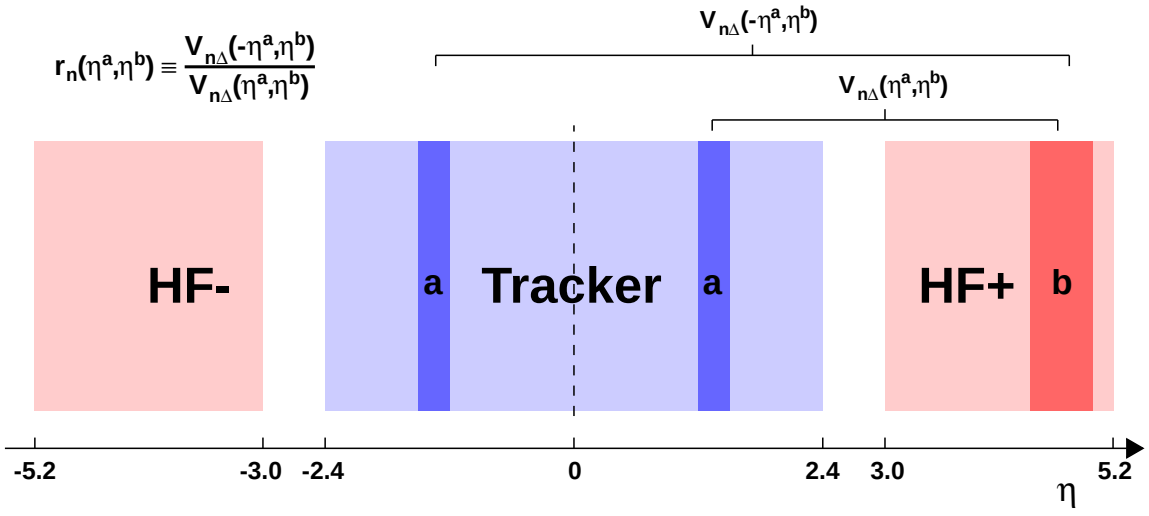

Figure 5.11: Illustration of $r_n(\eta^a, \eta^b)$ definition using CMS detector pseudorapidity bins [143]. Particles with pseudorapidity $|\eta^a| < 2.4$ are registered by the CMS "Tracker" calorimeter and are referred to by index a. Nearly beamline directed particles with pseudorapidity $3.0 < |\eta^b| < 5.0$, see Section 2.3.1, are registered by the Cherenkov hadronic forward (HF±) calorimeters and are labeled by index b. $r_n(\eta^a, \eta^b)$ corresponds to the measurement of the ratio between the two-particle correlations of yield with pseudorapidities η^b and $\pm\eta^a$, see equation (5.10).

where the discussed above constraint of wide rapidity cuts/gaps is fulfilled, because correlations are only considered between particles in bins a and b, see Fig. 5.11.

By construction, the $r_n(\eta^a, \eta^b)$ observable is dominated by flow [143]. This allows one to use a pure hydrodynamical approach (without an afterburner, see Section 4.4) in its modeling [298]. We will elaborate on this in the next section. Here we will only mention that the above "pseudorapidity cuts" play an important role in suppressing non-flow contributions to $r_n(\eta^a, \eta^b)$. If they were entirely absent, $r_n(\eta^a, \eta^b)$ would reduce to the following expression:

$$r_n(\eta^a, \eta^b) \overset{\text{hydro}}{=} \frac{\left\langle v_n(-\eta^a) v_n(\eta^b) \cos\left[\Psi_n(-\eta^a) - \Psi_n(\eta^b)\right]\right\rangle}{\left\langle v_n(\eta^a) v_n(\eta^b) \cos\left[\Psi_n(\eta^a) - \Psi_n(\eta^b)\right]\right\rangle}, \tag{5.11}$$

where the angular bracket denotes averaging over events, see equations (5.9) and (4.8).

Relation (5.11) helps to better understand the physical essence of the $r_n(\eta^a, \eta^b)$ observable. In HIC collisions of identical nuclei, experimental set-up is entirely symmetric with respect to the $\eta \to -\eta$ transformation. However, due to quantum fluctuations in the initial conditions, the corresponding equality of flow coefficients holds only approximately in every event:

$$v_n(\eta) \approx v_n(-\eta). \tag{5.12}$$

If one applies it while also assuming that flow coefficients do not change considerably event to event, one will obtain:

$$r_n(\eta^a, \eta^b) \approx \frac{\left\langle \cos\left[\Psi_n(-\eta^a) - \Psi_n(\eta^b)\right]\right\rangle}{\langle \cos\left[\Psi_n(\eta^a) - \Psi_n(\eta^b)\right]\rangle}. \tag{5.13}$$

Thus, $r_n(\eta^a, \eta^b)$ approximately probes the measure of the relative event-plane angle decorrelation (conventionally referred to as "torque") between pseudorapidities $|\eta^a + \eta^b|$ and $|\eta^a - \eta^b|$.

In case of asymmetric systems, torque effect could be calculated from the following generalization of the longitudinal flow breaking observable, (5.10):

$$\sqrt{r_n(\eta^a, \eta^b) \times r_n(-\eta^a, -\eta^b)}, \tag{5.14}$$

which is by definition symmetric under parity transformation in longitudinal direction. The observable defined by equation (5.14) measures torque effect between four pseudorapidity planes, which becomes clear if one uses the assumptions that led to approximation (5.13):

$$\sqrt{r_n(\eta^a, \eta^b) \times r_n(-\eta^a, -\eta^b)} \approx \sqrt{\frac{\langle \cos\left[\Psi_n(-\eta^a) - \Psi_n(\eta^b)\right]\rangle}{\langle \cos\left[\Psi_n(\eta^a) - \Psi_n(\eta^b)\right]\rangle} \frac{\langle \cos\left[\Psi_n(\eta^a) - \Psi_n(-\eta^b)\right]\rangle}{\langle \cos\left[\Psi_n(-\eta^a) - \Psi_n(-\eta^b)\right]\rangle}}. \tag{5.15}$$

5.2.2 Qualitative estimate of the $r_n(\eta^a, \eta^b)$ observable

In this section, we will dwell upon the logic behind the definition of $r_n(\eta^a, \eta^b)$ and the way this observable's dependence on pseudorapidity can be qualitatively estimated [296].

One might wonder why the definitions of r_n as a function of transverse (momenta) and longitudinal (pseudorapidities) kinematic variables differ, see equations (4.17) and (5.10). In this work, we are interested in probing the long-range[1] structure of particle correlations, because as we discussed in Sections 2.1.1 and 4.1 it is closely related to the notion of collective flow and the evidence of QGP formation in collision systems. Thus, it is important to subtract from the analyzed observables short-range contributions coming from non-flow sources, such as jets. This can be done for the two-particle correlation function by introducing wide rapidity cuts, see equations (4.3), (5.7) and Section 4.2.1. However, one cannot straightforwardly extend the definition of $r_n(p_T^a, p_T^b)$, (4.17), to the longitudinal case by simply replacing p_{T}^a with η^a and p_{T}^b with η^b, because this will give rise to the $V_{n\Delta}(\eta^a, \eta^a)$ and $V_{n\Delta}(\eta^b, \eta^b)$ terms that contain short-range correlations. For that reason CMS introduced another definition of r_n as a function of longitudinal variables[2], see equation (5.10), which combines two-particle correlation functions in a way that suppresses contributions of short-range effects.

As we discussed in Sections 1.2.2 and 2.2.4, most existing models of initial conditions are two-dimensional. They suffice for the description of the transverse flow in symmetric A-A collisions, as the values of flow coefficients barely change across several units of rapidity, see Section 4.2. However, one cannot entirely neglect fluctuations in pseudorapidity, because in this case $r_n(\eta^a, \eta^b)$ observable would be identically equal to unity, which experiments show is not the case [143].

Nevertheless, for the reasons discussed in the previous paragraph, it is reasonable to assume that flow barely changes its magnitude, $v_n(\eta)$, and slightly alternates its direction, $\psi_n(\eta)$, along the beam line. The two-particle correlation function, (5.7),

[1] In this section we refer to proximities in pseudorapidity coordinates between pairs yield when discussing ranges.

[2] Note that due to the difference in definitions of $r_n(p_{\mathrm{T}}^a, p_{\mathrm{T}}^b)$ and $r_n(\eta^a, \eta^b)$, see equations (4.17) and (5.10), constraints (4.15) and (4.16) do not hold for the latter observable. Hence, $r_n(\eta^a, \eta^b)$ does not offer a test of *all* hydrodynamical models applicability to HIC, see Section 4.3.1, and the analysis needs to be performed on a case to case basis.

can be represented in the following mathematically equivalent way:

$$V_{n\Delta}(\eta^a,\eta^b)=\left\langle\langle e^{in(\phi^a-\phi^b)}\rangle\right\rangle=\left\langle\langle e^{in(\psi_n(\eta^a)+\delta\psi(\eta^a)-\psi_n(\eta^b)-\delta\psi(\eta^b))}\rangle\right\rangle, \tag{5.16}$$

where we separate the flow angle dependence on pseudorapidity into the event plane, $\psi_n(\eta)$, and the fluctuations, $\delta\psi_n(\eta)$, parts. The former one describes collective motion of matter, which corresponds to the long-range structure of the two-particle correlation. The latter is dominated by the short-range non-flow effects, such as jets. Thus, one expects that event-to-event correlator

$$\langle\delta\psi(\eta^a)\delta\psi(\eta^b)\rangle\simeq 0, \tag{5.17}$$

as particles in bins η^a and η^b are separated by a substantial distance in longitudinal direction. Equation (5.16) can be rewritten in the following way:

$$V_{n\Delta}(\eta^a,\eta^b)=\underbrace{\left\langle e^{in(\psi_n(\eta^a)-\psi_n(\eta^b))}\right\rangle}_{\text{long-range}}\underbrace{\left\langle\langle e^{in(\delta\psi(\eta^a)-\delta\psi(\eta^b))}\rangle\right\rangle}_{\text{short-range}}, \tag{5.18}$$

which explicitly manifests factorization of the long- and short-range contributions to the two-particle correlation function in pseudorapidity.

Representation of the two-particle correlation in the form of equation (5.18) elucidates why contribution of short-range fluctuations is considerably suppressed to the defined by equation (5.10) $r_n(\eta^a,\eta^b)$ observable. Indeed, if one applies approximation (5.17) to equation (5.18), one will notice that non-flow contributions to equation (5.10) approximately cancel out:

$$r_n(\eta^a,\eta^b)\simeq\frac{\left\langle e^{in(\psi_n(-\eta^a)-\psi_n(\eta^b))}\right\rangle}{\left\langle e^{in(\psi_n(\eta^a)-\psi_n(\eta^b))}\right\rangle}\simeq\frac{\langle\cos[n(\psi_n(-\eta^a)-\psi_n(\eta^b))]\rangle}{\langle\cos[n(\psi_n(\eta^a)-\psi_n(\eta^b))]\rangle}. \tag{5.19}$$

Taking into account that bin a is located in the vicinity of the origin, one can linearly expand flow angle, $\psi_n(\eta^a)$, dependence on pseudorapidity, η^a:

$$\psi_n(\pm\eta^a)\simeq\psi_n(0)\pm\frac{d\psi_n}{d\eta}(0)\eta^a. \tag{5.20}$$

Substituting this result into equation (5.19), one gets:

$$r_n(\eta^a,\eta^b)\simeq\frac{\langle\cos[n(\psi_n(0)-\psi_n(\eta^b))]-n\sin[n(\psi_n(0)-\psi_n(\eta^b))]\frac{d\psi_n}{d\eta}(0)\eta^a\rangle}{\langle\cos[n(\psi_n(0)-\psi_n(\eta^b))]+n\sin[n(\psi_n(0)-\psi_n(\eta^b))]\frac{d\psi_n}{d\eta}(0)\eta^a\rangle}. \tag{5.21}$$

Expanding equation (5.21) further, one arrives at the final result:

$$r_n(\eta^a, \eta^b) \simeq 1 - 2n^2 \langle (\psi_n(0) - \psi_n(\eta^b))) \frac{d\psi_n}{d\eta}(0) \rangle \eta_a, \tag{5.22}$$

which suggests that at small values of pseudorapidity deviation of the $r_n(\eta^a, \eta^b)$ observable from unity should depend linearly on η^a. We will test the validity of this qualitative conclusion quantitatively in our hydrodynamic model in Section 5.2.4.

5.2.3 Model of long-range longitudinal fluctuations

From the experimentally measured dependence of the $r_n(\eta^a, \eta^b)$ observable on pseudorapidity one aims to get an estimate of the extent to which quantum fluctuations alternate initial conditions longitudinal structure. This expectation is based on the assumption of the linear hydro response, which holds for the second and third flow harmonics on average around mid-rapidity, see Section 3.3. To verify this approximation rigorously, one needs to perform a full hydrodynamic calculation of the $r_n(\eta^a, \eta^b)$ observable, which we do in Section 5.2.4. However, we will start using this intuition immediately when discussing initial conditions models.

In Section 3.1 we specified the initial conditions profile of individual nucleons in longitudinal direction, see equation (3.2), which allows to reasonably model the particle yield asymmetry in small systems, see Fig. 3.1. This prescription was motivated by the observation that relativistic particles should preferably emit in the direction of their motion [299]. This asymmetry of matter deposition leads to event-by-event fluctuations of the initial longitudinal profile, which are further enhanced by folding with the NBD distribution, see equation (3.3) and specifically note prefactor s_i. However, it was shown that all these contributions are not able to reproduce the magnitude of the experimentally measured $r_n(\eta^a, \eta^b)$ observable in small systems, if one is to estimate it based on the initial conditions longitudinal profile anisotropy [296].

It was suggested to introduce an additional source of fluctuations by alternating event-to-event the end-points of the matter deposition profile of individual nucleons [300, 301]. Yet on average one still aims to reproduce the prescription specified by equation (3.2), as it proved to work well in describing small systems. This is possible

if one uses the following "step" function profile with variable η_i uniformly distributed in the $[-y_{\rm beam}, y_{\rm beam}]$ segment, see Fig. 5.12:

$$\rho^i_{L\pm}(\eta_s) \equiv 2\theta\left[\pm(\eta_i - \eta)\right] \exp\left[-\frac{\left(|\eta_s| - \eta_0\right)^2}{2\sigma^2_\eta}\theta\left(|\eta_s| - \eta_0\right)\right], \tag{5.23}$$

where $\theta(x)$ is the "step" function, which equals unity if its argument is greater than zero and evaluates to zero otherwise.

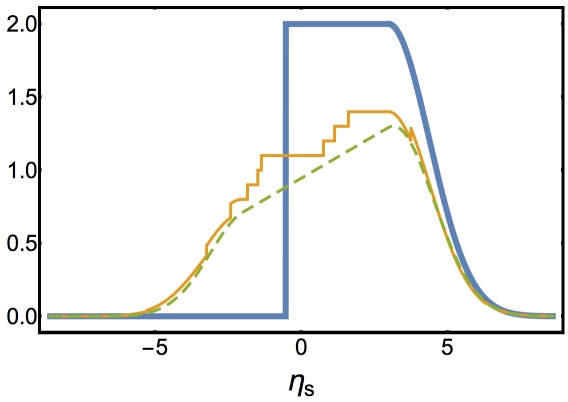

Figure 5.12: Illustration of the used in our model prescriptions describing longitudinal dependence of the matter density deposition in the initial conditions. Thick line corresponds to the contribution of an individual nucleon moving in the direction of the lead nucleus, $\rho^i_{L+}(\eta_s)$. In this case the value of η_i was chosen to be equal to one. Thin line corresponds to a randomly generated average profile, $\frac{1}{N}\sum_{i=1}^{N}\rho^i_{L+}(\eta_s)$. We used $N = 20$ as it represents a typical number of sources in a high multiplicity p-Pb event. Dashed line corresponds to a profile averaged over an infinite number of sources, N. As expected, it coincides with distribution $\rho_L(\eta_s)$, see equation (3.2).

The total initial entropy density distribution is then given by a formula similar to equation (3.3):

$$s(\mathbf{x}_{\rm T}, \eta_s, \tau = \tau_0) = \sum_{i=1}^{N_{\rm part}} s_i \; \rho_\perp(\mathbf{x}_{\rm T} - \mathbf{x}^i_{\rm T}) \; \rho^i_{L\pm}(\eta_s). \tag{5.24}$$

However, the difference introduced by the additional fluctuations of the longitudinal profile, $\rho^i_{L\pm}$, requires re-tuning of the NBD parameters. We used $\lambda = 5.5$ and $\kappa = 2.0$, which provide a good fit of the model to the CMS multiplicity data, see Fig. 5.13.

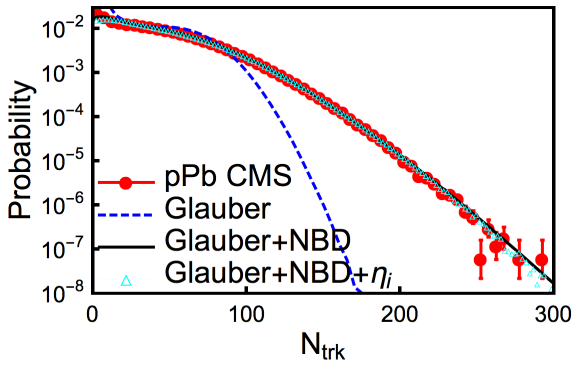

Figure 5.13: Distribution of (uncorrected) multiplicity N_{trk} at $|\eta| < 2.4$ and $p_T > 0.4$ GeV in p-Pb events from the CMS Collaboration [222] compared to the entropy distribution implied by a basic MC-Glauber model (with a fixed entropy per participant) that was discussed in Section 2.2.2 (Glauber), the model supplemented with additional negative binomial fluctuations of individual nucleon sources (Glauber + NBD) and described by equation (3.3), and the model with negative binomial fluctuations and uniformly distributed fluctuations of the longitudinal profile endpoints (Glauber + NBD + η_i) that is based on equation (5.24).

Before discussing the results of our model's calculations, we will for the reasons of completeness list the other initial conditions frameworks that were used in the studies of rapidity fluctuations [302, 303, 304, 305, 306, 274, 307]. All of them implicitly use the idea of MC-Glauber sampling in the transverse plane, but have various prescriptions for the longitudinal profiles. Those are either heuristically defined or use various (mostly kinetic) models such as AMPT, EPOS, HIJING, LEXUS, PYTHIA, UrQMD that can describe particle evolution and thus provide insights into the longitudinal matter distribution, but were not initially developed for the treatment of collective effects and thus are out of scope of this work. We also note that none of the aforementioned studies provided a hydrodynamic calculation of the $r_n(\eta^a, \eta^b)$ observables in small systems, which we do in the next section.

5.2.4 Comparison to experiment

We start the comparison of our model results to experimental data with the $r_n(\eta^a, \eta^b)$ observable, see Fig. 5.14. One can observe that the initial version of our model de-

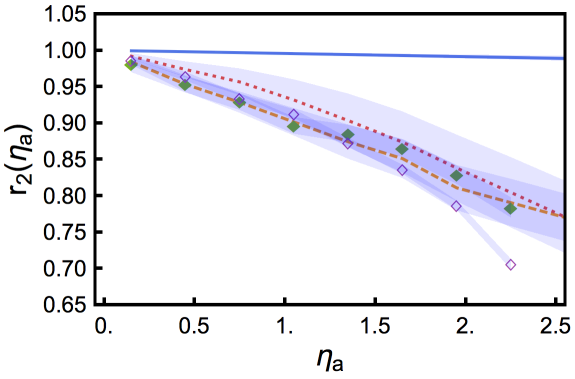

Figure 5.14: Effect of longitudinal fluctuations and bulk viscosity on the $r_n(\eta^a, \eta^b)$ observable defined by equation (5.10). Empty diamonds correspond to the experimental measurement of $r_n(\eta^a, \eta^b)$, which considers particles to pertain to bin b if their pseudorapidities satisfy the condition $3.0 < |\eta^b| < 4.0$. Full diamonds represent the measurement of the same observable, but defined using another constraint: particles in bin b have pseudorapidities in the range $4.4 < |\eta^b| < 5.0$. This should make the latter measurement a more appropriate quantity for a one-to-one comparison with a result obtained in hydrodynamic modeling, see equation (5.11) and Section 5.2.2 for details, which is why we calculate $r_n(\eta^a, \eta^b)$ in our model using the latter pseudorapidity range for bin b. However, we note that both definitions of the b bin pseudorapidity range provide similar results of the experimentally measured $r_n(\eta^a, \eta^b)$ observable. The solid line corresponds to the calculation based on our model of initial conditions described in Section 3.1, see equation (3.3). The dotted line illustrates the results obtained with the model discussed in Section 5.2.3, which has an additional mechanism of generating longitudinal fluctuations, see equation (5.24). In this (dotted line) computation we use zero bulk viscosity. The dashed line shows calculation performed using the latter model (with additional longitudinal fluctuations) and non-trivial "plateau" bulk profile illustrated in Fig. 5.5 with the dashed line.

scribed in Section 3.1, with the initial conditions specified by equation (3.3), has almost no torque effect. The value of the $r_n(\eta^a, \eta^b)$ observable evaluates almost identically to one in the entire pseudorapidity range, $0 < \eta^a < 2.4$. However, the final version of our model described in Section 5.2.3, with the initial conditions specified by equation (5.24) and the "plateau" scenario of the bulk profile, provides a reasonable agreement with experimental data. We also observe a nearly linear dependence of $r_n(\eta^a, \eta^b)$ calculated in our model on pseudorapidity, η^a, which quantitatively confirms the validity of the result discussed in 5.2.2. Finally, we check that although bulk viscosity modifies the value of the effective pressure in QGP medium, it does not affect the results of our calculation for the $r_n(\eta^a, \eta^b)$ observable.

Having confirmed that the final version of our model with additional longitudinal fluctuations and non-trivial bulk viscosity reasonably captures experimental trends of longitudinal dynamics is small collision systems, we turn to the transverse observables. In Fig. 5.15, we compare $\langle p_{\mathrm{T}} \rangle$, $\bar{v}_n\{2\}$, $v_n\{2\}(p_{\mathrm{T}})$, $r_n(p_{\mathrm{T}}^a, p_{\mathrm{T}}^b)$ observables obtained using our model of the initial conditions described in Section 3.1 (it includes shear viscosity, $\eta/s = 0.08$), its extended version discussed in Section 5.2.3 (with additionally added longitudinal fluctuations and bulk viscosity following the "plateau" temperature dependent scenario, $\zeta/s \sim 0.03$), and CMS experimental data [143].

We observe that our extended version of the model has even better agreement with the data: specifically, it provides the same quality description of flow observables, but (due to bulk viscosity) allows to also reasonably reproduce experimental results on the average transverse momentum of identified particles. The agreement holds in a wide $0 - 30\%$ centrality region, see Table 3.1, and gets violated only at lower multiplicities, where one does not expect hydrodynamics to be applicable, see Section 4.3.4. One can see that elliptical integrated and differential flow coefficients agree with the data within errorbars. Triangular flow is systematically overestimated, which signifies that the transverse fluctuations prescription of the initial conditions should be improved. This is not surprising as our model considers fluctuations at the nucleon level. Realistic CGC treatment of subnucleonic effects in the spirit of IP-Glasma is

required. We expect that the agreement with the data in small systems will improve once the glasma three-dimensional models of initial conditions become available.

Noticeably, we did not need to modify any parameters of the model ($\eta/s = 0.08$, $\sigma = 0.4\,\mathrm{fm}$) that we initially used for making our prediction of $r_n(p_{\mathrm{T}}^a, p_{\mathrm{T}}^b)$. Addition of a "plateau"-like bulk profile and longitudinal fluctuations within errorbars does not modify the results of the calculation of the transverse observables and thus does not affect their agreement with the data. Specifically, the extended model results agree with the $r_n(p_{\mathrm{T}}^a, p_{\mathrm{T}}^b)$ experimental measurements within errorbars. This is an important and non-trivial result, because it confirms that our prediction remains valid after the extension and our conclusion of $r_n(p_{\mathrm{T}}^a, p_{\mathrm{T}}^b)$ being a convenient probe of the initial conditions transverse granularity is further verified[1].

We summarize the results of the comparison with an overall observation that our extended hydro model at least qualitatively captures experimental trends of both longitudinal and transverse observables. Thus, hydrodynamics is a plausible explanation of the dynamics taking place in small colliding systems and alternative models have to provide at least equally good agreement with a wide range of the studied experimental observables to question this statement.

[1] We note that the characteristic scale of transverse fluctuations could not be accurately estimated from the average transverse momentum of identified hadrons, because bulk viscosity contributes to its value.

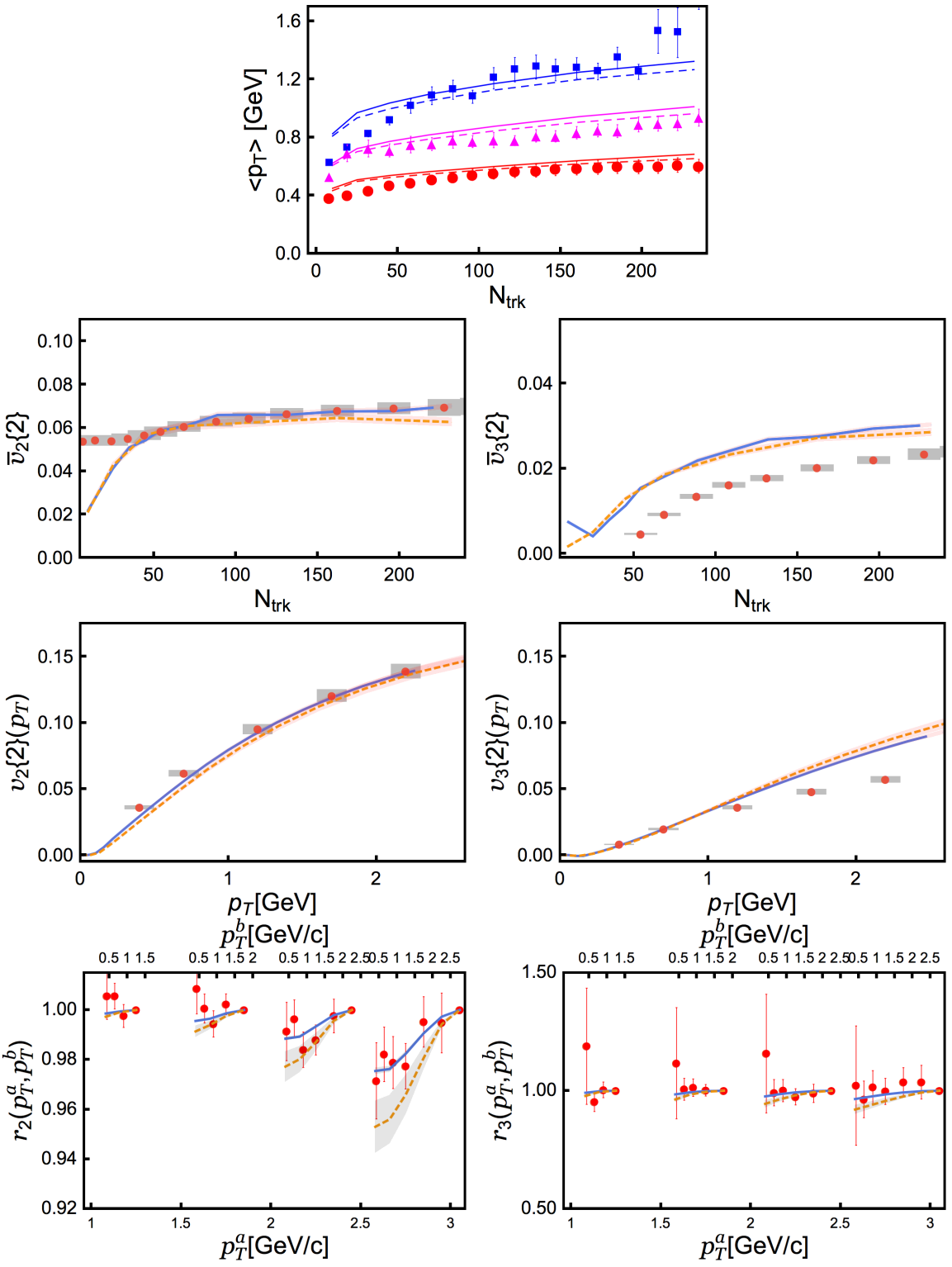

Figure 5.15: Comparison of the models described in Sections 3.1 (solid line), 5.2.3 (dashed line) and experimental data.

6

Conclusion

This work was completed during the time of a paradigm shift. Initially, small collision systems, as opposite to large ones, were considered as a reference lacking collective effects [97]. But later, evidences of flow in hadron collisions were observed ubiquitously across systems of all sizes [140, 308]. One of the possible explanations of this phenomenon is the transition of hadronic matter to the QGP state. In this work, we aimed to explore this hypothesis by performing a hydrodynamic calculations of p-Pb and Pb-Pb collisions at top LHC energy.

We proposed a robust fluid dynamics framework [139] that included all the latest developments utilized at the time when the first high multiplicity p-Pb data was published [222] for describing A-A collisions and that was able to account for the specific to p-A systems phenomena. Specifically, our approach treats hadron collisions event-to-event, which allows to describe initial conditions quantum fluctuations at nucleonic level consistently across systems of various sizes and energies, see Fig. 3.3. Importantly, this enables us to accurately describe the high multiplicity tail of the experimental p-Pb multiplicity distribution, which is important, because only in this range small systems demonstrate signatures of collective behavior, see Fig. 3.2 and Table 3.1. Our framework incorporates the possibility to describe the characteristic longitudinal anisotropy of p-Pb collisions (see Fig. 3.1) through the entire evolution due to the utilization of the 3+1D hydrodynamics equations solver MUSIC [214]. This package is based on the Kurganov-Tadmor algorithm [213], which allows to accurately treat propagation of matter density discontinuities that are expected to be substantial in small collision systems. It also fully incorporates the possibility to describe viscous

effects that proved to be important in the description of large systems, See. (2.38), (2.39), (2.59), and [309, 106, 310].

Our work of testing the applicability of hydrodynamics to the description of small collision systems is of an exploratory nature. There is still a number of theoretical challenges even in the case of large A-A collisions, where the QGP paradigm is now widely accepted [255]. Specifically, the 3D modeling of sub-nucleonic degrees of freedom in the initial conditions, the exact mechanism of thermalization, the first principle QCD calculation of the fluid dynamics transport coefficients and of the viscous correction to the particle distribution function are among the topics that require further clarification before it is possible to claim that the processes taking place in HIC are fully understood and their modeling is performed accurately. For that reason, we use a robust framework that includes all relevant well-understood effects of collision systems and explore its parameter space to assess the overall phenomenological capabilities of hydrodynamics.

We started our study with performing the conventional analysis of flow observables ($v_2\{2\}, v_3\{2\}, v_2\{4\}$) that strongly contributed to the establishment of the QGP paradigm in large systems [102]. We compared the results obtained using our fluid dynamics framework [139] to the available at the time p-Pb data [222] and studied the parameter space of the model. We focused mainly on the two parameters that were considered to be specifically important in the description of the observed final particle anisotropy in large systems: σ, which is the granularity of the initial conditions transverse fluctuations, and η/s, which is the ratio of shear viscosity to entropy density. Bulk viscosity was not considered in our calculation at that point based on the expectation that similarly to large systems [282] its effect on flow will be subdominant compared that of shear.

Result of the comparison presented in Chapter 3 showed that hydrodynamics can at least qualitatively describe experimental data trends in small systems. We observed that the values of the model's parameters $\sigma = 0.4\,\text{fm}$ and $\eta/s = 0.08$ work reasonably well. They perfectly fit the high multiplicity elliptic flow data, but some-

what systematically overestimate its triangular component. This result may suggest the inclusion of sub-nucleonic fluctuations which are expected to affect primarily the triangular flow component. Moreover, the temperature dependence of η/s is still not known with any degree of precision, while our studies show that shear viscosity affects the results of the triangular flow component calculation to a larger extent than those of the elliptic one. Finally, the exact prescription for the viscous correction that also greatly influences particles' final anisotropy is also not available at the moment. All the aforementioned effects introduce systematic uncertainties and define the precision that one could expect from a hydrodynamic model of hadron collisions. This is one of the main reasons that in this work, we are focused on exploring the overall capabilities of the fluid dynamics paradigm. The fact that our calculation's triangular flow multiplicity profile reproduces the shape of the experimental data one suggests that our framework captures the relevant small systems' phenomena.

In Chapter 3, we also showed that our model can explain hydrodynamically the striking similarity in triangular flow between p-Pb and Pb-Pb events with the same multiplicity, see left panel of Fig. 3.6 and [222]. This is a non-trivial result, because one expects small and large systems to have different eccentricities. We confirm this expectation in our calculations, see Fig. 3.14, and explore the difference between the systems characteristics. Specifically, we observe that the wounded nucleon number and the transverse size of the systems has different dependence on multiplicity in the p-Pb and Pb-P collisions. We conclude that the general dependence on system size is not a trivial matter. A proper hydrodynamic calculation should be performed in order to evaluate the interplay of the competing contributions of the system's size (initial pressure gradients) and viscous (energy dissipation and thus evolution time) effects on the magnitude of particle flow.

Additionally, in Chapter 3, we presented a prediction of the multiplicity dependence of the $v_3\{4\}$ flow component in p-Pb collisions at 5.02 TeV, see right panel of Fig. 3.7. We note that its non-zero value is an even more convincing evidence (compared to the same result for $v_2\{2\}$ and $v_3\{2\}$) of collectivity in the system, be-

cause the observable is defined based on the multi-particle correlator. If confirmed, this finding will serve a further non-trivial confirmation of QGP formation in small systems and will put additional constraints on alternative explanations.

In Chapter 4, we discussed how signatures of collective behavior could be observed using the the entire dataset of the two-particle correlation matrix. This approach provides a considerably stricter test on the applicability of hydrodynamics to describing the hadron collisions dynamics compared to the conventional flow analysis that we performed in Chapter 3. First, $v_n\{2\}$ and $\bar{v}_n\{2\}$ coefficients represent averaging over groups of the two-particle correlation matrix elements, which means that the conventional analysis is less restrictive than the comparison of the model's calculation results to the entire matrix. Second, it was shown on the example of large collision systems [141] that if the comparison of the hydrodynamics results to the two-particle correlation matrix is performed in terms of the $r_n(p_{\mathrm{T}}^a, p_{\mathrm{T}}^b)$ variable, one can obtain general restrictions on the applicability of the fluid dynamics regardless of its specific implementation. That is the reason that we suggested to measure the $r_n(p_{\mathrm{T}}^a, p_{\mathrm{T}}^b)$ observable in small systems and made a *prediction* of its dependence on multiplicity that was later *confirmed* by CMS collaboration, see Fig. 4.7 and [143]. This fact indicates that our framework is applicable for the at least qualitative description of small colliding systems and that hydrodynamics is a plausible explanation of the collective effects in p-Pb collisions in the region of high multiplicity ($N_{\mathrm{trk}} > 150$ or $0\% - 2\%$ centrality) and low transverse momentum ($p_{\mathrm{T}} < 2.5\,\mathrm{GeV}$).

Our studies of the parameter dependence of the $r_n(p_{\mathrm{T}}^a, p_{\mathrm{T}}^b)$ observable clarified the previous studies made for the case of large colliding systems. We found out that $r_n(p_{\mathrm{T}}^a, p_{\mathrm{T}}^b)$ is more sensitive to the granularity of the initial conditions than the viscosity used during the hydrodynamical expansion of the system. This makes it a promising probe for studying the initial conditions in hadron collisions at least compared to the other conventionally used observables. This finding and the agreement of our *prediction* for $r_n(p_{\mathrm{T}}^a, p_{\mathrm{T}}^b)$ with experimental data suggests that the transverse size of longitudinal fluctuations should be in the ballpark of $\sigma = 0.4\,\mathrm{fm}$, which agrees

with other studies [131, 236, 200].

Finally, in Chapter 4, we study the final state effects contribution to flow observables using UrQMD [171]. We find out that they have moderate effect on the transverse flow observables, which we conclude is the result of the considerably low final multiplicity in p-Pb systems. Overall, the UrQMD afterburner improves the agreement of our model with the $r_n(p_{\mathrm{T}}^a, p_{\mathrm{T}}^b)$ experimental measurements and supports the conjecture of the fluid dynamics applicability to the description of high multiplicity events in small systems.

In Chapter 5, we address the recent findings of the importance of bulk viscosity for the accurate description of the transverse particle momentum in large systems [144] and the new experimental data on the longitudinal fluctuations in p-Pb collisions that are described with the $r_n(\eta^a, \eta^b)$ observable [143]. For that reason we explain how we extend the model to account for the appropriate effects and then perform a hydrodynamical calculation trying several different prescriptions for the bulk temperature dependence. We find out that the small magnitude of the used bulk profile ($\zeta/s \sim 0.03$, "plateau" scenario, dashed line in Fig. 5.5) is favorable for the description of the transverse momentum observables. Thus, similarly to the case of large systems [144] we conclude that bulk viscosity plays an important role in describing final particles' velocities. We also observe similar effect of bulk viscosity on differential flow observables $v_n\{2\}(p_{\mathrm{T}})$: they get slightly suppressed in the low and slightly enhanced in the high transverse momentum regions. However, unlike in [144], the inclusion of bulk viscosity into the model does not require us to alter the value of the shear counterpart, because the magnitude of the bulk profile that we use is considerably smaller (it is in line with the results of the calculations presented in [200]). Interestingly, the consideration in the model of both bulk or longitudinal fluctuations effects does not require us to alter any of the previously used parameters: the results of our flow calculations and predictions remain the same within errorbars, and our conclusions on the role of the $r_n(p_{\mathrm{T}}^a, p_{\mathrm{T}}^b)$ observable as a probe of initial conditions stays valid. Moreover, our model can now capture experimental trends of $< p_{\mathrm{T}} >$

and $r_n(\eta^a, \eta^b)$ observables, see Fig. 5.15.

The, although qualitative, simultaneous description of such a large number of experimental observables, including the confirmed prediction of the model for $r_n(p_{\mathrm{T}}^a, p_{\mathrm{T}}^b)$, makes a strong case towards the plausibility of QGP formation in high multiplicity small collision systems. It is even further reinforced by the observation that the obtained in this work estimates of the model's parameters – $\sigma = 0.4\,\mathrm{fm}$, $\eta/s = 0.08$, $\zeta/s \sim 0.03$ – are in line with the later performed detailed studies of the properties of QGP from large systems experiments [311], which suggests that the same type of matter is being created in hadron collisions of all sizes. Of course, despite these convincing results, much further work is required to clarify that one accurately understands the mechanisms taking place in hadron collisions. All of the mentioned above theoretical challenges of fluid dynamics applicability to the description of hadron collisions should be addressed. We see the following two directions for future research: phenomenological and oriented towards first principles. The former could proceed with the approach applied in [182]. It is clear that sub-nucleonic fluctuations are substantial in the description of small systems [182, 312, 181]. One could come up with an extension of the TRENTO model to include them and tune the parameters of this phenomenological model to experimental data. Moreover, there is a suggestion [313] that one would not be able to differentiate between the specific implementations of the sub-nucleonic fluctuations as they will quickly smooth out by viscous effects, which actually supports the generality of the conclusions obtained in this work and provides an explanation on why we were able to obtain a reasonable estimate of the transverse granularity that agrees with the results of other studies. However, the extraction of such effective model parameters in practice will merely indirectly advances us towards the understanding of the physical mechanisms taking place in hadron collisions. That is the reason why we find to be more promising the approaches that are oriented towards the first principles modeling of initial conditions, such as 3+1D IP-Glasma [314]. We expect these studies to shed light upon the theoretical origin of the applied in this work phenomenological approach to the description of

longitudinal fluctuations[1]. Similarly, theoretical calculations of bulk viscosity, such as [276], have the potential to elucidate what transport coefficients' profiles should be used in hydrodynamic calculations. Finally, we want to highlight that other barely studied theoretical effects, such as thermal fluctuations [315, 316] should be carefully considered before one states that the mechanism of QGP formation in small systems is entirely understood. We conclude by making an observation that theoretical, phenomenological, and experimental approaches proved to work specifically successful when applied simultaneously and collaboratively. We hope that it will continue to be the case in the future so that our understanding of the surrounding Universe progresses at a fast pace.

[1] After this conclusion was written, but before this work was submitted, the results of the following study were made publicly available [291]. Those explore the possibility of simultaneous description of small and large system with an extended TRENTO model (although still 2+1D) that includes parametric prescription for sub-nucleonic degrees of freedom. First, they are consistent with our model's estimates for the parameter values of σ, η/s, ζ/s. Second, they observe $\sim 10-15\%$ tension describing v_n flow observables in 5.02 TeV p-Pb. This is in line with our results. It also further supports our proposal that one needs to focus on developing a first principle model of initial conditions, because a parametric framework only indirectly suggests what physical phenomena should be taken into account in future calculations. Finally, this extensive parameter space exploration study agrees with the main conclusion of this work on the plausibility of the description of high multiplicity hadron collisions within the hydrodynamic paradigm.

Bibliography

[1] Wikipedia, "Science", https://en.wikipedia.org/wiki/Science.

[2] Wikipedia, "Standard Model", https://en.wikipedia.org/wiki/Standard_Model.

[3] E. D. Bloom *et al.*, Phys. Rev. Lett. **23**, 930 (1969). doi:10.1103/PhysRevLett.23.930

[4] M. Breidenbach *et al.*, Phys. Rev. Lett. **23**, 935 (1969). doi:10.1103/PhysRevLett.23.935

[5] F. Abe *et al.* [CDF Collaboration], Phys. Rev. Lett. **74**, 2626 (1995) doi:10.1103/PhysRevLett.74.2626 [hep-ex/9503002].

[6] S. Abachi *et al.* [D0 Collaboration], Phys. Rev. Lett. **74**, 2422 (1995) doi:10.1103/PhysRevLett.74.2422 [hep-ex/9411001].

[7] K. Kodama *et al.* [DONUT Collaboration], Phys. Lett. B **504**, 218 (2001) doi:10.1016/S0370-2693(01)00307-0 [hep-ex/0012035].

[8] Biever, C., "New Scientist", https://www.newscientist.com/article/dn22029-its-a-boson-but-we-need-to-know-if-its-the-higgs

[9] Y. Fukuda *et al.* [Super-Kamiokande Collaboration], Phys. Rev. Lett. **81**, 1562 (1998) doi:10.1103/PhysRevLett.81.1562 [hep-ex/9807003].

[10] Q. R. Ahmad *et al.* [SNO Collaboration], Phys. Rev. Lett. **89**, 011301 (2002) doi:10.1103/PhysRevLett.89.011301 [nucl-ex/0204008].

[11] B. P. Abbott *et al.* [LIGO Scientific and Virgo Collaborations], Phys. Rev. Lett. **116**, no. 6, 061102 (2016) doi:10.1103/PhysRevLett.116.061102 [arXiv:1602.03837 [gr-qc]].

[12] NASA Science: Astrophysics, "Dark Energy Dark Matter", `https://science.nasa.gov/astrophysics/focus-areas/what-is-dark-energy`.

[13] N. N. Bogoliubov and O. S. Parasiuk, Acta Math. **97**, 227 (1957). doi:10.1007/BF02392399

[14] S. Weinberg, Phys. Rev. **118**, 838 (1960). doi:10.1103/PhysRev.118.838

[15] M. Planck, 479 (1899).

[16] S. Dimopoulos and H. Georgi, Nucl. Phys. B **193**, 150 (1981). doi:10.1016/0550-3213(81)90522-8

[17] D. J. Gross and F. Wilczek, Phys. Rev. Lett. **30**, 1343 (1973). doi:10.1103/PhysRevLett.30.1343

[18] H. D. Politzer, Phys. Rev. Lett. **30**, 1346 (1973). doi:10.1103/PhysRevLett.30.1346

[19] R. P. Feynman, Phys. Rev. **76**, 749 (1949). doi:10.1103/PhysRev.76.749

[20] M. Botje, Lecture notes Particle Physics II, Nikhef (2013).

[21] L. D. Landau and E. M. Lifshitz, Course of Theoretical Physics Volume 3, "Quantum Mechanics: Non-Relativistic Theory", Pergamon Press (1965).

[22] V. B. Berestetskii, E. M. Lifshitz, L. P. Pitaevskii, Course of Theoretical Physics Volume 4, "Relativistic Quantum Theory", Pergamon Press (1982).

[23] J. A. Wheeler, Phys. Rev. **52**, 1107 (1937). doi:10.1103/PhysRev.52.1107

[24] W. Heisenberg, Z. Physik **120**, 513 (1943). doi.org/10.1007/BF01329800

[25] R. P. Feynman, Rev. Mod. Phys. **20**, 367 (1948). doi:10.1103/RevModPhys.20.367

[26] M. Gell-Mann and F. E. Low, Phys. Rev. **95**, 1300 (1954). doi:10.1103/PhysRev.95.1300

[27] A. Anastasi *et al.* [KLOE-2 Collaboration], Phys. Lett. B **767**, 485 (2017) doi:10.1016/j.physletb.2016.12.016 [arXiv:1609.06631 [hep-ex]], `http://w3.lnf.infn.it/the-variable-constant/`.

[28] M. Czakon, Nucl. Phys. B **710**, 485 (2005) doi:10.1016/j.nuclphysb.2005.01.012 [hep-ph/0411261].

[29] L. Landau, "Niels Bohr and the Development of Physics", ed W. Pauli, Pergamon Press, London (1955).

[30] C. G. Callan, Jr., Phys. Rev. D **2**, 1541 (1970). doi:10.1103/PhysRevD.2.1541

[31] K. Symanzik, Commun. Math. Phys. **18**, 227 (1970). doi:10.1007/BF01649434

[32] A. M. Polyakov, Phys. Lett. **103B**, 207 (1981). doi:10.1016/0370-2693(81)90743-7

[33] S. R. Coleman and E. J. Weinberg, Phys. Rev. D **7**, 1888 (1973). doi:10.1103/PhysRevD.7.1888

[34] C. Patrignani et al. (Particle Data Group), Chin. Phys. C, 40, 100001 (2016).

[35] R. Gupta, hep-lat/9807028.

[36] T. Ludlam *et al.* [BRAHMS and STAR and PHOBOS and PHENIX Collaborations], doi:10.2172/15015225

[37] K. G. Wilson, Phys. Rev. D **10**, 2445 (1974). doi:10.1103/PhysRevD.10.2445

[38] G. C. Wick, Phys. Rev. **96**, 1124 (1954). doi:10.1103/PhysRev.96.1124

[39] A. Bazavov *et al.*, Phys. Rev. D **80**, 014504 (2009) doi:10.1103/PhysRevD.80.014504 [arXiv:0903.4379 [hep-lat]].

[40] R. Sommer, F. Tekin and U. Wolff, PoS LATTICE **2010**, 241 (2010) [arXiv:1011.2332 [hep-lat]].

[41] S. Aoki *et al.* [PACS-CS Collaboration], Phys. Rev. D **79**, 034503 (2009) doi:10.1103/PhysRevD.79.034503 [arXiv:0807.1661 [hep-lat]].

[42] C. Amsler *et al.* [Particle Data Group], Phys. Lett. B **667**, 1 (2008). doi:10.1016/j.physletb.2008.07.018

[43] Z. Fodor and C. Hoelbling, Rev. Mod. Phys. **84**, 449 (2012) doi:10.1103/RevModPhys.84.449 [arXiv:1203.4789 [hep-lat]].

[44] M. Luscher, Nucl. Phys. B **364**, 237 (1991). doi:10.1016/0550-3213(91)90584-K

[45] F. Karsch and H.W. Wyld, Phys. Rev. D **35**, 2518 (1987).

[46] S. Huang, Phys. Rev. D **47**, 653 (1993).

[47] A. Nakamura and S. Sakai, Phys. Rev. Lett. **94**, 072305 (2005).

[48] H. B. Meyer, Phys. Rev. Lett. **100**, 162001 (2008) doi:10.1103/PhysRevLett.100.162001 [arXiv:0710.3717 [hep-lat]].

[49] F. Karsch, D. Kharzeev and K. Tuchin, Phys. Lett. B **663**, 217 (2008) doi:10.1016/j.physletb.2008.01.080 [arXiv:0711.0914 [hep-ph]].

[50] J. M. Maldacena, Int. J. Theor. Phys. **38**, 1113 (1999) [Adv. Theor. Math. Phys. **2**, 231 (1998)] doi:10.1023/A:1026654312961 [hep-th/9711200].

[51] G. Policastro, D. T. Son and A. O. Starinets, Phys. Rev. Lett. **87**, 081601 (2001) doi:10.1103/PhysRevLett.87.081601 [hep-th/0104066].

[52] S. S. Gubser, I. R. Klebanov and A. M. Polyakov, Phys. Lett. B **428**, 105 (1998) doi:10.1016/S0370-2693(98)00377-3 [hep-th/9802109].

[53] E. Witten, Adv. Theor. Math. Phys. **2**, 253 (1998) [hep-th/9802150].

[54] A. Karch and E. Katz, JHEP **0206**, 043 (2002) doi:10.1088/1126-6708/2002/06/043 [hep-th/0205236].

[55] J. Polchinski and M. J. Strassler, Phys. Rev. Lett. **88**, 031601 (2002) doi:10.1103/PhysRevLett.88.031601 [hep-th/0109174].

[56] J. Polchinski and M. J. Strassler, hep-th/0003136.

[57] T. Sakai and S. Sugimoto, Prog. Theor. Phys. **113**, 843 (2005) doi:10.1143/PTP.113.843 [hep-th/0412141].

[58] A. Buchel, Nucl. Phys. B **802**, 281 (2008) doi:10.1016/j.nuclphysb.2008.03.009 [arXiv:0801.4421 [hep-th]].

[59] P. Benincasa, A. Buchel and A. O. Starinets, Nucl. Phys. B **733**, 160 (2006) doi:10.1016/j.nuclphysb.2005.11.005 [hep-th/0507026].

[60] A. Buchel, Phys. Rev. D **72**, 106002 (2005) doi:10.1103/PhysRevD.72.106002 [hep-th/0509083].

[61] A. Buchel, Phys. Lett. B **663**, 286 (2008) doi:10.1016/j.physletb.2008.03.069 [arXiv:0708.3459 [hep-th]].

[62] S. S. Gubser, A. Nellore, S. S. Pufu and F. D. Rocha, Phys. Rev. Lett. **101**, 131601 (2008) doi:10.1103/PhysRevLett.101.131601 [arXiv:0804.1950 [hep-th]].

[63] S. S. Gubser, S. S. Pufu and F. D. Rocha, JHEP **0808**, 085 (2008) doi:10.1088/1126-6708/2008/08/085 [arXiv:0806.0407 [hep-th]].

[64] L. D. Landau and E. M. Lifshitz, Course of Theoretical Physics Volume 6, "Fluid Mechanics", Butterworth-Heinemann (1987).

[65] S. Chapman and T. G. Cowling, "The mathematical theory of non-uniform gases", Cambridge University Press (1970).

[66] S. R. de:Groot, W. A. van Leeuwen and C. G. van Weert, "Relativistic kinetic theory : principles and applications", Elsevier North-Holland (1980).

[67] W. A. Hiscock and L. Lindblom, Phys. Rev. D **31**, 725 (1985). doi:10.1103/PhysRevD.31.725

[68] P. Kostadt and M. Liu, Phys. Rev. D **62**, 023003 (2000). doi:10.1103/PhysRevD.62.023003

[69] I. Muller, Z. Phys. **198**, 329 (1967). doi:10.1007/BF01326412

[70] W. Israel, Annals Phys. **100**, 310 (1976). doi:10.1016/0003-4916(76)90064-6

[71] S. S. Gubser, Phys. Rev. D **82**, 085027 (2010) doi:10.1103/PhysRevD.82.085027 [arXiv:1006.0006 [hep-th]].

[72] L. D. Landau and E. M. Lifshitz, Course of Theoretical Physics Volume 10, "Physical Kinetics", Pergamon Press (1981).

[73] K. Dusling, G. D. Moore and D. Teaney, Phys. Rev. C **81**, 034907 (2010) doi:10.1103/PhysRevC.81.034907 [arXiv:0909.0754 [nucl-th]].

[74] H. Grad, Commun. Pure Appl. Math. **2**, 331 (1949).

[75] W. Israel and J. M. Stewart, Phys. Lett. A **58**, 213 (1976).

[76] W. Israel and J. M. Stewart, Annals Phys. **118**, 341 (1979). doi:10.1016/0003-4916(79)90130-1

[77] R. Baier, P. Romatschke and U. A. Wiedemann, Nucl. Phys. A **782**, 313 (2007) doi:10.1016/j.nuclphysa.2006.10.016 [nucl-th/0604006].

[78] P. Romatschke, Int. J. Mod. Phys. E **19**, 1 (2010) doi:10.1142/S0218301310014613 [arXiv:0902.3663 [hep-ph]].

[79] E. Calzetta and B. L. Hu, Phys. Rev. D **37**, 2878 (1988). doi:10.1103/PhysRevD.37.2878

[80] J. P. Blaizot and E. Iancu, Phys. Rev. Lett. **70**, 3376 (1993) doi:10.1103/PhysRevLett.70.3376 [hep-ph/9301236].

[81] E. A. Calzetta, B. L. Hu and S. A. Ramsey, Phys. Rev. D **61**, 125013 (2000) doi:10.1103/PhysRevD.61.125013 [hep-ph/9910334].

[82] J. P. Blaizot and E. Iancu, Nucl. Phys. B **557**, 183 (1999) doi:10.1016/S0550-3213(99)00341-7 [hep-ph/9903389].

[83] P. B. Arnold, G. D. Moore and L. G. Yaffe, JHEP **0301**, 030 (2003) doi:10.1088/1126-6708/2003/01/030 [hep-ph/0209353].

[84] U. W. Heinz, Phys. Rev. Lett. **51**, 351 (1983). doi:10.1103/PhysRevLett.51.351

[85] E. Braaten and R. D. Pisarski, Nucl. Phys. B **337**, 569 (1990). doi:10.1016/0550-3213(90)90508-B

[86] J. Frenkel and J. C. Taylor, Nucl. Phys. B **334**, 199 (1990). doi:10.1016/0550-3213(90)90661-V

[87] J. C. Taylor and S. M. H. Wong, Nucl. Phys. B **346**, 115 (1990). doi:10.1016/0550-3213(90)90240-E

[88] P. F. Kelly, Q. Liu, C. Lucchesi and C. Manuel, Phys. Rev. D **50**, 4209 (1994) doi:10.1103/PhysRevD.50.4209 [hep-ph/9406285].

[89] J. P. Blaizot and E. Iancu, Phys. Rept. **359**, 355 (2002) doi:10.1016/S0370-1573(01)00061-8 [hep-ph/0101103].

[90] M. A. York and G. D. Moore, Phys. Rev. D **79**, 054011 (2009) doi:10.1103/PhysRevD.79.054011 [arXiv:0811.0729 [hep-ph]].

[91] P. Romatschke and D. T. Son, Phys. Rev. D **80**, 065021 (2009) doi:10.1103/PhysRevD.80.065021 [arXiv:0903.3946 [hep-ph]].

[92] S. Bhattacharyya, V. E. Hubeny, S. Minwalla and M. Rangamani, JHEP **0802**, 045 (2008) doi:10.1088/1126-6708/2008/02/045 [arXiv:0712.2456 [hep-th]].

[93] R. Baier, P. Romatschke, D. T. Son, A. O. Starinets and M. A. Stephanov, JHEP **0804**, 100 (2008) doi:10.1088/1126-6708/2008/04/100 [arXiv:0712.2451 [hep-th]].

[94] E. Iancu and R. Venugopalan, In *Hwa, R.C. (ed.) et al.: Quark gluon plasma* 249-3363 doi:10.1142/9789812795533_0005 [hep-ph/0303204].

[95] F. Gelis, E. Iancu, J. Jalilian-Marian and R. Venugopalan, Ann. Rev. Nucl. Part. Sci. **60**, 463 (2010) doi:10.1146/annurev.nucl.010909.083629 [arXiv:1002.0333 [hep-ph]].

[96] A. Dumitru, K. Dusling, F. Gelis, J. Jalilian-Marian, T. Lappi and R. Venugopalan, Phys. Lett. B **697**, 21 (2011) doi:10.1016/j.physletb.2011.01.024 [arXiv:1009.5295 [hep-ph]].

[97] B. I. Abelev *et al.* [STAR Collaboration], Phys. Rev. C **80**, 064912 (2009) doi:10.1103/PhysRevC.80.064912 [arXiv:0909.0191 [nucl-ex]].

[98] R. D. Ball *et al.* [NNPDF Collaboration], JHEP **1504**, 040 (2015) doi:10.1007/JHEP04(2015)040 [arXiv:1410.8849 [hep-ph]].

[99] V. Khachatryan *et al.* [CMS Collaboration], Phys. Rev. Lett. **105**, 022002 (2010) doi:10.1103/PhysRevLett.105.022002 [arXiv:1005.3299 [hep-ex]].

[100] P. B. Arnold, Int. J. Mod. Phys. E **16**, 2555 (2007) doi:10.1142/S021830130700832X [arXiv:0708.0812 [hep-ph]].

[101] P. B. Arnold, J. Lenaghan, G. D. Moore and L. G. Yaffe, Phys. Rev. Lett. **94**, 072302 (2005) doi:10.1103/PhysRevLett.94.072302 [nucl-th/0409068].

[102] P. F. Kolb and U. W. Heinz, In *Hwa, R.C. (ed.) et al.: Quark gluon plasma* 634-714 [nucl-th/0305084].

[103] M. Luzum and P. Romatschke, Phys. Rev. C **78**, 034915 (2008) Erratum: [Phys. Rev. C **79**, 039903 (2009)] doi:10.1103/PhysRevC.78.034915, 10.1103/PhysRevC.79.039903 [arXiv:0804.4015 [nucl-th]].

[104] W. Broniowski, M. Chojnacki, W. Florkowski and A. Kisiel, Phys. Rev. Lett. **101**, 022301 (2008) doi:10.1103/PhysRevLett.101.022301 [arXiv:0801.4361 [nucl-th]].

[105] H. Song, S. A. Bass, U. Heinz, T. Hirano and C. Shen, Phys. Rev. C **83**, 054910 (2011) Erratum: [Phys. Rev. C **86**, 059903 (2012)] doi:10.1103/PhysRevC.83.054910, 10.1103/PhysRevC.86.059903 [arXiv:1101.4638 [nucl-th]].

[106] B. Schenke, S. Jeon and C. Gale, Phys. Rev. Lett. **106**, 042301 (2011) doi:10.1103/PhysRevLett.106.042301 [arXiv:1009.3244 [hep-ph]].

[107] J. J. Friess, S. S. Gubser, G. Michalogiorgakis and S. S. Pufu, JHEP **0704**, 080 (2007) doi:10.1088/1126-6708/2007/04/080 [hep-th/0611005].

[108] A. Donnachie and P. V. Landshoff, Phys. Lett. B **437**, 408 (1998) doi:10.1016/S0370-2693(98)00899-5 [hep-ph/9806344].

[109] V. N. Gribov and L. N. Lipatov, Sov. J. Nucl. Phys. **15**, 438 (1972) [Yad. Fiz. **15**, 781 (1972)].

[110] Y. L. Dokshitzer, Sov. Phys. JETP **46** (1977) 641 [Zh. Eksp. Teor. Fiz. **73** (1977) 1216].

[111] G. Altarelli and G. Parisi, Nucl. Phys. B **126**, 298 (1977). doi:10.1016/0550-3213(77)90384-4

[112] E. Iancu, Nucl. Phys. Proc. Suppl. **191**, 281 (2009) doi:10.1016/j.nuclphysbps.2009.03.135 [arXiv:0901.0986 [hep-ph]].

[113] L. N. Lipatov, Sov. J. Nucl. Phys. **23**, 338 (1976) [Yad. Fiz. **23**, 642 (1976)].

[114] E. A. Kuraev, L. N. Lipatov and V. S. Fadin, Sov. Phys. JETP **45** (1977) 199 [Zh. Eksp. Teor. Fiz. **72** (1977) 377].

[115] I. I. Balitsky and L. N. Lipatov, Sov. J. Nucl. Phys. **28**, 822 (1978) [Yad. Fiz. **28**, 1597 (1978)].

[116] A. N. Kolmogorov, N. G. Petrovskii, N. S. Piskunov, Moscow Univ. Bull. Math., **1** (1937), 1.

[117] R. A. Fisher, Ann. Eugenics, **7** (1937), 353.

[118] J. Jalilian-Marian, A. Kovner, A. Leonidov and H. Weigert, Nucl. Phys. B **504**, 415 (1997) doi:10.1016/S0550-3213(97)00440-9 [hep-ph/9701284].

[119] H. Weigert, Nucl. Phys. A **703**, 823 (2002) doi:10.1016/S0375-9474(01)01668-2 [hep-ph/0004044].

[120] E. Ferreiro, E. Iancu, A. Leonidov and L. McLerran, Nucl. Phys. A **703**, 489 (2002) doi:10.1016/S0375-9474(01)01329-X [hep-ph/0109115].

[121] J. L Albacete, "Saturation Physics", Fall meeting of the GDR PH-QCD: nucleon and nucleus structure studies with a LHC fixed-target experiment and electron-ion colliders, Oct 2011, IPN Orsay.

[122] F. Gelis, J. Phys. Conf. Ser. **381**, 012021 (2012) doi:10.1088/1742-6596/381/1/012021 [arXiv:1110.1544 [hep-ph]].

[123] A. Dumitru, L. McLerran and V. Skokov, Phys. Lett. B **743**, 134 (2015) doi:10.1016/j.physletb.2015.02.046 [arXiv:1410.4844 [hep-ph]].

[124] B. Schenke, S. Schlichting and R. Venugopalan, Phys. Lett. B **747**, 76 (2015) doi:10.1016/j.physletb.2015.05.051 [arXiv:1502.01331 [hep-ph]].

[125] T. Altinoluk, N. Armesto, G. Beuf, A. Kovner and M. Lublinsky, Phys. Lett. B **751**, 448 (2015) doi:10.1016/j.physletb.2015.10.072 [arXiv:1503.07126 [hep-ph]].

[126] A. Esposito and M. Gyulassy, Phys. Lett. B **747**, 433 (2015) doi:10.1016/j.physletb.2015.06.037 [arXiv:1505.03734 [hep-ph]].

[127] T. Lappi, B. Schenke, S. Schlichting and R. Venugopalan, JHEP **1601**, 061 (2016) doi:10.1007/JHEP01(2016)061 [arXiv:1509.03499 [hep-ph]].

[128] B. Schenke, S. Schlichting, P. Tribedy and R. Venugopalan, Phys. Rev. Lett. **117**, no. 16, 162301 (2016) doi:10.1103/PhysRevLett.117.162301 [arXiv:1607.02496 [hep-ph]].

[129] Y. Hagiwara, Y. Hatta, B. W. Xiao and F. Yuan, Phys. Lett. B **771**, 374 (2017) doi:10.1016/j.physletb.2017.05.083 [arXiv:1701.04254 [hep-ph]].

[130] K. Dusling, M. Mace and R. Venugopalan, Phys. Rev. Lett. **120**, no. 4, 042002 (2018) doi:10.1103/PhysRevLett.120.042002 [arXiv:1705.00745 [hep-ph]].

[131] B. Schenke, P. Tribedy and R. Venugopalan, Phys. Rev. Lett. **108**, 252301 (2012) doi:10.1103/PhysRevLett.108.252301 [arXiv:1202.6646 [nucl-th]].

[132] C. Gale, S. Jeon, B. Schenke, P. Tribedy and R. Venugopalan, Phys. Rev. Lett. **110**, no. 1, 012302 (2013) doi:10.1103/PhysRevLett.110.012302 [arXiv:1209.6330 [nucl-th]].

[133] B. Schenke and S. Schlichting, Nucl. Phys. A **967**, 285 (2017) doi:10.1016/j.nuclphysa.2017.05.028 [arXiv:1704.03018 [hep-ph]].

[134] S. Chatrchyan *et al.* [CMS Collaboration], Phys. Lett. B **718**, 795 (2013) [arXiv:1210.5482 [nucl-ex]].

[135] B. Abelev *et al.* [ALICE Collaboration], Phys. Lett. B **719**, 29 (2013) [arXiv:1212.2001 [nucl-ex]].

[136] G. Aad *et al.* [ATLAS Collaboration], Phys. Rev. Lett. **110**, no. 18, 182302 (2013) [arXiv:1212.5198 [hep-ex]].

[137] A. Adare *et al.* [PHENIX Collaboration], Phys. Rev. Lett. **111**, no. 21, 212301 (2013) [arXiv:1303.1794 [nucl-ex]].

[138] F. Wang [STAR Collaboration], Nucl. Phys. A **932**, 392 (2013) [arXiv:1404.2674 [nucl-ex]].

[139] I. Kozlov, M. Luzum, G. Denicol, S. Jeon and C. Gale, arXiv:1405.3976 [nucl-th].

[140] S. Chatrchyan *et al.* [CMS Collaboration], Eur. Phys. J. C **74**, no. 6, 2847 (2014) [arXiv:1307.3442 [hep-ex]].

[141] J. Y. Ollitrault and F. G. Gardim, Nucl. Phys. A **904-905**, 75c (2013) [arXiv:1210.8345 [nucl-th]].

[142] K. Popper, "The Logic of Scientific Discovery", Routledge (1959).

[143] V. Khachatryan *et al.* [CMS Collaboration], arXiv:1503.01692 [nucl-ex].

[144] S. Ryu, J. F. Paquet, C. Shen, G. Denicol, B. Schenke, S. Jeon and C. Gale, Phys. Rev. C **97**, no. 3, 034910 (2018) doi:10.1103/PhysRevC.97.034910 [arXiv:1704.04216 [nucl-th]].

[145] T. Schäfer, Physics **2**, 88 (2009).

[146] C. Gale, S. Jeon and B. Schenke, Int. J. Mod. Phys. A **28**, 1340011 (2013) doi:10.1142/S0217751X13400113 [arXiv:1301.5893 [nucl-th]].

[147] P. Huovinen and P. Petreczky, Nucl. Phys. A **837**, 26 (2010) doi:10.1016/j.nuclphysa.2010.02.015 [arXiv:0912.2541 [hep-ph]].

[148] L. D. Landau and E. M. Lifshitz, Course of Theoretical Physics Volume 2, "The Classical Theory of Fields", Butterworth-Heinemann (1975).

[149] K. H. Ackermann *et al.* [STAR Collaboration], Phys. Rev. Lett. **86**, 402 (2001) doi:10.1103/PhysRevLett.86.402 [nucl-ex/0009011].

[150] R. Nouicer, Eur. Phys. J. Plus **131**, no. 3, 70 (2016) doi:10.1140/epjp/i2016-16070-2 [arXiv:1512.08993 [nucl-ex]].

[151] A. M. Poskanzer and S. A. Voloshin, Phys. Rev. C **58**, 1671 (1998) doi:10.1103/PhysRevC.58.1671 [nucl-ex/9805001].

[152] E. V. Shuryak, Phys. Rept. **61**, 71 (1980). doi:10.1016/0370-1573(80)90105-2

[153] J. D. Bjorken, FERMILAB-PUB-82-59-THY and erratum (unpublished).

[154] K. Adcox *et al.* [PHENIX Collaboration], Phys. Rev. Lett. **88**, 022301 (2002) doi:10.1103/PhysRevLett.88.022301 [nucl-ex/0109003].

[155] C. Adler *et al.* [STAR Collaboration], Phys. Rev. Lett. **90**, 082302 (2003) doi:10.1103/PhysRevLett.90.082302 [nucl-ex/0210033].

[156] R. Hanbury Brown and R. Q. Twiss, Nature **178**, 1046 (1956). doi:10.1038/1781046a0

[157] C. Adler *et al.* [STAR Collaboration], Phys. Rev. Lett. **87**, 082301 (2001) doi:10.1103/PhysRevLett.87.082301 [nucl-ex/0107008].

[158] U. W. Heinz and P. F. Kolb, hep-ph/0204061.

[159] S. A. Voloshin, J. Phys. G **38**, 124097 (2011) doi:10.1088/0954-3899/38/12/124097 [arXiv:1106.5830 [nucl-th]].

[160] T. Niida [PHENIX Collaboration], Nucl. Phys. A **904-905**, 439c (2013) doi:10.1016/j.nuclphysa.2013.02.043 [arXiv:1304.2876 [nucl-ex]].

[161] C. Nonaka and M. Asakawa, PTEP **2012**, 01A208 (2012) doi:10.1093/ptep/pts014 [arXiv:1204.4795 [nucl-th]].

[162] T. Lappi, Phys. Lett. B **643**, 11 (2006) doi:10.1016/j.physletb.2006.10.017 [hep-ph/0606207].

[163] P. Romatschke and J. D. Hogg, JHEP **1304**, 048 (2013) doi:10.1007/JHEP04(2013)048 [arXiv:1301.2635 [hep-th]].

[164] D. Bazow, U. W. Heinz and M. Strickland, Phys. Rev. C **90**, no. 5, 054910 (2014) doi:10.1103/PhysRevC.90.054910 [arXiv:1311.6720 [nucl-th]].

[165] M. Alqahtani, M. Nopoush and M. Strickland, arXiv:1712.03282 [nucl-th].

[166] P. B. Arnold, G. D. Moore and L. G. Yaffe, JHEP **0112**, 009 (2001) doi:10.1088/1126-6708/2001/12/009 [hep-ph/0111107].

[167] C. Shen, U. W. Heinz, J. F. Paquet, I. Kozlov and C. Gale, Phys. Rev. C **91**, no. 2, 024908 (2015) doi:10.1103/PhysRevC.91.024908 [arXiv:1308.2111 [nucl-th]].

[168] F. Cooper and G. Frye, Phys. Rev. D **10**, 186 (1974). doi:10.1103/PhysRevD.10.186

[169] F. Cooper, G. Frye and E. Schonberg, Phys. Rev. D **11**, 192 (1975). doi:10.1103/PhysRevD.11.192

[170] S. A. Bass *et al.*, Prog. Part. Nucl. Phys. **41**, 255 (1998) [Prog. Part. Nucl. Phys. **41**, 225 (1998)] doi:10.1016/S0146-6410(98)00058-1 [nucl-th/9803035].

[171] M. Bleicher, E. Zabrodin, C. Spieles, S. A. Bass, C. Ernst, S. Soff, L. Bravina and M. Belkacem *et al.*, J. Phys. G **25**, 1859 (1999).

[172] U. W. Heinz, hep-ph/0407360.

[173] H. Sorge, Phys. Rev. Lett. **82**, 2048 (1999) doi:10.1103/PhysRevLett.82.2048 [nucl-th/9812057].

[174] J. Y. Ollitrault, Phys. Rev. D **46**, 229 (1992). doi:10.1103/PhysRevD.46.229

[175] J. D. Bjorken, Phys. Rev. D **27**, 140 (1983). doi:10.1103/PhysRevD.27.140

[176] M. L. Miller, K. Reygers, S. J. Sanders and P. Steinberg, Ann. Rev. Nucl. Part. Sci. **57**, 205 (2007) doi:10.1146/annurev.nucl.57.090506.123020 [nucl-ex/0701025].

[177] A. Bialas, M. Bleszynski and W. Czyz, Nucl. Phys. B **111**, 461 (1976). doi:10.1016/0550-3213(76)90329-1

[178] D. Kharzeev, C. Lourenco, M. Nardi and H. Satz, Z. Phys. C **74**, 307 (1997) doi:10.1007/s002880050392 [hep-ph/9612217].

[179] D. Kharzeev and M. Nardi, Phys. Lett. B **507**, 121 (2001) doi:10.1016/S0370-2693(01)00457-9 [nucl-th/0012025].

[180] B. S. Everitt, A. Skrondal , Cambridge Dictionary of Statistics, Cambridge University Press (2010).

[181] H. Mäntysaari, B. Schenke, C. Shen and P. Tribedy, Nucl. Phys. A **967**, 317 (2017) doi:10.1016/j.nuclphysa.2017.04.017 [arXiv:1705.03735 [nucl-th]].

[182] P. Bożek, W. Broniowski and M. Rybczyński, Phys. Rev. C **94**, no. 1, 014902 (2016) doi:10.1103/PhysRevC.94.014902 [arXiv:1604.07697 [nucl-th]].

[183] R. D. Weller and P. Romatschke, Phys. Lett. B **774**, 351 (2017) doi:10.1016/j.physletb.2017.09.077 [arXiv:1701.07145 [nucl-th]].

[184] P. Huovinen, P. F. Kolb, U. W. Heinz, P. V. Ruuskanen and S. A. Voloshin, Phys. Lett. B **503**, 58 (2001) doi:10.1016/S0370-2693(01)00219-2 [hep-ph/0101136].

[185] B. Alver *et al.* [PHOBOS Collaboration], Phys. Rev. Lett. **98**, 242302 (2007) doi:10.1103/PhysRevLett.98.242302 [nucl-ex/0610037].

[186] A. Adare *et al.* [PHENIX Collaboration], Phys. Rev. Lett. **98**, 162301 (2007) doi:10.1103/PhysRevLett.98.162301 [nucl-ex/0608033].

[187] B. Alver and G. Roland, Phys. Rev. C **81**, 054905 (2010) Erratum: [Phys. Rev. C **82**, 039903 (2010)] doi:10.1103/PhysRevC.82.039903, 10.1103/PhysRevC.81.054905 [arXiv:1003.0194 [nucl-th]].

[188] S. A. Voloshin, A. M. Poskanzer, A. Tang and G. Wang, Phys. Lett. B **659**, 537 (2008) doi:10.1016/j.physletb.2007.11.043 [arXiv:0708.0800 [nucl-th]].

[189] Z. Qiu, C. Shen and U. Heinz, Phys. Lett. B **707**, 151 (2012) doi:10.1016/j.physletb.2011.12.041 [arXiv:1110.3033 [nucl-th]].

[190] L. V. Gribov, E. M. Levin and M. G. Ryskin, Phys. Rept. **100**, 1 (1983). doi:10.1016/0370-1573(83)90022-4

[191] T. Hirano, U. W. Heinz, D. Kharzeev, R. Lacey and Y. Nara, Phys. Lett. B **636**, 299 (2006) doi:10.1016/j.physletb.2006.03.060 [nucl-th/0511046].

[192] S. McDonald, C. Shen, F. Fillion-Gourdeau, S. Jeon and C. Gale, Phys. Rev. C **95**, no. 6, 064913 (2017) doi:10.1103/PhysRevC.95.064913 [arXiv:1609.02958 [hep-ph]].

[193] L. D. McLerran and R. Venugopalan, Phys. Rev. D **49**, 2233 (1994) doi:10.1103/PhysRevD.49.2233 [hep-ph/9309289].

[194] J. Bartels, K. J. Golec-Biernat and H. Kowalski, Phys. Rev. D **66**, 014001 (2002) doi:10.1103/PhysRevD.66.014001 [hep-ph/0203258].

[195] H. Kowalski and D. Teaney, Phys. Rev. D **68**, 114005 (2003) doi:10.1103/PhysRevD.68.114005 [hep-ph/0304189].

[196] P. Tribedy and R. Venugopalan, Nucl. Phys. A **850**, 136 (2011) Erratum: [Nucl. Phys. A **859**, 185 (2011)] doi:10.1016/j.nuclphysa.2011.04.008, 10.1016/j.nuclphysa.2010.12.006 [arXiv:1011.1895 [hep-ph]].

[197] H. Kowalski, L. Motyka and G. Watt, Phys. Rev. D **74**, 074016 (2006) doi:10.1103/PhysRevD.74.074016 [hep-ph/0606272].

[198] F. Gelis, T. Lappi and R. Venugopalan, Phys. Rev. D **78**, 054019 (2008) doi:10.1103/PhysRevD.78.054019 [arXiv:0804.2630 [hep-ph]].

[199] J. S. Moreland, J. E. Bernhard and S. A. Bass, Phys. Rev. C **92**, no. 1, 011901 (2015) doi:10.1103/PhysRevC.92.011901 [arXiv:1412.4708 [nucl-th]].

[200] J. E. Bernhard, J. S. Moreland, S. A. Bass, J. Liu and U. Heinz, Phys. Rev. C **94**, no. 2, 024907 (2016) doi:10.1103/PhysRevC.94.024907 [arXiv:1605.03954 [nucl-th]].

[201] D. Kharzeev, E. Levin and M. Nardi, Nucl. Phys. A **747**, 609 (2005) doi:10.1016/j.nuclphysa.2004.10.018 [hep-ph/0408050].

[202] K. J. Eskola, P. V. Ruuskanen, S. S. Rasanen and K. Tuominen, Nucl. Phys. A **696**, 715 (2001) doi:10.1016/S0375-9474(01)01207-6 [hep-ph/0104010].

[203] B. Schenke, C. Shen, P. Tribedy, "Elucidating the properties of hot nuclear matter with a comprehensive description of ultra-relativistic heavy-ion collisions", Contribution ID 307, Quark Matter 2018.

[204] K. J. Eskola, H. Niemi, R. Paatelainen and K. Tuominen, Nucl. Phys. A **967**, 313 (2017) doi:10.1016/j.nuclphysa.2017.04.038 [arXiv:1704.04060 [hep-ph]].

[205] B. Alver *et al.* [PHOBOS Collaboration], Phys. Rev. C **81**, 034915 (2010) doi:10.1103/PhysRevC.81.034915 [arXiv:1002.0534 [nucl-ex]].

[206] Wikipedia, "Pseudorapidity", `https://en.wikipedia.org/wiki/Pseudorapidity`.

[207] F. Gelis and B. Schenke, Ann. Rev. Nucl. Part. Sci. **66**, 73 (2016) doi:10.1146/annurev-nucl-102115-044651 [arXiv:1604.00335 [hep-ph]].

[208] G. S. Denicol, S. Jeon and C. Gale, Phys. Rev. C **90**, no. 2, 024912 (2014) doi:10.1103/PhysRevC.90.024912 [arXiv:1403.0962 [nucl-th]].

[209] I. Kozlov, M. Luzum, G. S. Denicol, S. Jeon and C. Gale, Nucl. Phys. A **931**, 1045 (2014) doi:10.1016/j.nuclphysa.2014.09.054 [arXiv:1412.3147 [nucl-th]].

[210] C. Shen and B. Schenke, PoS CPOD **2017**, 006 (2018) doi:10.22323/1.311.0006 [arXiv:1711.10544 [nucl-th]].

[211] K. Walsh, "Supercomputing the Transition from Ordinary to Extraordinary Forms of Matter", `https://www.bnl.gov/newsroom/news.php?a=24281`.

[212] The Millennium Prize Problems, `http://www.claymath.org/millennium-problems/millennium-prize-problems`.

[213] A. Kurganov, and E. Tadmor, Journal of Computational Physics, **160**, 241 (2000).

[214] B. Schenke, S. Jeon and C. Gale, Phys. Rev. C **82**, 014903 (2010) [arXiv:1004.1408 [hep-ph]].

[215] S. Jeon, "Lectures on Partial Differential Equations in Physics", unpublished. Illustations by C. Shen.

[216] H. Nessyahu, and E. Tadmor, Journal of Computational Physics, **87**, 408 (1990).

[217] P. Bozek, Phys. Rev. C **81**, 034909 (2010) doi:10.1103/PhysRevC.81.034909 [arXiv:0911.2397 [nucl-th]].

[218] K. Hagiwara *et al.* [Particle Data Group], Phys. Rev. D **66**, 010001 (2002). doi:10.1103/PhysRevD.66.010001

[219] R. Peschanski and E. N. Saridakis, Phys. Rev. C **80**, 024907 (2009) doi:10.1103/PhysRevC.80.024907 [arXiv:0906.0941 [nucl-th]].

[220] P. F. Kolb and R. Rapp, Phys. Rev. C **67**, 044903 (2003) doi:10.1103/PhysRevC.67.044903 [hep-ph/0210222].

[221] A. Milov [ATLAS Collaboration], arXiv:1403.5738 [nucl-ex].

[222] S. Chatrchyan *et al.* [CMS Collaboration], Phys. Lett. B **724**, 213 (2013) [arXiv:1305.0609 [nucl-ex]]; ; Additional data on the CMS public wiki: `https://twiki.cern.ch/twiki/bin/view/CMSPublic/PhysicsResultsHIN13002`

[223] P. Bozek and I. Wyskiel, Phys. Rev. C **81**, 054902 (2010) [arXiv:1002.4999 [nucl-th]].

[224] B. B. Back *et al.*, Phys. Rev. Lett. **91**, 052303 (2003) doi:10.1103/PhysRevLett.91.052303 [nucl-ex/0210015].

[225] I. G. Bearden *et al.* [BRAHMS Collaboration], Phys. Rev. Lett. **88**, 202301 (2002) doi:10.1103/PhysRevLett.88.202301 [nucl-ex/0112001].

[226] B. B. Back *et al.* [PHOBOS Collaboration], Phys. Rev. Lett. **97**, 012301 (2006) doi:10.1103/PhysRevLett.97.012301 [nucl-ex/0511045].

[227] B. I. Abelev *et al.* [STAR Collaboration], Phys. Rev. Lett. **101**, 252301 (2008) doi:10.1103/PhysRevLett.101.252301 [arXiv:0807.1518 [nucl-ex]].

[228] K. Aamodt *et al.* [ALICE Collaboration], Eur. Phys. J. C **68**, 89 (2010) [arXiv:1004.3034 [hep-ex]].

[229] V. Khachatryan *et al.* [CMS Collaboration], JHEP **1101**, 079 (2011) [arXiv:1011.5531 [hep-ex]].

[230] P. Bozek, Phys. Rev. C **85**, 014911 (2012) [arXiv:1112.0915 [hep-ph]].

[231] P. Bozek and W. Broniowski, Phys. Lett. B **718**, 1557 (2013) [arXiv:1211.0845 [nucl-th]].

[232] P. Bozek and W. Broniowski, Phys. Rev. C **88**, no. 1, 014903 (2013) [arXiv:1304.3044 [nucl-th]].

[233] A. Bzdak, B. Schenke, P. Tribedy and R. Venugopalan, Phys. Rev. C **87**, no. 6, 064906 (2013) [arXiv:1304.3403 [nucl-th]].

[234] G. Y. Qin and B. Müller, Phys. Rev. C **89**, no. 4, 044902 (2014) [arXiv:1306.3439 [nucl-th]].

[235] B. Schenke and R. Venugopalan, Phys. Rev. Lett. **113**, 102301 (2014) [arXiv:1405.3605 [nucl-th]].

[236] H. Niemi, K. J. Eskola and R. Paatelainen, Phys. Rev. C **93**, no. 2, 024907 (2016) doi:10.1103/PhysRevC.93.024907 [arXiv:1505.02677 [hep-ph]].

[237] M. Luzum and H. Petersen, J. Phys. G **41**, 063102 (2014) [arXiv:1312.5503 [nucl-th]].

[238] B. H. Alver, C. Gombeaud, M. Luzum and J. Y. Ollitrault, Phys. Rev. C **82**, 034913 (2010) [arXiv:1007.5469 [nucl-th]].

[239] F. G. Gardim, F. Grassi, M. Luzum and J. Y. Ollitrault, Phys. Rev. C **85**, 024908 (2012) [arXiv:1111.6538 [nucl-th]].

[240] G. Basar and D. Teaney, Nucl. Phys. A **931**, 931 (2014) [arXiv:1408.3411 [hep-ph]].

[241] G. Torrieri, Phys. Rev. C **89**, no. 2, 024908 (2014) [arXiv:1310.3529 [nucl-th]].

[242] I.A. Kvasnikov, Thermodynamics and Statistical Mechanics Volume 2, "The theory of equilibrium systems Statistical Physics", Editorial URSS (2002).

[243] J. Takahashi, B. M. Tavares, W. L. Qian, R. Andrade, F. Grassi, Y. Hama, T. Kodama and N. Xu, Phys. Rev. Lett. **103**, 242301 (2009) doi:10.1103/PhysRevLett.103.242301 [arXiv:0902.4870 [nucl-th]].

[244] M. Luzum, Phys. Lett. B **696**, 499 (2011) doi:10.1016/j.physletb.2011.01.013 [arXiv:1011.5773 [nucl-th]].

[245] A. Adare *et al.* [PHENIX Collaboration], Phys. Rev. Lett. **109**, 122302 (2012) doi:10.1103/PhysRevLett.109.122302 [arXiv:1105.4126 [nucl-ex]].

[246] D. Lohner [ALICE Collaboration], J. Phys. Conf. Ser. **446**, 012028 (2013) doi:10.1088/1742-6596/446/1/012028 [arXiv:1212.3995 [hep-ex]].

[247] B. Alver *et al.* [PHOBOS Collaboration], PoS CFRNC **2006**, 023 (2006) [nucl-ex/0608025].

[248] A. R. Timmins [ALICE Collaboration], J. Phys. Conf. Ser. **446**, 012031 (2013) doi:10.1088/1742-6596/446/1/012031 [arXiv:1301.6084 [nucl-ex]].

[249] G. Aad *et al.* [ATLAS Collaboration], JHEP **1311**, 183 (2013) doi:10.1007/JHEP11(2013)183 [arXiv:1305.2942 [hep-ex]].

[250] S. A. Voloshin, A. M. Poskanzer and R. Snellings, Landolt-Bornstein **23**, 293 (2010) doi:10.1007/978-3-642-01539-7_10 [arXiv:0809.2949 [nucl-ex]].

[251] M. Luzum and J. Y. Ollitrault, Phys. Rev. C **87**, no. 4, 044907 (2013) doi:10.1103/PhysRevC.87.044907 [arXiv:1209.2323 [nucl-ex]].

[252] N. Borghini, P. M. Dinh and J. Y. Ollitrault, Phys. Rev. C **64**, 054901 (2001) doi:10.1103/PhysRevC.64.054901 [nucl-th/0105040].

[253] C. Adler *et al.* [STAR Collaboration], Phys. Rev. C **66**, 034904 (2002) doi:10.1103/PhysRevC.66.034904 [nucl-ex/0206001].

[254] F. G. Gardim, F. Grassi, M. Luzum and J. Y. Ollitrault, Phys. Rev. C **87**, no. 3, 031901 (2013) [arXiv:1211.0989 [nucl-th]].

[255] E. V. Shuryak, Nucl. Phys. A **750**, 64 (2005) doi:10.1016/j.nuclphysa.2004.10.022 [hep-ph/0405066].

[256] K. Aamodt *et al.* [ALICE Collaboration], Phys. Lett. B **708**, 249 (2012) [arXiv:1109.2501 [nucl-ex]].

[257] S. Chatrchyan *et al.* [CMS Collaboration], Eur. Phys. J. C **72**, 2012 (2012) doi:10.1140/epjc/s10052-012-2012-3 [arXiv:1201.3158 [nucl-ex]].

[258] E. Retinskaya, M. Luzum and J. Y. Ollitrault, Phys. Rev. Lett. **108**, 252302 (2012) [arXiv:1203.0931 [nucl-th]].

[259] C. Shen, Z. Qiu and U. Heinz, arXiv:1502.04636 [nucl-th].

[260] Y. Zhou [ALICE Collaboration], Nucl. Phys. A **931**, 949 (2014) [arXiv:1407.7677 [nucl-ex]]; You Zhou, PhD Thesis, 2015, Utrecht University

[261] G. Aad *et al.* [ATLAS Collaboration], Phys. Rev. C **90**, no. 4, 044906 (2014) [arXiv:1409.1792 [hep-ex]].

[262] D. Devetak [CMS Collaboration], Nucl. Phys. A **931**, 954 (2014).

[263] P. Huovinen and H. Petersen, Eur. Phys. J. A **48**, 171 (2012) doi:10.1140/epja/i2012-12171-9 [arXiv:1206.3371 [nucl-th]].

[264] H. Niemi and G. S. Denicol, arXiv:1404.7327 [nucl-th].

[265] C. Shen, J. F. Paquet, G. S. Denicol, S. Jeon and C. Gale, Phys. Rev. C **95**, no. 1, 014906 (2017) doi:10.1103/PhysRevC.95.014906 [arXiv:1609.02590 [nucl-th]].

[266] C. Shen, `https://github.com/chunshen1987/hydro_analysis`.

[267] Y. M. Makeenko and A. A. Migdal, Phys. Lett. **88B**, 135 (1979) Erratum: [Phys. Lett. **89B**, 437 (1980)]. doi:10.1016/0370-2693(79)90131-X

[268] H. Sorge, H. Stoecker and W. Greiner, Annals Phys. **192**, 266 (1989). doi:10.1016/0003-4916(89)90136-X

[269] V. Flaminio, W. G. Moorhead, D. R. O. Morrison, and N. Rivoire, CERN, Geneva Report No. CERN-HERA-84-01, (1984).

[270] R. M. Barnett *et al.* [Particle Data Group], Phys. Rev. D **54**, 1 (1996). doi:10.1103/PhysRevD.54.1

[271] G. Giacalone, J. Noronha-Hostler and J. Y. Ollitrault, Phys. Rev. C **95**, no. 5, 054910 (2017) doi:10.1103/PhysRevC.95.054910 [arXiv:1702.01730 [nucl-th]].

[272] H. Mäntysaari, B. Schenke, C. Shen and P. Tribedy, Phys. Lett. B **772**, 681 (2017) doi:10.1016/j.physletb.2017.07.038 [arXiv:1705.03177 [nucl-th]].

[273] U. Heinz, Z. Qiu and C. Shen, Phys. Rev. C **87**, no. 3, 034913 (2013) [arXiv:1302.3535 [nucl-th]].

[274] W. Ke, J. S. Moreland, J. E. Bernhard and S. A. Bass, Phys. Rev. C **96**, no. 4, 044912 (2017) doi:10.1103/PhysRevC.96.044912 [arXiv:1610.08490 [nucl-th]].

[275] P. B. Arnold, C. Dogan and G. D. Moore, Phys. Rev. D **74**, 085021 (2006) doi:10.1103/PhysRevD.74.085021 [hep-ph/0608012].

[276] A. Czajka, K. Dasgupta, C. Gale, S. Jeon, A. Misra, M. Richard and K. Sil, arXiv:1807.07950 [hep-th].

[277] K. Dusling and T. Schäfer, Phys. Rev. C **85**, 044909 (2012) doi:10.1103/PhysRevC.85.044909 [arXiv:1109.5181 [hep-ph]].

[278] D. Fernandez-Fraile and A. Gomez Nicola, Phys. Rev. Lett. **102**, 121601 (2009) doi:10.1103/PhysRevLett.102.121601 [arXiv:0809.4663 [hep-ph]].

[279] J. Noronha-Hostler, J. Noronha and C. Greiner, Phys. Rev. Lett. **103**, 172302 (2009) doi:10.1103/PhysRevLett.103.172302 [arXiv:0811.1571 [nucl-th]].

[280] A. Monnai and T. Hirano, Phys. Rev. C **80**, 054906 (2009) doi:10.1103/PhysRevC.80.054906 [arXiv:0903.4436 [nucl-th]].

[281] P. Bozek, Phys. Rev. C **85**, 034901 (2012) doi:10.1103/PhysRevC.85.034901 [arXiv:1110.6742 [nucl-th]].

[282] H. Song and U. W. Heinz, Phys. Rev. C **81**, 024905 (2010) doi:10.1103/PhysRevC.81.024905 [arXiv:0909.1549 [nucl-th]].

[283] M. Prakash, M. Prakash, R. Venugopalan and G. Welke, Phys. Rept. **227**, 321 (1993). doi:10.1016/0370-1573(93)90092-R

[284] D. Davesne, Phys. Rev. C **53**, 3069 (1996). doi:10.1103/PhysRevC.53.3069

[285] J. W. Chen and J. Wang, Phys. Rev. C **79**, 044913 (2009) doi:10.1103/PhysRevC.79.044913 [arXiv:0711.4824 [hep-ph]].

[286] K. Paech and S. Pratt, Phys. Rev. C **74**, 014901 (2006) Erratum: [Phys. Rev. C **93**, no. 5, 059902 (2016)] doi:10.1103/PhysRevC.74.014901, 10.1103/PhysRevC.93.059902 [nucl-th/0604008].

[287] D. Kharzeev and K. Tuchin, JHEP **0809**, 093 (2008) doi:10.1088/1126-6708/2008/09/093 [arXiv:0705.4280 [hep-ph]].

[288] A. Buchel, Phys. Lett. B **681**, 200 (2009) doi:10.1016/j.physletb.2009.10.007 [arXiv:0908.0108 [hep-th]].

[289] H. B. Meyer, JHEP **1004**, 099 (2010) doi:10.1007/JHEP04(2010)099 [arXiv:1002.3343 [hep-lat]].

[290] G. S. Denicol, T. Kodama, T. Koide and P. Mota, Phys. Rev. C **80**, 064901 (2009) doi:10.1103/PhysRevC.80.064901 [arXiv:0903.3595 [hep-ph]].

[291] J. S. Moreland, J. E. Bernhard and S. A. Bass, arXiv:1808.02106 [nucl-th].

[292] J. F. Paquet, C. Shen, G. Denicol, S. Jeon and C. Gale, Nucl. Phys. A **967**, 429 (2017). doi:10.1016/j.nuclphysa.2017.06.024

[293] B. Schenke, "Elucidating the properties of hot nuclear matter with a comprehensive description of ultra-relativistic heavy-ion collisions", Quark Matter 2018, `http://indico.cern.ch/event/656452/contributions/2869794/`.

[294] J. B. Rose, J. F. Paquet, G. S. Denicol, M. Luzum, B. Schenke, S. Jeon and C. Gale, Nucl. Phys. A **931**, 926 (2014) doi:10.1016/j.nuclphysa.2014.09.044 [arXiv:1408.0024 [nucl-th]].

[295] MADAI collaboration, `http://madai.msu.edu/`.

[296] P. Bozek and W. Broniowski, Phys. Lett. B **752**, 206 (2016) doi:10.1016/j.physletb.2015.11.054 [arXiv:1506.02817 [nucl-th]].

[297] M. Rybczynski, G. Stefanek, W. Broniowski and P. Bozek, Comput. Phys. Commun. **185**, 1759 (2014) doi:10.1016/j.cpc.2014.02.016 [arXiv:1310.5475 [nucl-th]].

[298] P. Bozek, W. Broniowski and A. Olszewski, Phys. Rev. C **91**, 054912 (2015) doi:10.1103/PhysRevC.91.054912 [arXiv:1503.07425 [nucl-th]].

[299] A. Bialas and W. Czyz, Acta Phys. Polon. B **36**, 905 (2005) [hep-ph/0410265].

[300] S. J. Brodsky, J. F. Gunion and J. H. Kuhn, Phys. Rev. Lett. **39**, 1120 (1977). doi:10.1103/PhysRevLett.39.1120

[301] A. Bialas and M. Jezabek, Phys. Lett. B **590**, 233 (2004) doi:10.1016/j.physletb.2004.03.070 [hep-ph/0403254].

[302] H. Petersen, J. Steinheimer, G. Burau, M. Bleicher and H. Stocker, Phys. Rev. C **78**, 044901 (2008) doi:10.1103/PhysRevC.78.044901 [arXiv:0806.1695 [nucl-th]].

[303] K. Werner, I. Karpenko, T. Pierog, M. Bleicher and K. Mikhailov, Phys. Rev. C **82**, 044904 (2010) doi:10.1103/PhysRevC.82.044904 [arXiv:1004.0805 [nucl-th]].

[304] L. G. Pang, G. Y. Qin, V. Roy, X. N. Wang and G. L. Ma, Phys. Rev. C **91**, no. 4, 044904 (2015) doi:10.1103/PhysRevC.91.044904 [arXiv:1410.8690 [nucl-th]].

[305] I. A. Karpenko, P. Huovinen, H. Petersen and M. Bleicher, Phys. Rev. C **91**, no. 6, 064901 (2015) doi:10.1103/PhysRevC.91.064901 [arXiv:1502.01978 [nucl-th]].

[306] A. Monnai and B. Schenke, Phys. Lett. B **752**, 317 (2016) doi:10.1016/j.physletb.2015.11.063 [arXiv:1509.04103 [nucl-th]].

[307] M. Okai, K. Kawaguchi, Y. Tachibana and T. Hirano, Phys. Rev. C **95**, no. 5, 054914 (2017) doi:10.1103/PhysRevC.95.054914 [arXiv:1702.07541 [nucl-th]].

[308] S. S. Padula [CMS Collaboration], EPJ Web Conf. **172**, 05005 (2018). doi:10.1051/epjconf/201817205005

[309] P. Romatschke and U. Romatschke, Phys. Rev. Lett. **99**, 172301 (2007) doi:10.1103/PhysRevLett.99.172301 [arXiv:0706.1522 [nucl-th]].

[310] H. Song, S. A. Bass and U. Heinz, Phys. Rev. C **83**, 024912 (2011) doi:10.1103/PhysRevC.83.024912 [arXiv:1012.0555 [nucl-th]].

[311] J. E. Bernhard, J. S. Moreland and S. A. Bass, Nucl. Phys. A **967**, 293 (2017) doi:10.1016/j.nuclphysa.2017.05.037 [arXiv:1704.04462 [nucl-th]].

[312] K. Welsh, J. Singer and U. W. Heinz, Phys. Rev. C **94**, no. 2, 024919 (2016) doi:10.1103/PhysRevC.94.024919 [arXiv:1605.09418 [nucl-th]].

[313] J. Noronha-Hostler, J. Noronha and M. Gyulassy, Phys. Rev. C **93**, no. 2, 024909 (2016) doi:10.1103/PhysRevC.93.024909 [arXiv:1508.02455 [nucl-th]].

[314] S. McDonald, S. Jeon and C. Gale, arXiv:1807.05409 [nucl-th].

[315] J. I. Kapusta, B. Muller and M. Stephanov, Phys. Rev. C **85**, 054906 (2012) doi:10.1103/PhysRevC.85.054906 [arXiv:1112.6405 [nucl-th]].

[316] M. Singh, C. Shen, S. McDonald, S. Jeon and C. Gale, arXiv:1807.05451 [nucl-th].